Towards the use of geometric parameters and blood-borne species concentration in the prediction of cerebral aneurysm growth and rupture

UNIVERSITY of LIMERICK

OLLSCOIL LUIMNIGH

Towards the Use of Geometric Parameters and Blood-Borne Species Concentration in the Prediction of Cerebral Aneurysm Growth and Rupture

AUTHOR
Jennifer Ann Costelloe

SUPERVISOR
Dr. Michael T. Walsh
DEPARTMENT OF MECHANICAL, AERONAUTICAL AND BIOMEDICAL ENGINEERING, UNIVERSITY OF LIMERICK, IRELAND.

THESIS SUBMITTED IN FULFILMENT OF THE REQUIREMENTS FOR THE DEGREE OF DOCTOR OF PHILOSOPHY AT THE FACULTY OF SCIENCE AND ENGINEERING, UNIVERSITY OF LIMERICK

SUBMITTED TO THE UNIVERSITY OF LIMERICK, JANUARY 2015

DECLARATION

The substance of this thesis is the original work of the author and due reference and acknowledgement has been made, where necessary, to the work of others. No part of this thesis has already been submitted for any degree and is not being concurrently submitted in candidature for any degree.

Candidate:	**Supervisor:**
_____	_____
Ms. Jennifer Costelloe	Dr. Michael Walsh
Date:	**Date:**
_____	_____

DEDICATION

I dedicate this thesis to my mother, for her endless support, guidance and love.

“A mother is one to whom you hurry when you are troubled” Emily Dickenson

ABSTRACT

The rupture of a cerebral aneurysm can have devastating effects, with high rates of morbidity and mortality associated with the event. Approximately 12% of patients who suffer a subarachnoid haemorrhage due to the rupture of an aneurysm die immediately, a further 40% die within one month and one third of those that survive are left with neurological defects. Although the exact mechanisms behind the formation, growth and rupture of aneurysms are unknown, it is believed that a combination of geometric, morphological and haemodynamic factors may play an important role. The primary aim of this research was to investigate the links between geometric features and the mass transport of blood-borne species, and their combined relationship with cerebral aneurysm growth and rupture potential.

Improved imaging techniques have allowed for better detection of unruptured cerebral aneurysms. However, the management of unruptured aneurysms, which are estimated to affect 5-8% of the population, is disputed and current intervention methods carry substantial risks for the patient. Currently, the decision to treat patients is based on the likelihood of aneurysm rupture, thus identifying factors that can adequately indicate aneurysm rupture potential is paramount to distinguishing patients at need of surgical or endovascular intervention from those who can undergo observation. However, an issue with many of the parameters previously shown to have a relationship with rupture is that they cannot be directly measured using typical imaging techniques. Consequently, this study investigated the influence of radiologically relevant and measurable parameters on aneurysm rupture in order to determine if geometric features could be used to predict aneurysm rupture potential. A study of 168 patient-specific cerebral aneurysms suggested that aneurysm rupture risk is increased for aneurysms of the posterior circulation, bifurcating in shape, with increasing tilt angle and with increasing aspect ratio.

Computational fluid dynamics has become a popular tool for haemodynamic studies of cerebral aneurysms. Current studies focus mainly on factors such as inflow jets, impingement sites, wall shear stress and oscillatory shear index: however, few studies address the influence of the mass transport of blood-borne species on aneurysm rupture. Computational analysis of mass transport of the blood-borne species adenosine triphosphate carried out on a sample set of 12 patient-specific aneurysms of both lateral and bifurcating shape. A species concentration threshold is introduced, which indicates the amount of the aneurysm dome that is exposed to concentrations at

1%, 5% , 10% a nd 20 % l ess t han t he i nlet c oncentration, s uggesting a n unde r-expression of vi tal bl ood-borne s pecies. T he c omputational a nalysis id entified aneurysms t hat d emonstrated ar eas o f r educed co ncentration as a r esult o f t heir geometric configuration. Statistical analysis was carried out on the results and rupture probability equations were developed based on the species threshold values, allowing for t he pr ediction of t he r upture s tatus of a n a neurysm t o be m ade ba sed on t he concentration distribution seen within the dome.

Results from the geometric and mass transport studies were tested on an independent cohort of ten patient-specific aneurysms, where the rupture status of 8/10 (80%) of the cohort were correctly predicted by the rupture probability equation based on a species threshold of 1% . F urthermore, a c ombined r upture pr obability equation, de veloped based o n g eometric f eatures a nd t he 1% s pecies c oncentration t hreshold l ed t o t he rupture status of 7/10 (70%) of the aneurysms being correctly predicted.

In pr evious C FD s tudies, i dealised m odels were i nitially us ed t o i dentify general trends in aneurysm haemodynamics. Idealised models can neglect significant aspects of the geometry such as aneurysmal blebs and irregularities of the aneurysm wall, and so in r ecent years a s hift has b een m ade t owards t he u se o f p atient-specific mo dels. Patient-specific s imulations can b e computationally expensive a nd require l arge amounts of medical imaging and flow data, and so in this study it was investigated if representative m odels a re a v iable alternative. T hese r epresentative models w ere developed based on key geometric measurements taken from patient-specific models, and w ere ba sed on t wo l ocations w ithin t he C oW: t he oph thalmic s egment of t he internal carotid artery, representing typical lateral shaped aneurysms, and the sylvian bifurcation, r epresenting bi furcation/terminal t ype a neurysms. R esults from ma ss transport a nalyses w ithin i dealised, pa tient-specific an d r epresentative m odels demonstrated th at while r epresentative mo dels may neglect a spects o f the p atient-specific geometry such as aneurysmal bl ebs o r undulations, improved information is gained compared to simplified, idealised models in the mass transport of blood-borne species within cerebral aneurysms.

Overall, t his s tudy i ndicates t hat aneurysm rupture r isk m ay b e i nfluenced b y t he amount of the aneurysm dome that is exposed to a species concentration less than 1% of the inlet concentration. The results and conclusions presented throughout this thesis contribute a dvancements t o r esearch i n bot h e xperimental a nd c omputational

approaches, increasing our knowledge of the factors that influence cerebral aneurysm rupture potential and may aid in the development of improved aneurysm rupture risk assessment methods, ultimately improving clinical management of this devastating disease.

TABLE OF CONTENTS

TABLE OF FIGURES

LIST OF TABLES

NOMENCLATURE

Symbol	Description	Units
C	concentration of species	mol/m^3
C_{in}	inlet concentration	mol/m^3
C_w	wall concentration	mol/m^3
D	diffusivity	m^2/s
J	diffusional flux	$mol/(m^2s)$
K	mass transfer coefficient	m/s
L	length	m
R	radius	m
Pe	Peclet number	-
Re	Reynolds number	-
Sc	Schmidt number	-
d	diameter	m
g	acceleration due to gravity	m/s^2
n	unit normal vector	-
r	radius	m
t	time	s
u	x component of velocity	m/s
u_{max}	max velocity	m/s
u_{mean}	mean velocity	m/s
u_w	filtration velocity	m/s
v	y component of velocity	m/s
w	z component of velocity	m/s
x	x-direction Cartesian co-ordinate	-
y	y-direction Cartesian co-ordinate	-
z	z-direction Cartesian co-ordinate	-
δ	boundary layer thickness	m
ρ	density	kg/m^3
μ	dynamic viscosity	Pa·s
τ	shear stress	Pa
$\dot{\gamma}$	Shear rate magnitude	s^{-1}
υ	kinematic viscosity	m^2/s

ABBREVIATIONS

ACA	Anterior Cerebral Artery
AChA	Anterior Choroidal Artery
ACoA	Anterior Communicating Artery
AICbA	Anterior Inferior Cerebellar Artery
ADP	Adenosine Diphosphate
AMP	Adenosine Monophosphate
AR	Aspect Ratio
ATP	Adenosine Triphosphate
BA	Basilar Artery
BSMT	Blood Side Mass Transport
CAD	Computer Aided Design
CFD	Computational Fluid Dynamics
CoW	Circle of Willis
CPU	Central Processing Unit
CT	Computed Tomography
ECM	Extracellular Matrix
EEL	External Elastic Lamina
EI	Ellipticity Index
FEM	Finite Element Method
FVM	Finite Volume Method
ICA	Internal Carotid Artery
IEL	Internal Elastic Lamina

ISAT	International Subarachnoid Aneurysm Trial
ISUIA	International Study of Unruptured Intracranial Aneurysms
LDL	Low-Density Lipoprotein
MCA	Middle Cerebral Artery
MRA	Magnetic Resonance Angiogram
NSI	Non-Sphericity Index
PCA	Posterior Cerebral Artery
PCoA	Posterior Communicating Artery
PICbA	Posterior Inferior Cerebellar Artery
PIV	Particle Image Velocimetry
PTV	Particle Track Velocimetry
SAH	Subarachnoid Haemorrhage
SCbA	Superior Cerebellar Artery
STL	Stereolithography
UI	Undulation Index
VA	Vertebral Artery
VTK	Visualization Toolkit
WSMT	Wall Side Mass Transport
WSS	Wall Shear Stress

CHAPTER 1

INTRODUCTION

Chapter 1 Introduction

Cerebral aneurysms are defined as a swelling or dilation of the arterial wall within the cerebral vasculature. Typically saccular in shape, cerebral aneurysms are usually found within the circle of Willis. The rupture of a cerebral aneurysm can have devastating effects, with up to 12% of patients dying immediately, while a further 40% die within one month of rupture. Of those that survive, up to 30% suffer severe neurological defects. Although techniques such as clipping, coiling, and more recently flow diverting stents have been successful in the treatment of aneurysms, the risks associated with interventional treatments is significant. As a result, the importance of aneurysm rupture risk analysis is clear, with recent research into cerebral aneurysms focusing on the determination of factors that indicate whether an aneurysm is at risk of growth or rupture.

This study begins with an extensive review of existing literature and research into cerebral aneurysms and their rupture. Firstly, the literature review describes cerebral aneurysms and the surrounding cerebral vasculature. Current formation, growth and rupture theories of cerebral aneurysms are outlined, and the classification of aneurysms in previous studies is presented. Current interventional techniques are compared and contrasted. Results from previous computational analyses investigating the flow within cerebral aneurysms are outlined, and a description of previous experimental studies and the development of experimental models, flow systems and investigation of mass transport are presented. Chapter 2 concludes with a description of the overall aims and objectives of the study.

Chapter 3 introduces the database of patient-specific aneurysms used in this study, followed by a description of the classification of the aneurysms into different categories based on their geometric and morphological features. The technique used to extract key geometric measurements is described, before the development of idealised and representative versions of patient-specific geometries for computational analysis is discussed.

In Chapter 4, the concept of numerically modelling the mass transport of blood-borne species within cerebral aneurysms is introduced. Initially, the methods developed to present the unwrapped WSS and concentration plots are outlined, and the governing

equations applied to this study are presented. Subsequently, a detailed review of the assumptions, boundary conditions and flow parameters adopted in the fluid flow and mass transport analyses is provided. The chapter concludes with a description of the process of mesh generation and a grid independency study.

In order to ensure the computational methods employed in this study are appropriate, an experimental validation of the mass transport of blood-borne species within two lateral cerebral aneurysms was carried out, which is presented in Chapter 5. Using a dye density technique, the distribution of species within two experimental models was investigated and compared to computational results.

The study described in Chapter 6 outlines an investigation into the relationship between geometric parameters and cerebral aneurysm growth and rupture. Statistical analysis of the relationship between key geometric and morphological features of 168 patient-specific aneurysms is carried out, before the results and the implication on current rupture risk techniques are discussed.

Computational analysis into the mass transport of blood-borne species within cerebral aneurysms, and the relationship between results and aneurysm rupture is investigated in Chapter 7. A study is carried out to establish if the representative geometries developed in Chapter 3 can accurately predict the mass transport distribution seen within patient-specific aneurysm geometries. The influence of different blood-borne species on mass transport is simulated. Lastly, rupture prediction models are developed that indicate whether an aneurysm is at risk of rupture based on the amount of the aneurysm dome that is exposed to an under-expression of blood-borne species.

Chapter 8 introduces a cohort of 10 patient-specific cerebral aneurysms that have their rupture status blinded in order to carry out a test of the viability of the rupture prediction models developed in Chapters 6 and 7. Each rupture prediction model is tested on the blind cohort, and the ability of the prediction model to accurately predict the growth or rupture status of the blind study geometries is investigated.

Although each chapter includes a discussion of the methods used and the results gained from the different aspects of the study, an overview of the results and the effect that they may have on growth and rupture prediction is presented in Chapter 9. Limitations of the study are also discussed, and recommendations for future work are made.

CHAPTER 2

LITERATURE REVIEW

Chapter 2 Literature Review

2.1 Introduction

The following literature review is divided into three main sections. First, the background and motivation for the study are supplied, with an introduction to arteries, the cerebral vasculature and cerebral aneurysms given. Theories behind the formation, growth and rupture of aneurysms are discussed, and common interventional procedures are presented. The second section outlines previous studies of computational modelling of cerebral aneurysms, with flow haemodynamics, the representation of the arterial wall and mass transport studies discussed. The final section describes previous experimental studies of aneurysms, with model development, flow systems and mass transport simulations are discussed. The literature review concludes with a description of the aims and objectives of the current study.

2.2 Biological Study

2.2.1 Structure of the Artery Wall

Arteries are cylindrical tubes that transport oxygenated blood away from the heart to deliver essential nutrients to organs around the body. Dense in structure, arteries contain a hollow lumen that allows a pathway for blood to flow through. As illustrated in Figure 2.1, healthy arteries are composed of three distinct layers – the tunica intima, the tunica media and the tunica adventitia, each of which has a separate and specific function.

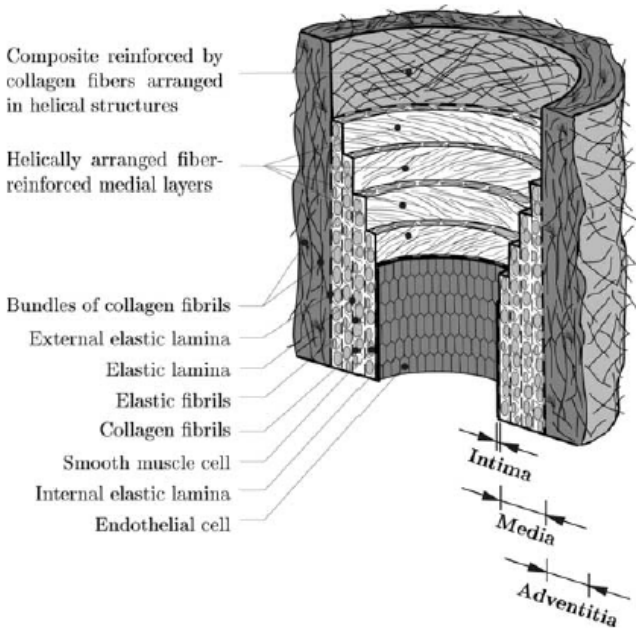

Figure 2.1: Structure of an elastic artery (Holzapfel and Gasser 2000)

The innermost layer of the artery is called the tunica intima or intimal layer, and is composed of a single layer of endothelial cells and a sub-endothelial layer containing connective tissue, elastic fibrils and bundles of collagen. The endothelial layer acts as a protective barrier, limiting some blood-borne species from entering the arterial wall. The intima is separated from the medial layer by the internal elastic lamina (IEL), a layer of elastic fibres. The tunica media or medial layer is the middle layer of the artery and is composed of layers of smooth muscle cells, elastin and bundles of collagen fibrils. The medial layer is the thickest layer and determines the mechanical properties, giving strength, resilience and load-bearing ability to the artery. The medial and adventitial layers are separated by another layer of elastic fibres known as the external elastic lamina (EEL). The outermost layer of the artery, the tunica adventitia or adventitial layer, is comprised of fibroblasts, fibrocytes and collagen fibres. It is surrounded by loose connective tissue, stabilising the artery within the body (Holzapfel and Gasser 2000, Lasheras 2007).

Vital nutrients and oxygen are supplied to the artery wall via diffusion from luminal blood flow to the intimal layer and the inner layers of the media, while the outer layers of the media and the adventitial layers are supplied by the vasa vasorum. This complex network of small blood vessels delivers nutrients to the walls of larger arteries, while removing waste products that have either been produced by cells or diffused through the main vessel wall (Ritman and Lerman 2007).

Arteries are typically subdivided into two main types – elastic and muscular. In general, elastic arteries are found closer to the heart and have a larger lumen than their muscular counterparts. Further differences are found within the medial layer: elastic arteries tend to have a thick, highly developed medial layer with a main component of elastin, while the medial layer of muscular arteries is composed almost entirely of smooth muscle cells (Gussenhoven *et al.* 1989). Although the walls of cerebral arteries are similar in their organisation and composition to muscular arteries throughout the body, they differ in their structure and elasticity. Arteries of the cerebral vasculature possess lower levels of elastin in their medial layer, have thinner adventitial layers, have medial defects or discontinuities and can lack an internal or external elastic lamina, all features which are believed to make cerebral arteries more susceptible to the formation of aneurysms (Bacigaluppi *et al.* 2014, Holzapfel and Gasser 2000, Lasheras 2007, Mehra *et al.* 2011).

2.2.2 Cerebral Vasculature and the Circle of Willis

The human brain, while accounting for only approximately 1.5% of total body mass, accounts for almost one fifth of the body's oxygen consumption (Levick 2010). An adequate blood supply to the brain is essential in order to allow it to function at its maximum capacity and to avoid cerebral injury. Sufficient blood flow is provided through an intricate network of arteries that sits at the base of the brain, known as the circle of Willis (see Figure 2.2).

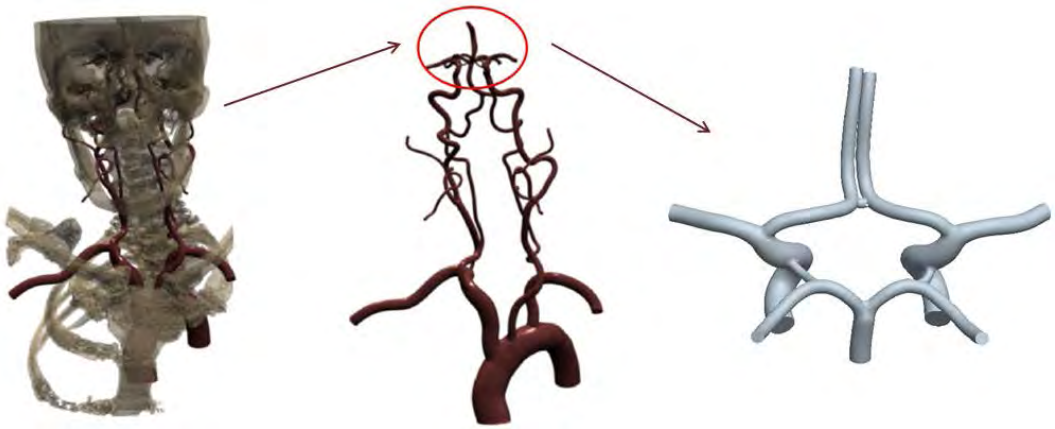

Figure 2.2: Location and geometry of the circle of Willis

As discussed by Alastruey *et al.* (2007), in an anatomically complete circle of Willis (CoW) blood is supplied from three main inlets – the left and right internal carotid arteries (ICA) and the anastomosis of the left and right vertebral arteries (VA) into the basilar artery (BA). The ICAs bifurcate to form the left and right middle cerebral (MCA) and anterior cerebral (ACA) arteries, which supply blood to the anterior circulation within the cerebral vasculature. The posterior circulation is supplied by the bifurcation of the basilar artery into the left and right posterior cerebral arteries (PCA). The anterior and posterior circulations are connected through three communicating arteries: the single anterior (ACoA) and left and right posterior communicating arteries (PCoA). Several minor efferent vessels are also found within the CoW, including the anterior choroidal artery (AChA), the superior cerebellar artery (SCbA) and the anterior inferior cerebellar artery (AICbA). The anterior and posterior cerebral arteries are often further subdivided into the A1 and A2, and P1 and P2 segments respectively. The A1 segment represents the section of the artery proximal to the ACoA, while the A2 segment refers to the artery distal to the ACoA. Similarly, the P1 segment is found proximal to the PCoA while the P2 segment is found distal to the PCoA. The main arteries of the circle of Willis are illustrated in Figure 2.3.

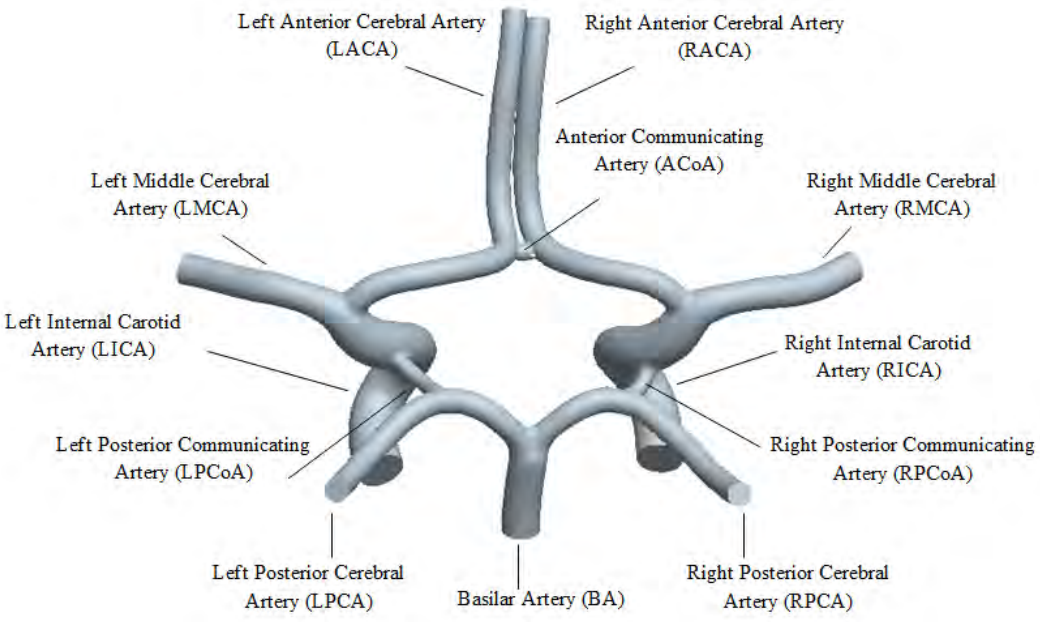

Figure 2.3: Main arteries of the circle of Willis

One of the main advantages of the ring-like structure of the CoW is that in the event of an obstruction occurring in one or more blood vessels in the cerebral circulation, it supplies collateral blood flow to the efferent vessels on the deprived side, ensuring

adequate blood flow to the brain. However, studies have demonstrated the high level of morphological variation in the CoW, with approximately 50% of the population possessing a complete CoW. The remaining 50% possess at least one absent or hypoplastic artery (Alastruey *et al.* 2007).

2.2.3 Cerebral Aneurysms

Cerebral or intracranial aneurysms are balloon-like swellings or dilations of the arterial wall, found within the cerebral vasculature. They are common lesions, occurring in 1-5% of all adults in the United States. Although the majority of aneurysms are small and do not rupture, rupture can lead to a subarachnoid haemorrhage (SAH), which is an extremely serious condition. The mortality rate associated with SAH following aneurysm rupture is 50%, with a 50% morbidity rate for those that survive (Ma *et al.* 2004). It is believed that less than 1% of aneurysms rupture annually, yet the demand for improved rupture prediction and preventative intervention techniques is increasing (Jeong and Rhee 2012). The following section describes the theories behind the formation of cerebral aneurysms, their classification based on location, type, size, morphology and shape, the mechanisms behind aneurysm rupture, and the current treatment techniques in use.

2.2.3.1 Formation Theories

The pathogenesis of cerebral aneurysms has long been debated. Although the exact mechanisms behind their formation remains unknown, recognised risk factors for the development of cerebral aneurysms include hypertension, smoking and family history (Meng *et al.* 2007), along with congenital risk factors associated with diseases of the connective tissue, adult polycystic kidney disease, fibromuscular dysplasia, Marfan syndrome, Ehlers-Danlos syndrome and pituitary gland tumours (Bacigaluppi *et al.* 2014, Schievink 1997, Wiebers *et al.* 2004). Cerebral aneurysm formation is thought to be a multifactorial process involving flow haemodynamics, wall biomechanics, mechanobiology and the intracranial environment (Sforza *et al.* 2009).

Cerebral flow haemodynamics is one of the most recognised factors associated with aneurysm formation with the interaction between haemodynamic forces, biology of the vessel wall and the impact on the mechanics of the wall all hypothesised to

contribute to the formation, growth and rupture of cerebral aneurysms (Meng *et al.* 2011, Sforza *et al.* 2009). Aneurysms are typically found along arterial curves, branching points and at bifurcations - all areas that are exposed to increased haemodynamic stress. Although it has been suggested that the impacting force of blood flow induces a local pressure elevation that may contribute to aneurysm development (Foutrakis *et al.* 1999), studies have shown that the increased pressure at flow impingement sites is insignificant (Hashimoto *et al.* 2006). Instead, wall shear stress (WSS), the frictional force created by the flow of blood tangential to the vessel wall, is considered to be an important factor in cerebral aneurysm initiation (Boussel *et al.* 2008, Mantha *et al.* 2006, Meng *et al.* 2011).

Although physiologically normal levels of WSS have been shown to promote endothelial cell survival, vasodilation and anticoagulation (Paszkowiak and Dardik 2003), high levels of WSS are associated with extracellular matrix (ECM) degradation, IEL damage, cell death and vascular remodelling (Meng *et al.* 2013). Due to the complexity of the geometry of arterial branch points and bifurcations, asymmetric vascular remodelling can occur, leading to an outward bulging of the artery wall or the formation of a pre-aneurysmal bleb. Once this bleb starts to develop, the distal neck of the growing aneurysm is under continuous high pressure and shear stress, one of the main elements of vascular remodelling. This increased stress causes endothelial cells to be either activated or damaged, further causing the accumulation of inflammatory cells at the site. When this inflammation becomes more intense, some of the main structural components of the arterial wall can become damaged or destroyed, leading to aneurysm rupture. This implies that an important aspect of aneurysm formation is a prolonged concentrated area of outward vascular remodelling, coupled with inflammation (Hashimoto *et al.* 2006).

It has also been suggested that the presence of blood-borne species such as low-density lipoproteins (LDLs) may play a role in the genesis and development of aneurysms. A computational study was undertaken by Wada and Karino (2000) in which the flow and mass transport of LDLs in arterial segments was examined. The vascular endothelium has been shown to be a semi-permeable membrane which only allows the passage of water and water-dissolved ions, restricting the transport of certain larger molecules such as lipoproteins. As a result, a flow dependent concentration or depletion of proteins can occur at the boundary between the endothelium and blood flow, which in turn affects the transport of lipoproteins. In

areas of high shear stress, it is suggested that a depletion of these molecules occurs, leading to the formation of cerebral aneurysms.

Hypertension has been proposed as a contributing factor to cerebral aneurysm formation due to its influence on the endothelium, the vasa vasorum and the balance of collagen and elastin in the arterial wall. The association between these factors and their relationship with aneurysm formation is illustrated in Figure 2.4. It is evident from previous studies that the formation of cerebral aneurysms is complex, with several different factors contributing to the intricate process.

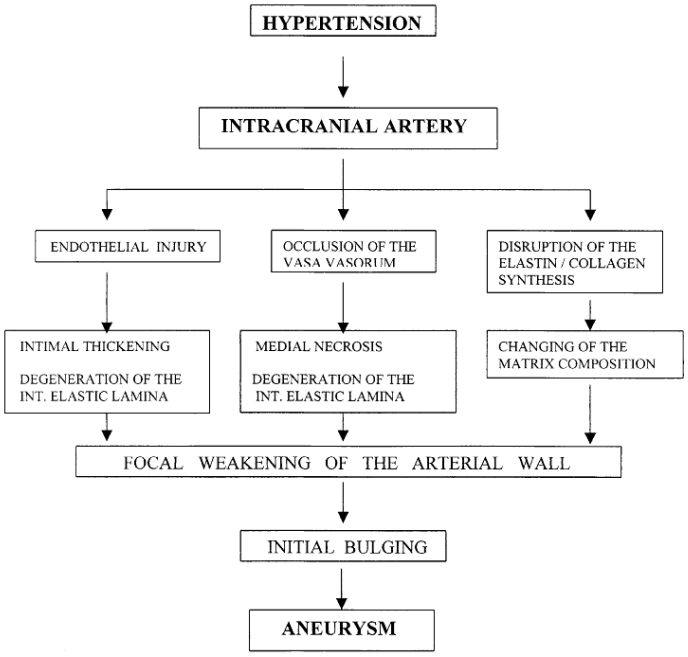

Figure 2.4: Proposed mechanisms of development for cerebral aneurysms (Inci and Spetzler 2000)

2.2.3.2 Classification

Cerebral aneurysms can be classified based on many variables, but typical characteristics used include their location, type, size, anatomical characteristics and shape. The following section describes the different classifications used within each characteristic category.

Location

Cerebral aneurysms tend to develop in areas such as at bifurcations, arterial branch points and along curved arteries, rather than along straight arterial segments (Brisman

et al. 2006, Schievink 1997). It has been reported that the majority of aneurysms are found in the anterior circulation, particularly at the junction of the ICA and the PCoA, the ACoA and along branching points of the MCA. Within the posterior circulation, aneurysms are typically found at the basilar bifurcation or at the posterior inferior cerebellar artery. Multiple aneurysms are found in 20-30% of patients (Schievink 1997).

In 1998, results from the International Study of Unruptured Intracranial Aneurysms (ISUIA), a study assessing the natural history of unruptured aneurysms, indicated that of the overall 1937 aneurysms analysed, the majority could be found at the MCA and the ICA. For ruptured lesions, the International Subarachnoid Aneurysm Trial (ISAT) investigated the efficacy of treatments on 2143 ruptured aneurysms, with the ACA and ICA being the most prevalent locations of aneurysms. The distribution of aneurysms from these studies is illustrated in Table 2.1.

Table 2.1: Distribution of unruptured and ruptured cerebral aneurysm (ISAT Collaborative Group 2002)

Location	Distribution of Aneurysms	
	ISUIA (n = 1937, unruptured)	**ISAT (n = 2143, ruptured)**
Cavernous Carotid Artery	256 (13.22%)	
ICA	413 (21.32%)	698 (32.57%)
ACoA/ ACA	177 (9.14%)	1084 (50.58%)
MCA	585 (30.20%)	303 (14.14%)
PCoA	299 (15.44%)	
Vertebrobasilar/ PCA	120 (6.20%)	
Tip of BA	87 (4.49%)	
Posterior Circulation		58 (2.71%)

Type

Cerebral aneurysms are typically separated into three types – saccular, fusiform and dissecting. Saccular or berry aneurysms are distinguished by a balloon-like out-pouching of the artery wall with a defined neck or opening. Saccular aneurysms are the most common, responsible for 80-90% of all cerebral aneurysms (Mehra *et al.* 2011). Fusiform aneurysms are described as spindle shaped, with a swelling occurring on both sides of the artery, and lacking a distinct neck. Dissecting aneurysms, which occur more rarely, have a split or dissection of the inner layer of the vessel wall causing blood to leak into the outer layers of the artery (Lasheras 2007, Mehra *et al.* 2011).

Size

Aneurysms can also be classified according to their size dimensions. When classifying with respect to size, results are typically reported in millimetres and refer to the largest diameter within the aneurysm dome (Mehra *et al.* 2011). There exists some inconsistency with regards to the grouping of aneurysms with respect to size, with studies reporting different group categories. Similarly, when reporting the neck size of aneurysms, some inconsistency is found between authors with regards to the size groupings. Reported size categories are presented in Table 2.2.

Table 2.2: Aneurysm size classification. All units in mm.

Study	Size Classification	Neck Size Classification
Hademenos *et al.* (1998)	Small (<12) Large (≤25) Giant (>25)	Small (≤4) Wide (>4)
Parlea *et al.* (1999)		Small (≤4) Large (≥4)
Jou *et al.* (2003)	Large (10-25) Giant (>25)	
Choi and David (2003)	Small (<10) Large (<25) Giant (>25)	
J. R. Cebral *et al.* (2005b)	Small (≤5) Medium (>5 and ≤15) Large (>15)	
Campi *et al.* (2007)	Small (≤5) Medium (6-10) Large (≥11)	Wide (>4)
Baumann *et al.* (2008)	Small (≤10) Large (11-25) Giant (≥25)	
Meyers *et al.* (2009)	Small (≤5) Medium (5<x<15) Large (15≤x<25) Giant (≥25)	Small (≤4) Wide (>4)
Mehra *et al.* (2011)	Small (<10) Large (10-25) Giant (>25)	Wide (>4 or Dome-to-Neck Ratio of ≤2)
Ujiie *et al.* (1999)	Small (<5) Large (>5)	

Anatomical Classification

Further classification of aneurysms can be carried out based on their anatomical characteristics, namely their morphology, location with respect to the parent artery,

and the angle made with the parent artery. The morphology of an aneurysm is described as the relationship between the eurysm and the parent artery and its branches; Juan R. Cebral *et al.* (2005) categorise eurysms into four different morphology types – lateral, bifurcating, terminal and fusiform - while Liou and Liou (1999) include the terminal-shaped aneurysms in the bifurcating category.

The location of the aneurysm with respect to the parent vessel e.g. inner, outer, side, inline, is also included in the anatomical description of aneurysms. Furthermore, aneurysms can be classified based on the angle made between the aneurysm dome and the parent artery vessel, with three categories described – acute, orthogonal and obtuse (Juan R. Cebral *et al.* 2005). These classifications are illustrated in Figure 2.5.

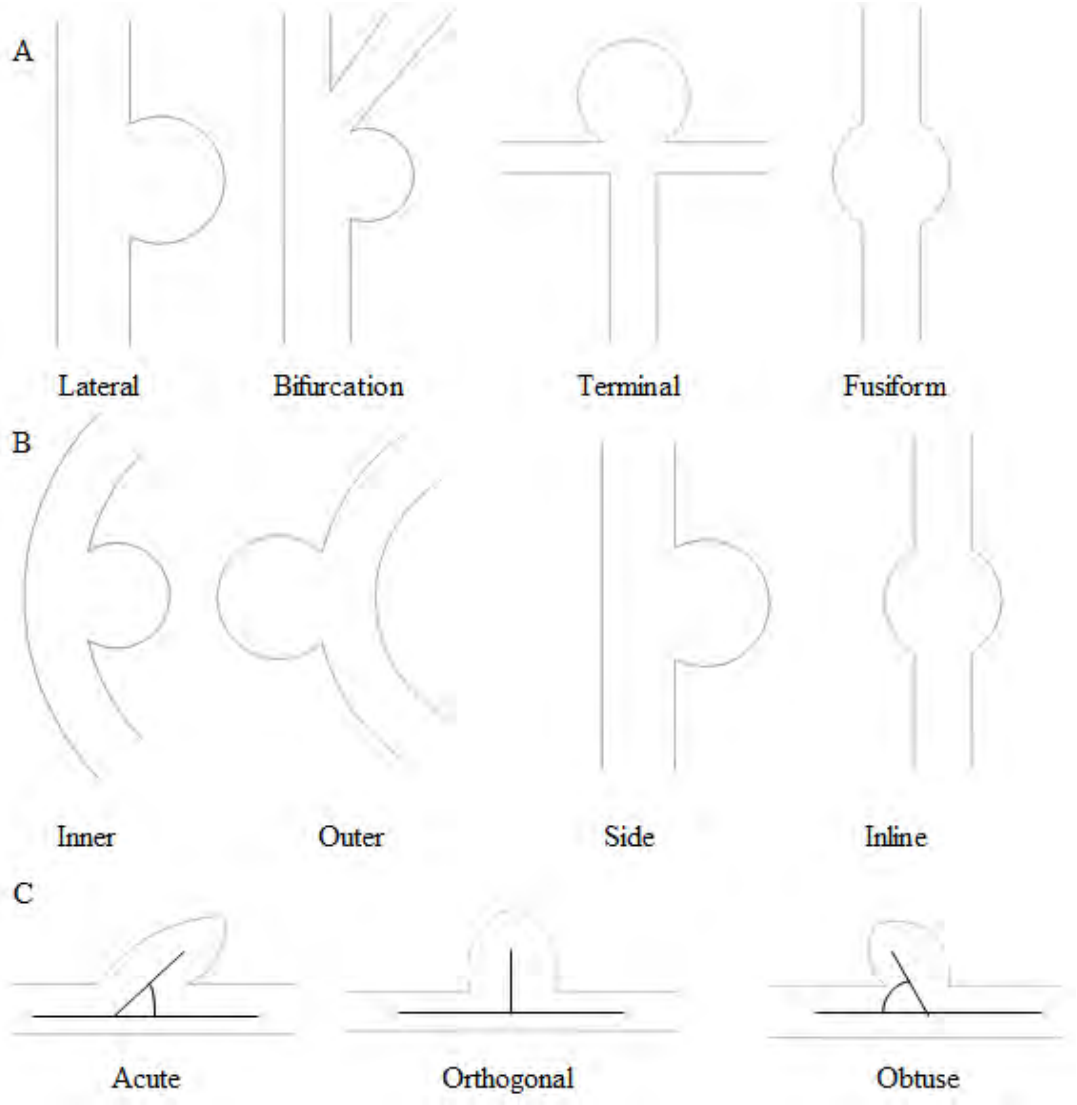

Figure 2.5: Aneurysm Characterisation (A) morphology (B) inclination of aneurysm with respect to parent artery and (C) angle of aneurysm with respect to parent artery (Juan R. Cebral *et al.* 2005)

Shape

The aneurysm sac can be divided into different regions. Ujiie *et al.* (1999) subdivided the aneurysm into the orifice (the opening at the entrance to the aneurysm), neck (the area within 30% of the aneurysm's length from the orifice) and dome (the main body of the aneurysm, more than 70% of the aneurysm's length from the orifice). Similarly, J. R. Cebral *et al.* (2005a) subdivided the regions within an aneurysm into the neck, body and dome. Dividing the overall aneurysm sac into regions, such as illustrated in Figure 2.6, allows for more concise analysis of flow impingement locations and rupture sites.

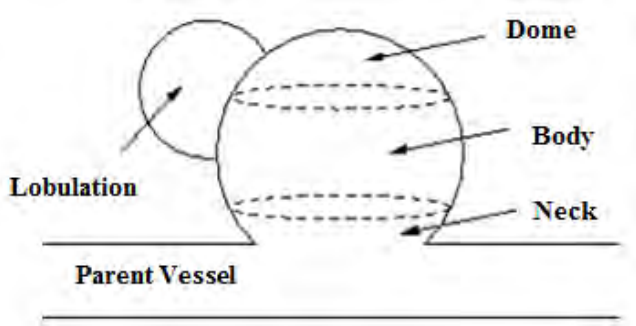

Figure 2.6: Regions within an aneurysm (J. R. Cebral *et al.* 2005a)

The aneurysm sac can contain lobulations, also known as blebs or daughter aneurysms, which can be used when describing the shape of the aneurysm. Hademenos *et al.* (1998) define the shape as either unilobular (circular or oval) or multilobular, while Parlea *et al.* (1999) classified their database of saccular aneurysms into simple-lobed, lobulated and complex. Simple-lobed refers to pear-shaped, spherical and beehive-shaped aneurysms with or without a lobulation, while a description of lobulated indicates the presence of at least one bleb with a size comparable to the overall aneurysm and complex indicated a partially thrombosed aneurysm.

Many studies have described the aneurysm sac based on shape parameters. One of the main parameters used to describe the shape of an aneurysm is the aspect ratio, defined as the ratio of the height of the aneurysm to the neck diameter (Baharoglu *et al.* 2010, Dhar *et al.* 2008, Ma *et al.* 2004). It has been suggested that aspect ratio may correlate with aneurysm rupture, a theory that will be discussed in Section 2.2.3.3. Raghavan *et al.* (2005) defines several parameters to describe the shape of the aneurysm. The

undulation index, a description of the degree of surface concavity, is determined using the convex hull, which represents the smallest volume that includes the entire aneurysm volume while still remaining convex at all points. The ellipticity index, determined using the volume and convex hull surface area, describes the deviation of the convex hull from a perfect hemisphere. The non-sphericity index represents the deviation of the aneurysm from a sphere while the aneurysm wall conicity is a measure of the location of the largest bulge in the aneurysm. Additionally, the bottleneck factor defines how much the neck acts as an obstruction to incoming blood flow and the wall curvature defines areas of the wall as concave, convex or saddle (convex from one plane and concave from another).

2.2.3.3 Rupture

The rupture of a cerebral aneurysm can lead to a subarachnoid haemorrhage, a devastating event with high mortality rates (Lall *et al.* 2009). It is believed that approximately 12% of patients who suffer a SAH due to the rupture of an aneurysm die instantly, before receiving medical attention. A further 40% die within one month, and of those that survive, more than 30% suffer severe neurological defects (Schievink 1997). As a result of the high morbidity and mortality associated with aneurysm rupture, determining the factors that cause and contribute to rupture has become an important focus of cerebral aneurysm research.

It is generally believed that the rupture of an aneurysm is found at areas of localised wall weakness and is caused by the wall tension or stress exceeding the wall strength (Cebral and Raschi 2013, Costalat *et al.* 2011, Jeong and Rhee 2012, Lu *et al.* 2008). However, the mechanisms behind the weakening of the aneurysmal wall and the changes found within the environment of the aneurysm that contribute to rupture is unknown. As with aneurysm formation, several mechanisms have been suggested to play a role in aneurysm growth and rupture, including haemodynamics, aneurysm location and geometric and morphological parameters.

Flow Haemodynamics

It is widely accepted that the environment created due to flow haemodynamics within an aneurysm contributes significantly to growth and rupture (Cebral *et al.* 2011b, Sforza *et al.* 2009, Steinman *et al.* 2003). Improvements in imaging techniques has allowed for image-based computational fluid dynamics (CFD) studies to be carried out using patient-specific aneurysm models for investigation into the role of haemodynamics in aneurysm rupture (Taylor and Figueroa 2009). In particular, wall shear stress (WSS) has been proposed as an important mechanism. However, there is contention regarding whether it is high or low WSS that triggers the events associated with rupture.

Recently, Meng *et al.* (2013) proposed that rather than aneurysm growth and rupture being influenced by either high or low WSS, it may be influenced by both, as illustrated in Figure 2.7. It is suggested that low WSS combined with low oscillating shear stress, caused by slow-moving recirculation zones within the aneurysm sac, can prompt an inflammatory response by the endothelial cells, leading to degradation of the extracellular matrix and eventually causing negative wall remodelling, growth and rupture. High WSS and positive WSS gradient, on the other hand, may be caused by impinging flow within the aneurysm, resulting in a mural rather than an inflammatory cell-mediated negative wall remodelling pathway.

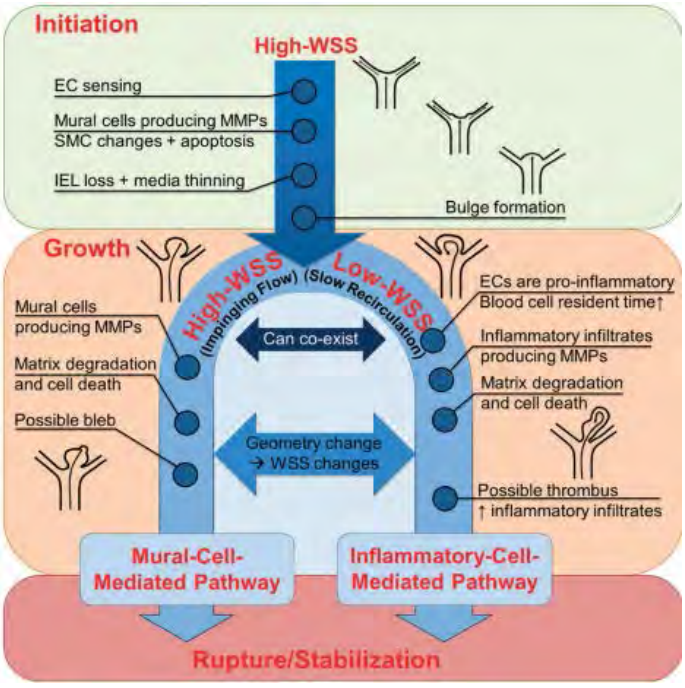

Figure 2.7: Role of high and low wall shear stress in aneurysm formation, growth and rupture (Meng *et al.* 2013)

Numerous other haemodynamic factors have also been suggested to contribute to rupture. In a qualitative haemodynamic analysis study of 210 patient-specific aneurysms, Cebral *et al.* (2011c) classified the blood flow within the aneurysms based on (1) flow complexity: simple or complex, (2) flow stability: stable or unstable, (3) inflow concentration: concentrated or diffuse and (4) flow impingement zone: small or large with respect to the area of the aneurysm. Results showed statistically different haemodynamic characteristics between ruptured and unruptured aneurysms, with ruptured lesions more likely to have complex flow, unstable flow patterns, concentrated inflow jets and small impingement regions. Further studies on the same sample set showed that a concentrated inflow jet and WSS distributions with maximum WSS and low aneurysmal viscous dissipation can also be associated with rupture (Cebral *et al.* 2011b).

Also associated with a higher risk of rupture is the presence of blebs or lobulations, and irregularly shaped aneurysms (Cebral and Raschi 2013). In a study of 110 paraclinoid aneurysms, irregular-shaped aneurysms (i.e. containing blebs) were found to be significantly correlated with increased rupture risk (Liu *et al.* 2014). Similarly, Beck *et al.* (2003) found that multilobular aneurysms are significantly more common in ruptured than unruptured aneurysms, while Raghavan *et al.* (2005) postulated that the undulation index, a measure of the degree of surface concavity due to the presence of lobulations, may be a good predictor of rupture risk. This is reported to be attributed to the low values of WSS found within the blebs of ruptured aneurysms (Shojima *et al.* 2004), although Tateshima *et al.* (2003) observed high WSS within or adjacent to the aneurysmal blebs examined in their study. Nevertheless, aneurysms that have irregular surfaces containing undulations and blebs have repeatedly been found to be at higher risk of rupture.

Location

The most common locations of cerebral aneurysm rupture within the CoW have been investigated by numerous previous studies, with disagreements arising as to whether ruptured aneurysms more frequently occur within the anterior or posterior circulation (Beck *et al.* 2006, Cebral and Raschi 2013, Hademenos *et al.* 1998, Rinkel *et al.* 1998). Beck *et al.* (2006) analysed the distribution of 155 saccular ruptured and unruptured aneurysms throughout the cerebral vasculature and found that the majority

of ruptured aneurysms of <7mm in size were found within the anterior circulation. The site of aneurysm rupture within the anterior circulation has also been investigated, with an increased risk of rupture associated with the ACA and the ACoA (Cebral and Raschi 2013).

In contrast to the results of Beck *et al.* (2006), Hademenos *et al.* (1998) found that posteriorly located aneurysms were more prone to rupture than those in the anterior circulation. Similarly, it has been reported that although aneurysms are less commonly found within the posterior circulation, the risk of rupture associated with posterior circulation aneurysms is much higher than other locations (Rinkel *et al.* 1998). Furthermore, in a review of the risk factors associated with cerebral aneurysms conducted by Cebral and Raschi (2013), it was reported that posterior circulation aneurysms are at higher risk of rupture, with the most common locations associated with rupture suggested to be the basilar tip and the origin of the posterior inferior cerebellar artery.

Geometric and Morphological Parameters

The influence of geometric and morphological parameters on aneurysm rupture has been investigated extensively (Dhar *et al.* 2008, Raghavan *et al.* 2005, J. Xiang *et al.* 2011). Until recently, it was believed that aneurysm size could be used to predict rupture risk, with large aneurysms (>10 mm) reported to be at higher risk of rupture (Cebral *et al.* 2011b, ISUIA Investigators 1998, Lall *et al.* 2009). However, more recent studies have established that size alone is not a reliable predictor, with small aneurysms <10mm found to rupture (Beck *et al.* 2006, Ohashi *et al.* 2004, Orz *et al.* 1997, Rinkel *et al.* 1998, Ujiie *et al.* 2001) while large aneurysms remain unruptured. As a result, the importance of investigations into the influence of other geometric and morphological parameters on rupture risk has become more prevalent.

One parameter that has consistently shown strong correlation with aneurysm rupture is the aspect ratio (Raghavan *et al.* 2005), the ratio of the aneurysm height to its neck width (see Figure 2.8). Ujiie *et al.* (2001) found significant differences between the aspect ratios of ruptured and unruptured aneurysms, with approximately 80% of ruptured aneurysms having an AR >1.6 and almost 90% of unruptured lesions with an aspect ratio <1.6. Lall *et al.* (2009) published results of a review of anatomical and morphological features of aneurysms reported in literature and found that although

differences in aspect ratio values for ruptured and unruptured aneurysms were statistically significant in several studies, there is some disagreement with regards to the threshold value for rupture potential. Results indicate that aneurysms with an aspect ratio AR >3 are at significant risk of rupture, while those with an aspect ratio <1.4 a less likely to rupture.

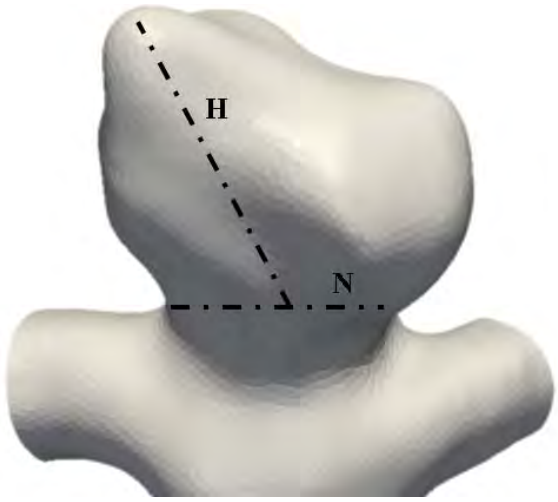

$$\text{Aspect Ratio} = \frac{\text{Height(H)}}{\text{Neck Width (N)}}$$

Figure 2.8: Definition of aspect ratio

Numerous other parameters have shown strong correlation with rupture risk, such as aneurysm size ratio, aneurysm angle, undulation index (UI), ellipticity index (EI), non-sphericity index (NSI), and shape (Baharoglu *et al.* 2010, Dhar *et al.* 2008, Liu *et al.* 2014, Raghavan *et al.* 2005, J. Xiang *et al.* 2011). A definition of the main parameters shown to be associated with rupture is presented in Table 2.3.

Table 2.3: Non-exhaustive list of geometric and morphological parameters found to be associated with aneurysm rupture (EI = ellipticity index, NSI = non-sphericity index, UI = undulation index)

Parameter	Description
EI	Deviation of aneurysm convex hull (smallest volume that fully encloses the aneurysm volume, convex to all points) from a hemisphere
Inclination angle	Angle at which the aneurysm tilts with respect to the incoming flow
Inflow angle	Angle between flow in the parent vessel and the axis of the aneurysm dome
Irregular shape	Aneurysms containing multiple irregularities due to the formation of blebs
NSI	Deviation of the aneurysm shape from a perfect hemisphere
Size ratio	Ratio of the maximum height of the aneurysm to the average vessel diameter
UI	Measure of the degree of aneurysm surface concavity

2.2.3.4 Interventional Procedures

Aneurysms are unique to each patient, and so the choice of treatment varies depending on factors such as type, size, location and risk of rupture. There are several imaging techniques used to detect the presence of an aneurysm: computed tomography (CT) angiography, magnetic resonance angiogram (MRA) and intra-arterial digital subtraction angiography (Bederson *et al.* 2000, Brisman *et al.* 2006, Mehra *et al.* 2011, Vega *et al.* 2002)

In the case of cerebral aneurysms, there are four main treatment options – observation, clipping, coiling and flow diverting stents. Observation, or monitoring, is the usual choice of treatment in cases where the risks associated with surgical treatment are significantly higher than the risk of rupture of the aneurysm. Observation, which involves regular physician visits and follow-up imaging, is often employed in the case of small aneurysms at low risk of rupture, in elderly people or in those with short life expectancies (Geyer and Gomez 2009).

For aneurysms that pose a threat of rupture, microsurgery with clipping is often employed. Under general anaesthetic, a craniotomy is performed and a metal clip is placed across the neck of the aneurysm, restricting the flow of blood into the aneurysmal bulge and excluding it from the main circulation (see Figure 2.9). This immediately limits the growth of the aneurysm, reducing the risk of rupture, bleeding and regrowth. In 1990, a less-invasive alternative to clipping was introduced (Johnston *et al.* 2000). This method, known as endovascular coiling, involves small detachable coils, usually made of platinum, being inserted through a microcatheter until the aneurysm is densely packed. This aims to reduce or prevent the flow of blood into the aneurysm, thus removing it from the circulation. More recently, biologically active coils have been introduced to induce thrombosis within the aneurysm, further ensuring occlusion from the parent artery blood flow (Brisman *et al.* 2006).

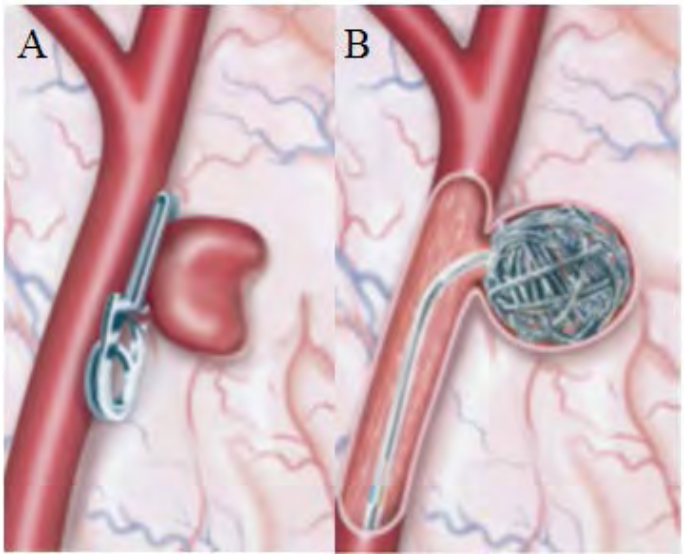

Figure 2.9: (A) Clipping and (B) Coiling of an Aneurysm (Johnston *et al.* 2000)

The efficacy of clipping versus coiling has long been debated, with the risks associated with both discussed. Although clipping tends to have low rates of reoccurrence and rebleeding, it is seen as invasive, having the typical risks of surgery associated with it along with risk of incomplete occlusion, aneurysm recurrence and haemorrhage. Furthermore, clipping of aneurysms of the posterior circulation poses difficulties due to the narrow arteries and presence of perforators (Mehra *et al.* 2011). While endovascular coiling is a less-invasive option, it is not always suitable, in particular for wide-necked aneurysms (Schievink 1997). The coiling process carries serious risks, including intra-procedural rupture, arterial dissection and parent-artery occlusion. However, coiling also tends to have a lower rate of inpatient mortality, is a less costly treatment and involves a shorter hospital stay (Brisman *et al.* 2006). Studies have suggested that endovascular coiling is significantly safer, less physiologically stressful and more effective than surgical clipping (Brisman *et al.* 2006, ISAT Collaborative Group 2002, Johnston *et al.* 2000, Johnston *et al.* 2001).

However, endovascular treatment is not always suitable for the treatment of aneurysms such as fusiform, wide-necked, large or giant aneurysms due to their susceptibility for recurrence or recanalization(Cebral *et al.* 2011a). As a result, flow diverting stents have been introduced with the aim of redirecting the flow of blood away from the aneurysm, removing the aneurysm from the circulation and promoting thrombosis within the aneurysm sac. An example of a flow diverting stent can be seen in Figure 2.10.

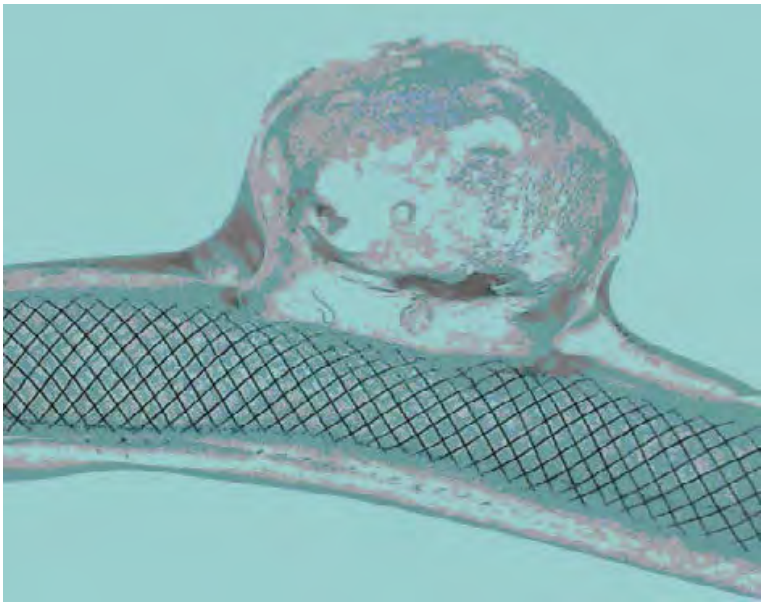

Figure 2.10: Flow diverting stent device (Kallmes *et al.* 2007)

2.3 Computational Studies

The following section presents a review of previous studies that have used computational methods in the analysis of flow within cerebral aneurysms. First, differences in haemodynamics as a result of the aneurysm geometric configuration is discussed, followed by characterisation of flow patterns found within aneurysms. The influence of the parent artery geometry on intra-aneurysmal flow is discussed, before previous studies of the mass transport of blood-borne species within the cerebral vasculature are presented.

2.3.1 Flow Haemodynamics

As previously discussed, it is believed that flow haemodynamics play an important role in cerebral aneurysm formation, growth and rupture risk. Aneurysms are commonly found along curved arteries and at arterial branch points and bifurcations (Lasheras 2007); thus, it is believed that the curvature of the parent artery may play a role in the formation, growth and rupture of an aneurysm.

Liou and Liao (1997) noted a lack of published information regarding the relationship between the curvature of the parent artery and cerebral aneurysm flow characteristics. Using particle track velocimetry (PTV) and flow visualisation, the authors investigated

pulsatile and steady flow fields in a lateral aneurysm model, varying the vessel curvature to vessel diameter ratio. It was found from this study that the flow vorticity, velocity and the wall shear stresses all increased as the radius of curvature of the parent vessel was increased. Furthermore, it was suggested that a lateral aneurysm that forms on a straight vessel or one with a small degree of curvature tends to have intimal thickening and undergoes thrombosis as a result of the low wall shear stress and velocities found within the sac, in contrast to aneurysms that form on a more curved artery, which tend to have higher velocities and higher wall shear stresses. Results from this study suggest that aneurysms that form on arteries with a larger radius of curvature are more likely to become damaged, increasing risk of rupture.

A computational investigation was carried out by Foutrakis *et al.* (1999) in order to investigate the high pressures and shear stresses that are associated with curved arteries and arterial bifurcation, and to examine their relationship with aneurysm formation and growth. Two main geometries were examined – a curved 90° arterial segment and an arterial bifurcation. For the curved arterial segment, the first model involved the addition of a small aneurysmal bleb to the curved 90° arterial segment. Within the aneurysmal bleb, the fluid particles are initially aligned across the lumen at the proximal neck. It is evident from the flow images (see Figure 2.11) that flow impinges on the distal neck before entering the aneurysm. Following circulation through the bleb, the outer fluid particles re-enter the main arterial flow, while a small local recirculation region forms within the bleb. The local pressure increases at the bend, and a secondary pressure increase is detected at the distal aneurysm neck, suggesting the distal neck is subjected to greater haemodynamic stress than its proximal counterpart.

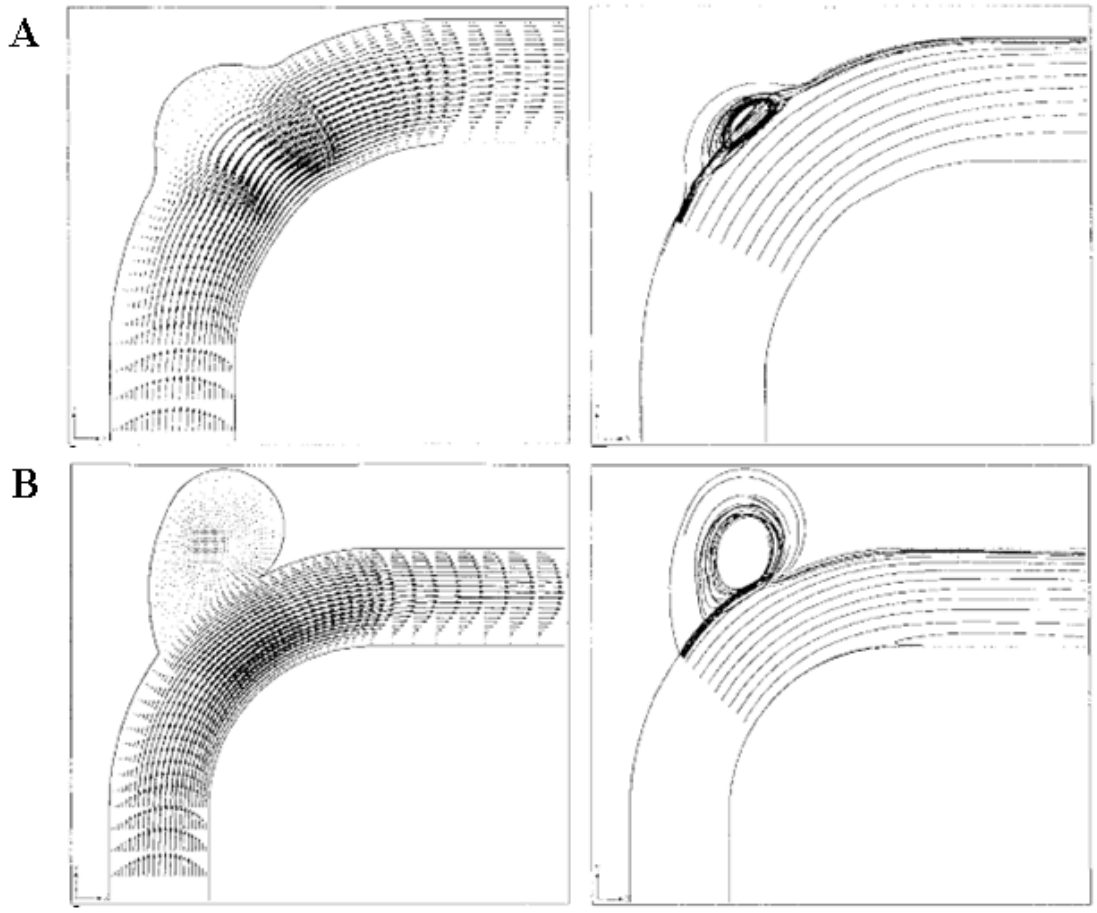

Figure 2.11: Velocity vector plot (left) and particle paths (right) for curved arterial segment with (A) aneurysmal bleb and (B) saccular aneurysm (Foutrakis *et al.* 1999)

The addition of a saccular aneurysm illustrated similar results to the aneurysmal bleb, with flow impinging on the distal aneurysm neck (see Figure 2.11). Flow recirculation occurs within the aneurysm dome, flowing in a direction retrograde to the flow in the main parent artery. Slow-moving flow recirculates through the aneurysm before re-entering the main arterial flow. Similar to the previous model, an increase in local pressure is found at the bend of the artery. However, a secondary pressure increase is not found at the distal neck, with a constant pressure seen along the aneurysm wall. Throughout the cardiac cycle, the distal neck is exposed to increased shear, again suggesting that the distal neck is subjected to greater haemodynamic stresses than other locations within the aneurysm.

An arterial bifurcation was altered to include an aneurysmal bleb in order to elucidate the haemodynamics during the formation of an aneurysm. As can be seen in Figure 2.12, the fluid particles are initially aligned across the lumen of the parent artery proximal to the location of the bifurcation. Flow impingement occurs at the side of the

larger daughter artery, with a stagnation point evident at the dome of the bleb. The side of the larger daughter vessel is the site of high-impact pressures of twice that of the luminal pressure in the parent vessel, with the aneurysm neck on the side of the smaller daughter branch being the location of the highest shear rates. Therefore, both sides are subjected to increased states of haemodynamic stress – one arising from pressure, the other arising from shear.

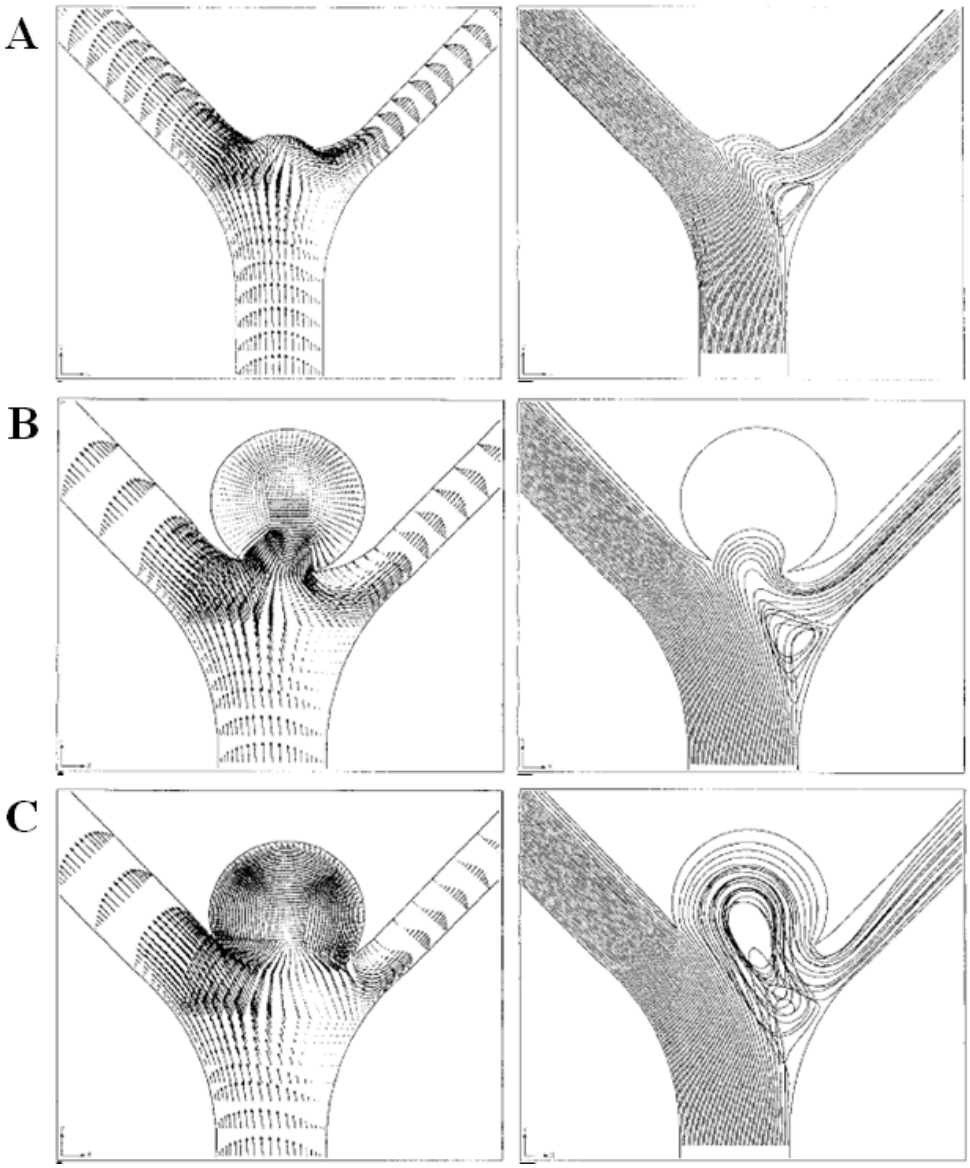

Figure 2.12: Velocity vector plot (left) and particle paths (right) for curved arterial segment with (A) aneurysmal bleb and (B) saccular aneurysm and (C) saccular aneurysm with wide neck (Foutrakis *et al.* 1999)

The second bifurcation model incorporated a saccular aneurysm at the tip, in which a slow-moving anti-clockwise rotating vortex can be seen within the aneurysm sac. Virtually all of the fluid that enters the smaller daughter artery first recirculates

throughout the aneurysm. Little flow penetrates deply into the aneurysm dome, indicating an increased chance for intra-aneurysmal thrombus development. High haemodynamic stresses are found at the aneurysm neck, suggesting the possibility of an increase in the aneurysm neck size over time.

The final bifurcation model increased the neck size of the aneurysm. Similar results are seen in the previous bifurcation models, with flow entering the aneurysm close to the larger daughter artery and the majority of flow that passes into the smaller daughter aneurysm first recirculating throughout the aneurysm dome. An increase in pressure is seen at the aneurysm neck on the side of the larger daughter artery, while higher shear rates are seen at the opposite side. It can also be seen that the amount of intra-aneurysmal flow is increased dramatically when compared to the previous narrow necked aneurysm, reducing the risk of thrombus formation.

Further analysis has been carried out into the effects of aneurysm neck size and vessel curvature on the haemodynamics within an aneurysm in an attempt to further knowledge on these parameters and their links to aneurysm growth and rupture (Hoi *et al.* 2004). During the course of the study, anatomically realistic aneurysm geometries were developed, and the range of curvature of the parent vessel and the neck size of the aneurysm were varied, while other parameters were kept stable. The ten models developed were split into two groups – the first kept the neck size at 7.5mm with the curvature of the parent artery ranging from 0 to 0.167 mm^{-1}, while the second group varied the neck size from 6 to 9.56mm, with the curvature fixed at 0.083mm^{-1}. It was found from this study that flow impingement tended to intensify with increasing parent artery curvature (see Figure 2.13).

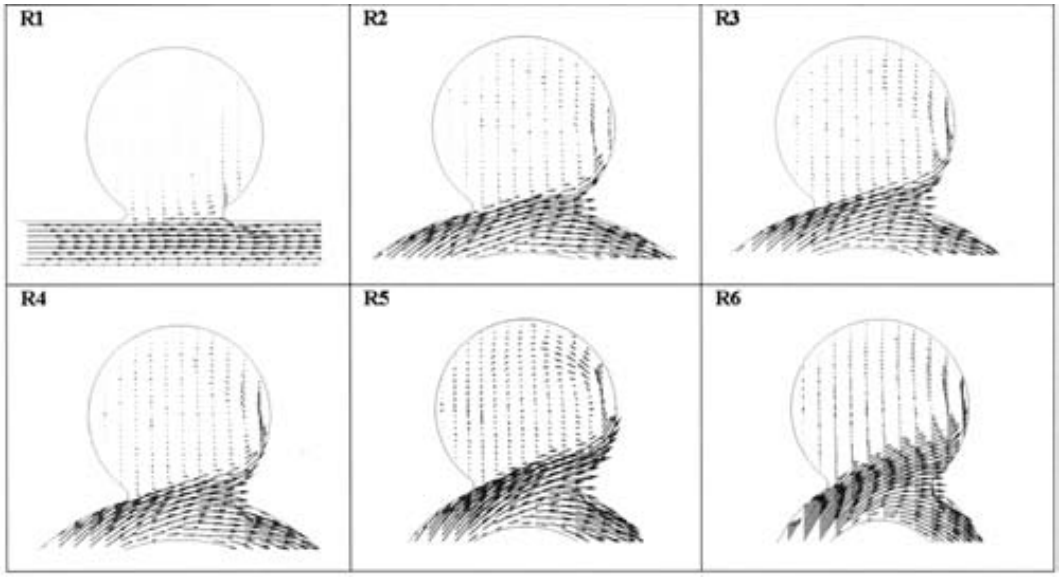

Figure 2.13: Velocity vectors seen within aneurysms of varying parent artery curvature (Hoi *et al.* 2004)

When the curvature of the parent artery was low or zero, flow was weakly entrained into the aneurysm, but as the curvature increased, the velocity profiles shifted towards the outer wall of the aneurysm, with a larger volume of blood impacting on the distal side of the aneurysm neck. A vortex formed within the aneurysm sac, with the distal neck acting as a flow divider. Increasing the arterial curvature increased the impact zone linearly; therefore more active vascular remodelling may be seen, increasing further growth of the aneurysm. Increasing the neck size caused the flow impingement to enlarge the impact zone, increasing the risk of aneurysm growth. The study concludes that a large neck size coupled with a high degree in curvature leads to a higher risk of continuous aneurysm growth.

2.3.2 Flow Characterisation

Through the use of 3D rotational angiography images, a database of over 200 patient-specific models of cerebral aneurysms was created with the aim of studying and characterising the haemodynamic environment of aneurysms, in order to further investigate their growth and rupture (Cebral *et al.* 2010). The haemodynamic environment of the aneurysms were characterised qualitatively through the visual inspection of blood flow visualisation using set properties:

(1) Flow complexity: simple flows contain only a single recirculation zone or vortex, while complex flows contain more than one vortex, along with flow divisions or separations within the aneurysm sac.

(2) Flow stability: stable flow patterns are those that do not move or change during the cardiac cycle, while unstable flow patterns have flow divisions or vortex structures that move, are created and/or are destroyed during the cycle.

(3) Inflow Concentration: concentrated inflow jets tend to be thin or narrow and penetrate deep into the aneurysm sac, while diffuse jets are thicker and disperse once they enter the aneurysm.

(**4) Flow impingement**: a small flow impingement region is one in which the region where the inflow jet impacts on the aneurysm wall is small (<50%) compared to the overall aneurysm area, or large if it is large (>50%) compared to the aneurysm area.

The results, which correlate well with previously published data, showed that ruptured aneurysms more commonly display complex flows, unstable flow patterns, concentrated inflows and small impingement regions when compared to unruptured aneurysms. Furthermore, it was found that ruptured aneurysms are typically larger in size and have larger aspect ratios than unruptured aneurysms.

2.3.3 Influence of Parent Artery Geometry

It has been suggested that curvatures in the upstream segment of the parent artery vessel of an eurysm geometries in CFD models play a role in the haemodynamics within the aneurysm itself, due to the influence that the curvature might have on the inflow jet and zone of impaction on the aneurysm wall. As a result, the influence that the upstream parent artery has on the haemodynamics of intracranial aneurysms was investigated. In a study conducted by Castro *et al.* (2006), four patient specific aneurysms (two of the ICA, one of the MCA and one of the ACoA) were analysed using CFD. Models of both the original aneurysm along with the parent artery geometry, and a truncated model version were created and compared.

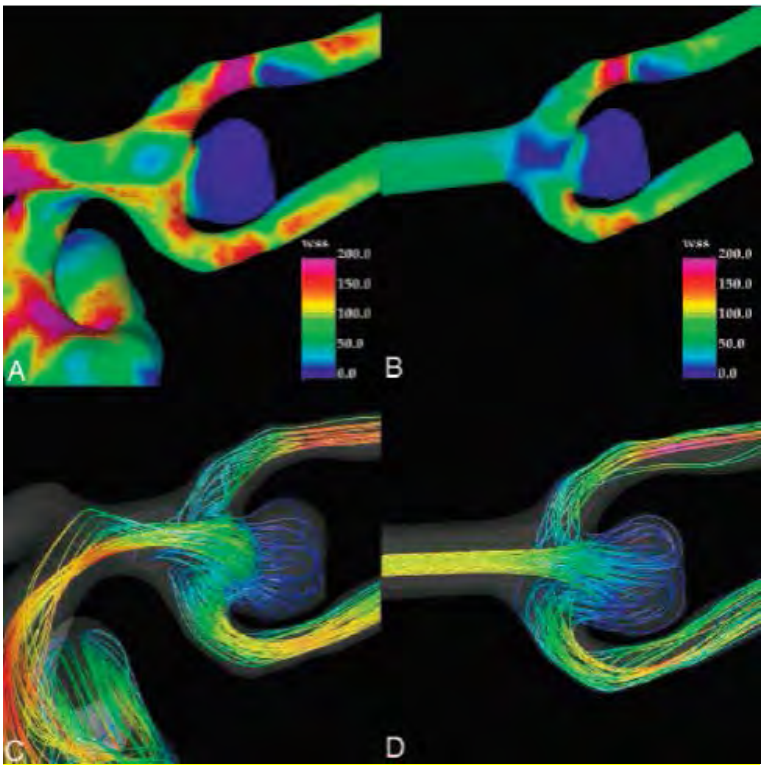

Figure 2.14: Visualisation of haemodynamics in a cerebral artery aneurysm with (A) wall shear stress distribution in the original model (B) wall shear stress distribution in the truncated model (C) streamlines in the original model and (D) streamlines in the truncated model (Castro *et al.* 2006)

It is evident from this study that the exclusion of the upstream parent artery geometry in CFD simulations tends to result in lower WSS values in the aneurysm wall, and the shifting of the flow impingement site away from the dome and towards the aneurysm neck. An example of this can be seen in Figure 2.14. Furthermore, less complex, simplified flow patterns are seen in the truncated models, with arteries of more curved upstream geometries showing significant differences. Although it is acknowledged that the study does not define how much of the parent artery should be included, it is concluded by Castro *et al.* (2006) that it is necessary to include the upstream anatomy in any computational models in order to avoid inaccurate non-physiologic near laminar inflow, such as that seen in the truncated models.

2.3.4 Mass Transport

Mass transport is the movement of species i.e. fluid, gas or solids, from an area of high concentration to an area of low concentration within a defined system, and can be as a result of both diffusion and convection. This movement can be provoked by concentration gradients, but typically it is due to complex flow dynamics, such as

within the vasculature. Mass transport can be broken into two main types within the cerebral vasculature – blood side mass transport (BSMT), and wall side mass transport (WSMT). Blood side mass transport refers to the transport of species within the lumen of the blood vessel, and is driven by the blood flow itself. Wall side mass transport refers to transport within the wall of the artery or blood vessel itself and is governed by two transport forces, the first being a pressure driven convection force, while the second is a diffusive force (O'Connell 2009).

2.3.4.1 Arterial Wall Representation

Computational studies of the mass transport of species within the arterial network can be classified based on their description of the arterial wall and the underlying assumptions associated with the wall type (Khakpour and Vafai 2008b). Three main types of arterial wall representation have been established by Prosi *et al.* (2005), namely the wall-free model, fluid-wall or homogeneous wall model and finally the multi-layer model.

Wall-free models are the simplest way of computationally representing the arterial wall in mass transport studies. These models solve for the blood flow in the artery while the arterial wall is represented by a simple set of appropriate boundary conditions. Therefore, the solution is independent of the mass transport that occurs within the arterial wall (Khakpour and Vafai 2008b). The main advantage of wall-free models over the more complex fluid-wall or multi-layer models is that a small number of parameters is required, typically the diffusivity of the species in blood, the overall mass transfer coefficient of the arterial wall to the species and the wall filtration velocity (Prosi *et al.* 2005). An example of the use of a wall-free model is found in the work of Wada and Karino (2002), who studied the concentration polarisation of LDL at the surface of an artery with a multiple bend. In this study, the wall was assumed to be rigid and uniformly permeable to water. A mass conservation boundary condition was set at the wall, which stated that the amount of LDL passing through the wall was equal to the difference between the amount transported to the wall by the filtration flow, and the amount diffused back into the main luminal flow. Similar boundary conditions are found in the wall-free models of Imai *et al.* (2010), Rappitsch and

Perktold (1996) and Soulis *et al.* (2008), in the study of mass transport of adenosine triphosphate (ATP), oxygen and LDLs respectively.

The second type of arterial wall model is the fluid-wall or homogeneous model. Used in many previous studies, such as by Stangeby and Ethier (2002) and Sun *et al.* (2006), homogenous models use a simple homogeneous layer to account for the arterial wall, in an attempt to compromise between the complex amount of input data required for the simulation and the accuracy of the solutions (Prosi *et al.* 2005). According to Khakpour and Vafai (2008b), these models typically assume the arterial wall is a homogenous porous medium, and are effective in cases where it is not necessary to elucidate on the distribution of species concentration within the wall. In a study carried out by Sun *et al.* (2006) into the effects of wall shear stress on the transport of species such as oxygen and LDL from blood to and across the arterial wall within a stenosed artery geometry, the arterial wall was treated as a single layered porous medium. The flow across the wall was modelled using Darcy's Law, with the flow and mass transport represented by Navier-Stokes and convection-diffusion equations.

Multi-layer models are the final arterial wall models described by Prosi *et al.* (2005), and are the most complex proposed, as they incorporate several heterogeneous layers to describe the wall, such as the endothelium, the intima, the internal elastic lamina and the medial layer. The main advantage of the multi-layer models over the wall-free and homogenous types is that it provides more realistic information regarding the transport of species within the arterial wall. However, a large number of parameters are required to describe the properties of each layer, which cannot be measured directly from patients. Therefore, many studies have attempted to characterise these parameters so as to improve the accuracy of multi-layer models. An example of the implementation of a multi-layer model is seen in a study by Ai and Vafai (2006), who used fundamental porous media equations and individual parameters for each layer for a coupled analysis of the transport of LDLs in the main arterial blood flow and within the arterial wall for a four-layer model. Similar analysis of mass transport across the arterial wall in multi-layer models can be found in studies conducted by Karner and Perktold (2000), Khakpour and Vafai (2008a) and Prosi *et al.* (2005).

2.3.4.2 Transport of Blood-Borne Species

Adenosine Triphosphate

Adenosine triphosphate is a blood-borne nucleotide that is known to influence the modulation of vascular tone and play an important role in platelet aggregation, neurotransmission, cardiac function and muscle contraction (Gordon 1986). ATP reacts with receptors on the endothelial cells, controlling vasodilation through the production of nitric oxide, which has been suggested to play a role in endothelial regulation (Imai *et al.* 2010). At the arterial wall, ATP is degraded by enzymes to form adenosine diphosphate (ADP) (Tarbell and Qiu 2000), which is catabolised to adenosine monophosphate (AMP) and then finally to adenosine (Shen *et al.* 1993). It has also been suggested that flow induces ATP release in endothelial cells (Choi *et al.* 2007). In order to regulate responses by the endothelium, ATP needs to be transported continuously via convective and diffusive forces to the endothelial surface (Comerford *et al.* 2006). The concentration of ATP at the endothelial surface is determined by the balance between the convection and diffusion, as well as the consumption of ATP during its hydrolysis to ADP (John and Barakat 2001). The delivery of ATP to the arterial wall, and more recently within cerebral aneurysms, has been the focus of numerous mass transport studies.

The transport of ATP to the arterial wall has been investigated for links with atherosclerosis. The mass transport of blood-borne species in a realistic human right coronary artery was investigated by Kaazempur-Mofrad and Ethier (2001), using a steady, incompressible, Newtonian fluid to represent blood. It was reported that the geometry of the model strongly affected the mass transport of species, with high concentrations found in areas of increased axial momentum, while lower concentrations corresponded with slow-moving flow. Similarly, Comerford *et al.* (2006) investigated the influence of different arterial bifurcation geometry configurations on the concentration of ATP and ADP at the endothelium, reporting that the geometry has a significant influence on the concentration at the endothelial surface. For an arterial configuration with a large bifurcation angle (>90º), a stagnation point evolves surrounded by a region of low WSS. Within this region, low convection takes place and the hydrolysis of ATP to ADP at the arterial wall dominates the mass transport, leading to a decrease in ATP concentration at the wall. This is in contrast with bifurcations with small angles (<90º), where high WSS is found and convection

dominates the transport mechanisms. As a result, the difference in concentration between ATP at the wall and within the main arterial blood flow is smaller than that of the geometry with a large bifurcation angle.

The influence of fluid flow and shear stress on the concentration of ATP and ADP at the endothelial surface was investigated by John and Barakat (2001), in which a parallel-plate flow chamber containing a monolayer of endothelial cells was exposed to ATP nucleotides under both steady and pulsatile conditions. Results indicate that, for steady flow neglecting flow-induced release of ATP, the concentration of ATP at the endothelial surface decreases and the ADP levels increase in the flow direction as a diffusion boundary layer develops. Choi *et al.* (2007) applied the aforementioned model of John and Barakat (2001) to steady and pulsatile flow over a backwards facing step, with the aim of elucidating the effect of flow separation and recirculation regions on nucleotide concentration at the endothelial surface. It is demonstrated that the concentration of ATP within a flow separation zone found close to the step is much lower than the concentration downstream of the step. The low ATP concentration in the recirculation region is attributed both to low WSS levels which reduces the amount of flow-induced ATP release and to the increased residence time of the nucleotides allowing increased hydrolysis to ADP, compared to areas of regular flow.

Few studies have investigated the transport of blood-borne species within cerebral aneurysms; however, Imai *et al.* (2010) modelled the transport of ATP within saccular cerebral aneurysms at arterial bends. The ATP concentration distribution in each arterial geometry, normalised to the concentration within the twisted artery without an aneurysm, are illustrated in Figure 2.15.

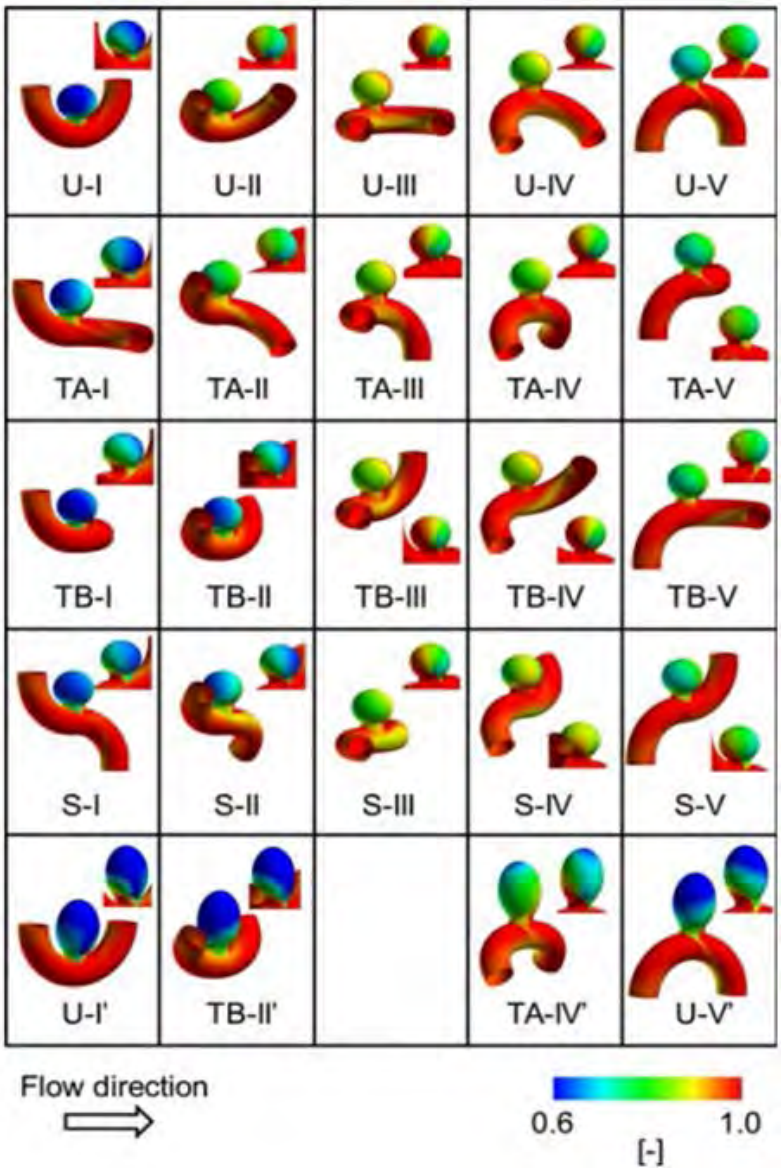

Figure 2.15: Normalised ATP concentration distribution (Imai *et al.* 2010)

Results for this study highlight the difference in concentration levels between the aneurysm dome and the parent artery, with the latter exhibiting higher levels of ATP. Within the aneurysm, the proximal wall tended to have lower concentrations than the distal wall, and the concentration distribution was influenced strongly by the parent artery geometry. It is also reported in this study, similar to that reported by Choi *et al.* (2007), that the areas of low concentration correspond to areas of low WSS, which has been linked to aneurysm rupture, suggesting that a combination of low species concentration and low WSS may play a role in aneurysm growth and rupture.

Low-Density Lipoproteins

Low-density lipoproteins are complex molecules composed of multiple proteins that transport fats around the body in blood. LDL is the main carrier of cholesterol, and is transported across the arterial wall into the intimal layer, where it can become oxidised, resulting in the recruitment of monocytes into the arterial wall (Vincent and Weinberg 2013). It is thought that LDL may be one of the main factors in the initiation of atherosclerosis, as oxidization of LDL causes damage to the cells and to the function of the arterial wall which can result in the formation of plaque and lumen stenosis (Chung and Vafai 2014). It has been hypothesised that the transport of LDLs and cholesterol may play a role in the initiation of cerebral aneurysms (Wada and Karino 2002).

For the mass transport of proteins or molecules such as LDLs, it is believed that a small transmural flux of water from the arterial lumen to the adventitial layer exists that is driven by pressure within the artery (Ethier 2002). This flux, called a filtration velocity, leads to the convective mass transport dominating over diffusive mass transport. When the convection of the molecules towards the endothelium is balanced with the diffusion away from it and with the transport across the arterial wall, a steady-state distribution of LDL molecules is reached (Vincent and Weinberg 2013). When this occurs, the concentration of the molecules at the endothelial surface is higher than within the main arterial flow, which is termed concentration polarization. This phenomenon of concentration polarization is illustrated in Figure 2.16. It is thought that for LDLs, concentration polarization occurs due to the difference between the water filtration velocity, and the mass transport coefficient controlling the transport through the endothelium. The convection of LDL molecules towards the endothelium is greater than the rate of transport across the arterial wall, thus concentration polarization occurs at the endothelial surface. It is hypothesised by Wada and Karino (2002) that the transport of cholesterol may be affected by concentration polarization, and that the transport of cholesterol may be related to cerebral aneurysm formation in areas of high wall shear stress where a depletion of LDLs is found.

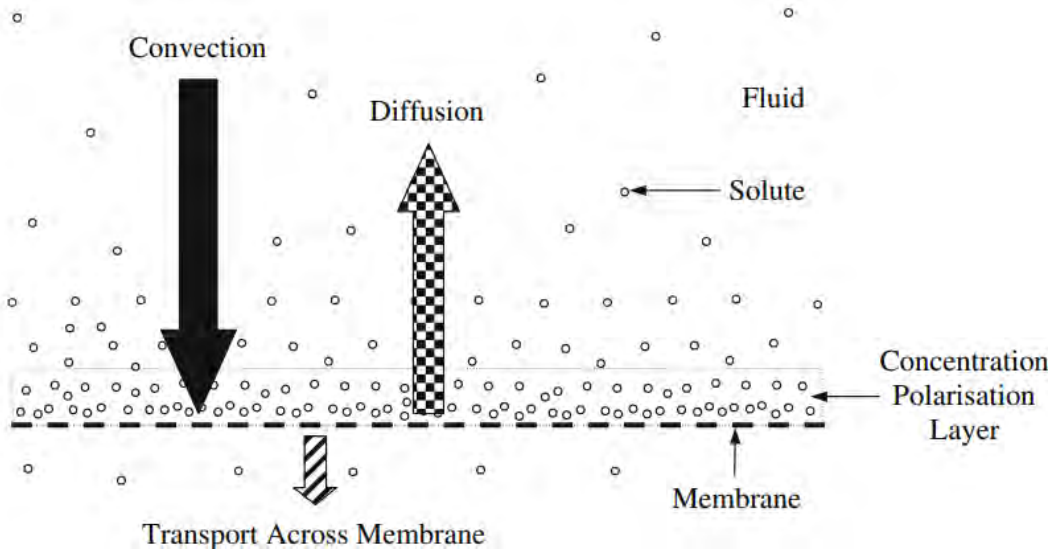

Figure 2.16: Illustration of concentration polarization (Vincent and Weinberg 2013)

Chen *et al.* (2014) carried out a numerical investigation of mass transport in 3D patient-specific deformed aortae models using steady flow. Examination of the WSS and the distribution of LDLs at the luminal surface highlighted the effect of geometric features on haemodynamics and mass transport. It is interesting to note that areas of low WSS within the models corresponded with increased LDL surface concentration. However, areas of increased concentration also differed from low WSS areas, suggesting that other flow characteristics may play a role in LDL concentration distribution. Similar results are seen in a steady flow analysis of the concentration distribution of LDL in the normal left coronary artery carried out by Soulis *et al.* (2008), in which regions of low WSS demonstrate elevated concentration of LDL. However, it is again suggested that other flow parameters may also influence the concentration of LDL.

Wada and Karino (2002) investigated the influence of a number of factors on the surface concentration of LDLs, including Reynolds number, water filtration velocity, lipoprotein size and the fluid viscosity, where it was determined that the water filtration velocity influenced the surface concentration of LDLs the most. This is due to the fact that without a filtration velocity induced at the arterial wall, concentration polarization does not occur.

Geometric features have been shown to play a role in the mass transport of LDLs. In a steady flow analysis of blood flow and the mass transport of lipoproteins in an arterial segment with multiple bends, results illustrated that although the concentration at the

arterial wall remained the same as the inlet concentration at most locations, the LDL concentration was locally elevated at the inner wall of the arterial bends, where the flow was slow and relatively low wall shear stress occurred (Wada and Karino 2002). The influence of geometric features on mass transport is further evidenced in a study of mass transport of LDLs within an axisymmetric stenosed artery (Stangeby and Ethier 2002). Results demonstrate elevated LDL concentration at the downstream section of the stenosis, where the velocity and wall shear stress decrease. Furthermore, a sharp elevation in LDL concentration corresponds with the flow separation point. Also computed within this study was the net uptake of LDL into the arterial wall. It was determined that high WSS on the proximal segment of the stenosis increased the endothelial permeability and hence increased the uptake of LDLs. It is clear from these previous studies, and others such as Kaazempur-Mofrad *et al.* (2005), Nematollahi *et al.* (2012) and Tarbell and Qiu (2000) that the mass transport of molecules such as LDLs is strongly influenced by the geometry of the area of interest.

2.4 Experimental Studies

Due to the complex nature of cerebral aneurysms and the surrounding cerebral vasculature, experimental-based studies of flow haemodynamics and mass transport within aneurysms have been somewhat limited. Although several studies have examined flow dynamics within aneurysms using experimental flow phantoms, few studies have attempted to mimic the mass transport behaviour of the arterial wall, and, to the best of the author's knowledge, none have attempted to experimentally model mass transport within cerebral aneurysms. The following section examines the geometric model development and flow systems used in previous experimental flow haemodynamic studies of cerebral aneurysms and the cerebral vasculature. Previous experimental mass transport studies are also discussed.

2.4.1 Model Development

The development of geometric models for experimental studies of cerebral aneurysms and the cerebral vasculature has varied throughout previous studies. Early studies employed the use of idealised models, developed based on average measurements

from literature. The choice of material and model development technique has also varied throughout literature, depending on the objective of the experimental analysis. Fahrig *et al.* (1999) grouped the different types of flow phantom models into three categories:

(1) Simple models developed from glass or plastic
(2) Models constructed using castings from cadavers
(3) Models developed from patient-specific data, typically constructed from milling machines or advanced rapid prototyping

In recent years, advances in imaging techniques has allowed for the development of geometrically accurate, patient-specific models such as those described in category three. Using results from computed rotational angiography, MRA or CT, patient-specific models have been developed using the lost-wax method, rapid-prototyping, or a combination of both techniques.

The lost-material or lost-wax method, also known as investment casting, is a popular technique for the development of realistic cerebral aneurysm models. The method involves the use of a two-part negative mould to develop a solid inner core, often made from wax. The solid wax model is then either placed in another mould where the surrounding material is injected around it, or it is embedded in the surrounding material, typically a silicone elastomer. Once the silicone has cured and solidified, the wax core is melted out, resulting in either a silicone block with a hollow artery and aneurysm geometry embedded, or a hollow silicone flow phantom (Ford *et al.* 2008).

Rapid prototyping or 3D printing has become a popular tool for the development of 3D physical models (Rengier *et al.* 2010). The process involves the use of 3D computer aided design (CAD) drawings or geometries to control a machining process that either removes material from a solid block or deposits material to develop a 3D model (Kimberly Knox *et al.* 2005). Several studies have incorporated rapid prototyping into the lost-material method, developing the inner cores used to create the arterial and aneurysm lumen using rapid prototyping machinery (Fahy *et al.* 2013, Steinman *et al.* 2013, Wetzel *et al.* 2005). The attraction of rapid prototyping as a material development technique over traditional wax models lies in its ability to create complex shapes and geometries from a range of materials in a relatively short time-frame (Rengier *et al.* 2010). Examples of 3D models that included rapid prototyping in the development process are illustrated in Figure 2.17 below.

Figure 2.17: Examples of 3D cerebral aneurysm models created using rapid prototyping (A) wax inner lumen of ICA aneurysm (Wetzel *et al.* 2005) (B) low melting point alloy inner core of ICA aneurysm (Steinman *et al.* 2013) (C) wax inner lumen replica of BA aneurysm (K. Knox *et al.* 2005)

One issue that is raised by several authors is the use of rigid-walled models to replicate cerebral aneurysms. Although arteries are thought to be compliant and distend under the pressure of pulsing blood, cerebral arteries are reportedly stiffer than other arteries (Liou *et al.* 2007). Furthermore, previous studies have reported no significant differences between rigid-walled and distensible models (Tateshima *et al.* 2003).

2.4.2 Flow Systems

The test systems employed in haemodynamic studies of cerebral aneurysms have varied in their set-up, with both steady (Babiker *et al.* 2010, Carroll *et al.* 2010, Steinman *et al.* 2013, Yu and Zhao 1999) and pulsatile flows utilised (Ernemann *et al.* 2003, Fahy *et al.* 2013, Ford *et al.* 2008, Liou *et al.* 1997). Although more recent studies tend to include pulsatile flow so as to mimic the pulsatile effects of the heart on blood flow, Liou *et al.* (1997) report that using steady flow to simulate pulsatile flow in flow phantoms of aneurysms adequately captures the mean flow patterns, although discrepancies may be found in the location of maximum fluctuations. Yu and Zhao (2000) carried out a particle image velocimetry (PIV) study on the pulsatile flow characteristics within sidewall aneurysm models. Results for this study highlighted differences between steady and pulsatile flows, in which the location of the centre of a recirculation vortex that formed within the aneurysmal bulge didn't remain constant for the pulsatile flow cycle. As a result, the regions exposed to high and low shear stresses were not permanent, and wall shear oscillation could appear. A similar study reports that the main differences between steady and pulsatile flows is that the effects of flow pulsatility tend to increase the possibility of higher shear stress magnitude and

rapid changing of the shear stress direction within the aneurysm (Yu and Zhao 1999). Furthermore, Takeuchi and Karino (2010) experimentally examined the relationship between flow patterns and sites of aneurysm formation within the ICA and MCA under steady and pulsatile flow conditions, and reported that qualitatively, the same flow phenomena occurred in both steady and pulsatile flow simulations. However, the secondary and recirculating flows differed for the pulsatile simulation, disappearing at the minimum flow velocity for each cycle.

Although water is often used as the working fluid in experimental flow models (Carroll *et al.* 2010, Liou *et al.* 1997, Lutostansky *et al.* 2003), several studies have opted to use water/glycerol solutions in an attempt to mimic the viscosity of blood as closely as possible, while also allowing for direct comparisons with computational analyses. The ratio of water to glycerol has differed throughout previous studies; Yu and Zhao (1999) employed a volume ratio mixture of water to glycerol of 40:60, Ford *et al.* (2008) used a 50:50 ratio and Fahy *et al.* (2013) opted for a 54.6:45.4% by weight ratio of de-ionised water to glycerol mixture.

2.4.3 Mass Transport

A novel experimental method to examine the mass transport behaviour of blood-borne molecules within a recirculation region was developed by Lutostansky *et al.* (2003). Using a sudden expansion impermeable glass flow chamber as the test section, the test fluid contained a water/food dye mixture, with the dye representing blood-borne species such as ATP. Using a dye density technique, a small sample of the test fluid was extracted from different sampling locations over the course of the experiment, allowing the changes in fluid concentration at the wall to be determined. Results for the study illustrated a slow build-up of species at the test region, with an increase in species concentration evident in the upstream and downstream tubes of the sudden expansion geometry.

A similar method was adopted by Carroll *et al.* (2010) in their study of biological blood-side mass transfer within an idealised abdominal aortic aneurysm. Using a water/dye mixture, the changes in concentration at the aneurysm wall over time was

determined and compared to computational results using different discretisation schemes. Results for this study are shown in Figure 2.18 in which the concentration of species found at the aneurysm wall is seen to increase slowly over time, due to the slow-moving recirculation zone found within the aneurysm bulge.

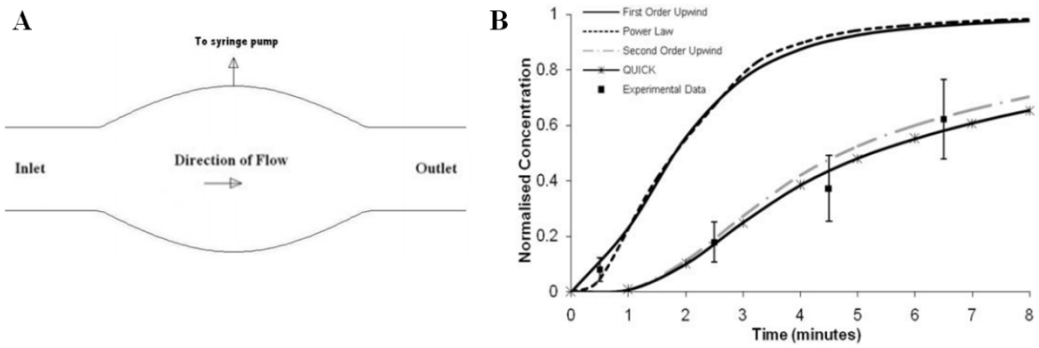

Figure 2.18: (A) Idealised axi-symmetric aneurysm test model (B) Comparison of computational and experimental results, highlighting increase in concentration along aneurysm wall over time (Carroll *et al.* 2010)

2.5 Hypothesis and Objectives

It is evident from this extensive review that the exact mechanisms behind the rupture of cerebral aneurysms are still unknown, although it appears to be a multifactorial process involving geometric features and haemodynamics. Due to significant risks associated with current intervention methods, the importance of the development of a definite rupture prediction method is clear, so as to allow aneurysms that are at risk of rupture to be determined.

The hypothesis motivating this study is that cerebral aneurysm rupture potential may be related to the health of the aneurysm wall tissue. It is proposed in this study that the wall tissue health may be affected by the transport of vital blood-borne species to the aneurysm wall. The transport of nutrients and species to the aneurysm wall can result in aneurysm wall tissue stabilisation, or else an under- or over-expression of species at the wall. This could in turn lead to negative wall remodelling, aneurysm growth and eventual rupture. It has already been determined in previous studies that mass transport is strongly influenced by the flow haemodynamics within the vasculature, and flow is influenced in turn by the geometry of the aneurysm. Therefore, it is the aim of this study to establish if a link exists between the different geometric parameters and the mass transport of species to the aneurysm wall, and if this link may correlate with aneurysm rupture potential.

The main objective of this study is to investigate the relationship between geometric parameters, the mass transport of blood-borne species, and their relationship with cerebral aneurysm growth and rupture potential. In order to carry out this investigation, several sub-objectives were defined, including:

- The development of a database of patient-specific cerebral aneurysm geometries to be used in the investigation of the relationship between geometric parameters, mass transport and cerebral aneurysm growth and rupture potential
- The generation of idealised and representative cerebral aneurysm models, developed based on patient-specific aneurysm measurements, and the investigation of the efficacy of representative models as an alternative to idealised and patient-specific models
- The development of computational models for the computational fluid dynamics analysis of mass transport within cerebral aneurysms
- The validation of the computational methods used in this study through the use of experimental analysis
- The investigation into the relationship between radiologically measurable parameters and cerebral aneurysm growth and rupture potential using a database of patient-specific aneurysms
- The investigation into the relationship between the mass transport of blood-borne species and cerebral aneurysm growth and rupture potential using a database of patient-specific aneurysms
- The investigation into the combined relationship of geometric parameters and mass transport of blood-borne species with cerebral aneurysm growth and rupture potential using a database of patient-specific aneurysms
- To test the hypothesis that cerebral aneurysm growth and rupture is influenced by a combination of geometric parameters and mass transport on an independent cohort of patient-specific cerebral aneurysms

CHAPTER 3

GEOMETRY DEVELOPMENT

Chapter 3 Geometry Development

3.1 Introduction

As outlined in the previous chapter, the overall objective of this study is to investigate the relationship between geometric parameters, the mass transport of blood-borne species, and cerebral aneurysm growth and rupture potential. Recently, many of the studies of cerebral aneurysms in literature have focused on the use of patient-specific geometric models due to the inherent limitations of idealised models (Castro *et al.* 2006, J. R. Cebral *et al.* 2005b, Geers *et al.* 2011). However, patient-specific simulations require medical imaging and flow data that isn't typically extracted during medical procedures, and can be computationally intensive and time consuming. Therefore, the following chapter investigates the use of representative models to act as a compromise between simplified idealised and complex patient-specific geometries. If representative geometries can adequately predict the mass transport of species within cerebral aneurysms, then the rupture potential of an aneurysm could be calculated based on its key geometric measurements. This would potentially allow more immediate decisions to be made by clinicians as to whether surgical intervention is necessary for unruptured aneurysms.

In this chapter, the processes involved in the development of representative cerebral aneurysms geometries based on patient-specific data are presented. These representative models are developed using measurements taken from 168 patient-specific aneurysms consisting of key geometry-defining parameters (height, neck width, diameter, distance to maximum diameter, tilt angle and aspect ratio) to describe the aneurysm shape, and using location-specific average parent and daughter artery measurements. Idealised models are also created which, along with patient-specific models, will allow for a numerical investigation into the efficacy of representative models as an alternative to simple idealised and complex patient-specific geometries.

The chapter is organised as follows: at the outset, the study population of 168 patient-specific cerebral aneurysms used for the geometric, computational and experimental studies is introduced and classified based on several morphological parameters. Next, the technique used to extract the key geometric measurements from each of the patient-specific aneurysm geometries is described, following which the steps taken in the development of idealised and representative aneurysm models is outlined. Finally,

the preparation of the patient-specific models for computational analysis is detailed. The geometries developed in this chapter are used in the computational analyses to follow.

3.2 Study Population

The sample set used for this study is a subset of the @neurIST: Integrated Biomedical Informatics for the Management of Cerebral Aneurysms project. @neurIST was a 4 year multidisciplinary European initiative that began in January 2006 and ended in March 2010. 28 public and private institutions across 12 European countries were involved in the project, which aimed to improve the infrastructure for the management, integration and data processing of cerebral aneurysm and subarachnoid haemorrhage diagnosis and treatment (Villa-Uriol *et al.* 2011). Following the @neurIST project, access was granted by the CISTIB (Computational Imaging and Simulation Techniques in Biomedicine) group in the Universitat Pompeu Fabra (Barcelona) to a database of 265 patient-specific cerebral aneurysm geometries. These aneurysms, from 16 locations throughout the circle of Willis, had been collected and analysed as part of the @neurIST project. Several geometries were removed from the sample set due to incomplete data, and so the final database consisted of 168 patient-specific aneurysms from 13 locations.

Three-dimensional rotational angiography images of the aneurysms were used to construct patient-specific models, which were represented by triangular surface meshes (Geers *et al.* 2014). Each of the 168 aneurysm geometries were supplied in visualisation toolkit (VTK) format, with each aneurysm consisting of five files, which are illustrated in Figure 3.1: (A) extended 3D aneurysm and parent artery geometry (B) extended centreline skeleton (C) a section containing the aneurysm and a segment of the parent artery geometry (D) the aneurysm dome and (E) the neck surface. No patient data (i.e. gender, age, patient history etc.) other than the rupture status was made available for this study.

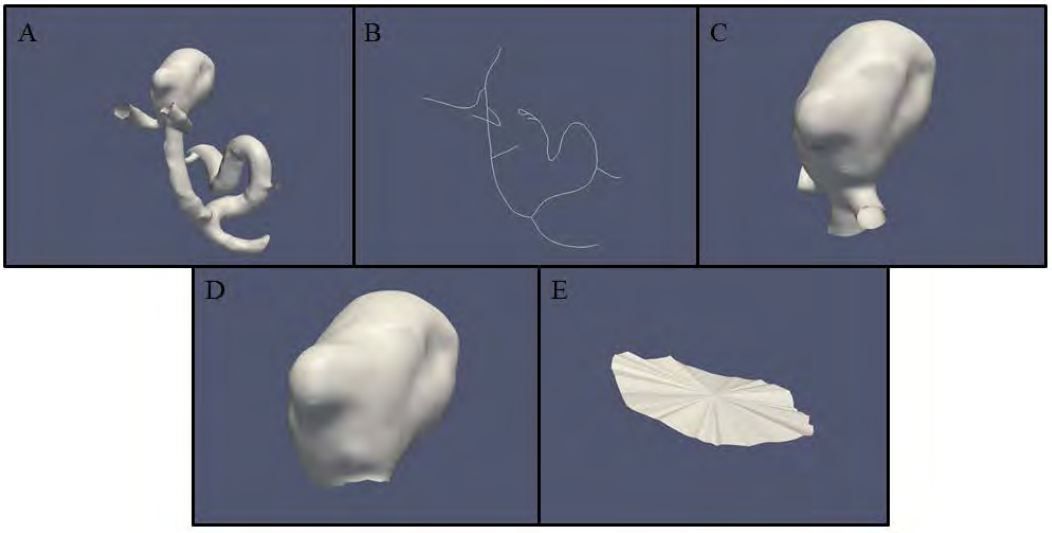

Figure 3.1: (A) Full geometry (B) Centreline skeleton (C) Aneurysm including arterial segment (D) Dome and (E) Neck surface

3.3 Anatomical Classification

The aneurysm database was classified based on several parameters, including location within the cerebral vasculature, shape morphology, size group and neck size group. Results from the classification are presented in Table 3.1.

Table 3.1: Aneurysm classification results

Parameter	No. of Aneurysms	%
Location		
Anterior	107	64
Posterior	61	36
Shape		
Lateral	56	33
Bifurcating/Terminal	112	67
Size		
Small	77	46
Medium	86	51
Large	4	2
Giant	1	1
Neck Size		
Narrow	74	44
Wide	95	56

Location

The database was first classified based on location within the cerebral vasculature. The 168 aneurysms were distributed in 13 different locations throughout the circle of

Willis, as illustrated in Table 3.2. Further classification was enabled based on their location in the anterior or posterior circulation. It can be seen from Table 3.2 that most of the aneurysms (26%, n = 44) were found at the PCoA, the ophthalmic segment of the ICA (19%, n = 32) and the sylvian bifurcation (22%, n = 37), a distal branch of the MCA. The smallest number of aneurysms (<1%, n = 1) were found distal to the sylvian bifurcation, at the medial wall of the ICA and at the pericallosal artery. The database was further classified as consisting of 64% anterior circulation aneurysms and 36% posterior circulation aneurysms.

Table 3.2: Distribution of aneurysms across anterior and posterior circulations

Location	No. of Aneurysms	%	
Anterior Circulation			
A1 Segment ACA	5	2.98	
Anterior Choroidal Segment ICA	10	5.95	
Carotid Bifurcation	11	6.55	
Distal to Sylvian Bifurcation	1	0.60	
Intracavernous Segment ICA	4	2.38	64%
M1 Segment ICA	5	2.98	
Medial Wall ICA	1	0.60	
Ophthalmic Segment ICA	32	19.05	
Pericallosal Artery	1	0.60	
Sylvian Bifurcation	37	22.02	
Posterior Circulation			
Basilar Tip	13	7.74	
Posterior Communicating Artery	44	26.19	36%
Superior Cerebellar Artery	4	2.38	
Total	168	100	

Shape Morphology

Further classification of each aneurysm was completed based on its anatomical characteristics, with each aneurysm shape defined as either lateral or bifurcation (including terminal), similar to Liou and Liou (1999). The database consisted mainly of bifurcating/terminal aneurysms (66.7%, n = 112), with just one third of the database consisting of lateral shaped aneurysms. Furthermore, each aneurysm was sub-divided into two regions, similar to the definition by Ujiie *et al.* (1999). The aneurysm neck refers to the area immediately adjacent to the orifice or entrance to the aneurysm, while the dome refers to the sac or body of the aneurysm (see Figure 3.2).

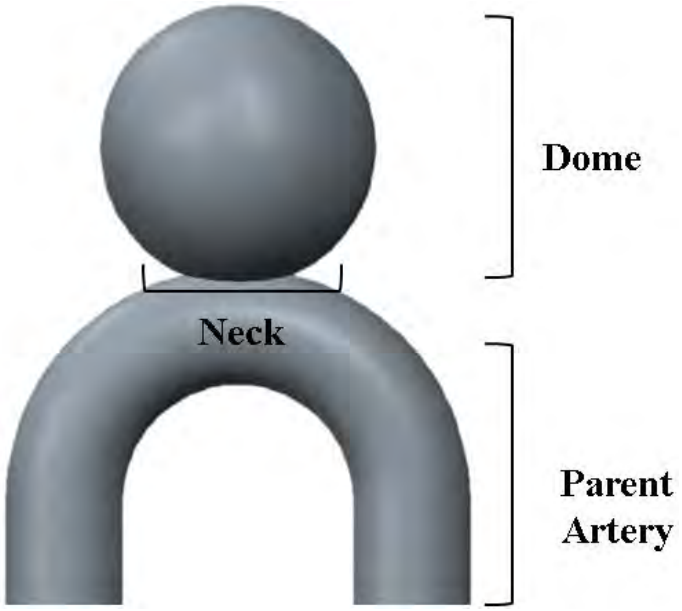

Figure 3.2: Illustration highlighting regions of aneurysm geometry, including dome, neck and parent artery

Size

It has previously been established in Section 2.2.3.2 that some inconsistency remains between studies with regards to the classification of aneurysms in terms of size i.e. largest diameter within the dome (Campi *et al.* 2007, J. R. Cebral *et al.* 2005b, Choi and David 2003, Hademenos *et al.* 1998, Mehra *et al.* 2011, Meyers *et al.* 2009). The aneurysm size categories - which refer to the largest diameter within the dome - were grouped in accordance with Meyers *et al.* (2009), with four categories of small ($\leq$5 mm), medium (5<x<15 mm), large (15$\leq$x<25 mm) and giant ($\geq$25 mm) aneurysms. The aneurysms ranged in size from 1.5 mm to 25 mm, with an average size of 6.3 mm. Medium aneurysms were most common (51.2%, n = 86), with 45.8% small and 2.4% large aneurysms. There was just 1 giant aneurysm within the database, found at the ophthalmic segment ICA.

Neck Size

Aneurysms can also be defined based on their neck size. As outlined previously, the definition of a narrow neck is typically x$\leq$4 mm. Neck widths larger than this value are classified as wide-necked. In the database of 168 aneurysms used in this study, wide necks were more common (56%, n = 95) as compared to narrow necks (44%, n = 73), with an average neck size of 4.5 mm found.

3.4 Measurement Extraction

The development of the representative cerebral aneurysm models took place over several steps, which are outlined in the following section. First, several key patient-specific measurements were extracted that could be used to describe the geometry of the individual aneurysm. Each aneurysm geometry was imported into Paraview 4.0.1 (Kitware, Villeurbanne, France) and converted into STL (Stereolithography) format - representations of 3D objects in which the surface of the object is described by a series of triangles. The STL files were then imported into Creo Parametric 2.0 (PTC, MA, USA) to facilitate the calculation of measurements.

Section 2.2.3.3 detailed how numerous previous studies have attempted to correlate geometric features with rupture risk (Dhar *et al.* 2008, Ma *et al.* 2004, Raghavan *et al.* 2005), and so have characterised aneurysms through the definition of geometric parameters and ratios. However, some variation is seen in the exact definition of these parameters. For example, Beck *et al.* (2006) define the height as the maximum length computed between the base and the dome of the aneurysm, whereas Parlea *et al.* (1999) suggest the height can be measured as the right bisector to the neck. This study intends to define the aneurysm shape based on radiologically measurable parameters that are easily extracted from 3D scans or geometries. This is discussed in more detail in Chapter 6.

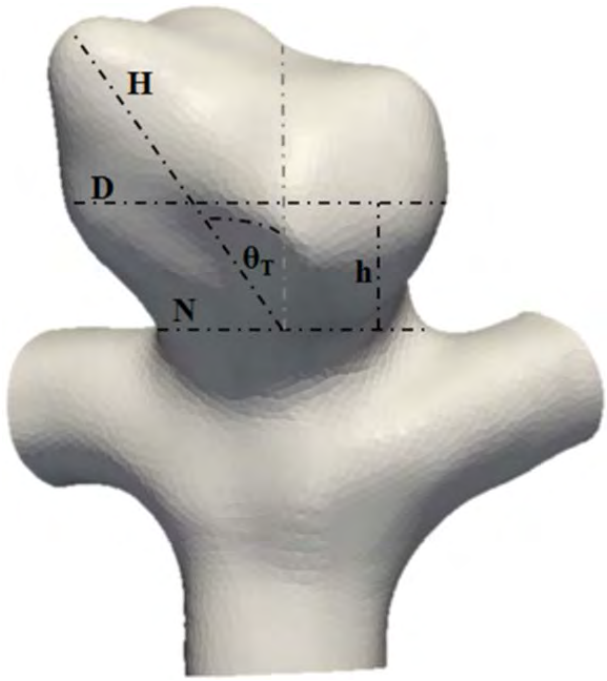

Figure 3.3: Geometric Parameters Measured (H = height, D = diameter, N = neck width, h = distance from neck to diameter, θ_T = tilt angle)

The geometric parameters measured in this study are illustrated in Figure 3.3. The neck width (N) was defined as the widest distance across the neck orifice. Next, the diameter (D) of the aneurysm was determined as the largest separation of the aneurysm walls in parallel with the neck plane. For the aneurysm height (H), the furthest distance between the centre of the neck and aneurysm dome was computed. The distance to the maximum diameter (h) - also known as the semi-axis height or bulge location (Parlea *et al.* 1999, Raghavan *et al.* 2005) - was measured as the height between the neck width and diameter lines. The tilt angle (θ_T) was defined as the in-plane angle between the line perpendicular to the centre of the neck width and the line formed by the height (H), and represents the angle that the aneurysm makes with respect to the parent artery. The tilt direction of the aneurysm i.e. whether it tilts anteriorly or posteriorly was also recorded. Results from the measurement extraction are illustrated in Table 3.3.

Table 3.3: Measured parameter values. Results presented as Mean ± Standard Deviation. All values presented are in mm, except Tilt Angle (º).

Location	No.	Height (H)	Neck Width (N)	Diameter (D)	Distance to Maximum Diameter (h)	Tilt Angle (θ_T)	Aspect Ratio (AR)
Anterior Circulation							
A1 Segment ACA	5	3.31 ± 1.44	2.76 ± 0.86	2.91 ± 0.92	1.95 ± 1.54	21.43 ± 4.82	1.23 ± 0.42
Ant. Choroidal Segment ICA	10	4.79 ± 2.44	3.14 ± 0.61	3.87 ± 1.69	1.94 ± 1.56	27.54 ± 11.70	1.48 ± 0.65
Carotid Bifurcation	11	4.77 ± 1.96	3.88 ± 0.77	5.48 ± 2.12	1.96 ± 1.04	31.19 ± 19.47	1.23 ± 0.38
Distal to Sylvian Bifurcation	1	4.45	3.79	3.99	2.91	37.58	1.17
Intracavernous Segment ICA	4	3.57 ± 2.38	3.99 ± 0.89	4.30 ± 1.89	1.04 ± 0.60	42.31 ± 25.07	0.84 ± 0.46
M1 Segment MCA	5	4.17 ± 1.78	4.46 ± 1.36	5.29 ± 2.57	1.55 ± 1.15	28.46 ± 11.23	0.92 ± 0.26
Medial Wall ICA	1	4.86	3.67	4.95	2.28	18.78	1.33
Ophthalmic Segment ICA	32	7.22 ± 5.04	5.50 ± 1.70	8.26 ± 4.86	2.89 ± 2.98	30.23 ± 16.45	1.28 ± 0.72
Pericallosal Artery	1	6.24	4.24	7.17	1.12	28.12	1.47
Sylvian Bifurcation	37	5.35 ± 2.82	4.40 ± 1.57	5.83 ± 2.83	2.00 ± 1.45	30.53 ± 20.11	1.20 ± 0.50
Posterior Circulation							
Basilar Tip	13	8.27 ± 3.47	5.67 ± 1.55	10.50 ± 3.98	2.87 ± 1.51	43.54 ± 15.11	1.45 ± 0.43
PCoA	44	5.14 ± 2.43	4.15 ± 1.52	5.38 ± 2.63	1.74 ± 1.29	30.81 ± 16.70	1.28 ± 0.57
SCbA	4	4.91± 2.92	4.51 ± 1.16	5.30 ± 2.34	1.51 ± 0.96	36.12 ± 17.43	1.03 ± 0.47

3.5 Idealised, Representative and Patient-Specific Geometry Development

The following section describes the development of idealised and representative aneurysm models, and the preparation of patient-specific aneurysm geometries for computational analysis. These geometries will then be used in a comparative computational study into the efficacy of representative geometries as an alternative to simple idealised and complex patient-specific models.

3.5.1 Idealised Geometry Development

Numerous previous studies have incorporated idealised geometric models into their computational analyses of haemodynamics within cerebral aneurysms (Appanaboyina *et al.* 2008, Baharoglu *et al.* 2010, Fisher and Rossmann 2009, Sato *et al.* 2008). Although it is acknowledged that idealised models can neglect aspects of the geometry and cannot be extrapolated to the individual case (A. A. Valencia *et al.* 2006), they are useful in identifying general trends in flow behaviour. In this study, idealised cerebral aneurysm geometries were developed so as to compare flow and mass transport patterns to those seen in complex patient-specific models, and to the newly developed representative geometries.

Aneurysms are typically found along curved arterial segments and at arterial branching points (Lasheras 2007), and so idealised models of both lateral and bifurcation shape morphologies were developed in this study, representing the different arterial configurations that are found throughout the CoW. Two models were developed: a lateral model of a curved arterial segment with a spherical aneurysm protruding from the side of the artery, and a bifurcation model with a saccular aneurysm found at the bifurcation of the parent artery into two daughter arteries. The final idealised models are illustrated in Figure 3.4.

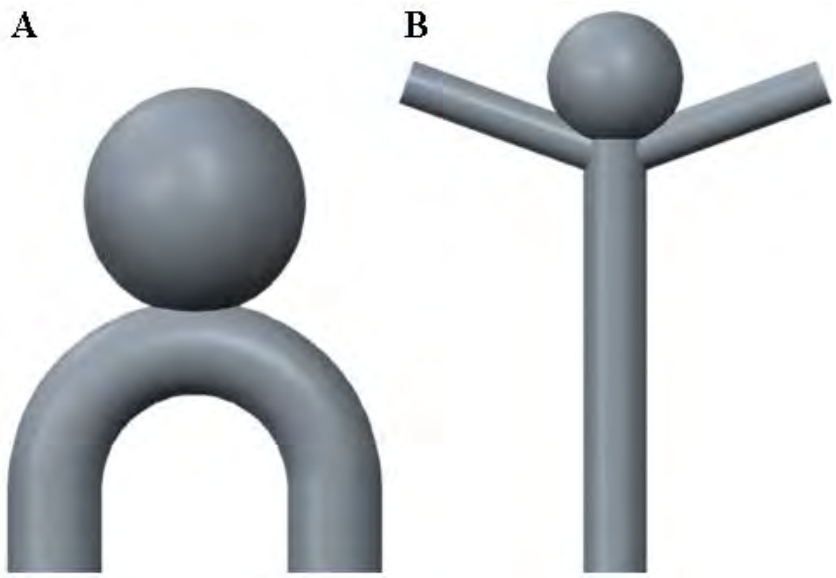

Figure 3.4: Illustration of (A) idealised lateral aneurysm and (B) idealised bifurcation aneurysm

For the lateral saccular model, an aneurysm of the ophthalmic segment of the ICA was selected, which is defined as the arterial section between the ophthalmic artery and the PCoA branch (Roy *et al.* 1997). These saccular sidewall aneurysms represent typical lateral aneurysms, having a spherical sac attached to the side of an arterial segment. Created in Creo Parametric 2.0 (MA, USA), the lateral aneurysms consisted of an arterial segment of constant diameter 4.02 mm, representing the average ICA diameter (Alastruey *et al.* 2007, Devault *et al.* 2008, Fahrig *et al.* 1999, Hartkamp *et al.* 1999, Moore *et al.* 2006, Roessler *et al.* 2006). An arterial curvature radius of 6 mm was incorporated (Sato *et al.* 2008). The aneurysm dome was defined based on average height, neck width and diameter measurements (see Table 3.4) taken from a study of 41 patient-specific internal carotid-ophthalmic artery segment aneurysms (Chien *et al.* 2013).

Table 3.4: Parameter measurements used to develop idealised aneurysm models. Results for ophthalmic segment ICA and sylvian bifurcation taken as mean values from Chien *et al.* (2013) and Parlea *et al.* (1999) respectively.

Parameter	Mean Value (mm)	
	Ophthalmic Segment ICA	Sylvian Bifurcation
Height (H)	9.2	5.6
Neck Width (N)	4.4	3.4
Diameter (D)	9.5	6.1

For the idealised bifurcation model, aneurysms of the sylvian bifurcation - a distal branch of the MCA - were used. Aneurysms at this location represent typical bifurcation or terminal type aneurysms, where a saccular lesion forms at the bifurcation of an artery into two or more daughter arteries. The idealised geometry consisted of a straight cylindrical artery of 2.84 mm (Alastruey *et al.* 2007, Cieslicki and Ciesla 2005, Devault *et al.* 2008, Fahrig *et al.* 1999, Moore *et al.* 2006, Roessler *et al.* 2006) which branched into two daughter arteries of 2mm (Cieslicki and Ciesla 2005) at a bifurcation angle of 140 degrees (Liou and Liou 1999, Valencia and Solis 2006). A saccular symmetrical aneurysm is included at the bifurcation point, with the parameter values taken from Parlea *et al.* (1999).

3.5.2 Representative Geometry Development

As mentioned previously, the use of patient-specific geometries for computational analysis of cerebral aneurysms has increased in recent years. However, although patient-specific models give improved information relating to the individual case when compared to idealised models, simulations using patient-specific data require flow data that isn't usually acquired during standard medical procedures (Mut *et al.* 2011). Therefore, questions arise as to the patient-specific relevance of the results. Additionally, patient-specific flow simulations are computationally expensive. Therefore, this study involved the development of representative geometric models to act as a compromise between simplified idealised and complex patient-specific geometric models.

In this study, representative aneurysms are defined as having the same key geometric measurements of the aneurysm dome as a patient-specific aneurysm, with a location-specific average parent and daughter artery geometry. Similar to the idealised geometries outlined previously, both lateral (ophthalmic segment ICA) and bifurcation (sylvian bifurcation) shape morphologies were developed so as to represent the typical arterial configurations at which aneurysms are most commonly found. The development of the representative cerebral aneurysm geometries took place over three main steps: (1) centreline averaging, (2) diameter sweep and (3) final geometry development.

Centreline Averaging

In order to develop the average parent and daughter artery for both locations within the CoW, the average artery centrelines were determined. The steps involved in this stage are shown in Figure 3.5. Using the sylvian bifurcation as an example, one of the patient-specific overall geometry centrelines was imported into Paraview. The geometry skeleton or centreline was segmented so as to remove all major and minor branch vessels, leaving the main parent artery centreline remaining. Each centreline was exported as a series of coordinate points which were translated so that the 0, 0, 0 coordinate corresponded with the aneurysm neck orifice. This was repeated for each of the 37 patient-specific sylvian bifurcation geometries. The length of each parent artery centreline was computed and the centrelines were clipped to the same length before being divided into 10 equidistant points. Next, the representative sylvian bifurcation parent artery centreline was drawn in CAD software by averaging the X, Y, Z components of each point and passing a curve through the average points. The steps were repeated for each daughter artery of the sylvian bifurcation, and for the 32 ophthalmic segment ICA geometries. This resulted in average sylvian bifurcation and ophthalmic segment ICA centreline geometries.

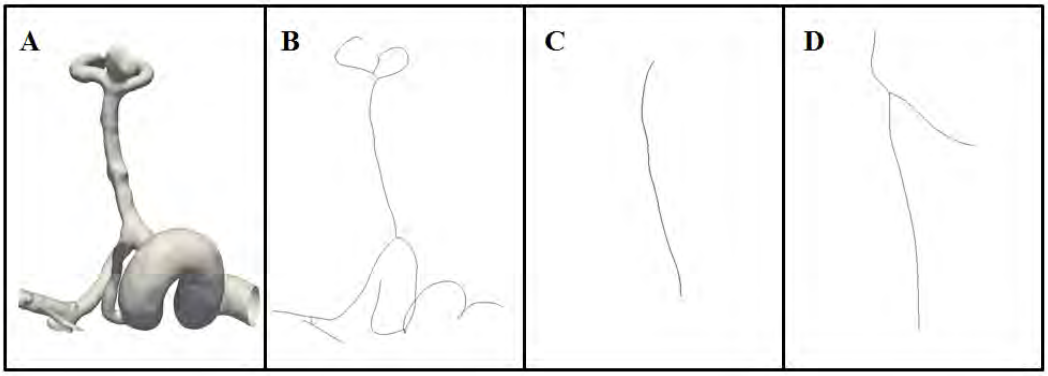

Figure 3.5: Centreline extraction with (A) full patient-specific geometry (B) geometry centreline (C) isolated parent artery centreline and (D) final averaged sylvian bifurcation centreline

Diameter Extraction

The next step in the representative aneurysm geometry development was to determine the individual and average parent and daughter artery diameters. Each of the patient-specific aneurysm geometries were imported into the open source software Blender 2.68a (Amsterdam, The Netherlands). An orthogonal cross-section of the arterial segment was taken at two locations, distal to the aneurysm at the entrance to the

artery, and within two diameters of the aneurysm neck so as to account for any decrease in vessel diameter along its length (Volkau *et al.* 2005). The diameter measurements were exported from Creo as coordinate points, before being imported into Matlab2008b (Mathworks, Cambridge, UK) where a best-fit circle was fitted to the points. Although arteries are not typically circular in shape in vivo, several studies have suggested that approximating their cross-section as circular is a reasonable approach (Volkau *et al.* 2005, Zakaria *et al.* 2008). An example of the artery inlet diameter points and best-fit circle are shown in Figure 3.6, with results from the diameter measurement illustrated in Table 3.5.

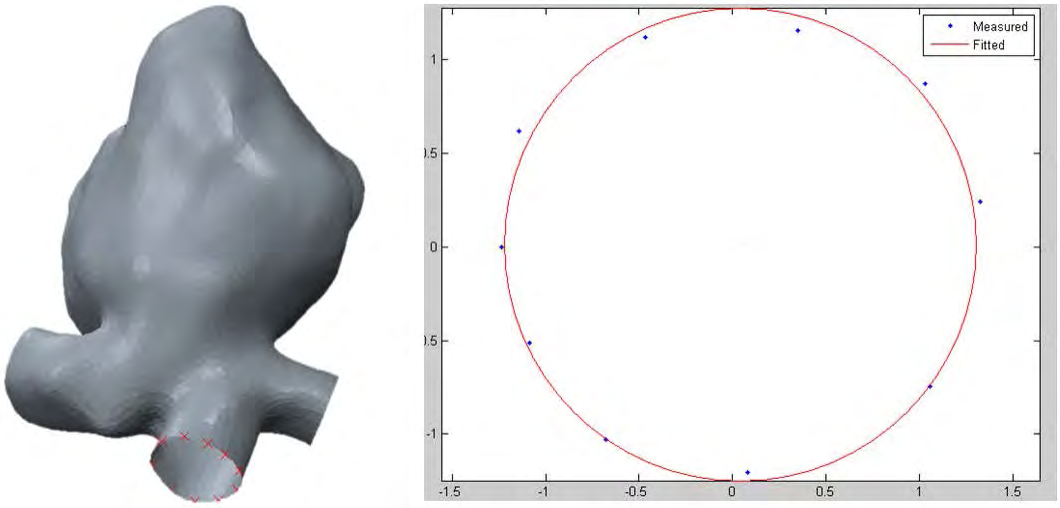

Figure 3.6: Best-fit circle fitted to artery diameter points

Table 3.5: Measured aneurysm inlet and outlet diameter values. Results presented as Mean ± Standard Deviation.

Location	No.	Inlet	Outlet 1	Outlet 2	Outlet 3	Outlet 4
Anterior Circulation						
A1 Segment ACA	5	3.31 ± 0.99	2.74 ± 0.57	2.50 ± 0.41		
Ant. Choroidal Segment ICA	10	3.34 ± 0.62	2.60 ± 1.13	2.47 ± 0.94		
Carotid Bifurcation	11	3.44 ± 0.40	2.53 ± 0.37	2.40 ± 0.47		
Distal to Sylvian Bifurcation	1	3.20	2.60	1.09		
Intracavernous Segment ICA	4	3.75 ± 0.09	4.00 ± 0.71	0.88 ± 0.29		
M1 Segment MCA	5	2.36 ± 0.47	1.77 ± 0.59	1.65 ± 0.16	1.84	
Medial Wall ICA	1	4.00	3.20			
Ophthalmic Segment ICA	32	3.99 ± 0.69	3.34 ± 1.15	1.23 ± 0.92	0.99 ± 0.07	
Pericallosal Artery	1	1.94	2.00	1.23		
Sylvian Bifurcation	37	2.53 ± 0.46	2.06 ± 0.32	1.79 ± 0.38		
Posterior Circulation						
Basilar Tip	13	2.53 ± 0.45	1.10 ± 0.46	1.72 ± 0.43	1.66 ± 0.43	1.12 ± 0.26
PCoA	44	3.46 ± 0.69	3.28 ± 0.76	1.62 ± 0.69	0.70 ± 0.22	
SCbA	4	2.70 ± 0.17	2.39 ± 0.73	1.95 ± 0.34	1.47 ± 0.17	1.08 ± 0.25

Geometry Development

The final step was to create the representative aneurysm dome and surrounding geometry in Creo Parametric. First, the average parent and daughter artery centreline was imported, and using a swept blend, the artery diameters were swept along the centrelines. Next, the aneurysm dome was drawn based on the key geometric measurements taken from its patient-specific counterpart (see Figure 3.7). The aneurysm height (H), neck width (N), diameter (D), distance to maximum diameter (h) and tilt angle (θ_T) were defined and the 2D aneurysm sketch was revolved around its centreline.

Modelling the aneurysm dome in this fashion leads to a sharp junction between the aneurysm neck and the parent artery, which could lead to locally increased wall pressure and shear stress, and isn't physiologically accurate. Thus, a rounded curve with a minimum radius of curvature of 0.36 mm, as recommended by Haljasmaa *et al.* (2001), was added to the junction between the aneurysm and the parent artery, outlet(s) and at the tip of the aneurysm dome. This resulted in the development of a representative cerebral aneurysm based on a patient-specific model, with a location-specific average parent and daughter artery geometry.

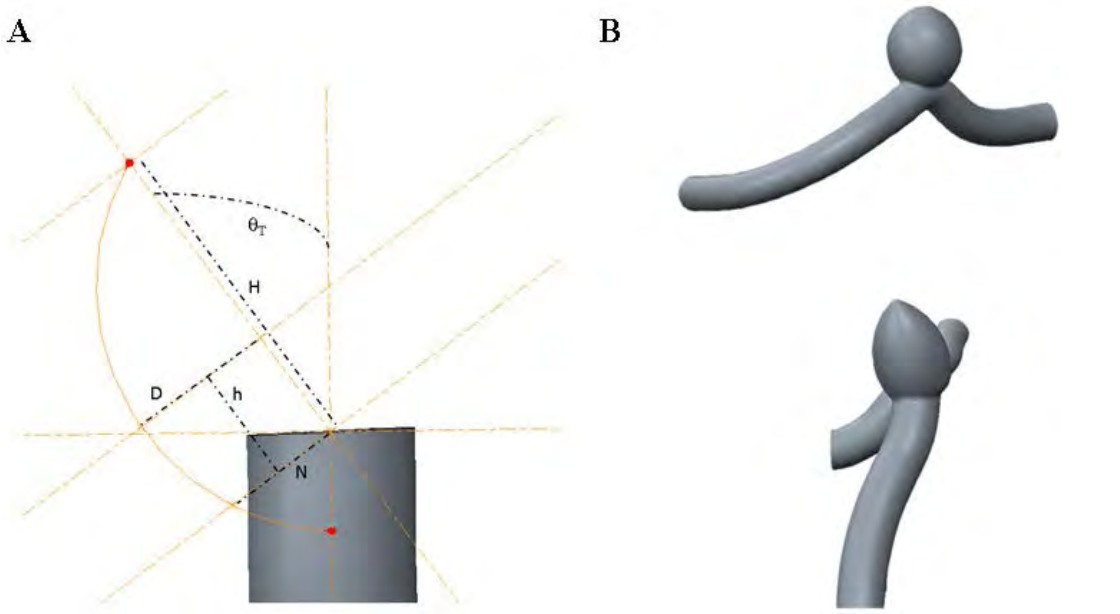

Figure 3.7: (A) Geometric measurements used to define an eurysm dome and (B) examples of representative aneurysms of the ophthalmic segment ICA (top) and sylvian bifurcation (bottom)

3.5.3 Patient-Specific Geometry Development

In order to prepare the patient-specific geometries for computational analysis, the extended aneurysm geometry containing all branch vessels was imported into Blender, where the geometry was segmented to a section containing just the aneurysm and its parent and daughter arteries. Previous studies have shown that the upstream parent artery geometry can significantly influence the haemodynamics within the aneurysm sac, and so as much of the inlet artery as possible was included in all geometries (Castro *et al.* 2006, Sato *et al.* 2008). In the case of some of the lateral aneurysms, smaller branching arteries were found along the ICA and so the geometry was segmented distal to the branch point. For the bifurcation geometries, segmentation took place at the branching of the ICA into the MCA and ACA. Parent and daughter artery inlet and outlet diameters were measured for their use in flow parameter calculations.

3.6 Final Geometries

Following implementation of the steps outlined in Sections 3.5.1 – 3.5.3, examples of the resulting idealised, representative and patient-specific lateral and bifurcation aneurysm geometries are illustrated in Figure 3.8. Using these geometries, a computational investigation into the efficacy of representative models as an alternative to idealised and patient-specific models will be carried out, with the aim of improving accuracy and reducing computational expense in cerebral aneurysm haemodynamic and mass transport studies.

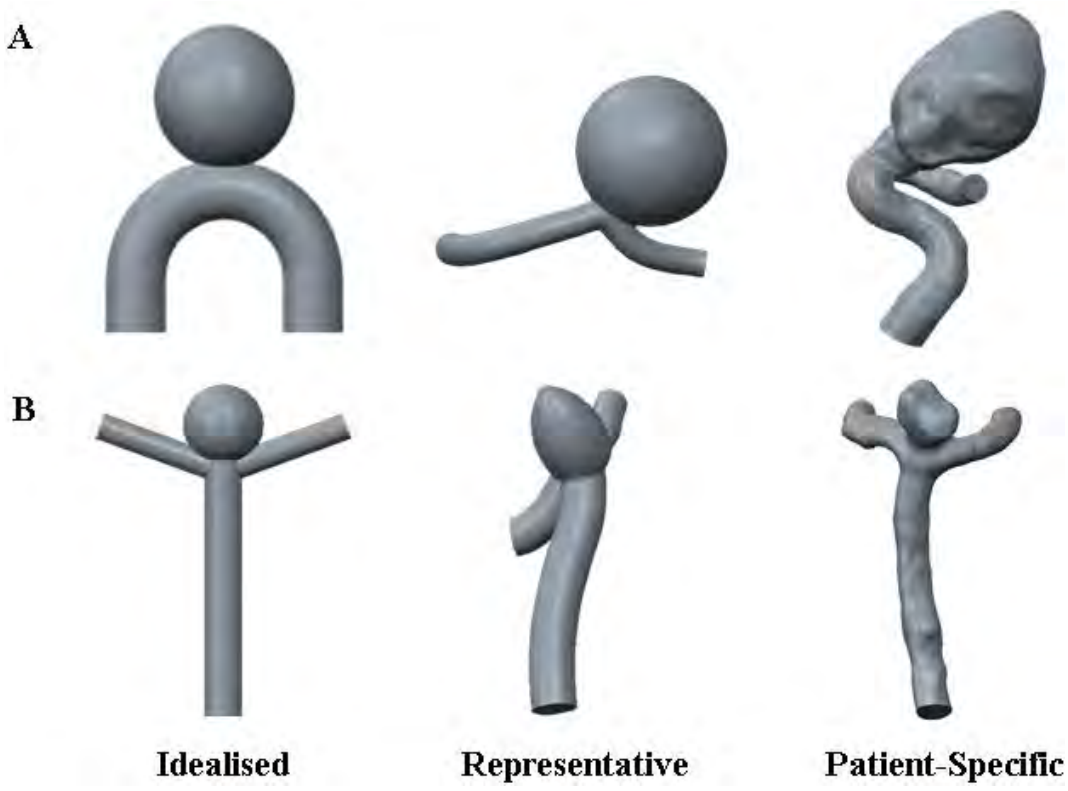

Figure 3.8: Example of idealised (left), representative (centre) and patient-specific (right) aneurysm geometries for (A) ophthalmic segment ICA and (B) sylvian bifurcation

3.7 Discussion

In this chapter, the steps involved in the development of idealised and representative models and the preparation of patient-specific models for computational analysis were outlined. The study population was introduced and classified based on geometric and morphological parameters. In classifying the study population, an insight into the distribution of the 168 patient-specific aneurysms in terms of location, shape, size and neck size is given. It is interesting to note that aneurysms within this study population are more commonly found within the anterior circulation, are bifurcating in shape, medium in size and have wide necks. However, a more detailed analysis of these morphological parameters and their relationship with aneurysm rupture is detailed in Chapter 6.

The main objective of this study is to determine if a relationship exists between geometric parameters, mass transport of species and cerebral aneurysm growth and rupture potential. A sub-objective within this study aims to determine if representative models, developed based on patient-specific data, can adequately predict the mass transport of species in cerebral aneurysms. If so, this would allow key radiologically

relevant measurements to be taken from patient-specific scans, and a decision as to whether an aneurysm is at risk of growth or rupture to be made based on these measurements. Previous studies have outlined the advantages of using patient-specific models over simplified idealised geometries, which can only give generalised information. However, the disadvantages of patient-specific models include the lack of patient-specific flow data, and the time and expense involved in their computational analysis. If representative models can be shown to adequately predict the flow and mass transport patterns of patient-specific models, representative models will provide an attractive alternative to patient-specific geometries. This will be further investigated in Chapter 7.

In order to develop representative geometries, several measurements were taken from the patient-specific aneurysms. The definition of the measured parameters in this study allows for more accurate measurements to be taken from 3D scans or geometries. Some previous studies investigating the influence of geometric parameters on rupture risk have extracted their measurements from 2D angiographic images, which may not account for the asymmetric nature of aneurysms (Raghavan *et al.* 2005). Therefore, the three-dimensional nature of the geometries used in this study allows for more accurate measurements that would not be possible using 2D scans (Larrabide *et al.* 2011). Looking at the measurement extraction results in Table 3.3, a large standard deviation is seen for some of the measured parameters. This is due to the high level of variation between cerebral aneurysms, which are unique in nature and vary significantly from patient to patient. However, each representative model is developed based on measurements from an individual patient-specific model, and so the variability between the aneurysms is neglected.

The representative geometries presented in this study are developed based on geometric measurements extracted from patient-specific aneurysm geometries. However, stark differences can be found between the representative models and their patient-specific counterparts. Looking to Figure 3.8, it can be seen for example in the sylvian bifurcation model, that the parent artery geometry of the representative model, calculated based on the average arteries of 37 sylvian bifurcation geometries, differs significantly from the patient-specific model. Furthermore, the aneurysm dome is smoother and does not account for undulations and aneurysmal blebs found throughout the dome. However, it remains to be established whether the representative

models can adequately account for the flow haemodynamics and mass transport found within the patient-specific model, which will be investigated in Chapter 7.

In summary, this chapter outlines the steps involved in the development of idealised, representative and patient-specific models for computational investigation into the use of representative models as an alternative to idealised and patient-specific models. Furthermore, these geometries will be used in the computational analysis of the relationship between geometric parameters, mass transport of species and cerebral aneurysm growth and rupture potential.

CHAPTER 4

COMPUTATIONAL MODELLING OF FLOW DYNAMICS AND MASS TRANSPORT IN CEREBRAL ANEURYSMS

Chapter 4 Computational Modelling of Flow Dynamics and Mass Transport in Cerebral Aneurysms

4.1 Introduction

Following the development of the geometries used in the computational analysis of mass transport within cerebral aneurysms, there are several important aspects that must be considered when modelling flow within an artery and aneurysm. According to Khakpour and Vafai (2008b), the most essential factors include the accurate description of the geometry being modelled (which has been discussed in Chapter 3), the application of suitable governing equations and the implementation of appropriate boundary conditions to describe the physical surroundings of the simulation. The following chapter describes the application of these essential factors (and several additional assumptions) included in this study.

Computational Fluid Dynamics, a branch of fluid mechanics, has become an important and powerful analytical tool in engineering studies. Using CFD, a computational or mathematical model can be built that represents the system being studied. CFD replaces the governing equations of fluid dynamics, namely the continuity, momentum and energy equations, with equivalent numerical descriptions. Numerical techniques are then used to analyse and solve these equations to determine information on different variables at specific locations within the flow field.

There are several methods that can be used to solve for governing flow equations, including the finite element method (FEM) and the finite volume method (FVM). In this study, the commercially available FEM solver Comsol Multiphysics 4.4 was employed to solve for the equations of fluid flow and mass transport. Using Comsol, the area of interest within the flow field is divided into cells, known as elements, to form a grid or mesh. These meshes can be either structured or unstructured, and can contain hexahedral, tetrahedral or polyhedral elements. Selected points, known as nodes, are appointed at set locations within the element where the unknown fluid property will be determined and stored (Massey 2006).

The aim of this chapter is to describe the preparation of the geometric models for computational analysis. Firstly, the method used to present the computational results is described. The governing equations applied in this study are stated and flow

conditions found within the cerebral vasculature are presented. The rationale behind assumptions made for the application of boundary conditions is discussed. Finally, the steps involved in mesh generation and a grid independence study are described.

4.2 Presentation of Results

In this section, the method used in the post-processing and presentation of results is outlined. As expressed by Goubergrits *et al.* (2012), the three-dimensional and spherical nature of aneurysm models, such as those utilised in this study, limits the visualisation of results, as the data not aligned with the viewer is obscured. An example of this can be seen in Figure 4.1, in which 2D images of the distribution of the blood-borne species adenosine triphosphate within a patient-specific aneurysm dome from different orientation views are illustrated. In order to examine the concentration distribution across the surface of the entire aneurysm dome, the surface must be unwrapped. This allows the concentration distribution to be expressed as a 2D disc. For studies using the same aneurysm but incorporating different parameters e.g. the comparison of Newtonian and non-Newtonian fluid properties, this allows a direct comparison between the results to be carried out.

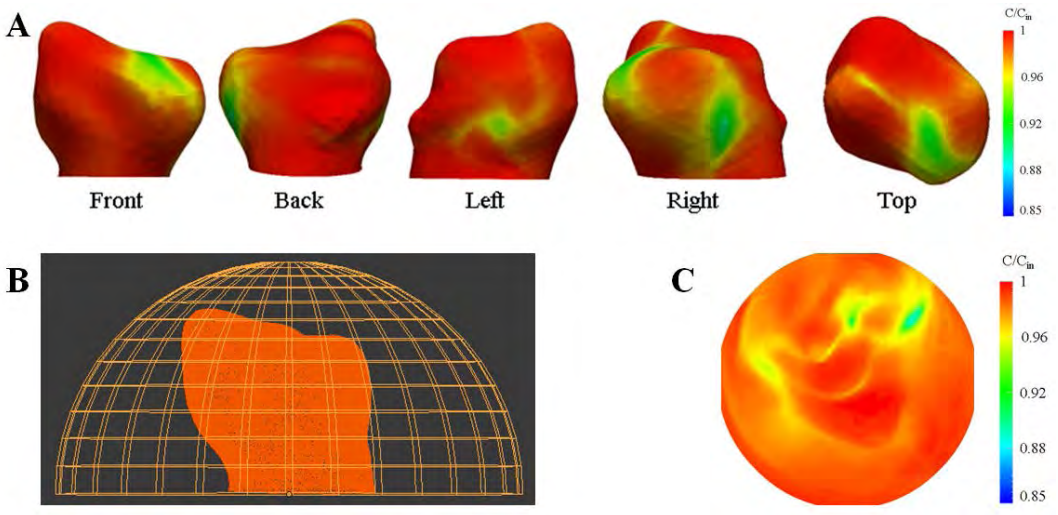

Figure 4.1: Illustration of steps involved in mapping of the normalised ATP concentration distribution within the aneurysm sac onto a 2D disc: (A) 3D aneurysm sac, coloured by normalised concentration (C/C_{in}) of ATP, in different orientation views (B) aneurysm sac (orange) surrounded by hemisphere (yellow) in Blender and (C) projected normalised concentration plot, unwrapped onto 2D disc

The development of the 2D discs took place over several steps, which are illustrated in Figure 4.1. Once each CFD simulation was completed, WSS or concentration surface plots were exported from Comsol. Each surface plot was exported in .txt format, with

each file containing the X, Y, Z coordinate points that described the aneurysm geometry, and the corresponding WSS or concentration values. The data was imported to Paraview where the geometry was cropped to the aneurysm dome, based on measurements from Section 3.4. The aneurysm dome surface plot, complete with WSS or concentration data, was then exported in .X 3d file format. Next, this file was imported into Blender.

Within Blender, a hemisphere was created around the aneurysm dome, with the orifice of the hemisphere oriented in line with the orifice of the aneurysm neck. Using the unwrap function, the hemisphere was unwrapped to create a 2D disc representation. The data from the aneurysm surface was projected onto the hemisphere using the bake rendering function, and thus the data was projected onto the 2D disc. This disc was then exported as an image file for analysis of data.

The development of 2D discs displaying the unwrapped concentration plots allows a comparison between aneurysms, despite the variation in geometries. Upon inclusion of a threshold value of species concentration, below which the aneurysm is at risk of rupture, a comparison can be performed between different aneurysms based on the percentage of the aneurysm dome surface that is under a defined threshold value. An example of the use of this method of presenting results in conjunction with threshold values is illustrated in Figure 4.2, where the surface concentration of three patient-specific sylvian bifurcation aneurysm models is compared for a threshold value of 1%, 5%, 10% and 20% of the inlet concentration.

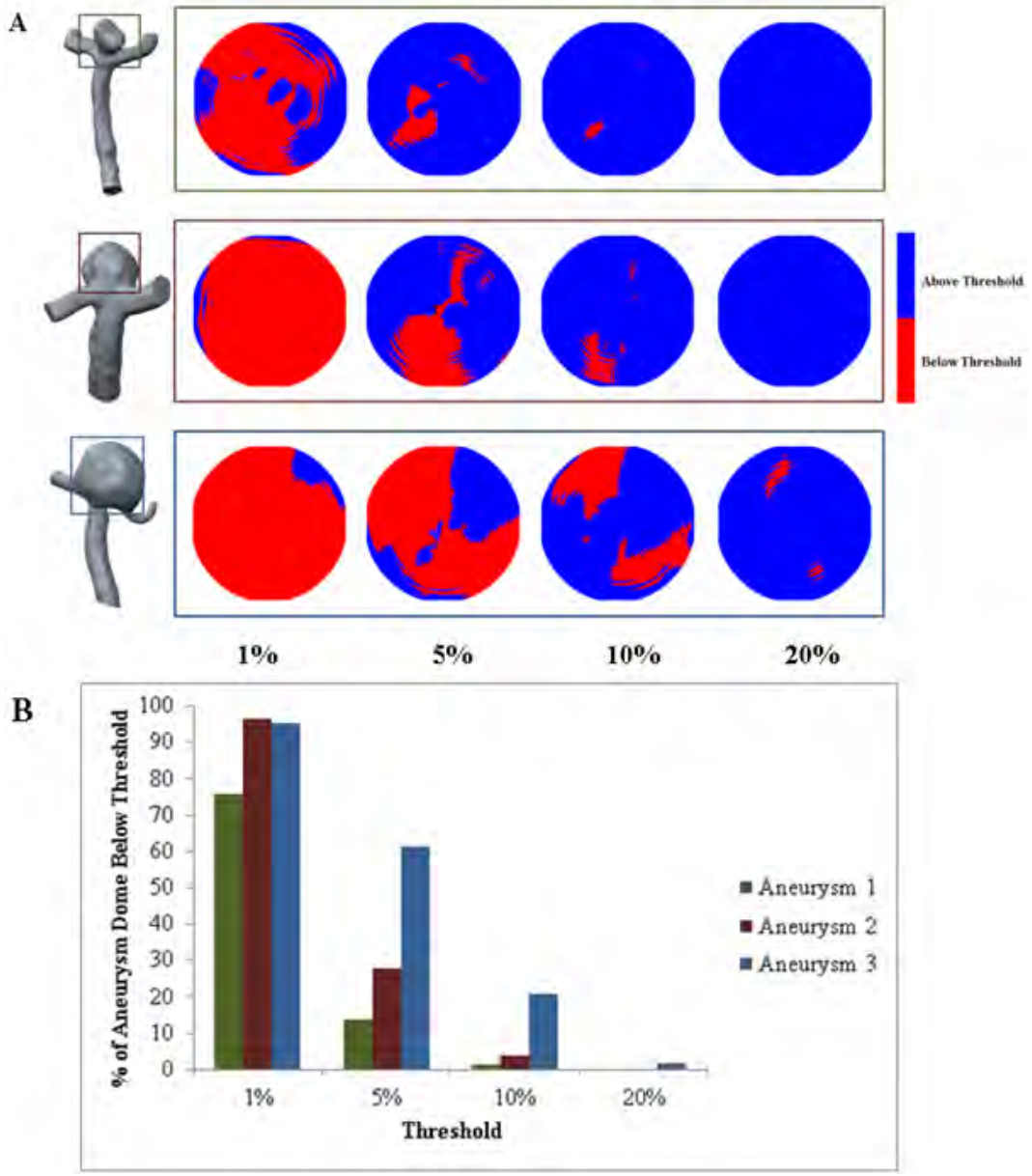

Figure 4.2: Example of unwrapped 2D concentration plots for Aneurysm 1 (green), Aneurysm 2 (red) and Aneurysm 3 (blue) illustrating (A) normalised concentration (C/C_{in}) values at threshold cut-offs of 1%, 5%, 10% and 20% below inlet concentration. Areas that are below the threshold value are shown in red in the 2D disc plot, while areas that are above the threshold are shown in blue. (B) Comparison of percentage of aneurysm dome found under the threshold value for 1%, 5%, 10% and 20% species threshold levels for aneurysms 1-3.

The concentration distribution within the aneurysm dome is calculated based on threshold cut-offs of 1%, 5%, 10% and 20% of the inlet concentration, with concentrations less than the threshold values shown in red. This allows for a comparison to be made between different aneurysm geometries as to the percentage of the aneurysm dome that is found lower than the threshold values for each of the cut-offs used. Further analysis of the species concentration threshold will be described in Chapter 7.

4.3 Governing Equations

As previously mentioned, CFD is fundamentally based on the governing equations of fluid flow that use mathematical statements to describe the conservation laws of physics:

(1) The mass of the fluid in the system is conserved.
(2) The rate of change of momentum equals the sum of the forces on a fluid particle (Newton's 2nd Law).

Before the numerical analysis of the mass transport of blood-borne species within cerebral aneurysms can be carried out, the governing equations must be defined within the solver. There are no thermal or chemical reactions involved in this study and so the conservation of energy equation is neglected.

4.3.1 Conservation of Mass: Continuity Equation

The conservation of mass is a form of the continuity equation which states that the rate at which mass enters a control volume must equal the rate at which mass leaves the control volume, providing there are no sinks or sources present. In Cartesian form with coordinates x, y, z and velocity components u, v, w, the conservation of mass can be written in 3D form as:

$$\frac{\partial \rho}{\partial t} + \frac{\partial (\rho u)}{\partial x} + \frac{\partial (\rho v)}{\partial y} + \frac{\partial (\rho w)}{\partial z} = 0 \tag{4.1}$$

In vector notation, the equation becomes:

$$\frac{\partial \rho}{\partial t} + \rho \nabla . \vec{u} = 0 \tag{4.2}$$

However, in this study, flow is assumed to be incompressible and therefore has a constant density. Equation 4.2 can be rewritten as:

$$\nabla . \vec{u} = 0 \tag{4.3}$$

4.3.2 Conservation of Momentum: Navier-Stokes Equation

The conservation of momentum for fluid flow is derived from Newton's 2nd law of motion (F = ma), which states that the rate of change of momentum of a fluid particle is equal to the sum of the forces acting on that particle. The full three-dimensional viscous nature of fluid flow in a control system is described by the Navier-Stokes equations:

$$\begin{aligned}
&\rho\left(\frac{\partial u}{\partial t}+u\frac{\partial u}{\partial x}+v\frac{\partial u}{\partial y}+w\frac{\partial u}{\partial z}\right)\\
&\qquad=\rho g_x+\mu\left(\frac{\partial^2 u}{\partial x^2}+\frac{\partial^2 u}{\partial y^2}+\frac{\partial^2 u}{\partial z^2}\right)-\frac{\partial p}{\partial x}\\
&\rho\left(\frac{\partial v}{\partial t}+u\frac{\partial v}{\partial x}+v\frac{\partial v}{\partial y}+w\frac{\partial v}{\partial z}\right)\\
&\qquad=\rho g_y+\mu\left(\frac{\partial^2 v}{\partial x^2}+\frac{\partial^2 v}{\partial y^2}+\frac{\partial^2 v}{\partial z^2}\right)-\frac{\partial p}{\partial y}\\
&\rho\left(\frac{\partial w}{\partial t}+u\frac{\partial w}{\partial x}+v\frac{\partial w}{\partial y}+w\frac{\partial w}{\partial z}\right)\\
&\qquad=\rho g_z+\mu\left(\frac{\partial^2 w}{\partial x^2}+\frac{\partial^2 w}{\partial y^2}+\frac{\partial^2 w}{\partial z^2}\right)-\frac{\partial p}{\partial z}
\end{aligned} \tag{4.4}$$

4.3.3 Fick's Law of Diffusion

Diffusion is the transport of species between two locations due to a concentration gradient. Fick's 1st law describes how the flux of species is proportional to the change in concentration due to a change in position:

$$J = -D\frac{\partial C}{\partial x} \tag{4.5}$$

The negative sign in Equation 4.5 indicates a positive flux in the presence of a negative concentration gradient. Biological mass transport processes tend to be time-dependent, and so an equation that can predict variations in concentration over time is needed. Fick's second law is derived using the conservation of mass:

$$\frac{\partial C}{\partial t} = D\left(\frac{\partial^2 C}{\partial x^2}+\frac{\partial^2 C}{\partial y^2}+\frac{\partial^2 C}{\partial z^2}\right) \tag{4.6}$$

4.3.4 Conservation of Species

Equation 4.6 represents diffusion dominated mass transport; however both diffusive and convective forces are present in this study. The addition of a convective term, represented by the product of the fluid velocity and the local concentration, results in the convection-diffusion equation:

$$\frac{\partial C}{\partial t} + u\frac{\partial C}{\partial x} + v\frac{\partial C}{\partial y} + w\frac{\partial C}{\partial z} = D\left(\frac{\partial^2 C}{\partial x^2} + \frac{\partial^2 C}{\partial y^2} + \frac{\partial^2 C}{\partial z^2}\right) \quad (4.7)$$

4.4 Blood Flow in the Cerebral Vasculature

Blood flow within the cerebral vasculature and cerebral aneurysms is a complex, three-dimensional process. Is this study, several assumptions are made in order to simplify the model, without compromising the accuracy of the results. For the 3D simulations of mass transport within a neurysms used in this study, the following assumptions are made: (1) arterial walls are rigid and stationary, (2) blood is a Newtonian fluid with constant physical properties and (3) flow is incompressible, laminar, steady and fully developed.

Rigid Wall Assumption

For the computational analysis undertaken in this study, the artery and aneurysm walls are assumed to be rigid and stationary. The rigid wall assumption has been debated extensively, with some studies suggesting that flow characteristics in rigid models do not differ significantly from elastic aneurysm models (Tateshima *et al.* 2003). Others have concluded that arterial wall compliance depends on the arterial geometry, with hemodynamic factors being affected more in terminal than in lateral aneurysms (Torii *et al.* 2007, Valencia *et al.* 2008). In young, healthy subjects it has been reported that, due to the pulsing nature of the heart, arterial vessel diameters can change up to 21% in smaller cerebral arteries such as the ACA (Kim *et al.* 2005). The elasticity of healthy arteries significantly affects the shape of the flow waveform, and may affect parameters such as wall shear stress magnitude (Cebral *et al.* 2003). However, numerous previous studies have neglected to include wall compliance, instead opting to model the wall as rigid (Cebral *et al.* 2003, Shojima *et al.* 2004, Steinman *et al.*

2003), which can serve to simplify the simulation and reduce computational expense. It has been suggested that for larger cerebral arteries such as the MCA and ICA, the pulsing of the heart causes changes in vessel diameter of less than 4% (Kim *et al.* 2005). Furthermore, cerebral arteries and aneurysms are stiffer in nature than other arteries, with studies reporting that, due to a lack of elastin, aneurysms may be up to twice as stiff as normal vessels(Jou *et al.* 2003). Therefore, for this study, a rigid wall assumption is employed.

Steady Flow Assumption

The second assumption made in the study was that the flow is laminar, incompressible, fully developed at the artery inlet and steady in nature. The decision to model flow as laminar is based on the Reynolds number, which is a dimensionless value that represents the ratio of inertial forces to viscous forces within a fluid. It can be determined using Equation 4.8:

$$Re = \frac{\rho u d}{\mu} \tag{4.8}$$

Flow through a pipe with Re<2000 is regarded as laminar, in which the flow is dictated by the viscous forces, and the particles of the fluid move in parallel lines or layers. Flow with Re>4000 is classified as turbulent, in which the particles move in a disorderly fashion, with mixing, recirculation and flow eddies occurring within the fluid (Massey 2006). However, turbulent flow has been found to develop at lower Reynolds numbers (Stehbens 1959), and so the values outlined above are typically seen as guidelines.

At the entrance to a straight, rigid, cylindrical artery, the velocity profile is practically uniform. The velocity at the walls must equal zero, and so the retarding effects of the wall cause the layers nearest the wall to slow. A boundary layer is formed that increases in thickness until it extends to the axis of the artery. The cross-sectional area of the artery is constant, and so the mean velocity across the section must remain constant. Thus, the reduction in velocity experienced close to the walls is compensated for by acceleration at the centre of flow. Flow is said to be fully developed when a parabolic distribution has been reached. The point along the artery where flow has fully developed is known as the entrance length, and can be calculated for laminar

flow using Equation 4.9. Theoretically, this is reached after an infinite distance; however, the entrance length is usually regarded as the point at which the maximum velocity, u_{max}, is within 1% of its final value (Massey 2006).

$$Entrance\ Length = 0.057 * Re * d \tag{4.9}$$

Depending on the diameter and length of the pipe being examined, this entrance length may be large in size. When modelling the entrance length computationally, this could add to the complexity of the model. Therefore, a parabolic Poiseuille velocity profile can be applied at the entrance to the pipe that assumes fully developed flow, reducing the time needed to return a solution. This is represented by the following equation:

$$u = 2u_{mean}\left(1 - \left(\frac{r}{R}\right)^2\right) \tag{4.10}$$

Blood is inherently pulsatile in nature. Therefore, many previous studies have opted to model the pulsatility of blood in CFD simulations (Appanaboyina *et al.* 2008, Boussel *et al.* 2008, Fisher and Rossmann 2009, Shojima *et al.* 2004). However, one of the main techniques to reduce computational expense for complex CFD simulations, such as those involving 3D patient-specific models, is to model the blood flow as steady rather than unsteady or pulsatile (Ethier 2002).

Although studies have reported differences in flow patterns between steady and pulsatile simulations, it has been argued that that the main flow features within an aneurysm do not change throughout the cardiac cycle. Geers *et al.* (2014) conducted a study in both lateral and terminal aneurysms to quantify the differences between time-averaged, peak systole and end diastole WSS results for steady and pulsatile simulations, reporting that although differences for WSS values at peak systole and end diastole were large, steady flow simulations can accurately predict the time-averaged WSS field. Müller *et al.* (2012) undertook an investigation into the sensitivity of aneurysmal flow patterns to different conditions, showing no significant sensitivity to variations in pulsatile flow rate, with the steady and pulsatile flow simulations predicting similar results. Additionally, following a comparative analysis of two pulsatile and three steady flow simulations of 210 patient-specific aneurysms, Cebral *et al.* (2011b) reported that steady flow could be used in the place of pulsatile

flow to extract information regarding the relationship between haemodynamic measures and aneurysm rupture.

Furthermore, it has been reported that the use of steady flow does not affect the mass transport of species across the arterial wall, with differences between pulsatile flow and steady flow found to be insignificant (Karner and Perktold 2000). John and Barakat (2001) reported that the effect of pulsatile flow on surface concentration of ATP is negligible, suggesting that for the sinusoidal flow pulsatility included in their model, the time constant that characterises the changes in species concentration is larger than the time constant characterising the unsteady flow, and so the endothelial surface is not affected by the unsteady flow patterns. Instead, it is suggested that it is the mean wall shear stress that determines the concentration of species. This was echoed by Comerford *et al.* (2006), who investigated the influence of pulsatile flows on ATP concentration at the endothelium of varying geometries of an artery bifurcation, showing negligible differences for the surface ATP concentration between the steady and pulsatile flow simulations. Similarly, when investigating the impact of hypertension on the transport of LDLs across the arterial wall in a straight, axisymmetric geometry, Yang and Vafai (2006) found the effect of pulsation to be negligible, due to the resistance offered by the arterial wall tissue. It has also been hypothesised by Sun *et al.* (2007) that, due to the accumulation of LDLs in the arterial wall being a long-term process, the use of steady flow can be deemed appropriate for initial approximations of mass transport across the arterial wall.

As part of the ASME 2012 Summer Bioengineering Conference CFD Challenge (see Appendix), both steady and pulsatile flow simulations were carried out on a giant patient-specific cerebral aneurysm, originally included in a study by Cebral *et al.* (2011a) where it was proposed that aneurysm rupture following treatment could be attributed to the redistribution of pressure following the implementation of a flow diverting stent. The main objective of the CFD challenge was to investigate the variability of CFD solutions in the prediction of the pressure drop seen across a cerebral aneurysm and consisted of the distribution of the same lumen geometry and flow rate conditions to the 25 participating groups, but no guidance was given regarding discretisation, grid size etc. The challenge consisted of two phases: Phase I assessed the variability of the solutions against each other, while Phase II compared the computational solutions to results determined from an experimental model. The

geometry consisted of a giant ICA aneurysm which contained a small (<50%) stenosis proximal to the aneurysm inlet (see Figure 4.3).

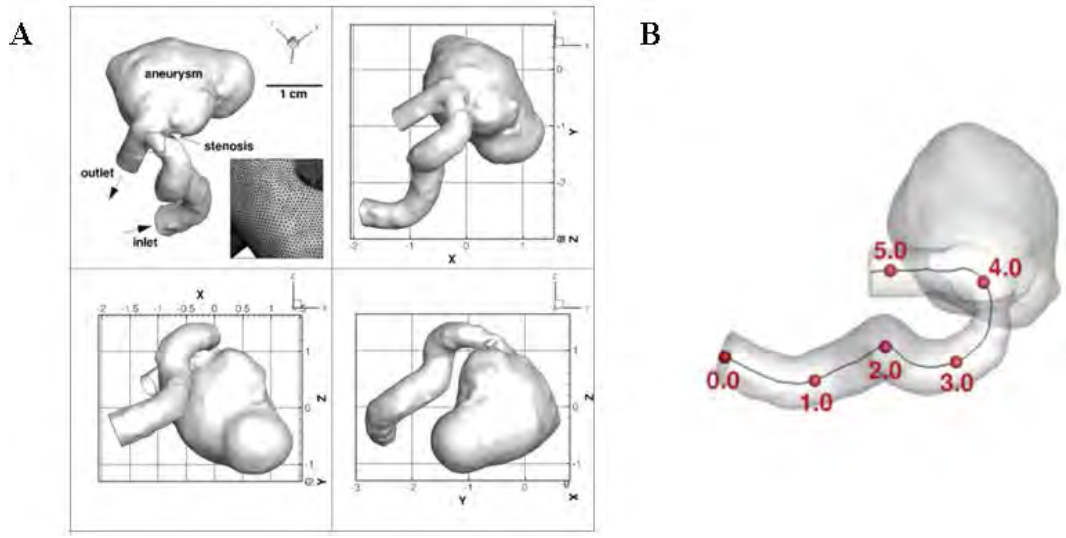

Figure 4.3: (A) ASME 2012 CFD Challenge geometry and (B) Aneurysm model centreline (Steinman *et al.* 2013)

Taking part in the CFD challenge, the CABER group conducted the study using two separate CFD softwares, in which I used the commercially available Star CCM+ 6.02.007 (CD-Adapco, USA). Focusing on Phase I of the challenge, blood was taken to be an incompressible, Newtonian fluid with a constant viscosity of 0.004 Pa·s and a density of 1000 kg/m³. Flow was assumed to be laminar, steady, and three-dimensional. Boundary conditions were applied as outlined in the original study by Cebral *et al.* (2011a) and two pulsatile cases were prescribed based on the same flow waveform but with mean flow rates of 5.13 and 6.41 ml/s, representing a mean inlet WSS of 1.2 and 1.5 Pa respectively (see Figure 4.4). A period of 0.99 s and a time-step of 0.001 s were used, with results presented at peak systole (t = 0.275 s). Four steady flow simulations with flow rates of 5.13, 6.41, 9.14 and 11.42 mL/s were also performed, corresponding to the mean and peak systolic flow rates of the pulsatile cases.

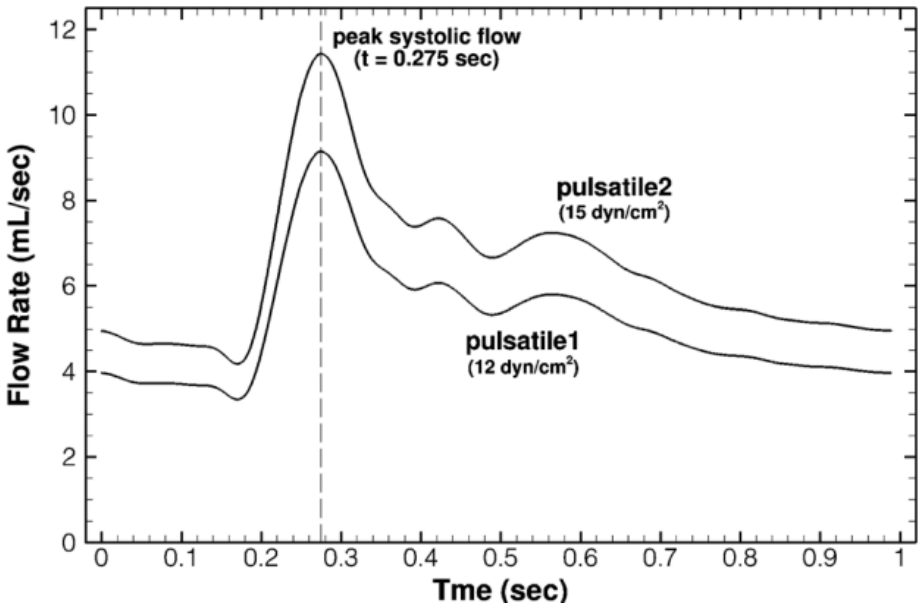

Figure 4.4: Pulsatile flow rates prescribed for Phase 1 of the CFD Challenge (Steinman *et al.* 2013)

A comparison of the pressure drop across the aneurysm centreline for both the steady and pulsatile flows as a result of simulations undertaken by the author for this study is shown in Figure 4.5. The steady flow rates of 5.13 ml/s, 6.41 ml/s, 9.14 ml/s and 11.42 ml/s are referred to as S1, S2, S3 and S4 respectively, with the cycle-averaged and peak systolic pulsatile flow rates referred to as AV1, PK1, AV2 and PK2 for the mean flow rates of 5.13 ml/s and 6.41 ml/s respectively.

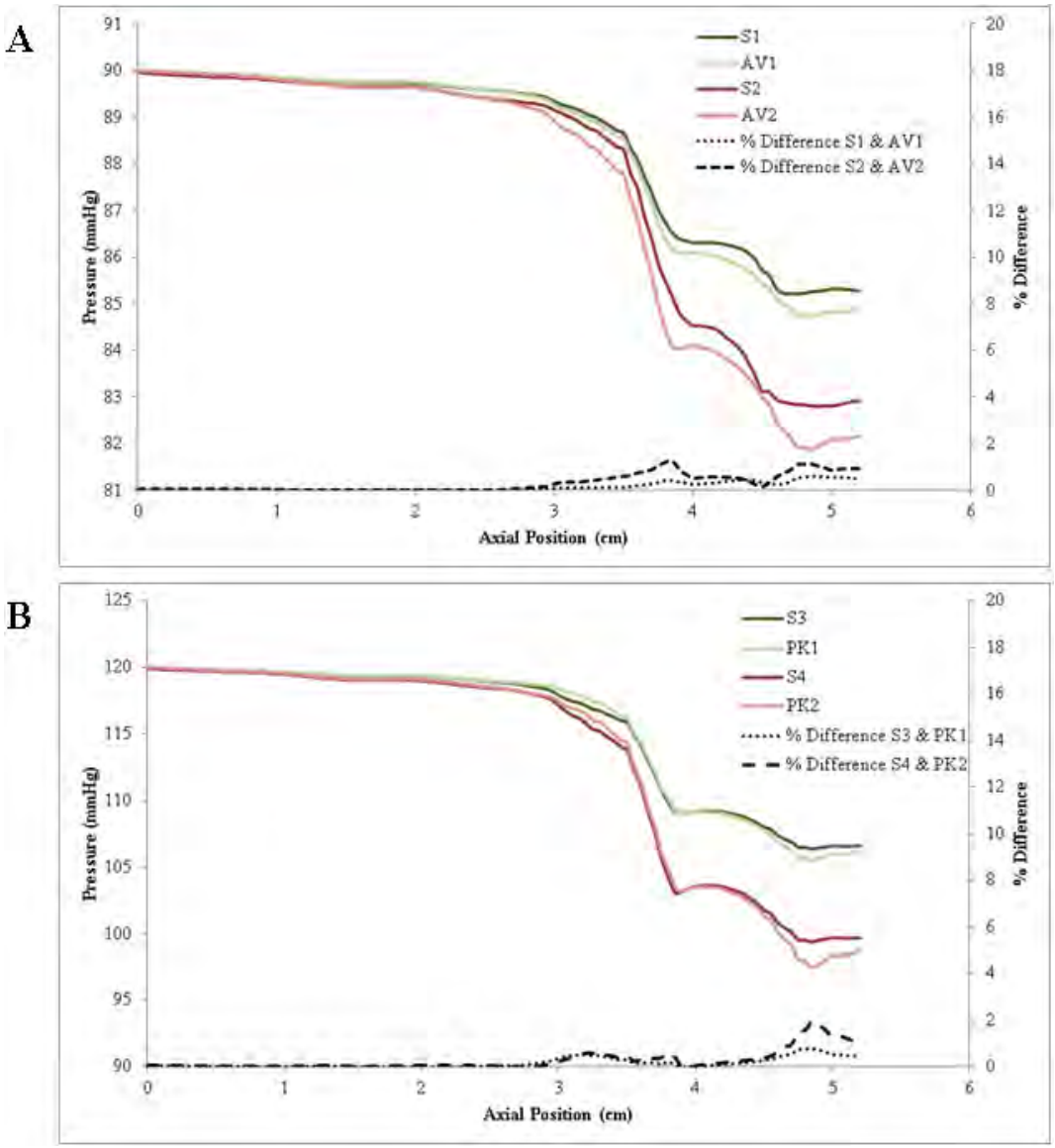

Figure 4.5: (A) Centreline pressure drop comparison for S1, S2, CA1 and CA2, (B) Centreline pressure drop comparison for S3, S4, PS1 and PS2 (S1, S2, S3, S4 = steady flow rates 5.13 ml/s, 6.41 ml/s, 9.14 ml/s and 11.42 ml/s. AV1, AV2, PK1, PK2 = pulsatile cycle-averaged and peak systolic flow rates 5.13 ml/s, 6.41 ml/s)

It is clear from Figure 4.5 that there is good agreement between the steady and pulsatile flow results, with similar pressure values found along the centreline for the steady and corresponding cycle-averaged or peak systolic pulsatile flow. The percentage difference between each set of results was calculated and found to be within ±2%, suggesting that the use of pulsatile flow had a negligible effect on the results of the study. This is further evidenced by results from the entire CFD challenge, shown in Figure 4.6, which highlights the negligible differences between the pulsatile peak systolic and cycle-averaged pressure drops compared to their steady flow counterparts. Also illustrated is the inlet to outlet pressure drop relative to the

inlet pressure for both the current study, and as predicted by the various solvers submitted to the CFD challenge. It is evident that the results simulated using Star CCM+ are comparable with the other groups, despite the wide variety of solvers and solution techniques used throughout the challenge.

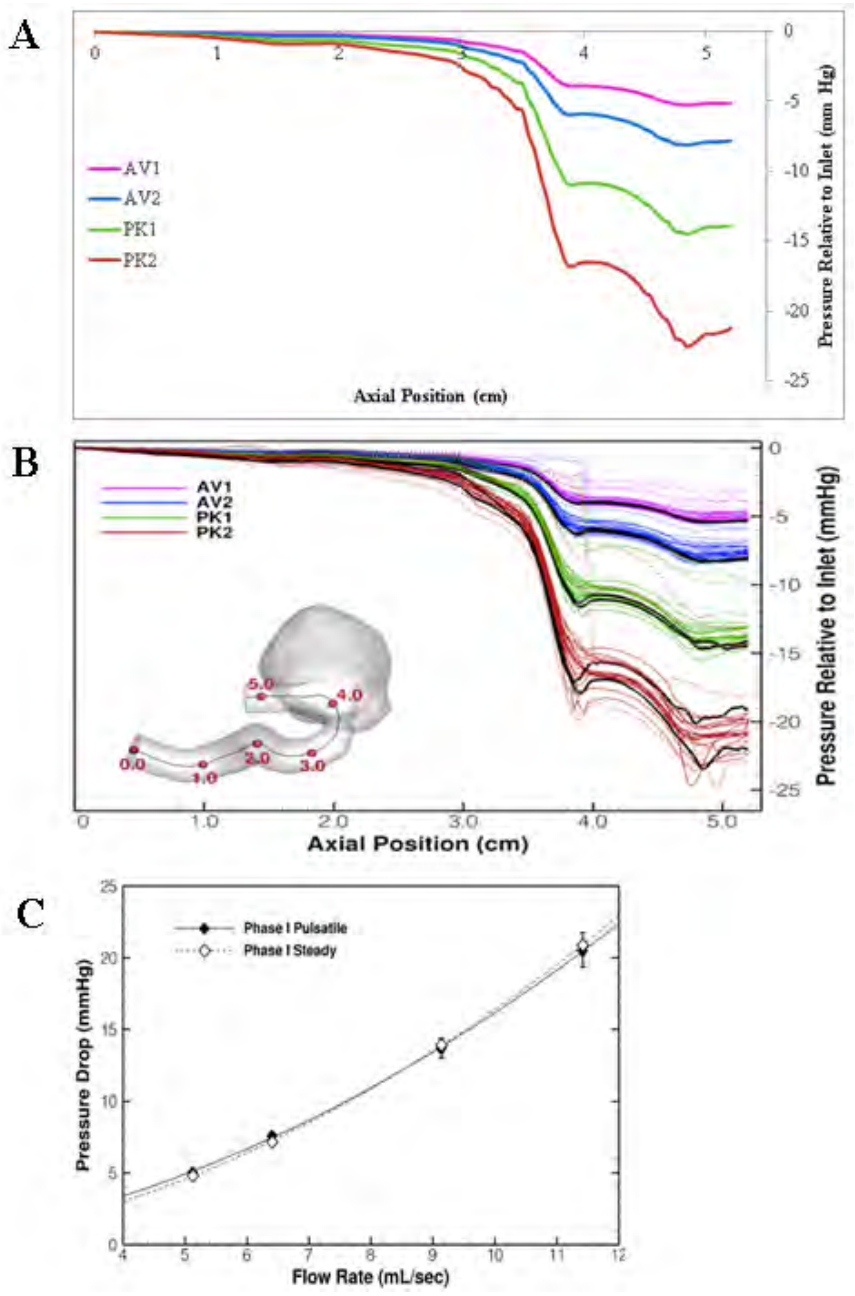

Figure 4.6: (A) Centreline pressure for pulsatile flow simulation for current study (B) centreline pressure for pulsatile flow simulations for overall CFD study and (C) Summary of pressure drop vs. flow rate results for Phase I for all steady and pulsatile flow results (Steinman *et al.* 2013)

Following results generated as part of the published ASME CFD challenge and following evidence from previous studies that suggest that steady flow is an appropriate assumption to reduce computational time for flow and mass transport

studies within the cerebral vasculature, the use of steady flow was employed in all following computational analyses.

Newtonian Fluid Assumption

In addition to rigid walls and steady flow, an assumption was made referring to the treatment of the rheological properties of blood. Blood can be described as a suspension of red and white cells and platelets in plasma (Morales *et al.* 2013). The viscosity of blood is dependent on the volume fraction of red blood cells, and their ability to deform and aggregate (Fisher and Rossmann 2009). Blood is known to exhibit shear-thinning behaviour, meaning that the viscosity decreases with increasing shear rate. It is well recognised that blood behaves as a non-Newtonian fluid, in particular at low shear rates i.e. $<100\ s^{-1}$ (Johnston *et al.* 2004). However, many studies choose to model blood as a Newtonian fluid, assuming that the viscosity remains constant and indicating a linear shear stress-strain rate relationship.

The importance of non-Newtonian behaviour has been examined in several previous studies, although there remains some disagreement regarding its influence on flow behaviour. While some studies have suggested that the effect of the shear-thinning properties of blood is not significant for arteries > 0.5mm in diameter (Hoi *et al.* 2004), and that the assumption of a Newtonian fluid is reasonable (J. R. Cebral *et al.* 2005b, Fisher and Rossmann 2009, Morales *et al.* 2013, A. Valencia *et al.* 2006), others have strongly emphasised the importance of the use of non-Newtonian properties to describe blood (Chen and Lu 2004, Ishikawa *et al.* 1998, Moon *et al.* 2014). Although there are no reports on the effects of the use of the Newtonian assumption on mass transport within cerebral aneurysms, X. Liu *et al.* (2011) investigated the effect of non-Newtonian blood flow on the transport of LDLs and oxygen and found that, under steady flow conditions, the inclusion of non-Newtonian properties had minimal effect on the transport of species in most regions of the aorta. Furthermore, blood is assumed to be Newtonian in numerous mass transport analyses in literature (Amili and Fatouraee 2005, Chen *et al.* 2014, Comerford and David 2008, Imai *et al.* 2008, Kaazempur-Mofrad *et al.* 2005).

In order to elucidate the effects of using a shear rate dependent viscosity on mass transport within cerebral aneurysms, a comparative study was carried out on flow

simulations performed using both Newtonian and non-Newtonian fluids. Numerous models have been used to describe the non-Newtonian behaviour of blood, such as the Casson, power law, Herschel-Bulkley, Carreau and Carreau-Yasuda models (J. R. Cebral *et al.* 2005a, Chen and Lu 2004, Fisher and Rossmann 2009, Morales *et al.* 2013, Jianping Xiang *et al.* 2011). However, the Carreau-Yasuda model, an extension of the Carreau model, has been suggested to be the most suitable to model the non-Newtonian behaviour of blood, due to limitations reported for other models regarding their range of shear rates, high gradients and possible infinite viscosity (Fisher and Rossmann 2009).

The Carreau-Yasuda model is described by Equation 4.11, where μ_∞ and μ_0 represent the infinite and zero shear rates respectively, a and n are the power law indices and λ is the relaxation time constant:

$$\mu(\dot{\gamma}) = \mu_\infty + (\mu_0 - \mu_\infty)[1 + (\lambda\dot{\gamma})^a]^{\frac{n-1}{a}} \tag{4.11}$$

The constitutive parameters used to develop the Carreau-Yasuda model have varied throughout literature. Figure 4.7 illustrates the behaviour of the non-Newtonian Carreau and Carreau-Yasuda models according to different authors, along with the typical Newtonian fluid of $\mu = 3.5$ mPa·s. It can be seen that while the different models provide similar viscosity values at high shear rates, different behaviours are evident for lower shear rates.

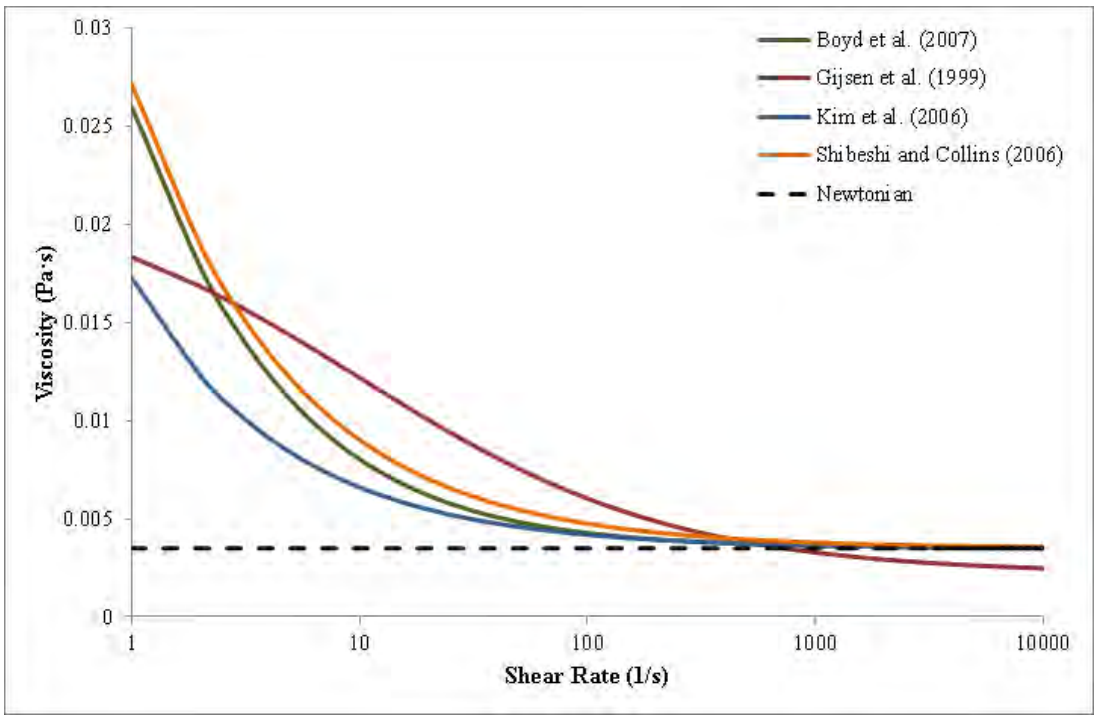

Figure 4.7: Illustration of shear-thinning behaviour of blood as described by previous non-Newtonian Carreau models

Previous studies have adopted parameters taken from the curve fitting of experimental data or from a blood analogue fluid (Gijsen *et al.* 1999, Kim *et al.* 2005, Shibeshi and Collins 2005). However, the parameters outlined by Boyd *et al.* (2007), which are listed in Table 4.1 are calculated from physiological measurements and so are used in this study to compare the influence of Newtonian and non-Newtonian fluid properties.

Table 4.1: Carreau-Yasuda model constitutive parameter values (Boyd *et al.* 2007)

Parameter	Value
μ_∞	3.5 (mPa·s)
μ_0	160 (mPa·s)
λ	8.2 (s)
a	0.64
n	0.2128

CFD simulations of fluid flow and mass transport of ATP within both a patient-specific lateral and bifurcation aneurysm was carried out using a Newtonian fluid with constant viscosity of 3.5 mPa·s, and the Carreau-Yasuda model parameters outlined in Table 4.1. Similar flow patterns were seen for both the Newtonian and Carreau-Yasuda models in both the lateral and bifurcation models, despite the minimum shear rates within both models found to be $< 100\ s^{-1}$. A quantitative comparison of the

averaged shear rate and WSS values within the aneurysm sac and parent artery are illustrated in Figure 4.8. Although slight differences are evident, results for the Carreau-Yasuda model for both the lateral and bifurcation aneurysms are found to be within ±2% of the Newtonian model results.

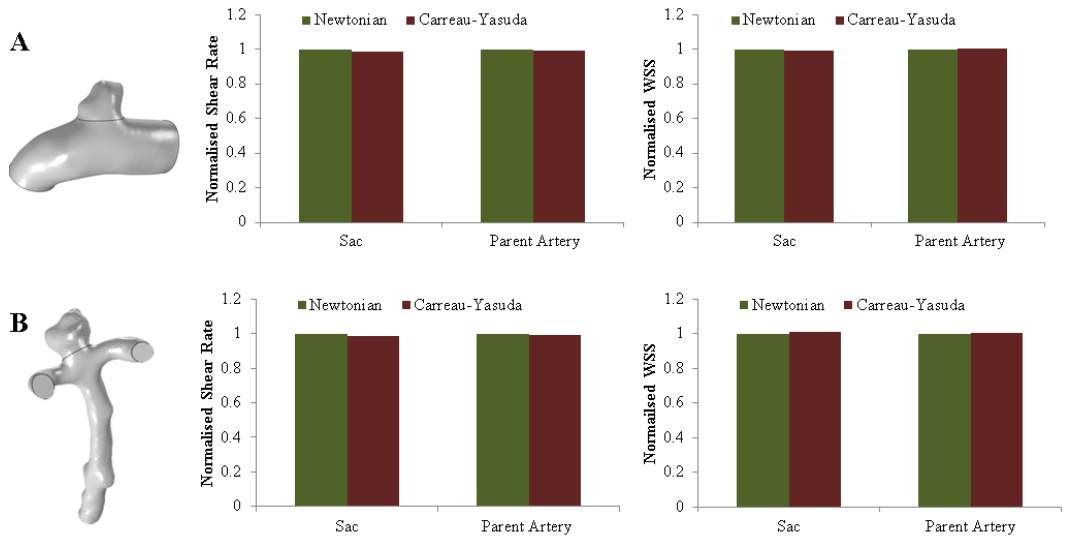

Figure 4.8: Shear rate (left) and WSS (right) values for Newtonian and Carreau-Yasuda models for (A) lateral and (B) bifurcation aneurysm within the aneurysm sac and parent artery. Values normalised to Newtonian results.

As discussed previously, Equation 4.8 can be used to establish the Reynolds number at the inlet to the aneurysm model. However, the Reynolds number at the inlet varies between the Newtonian and non-Newtonian models, due to differences in viscosity value. On comparison of the Newtonian and non-Newtonian models, it is found that the Reynolds number increases considerably for the non-Newtonian model. Taking the example of the lateral aneurysm, a Reynolds number of 549 is calculated when a constant viscosity Newtonian model is used. However, upon introduction of the non-Newtonian fluid properties, the Reynolds number at the inlet is found to increase to 1130. Similarly, for the bifurcation aneurysm, the inlet Reynolds number increases from 438 for the Newtonian model to 733 for the non-Newtonian model. However, despite the increase in Reynolds number associated with the non-Newtonian fluid properties, the classification of the flow involved does not change from laminar, and so the difference in Reynolds number at the arterial inlet as a result of the use of a Newtonian fluid is not deemed significant for this study.

The effect of the use of non-Newtonian blood properties on mass transport within a lateral and bifurcation aneurysm was also examined. Unwrapped projections of the

aneurysm sac for both the lateral and bifurcation aneurysms are illustrated in Figure 4.9, highlighting the normalised concentration distribution throughout the aneurysm sac.

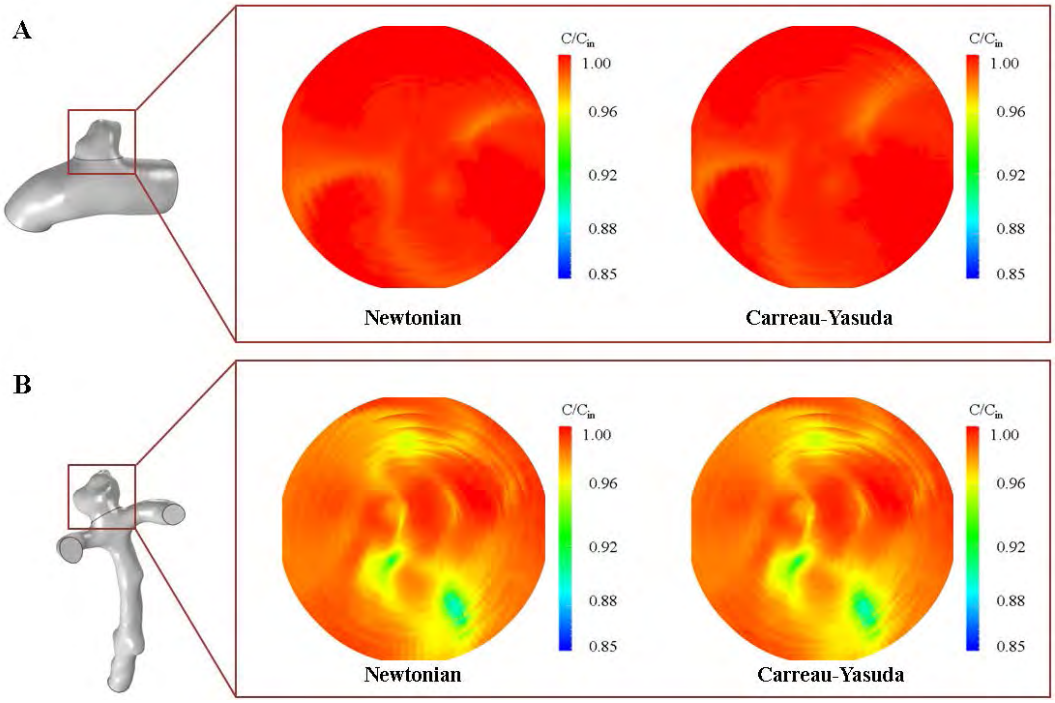

Figure 4.9: 2D unwrapped projections of aneurysm sac for (A) lateral and (B) bifurcation aneurysm models, showing normalised concentration (C/C_{in}) for the Newtonian (left) and Carreau-Yasuda (right) models

It is evident from results shown that the concentration distribution remains effectively unchanged, with the difference between results again found to be within 2%, despite the change in fluid properties. Therefore, it is concluded that the shear rate, WSS and concentration distributions do not differ significantly between the Newtonian and non-Newtonian model, and the inclusion of non-Newtonian fluid properties has little effect on the mass transport of blood-borne species within cerebral aneurysms. Thus, the non-Newtonian properties of blood are omitted from this study, and blood was modelled as Newtonian with a constant viscosity of 3.5 mPa·s.

Mass Transport

Mass transport is the movement of species, such as fluid, gas or drug, from an area of high concentration to a n area of low concentration, within a defined system. This movement can be provoked by concentration gradients, but typically it is due to

complex haemodynamics, such as that found within the cerebral vasculature. It can be categorised in to two main types within the human vasculature – blood side mass transport, and wall side mass transport. Blood side mass transport refers to the transport of species within the lumen of the blood vessel, and is exposed to the haemodynamic forces within the vessel. Wall side mass transport refers to transport within the wall of the artery or blood vessel itself. WSMT occurs as a result of two transport mechanisms: the first is a pressure driven convection force, while the second is a diffusive force as a result of concentration gradients (Khakpour and Vafai 2008b, O'Connell 2009).

Mass transport can be described by several dimensionless parameters. The Peclet number measures the relative contributions of diffusive and convective forces to the transport of species within a defined system, and is a product of the Reynolds number (see Equation 4.8) and the Schmidt number (Friedman 2008). A large Peclet number suggests that convection dominates, while a small Peclet number indicates diffusion dominated flow.

$$Pe = Re.Sc \tag{4.12}$$

The Schmidt number represents the ratio of the viscous momentum diffusivity to the mass diffusivity, and is defined as follows:

$$Sc = \frac{\upsilon}{D} = \frac{\mu}{\rho D} \tag{4.13}$$

Substituting Equation 4.12 and 4.13 into Equation 4.8 describes how the Peclet number can be influenced by the convective and diffusive forces:

$$Pe = \frac{ud}{D} \tag{4.14}$$

4.5 Boundary Conditions

Boundary conditions are statements that can be used to describe the environment of the flow simulation. The application of boundary conditions is based on two aspects:

the number of boundary conditions, and the type that should be implemented. The choice of the number of boundary conditions used in a numerical simulation is dictated by the governing equations chosen and the geometry used, while the type of boundary condition is user-defined, selected based on the primary variables being solved and should reflect physiologically realistic conditions. In numerical simulations, all external boundaries of the domain require boundary conditions for each of the main variables that are to be solved, and the incorrect application of boundary conditions can hinder the accuracy of the simulation (Datta and Rakesh 2010).

Comsol, the FEM solver used in this study, has the capability to solve for both momentum and mass transport equations simultaneously; however this can be computationally expensive. Instead, the governing equations for conservation of mass and momentum are solved initially using the CFD module within Comsol to establish fluid flow characteristics within the aneurysm model. Results from the fluid flow study are then applied to the mass transport analysis, which is carried out using the Transport of Diluted Species module. Therefore, a separate set of boundary conditions are required for the fluid flow and mass transport analyses, which are outlined in the following sections.

4.5.1 Fluid Flow Boundary Conditions

Inlet: Velocity

At the artery inlet, steady, laminar flow is induced using an existing "laminar inflow" boundary condition available in Comsol. This allows the mean fluid velocity and entrance length to be set at the artery inlet, ensuring a fully developed, parabolic profile is induced, based on Equation 4.11. The main advantage of the use of a parabolic profile at the artery inlet is the elimination of an entrance length domain, reducing the computational effort needed for mesh generation and solving time.

The mean velocity was determined based on the average flow rate for the specific location within the CoW. For aneurysms of the ophthalmic segment of the ICA, an average flow rate of 260 ml/min was used, while the average flow rate in the MCA, 138 ml/min, was applied for aneurysms of the sylvian bifurcation (Alastruey *et al.* 2007, Alnaes *et al.* 2007, Cebral *et al.* 2008, Cieslicki and Ciesla 2005, Fahrig *et al.*

1999, Ford *et al.* 2005, Moore *et al.* 2006). The Reynolds number and entrance length for each simulation was determined using Equations 4.10 and 4.11. The use of a steady, laminar flow condition at the inlet has been used in many previous studies found throughout literature in the analysis of fluid flow within cerebral aneurysms (Cebral *et al.* 2008, Cebral *et al.* 2011b, Kim *et al.* 2008, Miura *et al.* 2013, Sato *et al.* 2008, Yu and Zhao 1999, Zakaria *et al.* 2008).

Outlet: Pressure

A pressure boundary condition of $P = 0$ is applied at the outlet(s) of each aneurysm model which is commonly seen in previous studies in literature (Cebral *et al.* 2011a, Fisher and Rossmann 2009, Geers *et al.* 2014, Takao *et al.* 2012).

Lumen-Wall Interface: No Slip

A no-slip boundary condition is applied at the interface between the lumen and the arterial wall. The no-slip condition is common for simulations with a rigid wall, and assumes that the velocity of the fluid is equal to that of the wall, with $v = 0$ at the wall boundary (Alnaes *et al.* 2007, Appanaboyina *et al.* 2008, Cebral *et al.* 2011a, Sato *et al.* 2008, Takao *et al.* 2012).

4.5.2 Mass Transport Boundary Conditions

Inlet: Constant Uniform Concentration

For the mass transport analysis, a constant uniform species concentration, C_{in}, is set at the artery inlet (Ai and Vafai 2006, Amili and Fatouraee 2005, Chen *et al.* 2014, Chung and Vafai 2014, Soulis *et al.* 2008, Wada *et al.* 2002), representing the typical concentration of the species in arterial blood flow. The diffusion coefficient or diffusivity of the species in blood, D, is also included in the model. The C_{in} and D values for each species in this study are based on average values from literature, and are listed in Table 4.2. A sensitivity analysis was performed for ± 10% of the inlet concentration and species diffusivity values for each species. Variation of the values

led t o ne gligible di fferences of l ess t han 2 % i n t he resulting c oncentration distributions, and so the average values listed in Table 4.2 were deemed appropriate.

Table 4.2: Species mass transport parameter values (Amili and Fatouraee 2005, Chung and Vafai 2012, Comerford and David 2008, David 2003, Imai *et al.* 2010, Xiao Liu *et al.* 2011, Stangeby and Ethier 2002, Tada and Tarbell 2004, Wada and Karino 2002)

Species	C_{in} (mol/m³)	D (m²/s)	K (m/s)
ATP	0.0001	$2.4x10^{-10}$	$1.68x10^{-06}$
LDLs	0.0286	$5x10^{-12}$	$2x10^{-10}$

Outlet: Outflow

At each artery outlet, an outflow boundary condition is applied which implies that the blood-borne species is transported out of the domain as a result of the momentum of the f luid f low. T his b oundary condition a ssumes c onvection i s t he dom inating transport mechanism, and so diffusive transport is neglected:

$$\boldsymbol{n}.(-D\nabla \mathrm{C}) = 0 \tag{4.15}$$

Where n r epresents t he nor mal ve ctor poi nting out wards f rom t he c omputational domain (COMSOL 2012).

Lumen-Wall Interface: Flux

As de scribed i n S ection 2.3.4.1, t he m odelling of m ass t ransport o f bl ood-borne species across the arterial wall has been grouped by Prosi *et al.* (2005) into three main categories: (1) wall-free (2) homogeneous wall or fluid-wall and (3) multi-layer wall models. W all-free m odels d escribe t he t ransport o f t he s pecies acr oss t he w all b y means of a set of boundary conditions. F luid-wall mo dels take the arterial wall into account but c onsider i t t o be a s ingle, hom ogenous l ayer, w hile m ulti-layer mo dels model s everal he terogeneous l ayers of t he a rterial w all. In t his s tudy, due t o t he complex nature of the 3D patient-specific models, the use of fluid-wall or multi-layer models would be computationally demanding, and so wall-free models are used. Due to their simplicity, very few parameters are required for wall-free models i.e. species diffusivity, m ass t ransfer c oefficient a nd filtration v elocity. A limita tion a ssociated with wall-free models is the lack of information regarding transmural flow and mass

transport within the wall, and so the calculation of concentration profiles within the wall are not possible. However, an understanding can be gained into the distribution of species at the arterial wall using these models, thus wall-free models are appropriate for this study.

Wall-free models account for the constant transport of species across the artery and aneurysm wall through the use of boundary conditions, such as the application of a diffusive flux. The outward flux is the product of the mass transfer coefficient K, and the concentration of species at the wall. Transport across the wall differs depending on the species of interest. In some cases, a reaction occurs at the wall boundary, such as the hydrolysis of ATP to ADP, whereby K represents the rate of uptake or consumption of ATP at the arterial wall. Although the endothelium is a physiological source of ATP, its effect is neglected in this study so as to allow results to be applicable to other species with low diffusion coefficients.

For other species, such as LDLs and albumin, the species permeates the arterial wall without undergoing any reaction. In the case of LDLs, an assumption is made that the arterial wall is permeable to water, with a filtration velocity of $V_w = 4 \times 10^{-08}$ m/s applied (Soulis *et al.* 2008, Wada *et al.* 2002). The net amount of LDLs that passes through the endothelium to the vessel wall is defined as the difference between the amount transported to the vessel wall as a result of the filtration velocity, and the amount which diffuses back into the main luminal flow, as described by Equation 4.16 (Soulis *et al.* 2008).

$$C_w u_w - D\frac{\partial C}{\partial n} = KC_w \tag{4.16}$$

Therefore, the net amount transported across the wall is defined by the right hand side of the equation, where K represents the endothelial permeability to the species (Tarbell 2003). The mass transport coefficient values used in this study, calculated as average values from literature, are listed in Table 4.2. Similar to that performed for the inlet concentration and diffusivity values, a sensitivity analysis study was carried out for ±10% of the mass transport coefficient value. Differences between the results were less than 2%, and so the K values listed in Table 4.2 were used for the simulations in this study.

Time-step size

The number of time-step increments that the solver takes to solve the governing equations is an important aspect of any transient or time-dependent CFD analysis. The implementation of an appropriate time-step size is critical, as the use of too large a time-step can lead to unstable or incorrect results. Although smaller time-steps tend to be more accurate, they are computationally demanding. Therefore, a balance is required that allows for a time-step small enough to detect when the solution is changing rapidly over time, but does not require excessive computational time and power.

In order to determine the optimum time-step size for the mass transport analyses in this study, a time-step independence study was carried out. Figure 4.10 shows the concentration, normalised to C_{in}, at a point of low concentration within the aneurysm sac over time for the time-steps 0.01, 0.005, 0.001 and 0.0005s. Although differences are seen between the solutions during the initial concentration build-up at the aneurysm wall, differences between results for time-steps of 0.005, 0.001 and 0.0005s are less than 2% once the concentration stabilises. Thus, a time-step of 0.005s is deemed adequate to capture changes to the solution over time for all further mass transport analyses.

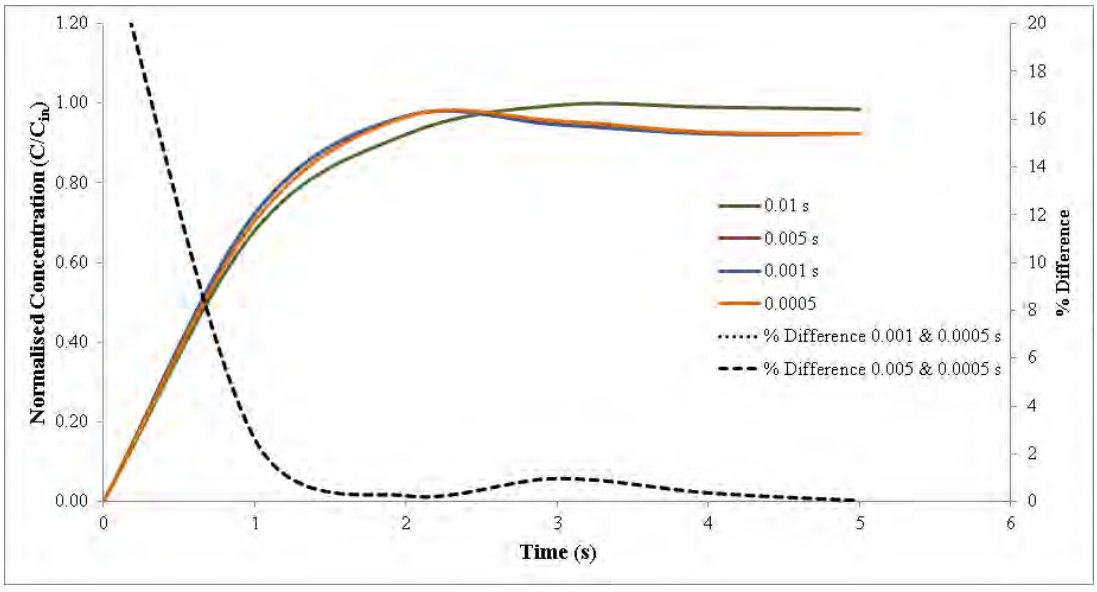

Figure 4.10: Normalised concentration and percentage difference at point of reduced concentration within aneurysm for time-step sizes 0.01s, 0.005s, 0.001s and 0.0005s

4.6 Mesh Generation

In a structured mesh, also known as a mapped mesh, an attempt is made to align the elements with a boundary or domain in a uniform pattern. Typically quadrilateral in 2D or hexahedral in 3D, structured meshes are simpler and offer more control over the size and shape of the elements. Unstructured meshes are more commonly used for complex geometries, using triangular, tetrahedral, quadrilateral or hexahedral element shapes. Unstructured meshes tend to be more flexible for complicated geometries and easier to refine. Using COMSOL, an option for a 3D combination or hybrid mesh is available, which consists of a combination of both structured and unstructured mesh elements. This involves building an unstructured mesh along a boundary and sweeping it to create the 3D mesh which is structured in the sweep direction and unstructured perpendicular to the sweep direction.

The decision as to what mesh is most suitable is not always obvious. An increased number of elements, while giving more accurate results, results in an increase in computational time. Therefore, the aim is to reduce the number of elements as much as possible, while still achieving accurate results. For the 3D complex cerebral aneurysm geometries being analysed in this study, an unstructured mesh is deemed more suitable as it allows greater flexibility with regards to the unusual shape of the domain and allows faster refinement of the mesh.

As a result of the no-slip condition of fluid flow, in which the velocity of a fluid relative to a solid surface is zero, a region known as the boundary layer forms close to the surface. The boundary layer is the region near the surface of the geometry or domain in which the velocity of the fluid increases rapidly and approaches the velocity of the fluid bulk flow (Massey 2006). In hemodynamic and mass transport analyses, the behaviour of the fluid close to the wall is extremely important. As a result, for computational analysis the mesh needs to be increased close to the domain boundary so as to capture the boundary layer phenomena and accurately compute the velocity, wall shear stress and concentration gradients (Bazilevs *et al.* 2010, Comerford *et al.* 2006).

For previous hemodynamic studies of the cerebral vasculature, the thickness of the first boundary layer ranged from 10 μm to 40 μm, with the number of layers of elements within the boundary layer varying from 3 to 7 layers (Goubergrits *et al.* 2012, Manguoglu *et al.* 2010, Qian *et al.* 2011, Sen *et al.* 2014, Spiegel *et al.* 2011,

Takizawa *et al.* 2010). For mass transport studies, the thickness of the first layer ranged from 7.6 µm to 26 µm, while the number of layers of elements was increased compared to hemodynamic studies, with a range from 3 to 19 layers seen (Chen *et al.* 2014, Comerford *et al.* 2006). In this study, the boundary layer thickness for each aneurysm geometry was calculated using the following equation (Wood 1999):

$$\delta \sim \sqrt{\frac{vd}{u_{max}}} \tag{4.17}$$

4.7 Grid Independence

In order to ensure the mesh employed in the computational flow simulations is appropriate, a grid independence study is carried out. This process involves refining the mesh until the solution has stabilised and is independent of the mesh size, with ±2% difference between results yielded for the different mesh sizes (Balakrishnan *et al.* 2007, Kolachalama *et al.* 2009). One parameter that is often used as an indicator of grid independence in flow haemodynamics studies is wall shear stress, due to its importance in evaluating cerebral aneurysm pathology, and its sensitivity as a measure of changes in flow (Prakash and Ethier 2000, Valencia *et al.* 2008). However, a solution that is grid independent for wall shear stress is not necessarily independent in terms of concentration, and so a mesh sensitivity study was carried out for both the wall shear stress and species concentration within the aneurysm geometry.

Determination of Grid Independence via Wall Shear Stress

Initially, wall shear stress was used as an indicator of grid independence, which is defined by the following equation:

$$\tau = \mu \frac{du}{dy} \tag{4.18}$$

Flow simulations were carried out using a patient-specific sylvian bifurcation aneurysm geometry at a Reynolds number of 415. WSS values were calculated both within the aneurysm sac and within the parent artery vessel for four different grid sizes, ranging from ~280,000 to ~1.2 million elements (see Table 4.3). The percentage

difference between the coarser grids and the finest grid was computed, and a decrease in percentage difference is found between the results as the number of elements increases.

Table 4.3: Mesh refinement comparisons of average, maximum and minimum WSS within the aneurysm dome for increasing mesh sizes

	Aneurysm Sac		Parent Artery Vessel	
No. of Elements	**Average WSS (Pa)**	**% Difference**	**Average WSS (Pa)**	**% Difference**
281055	7.25895	2.01	13.22148	3.08
558686	7.12279	0.09	13.47927	1.19
816569	7.07989	0.51	13.54363	0.72
1288409	7.11606	0	13.64166	0

It is evident from Figure 4.11, which illustrates the percentage difference between the solutions for each mesh size, that a difference of less than 2% is found between results for a mesh size of 558, 686 elements, suggesting that a mesh size of greater than ~550,000 is grid independent in terms of WSS.

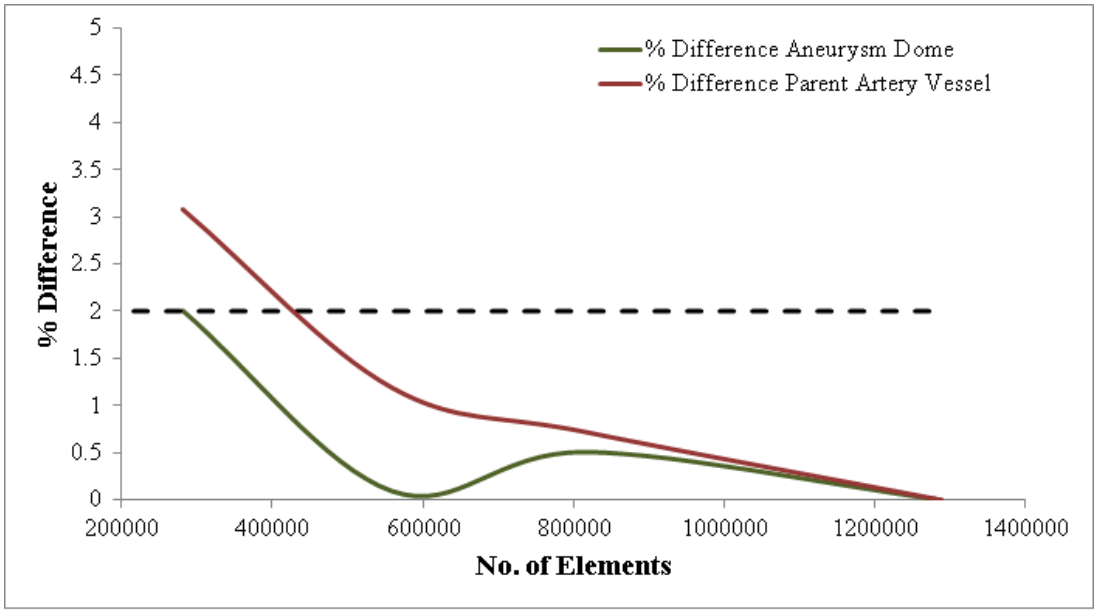

Figure 4.11: Percentage difference between mesh sizes for average WSS within aneurysm dome (green) and parent artery vessel (red)

Determination of Grid Independence via Species Concentration

The previous section demonstrates that a mesh size of ~550,000 elements will produce a grid independent solution in terms of WSS. However, as previously mentioned, a solution that is grid independent in terms of WSS may not be so in terms of

concentration. Therefore, a separate grid independence study was carried out to ensure that the mesh used in the computational analysis was grid independent for concentration also. Using the same patient-specific sylvian bifurcation aneurysm geometry and flow conditions as in the WSS grid independence study, the mass transport of ATP was examined, with an inlet concentration of 0.0001 mol/m³, species diffusivity of 2.4×10^{-10} m²/s and a mass transport coefficient of 1.68×10^{-6} m/s (Imai *et al.* 2010).

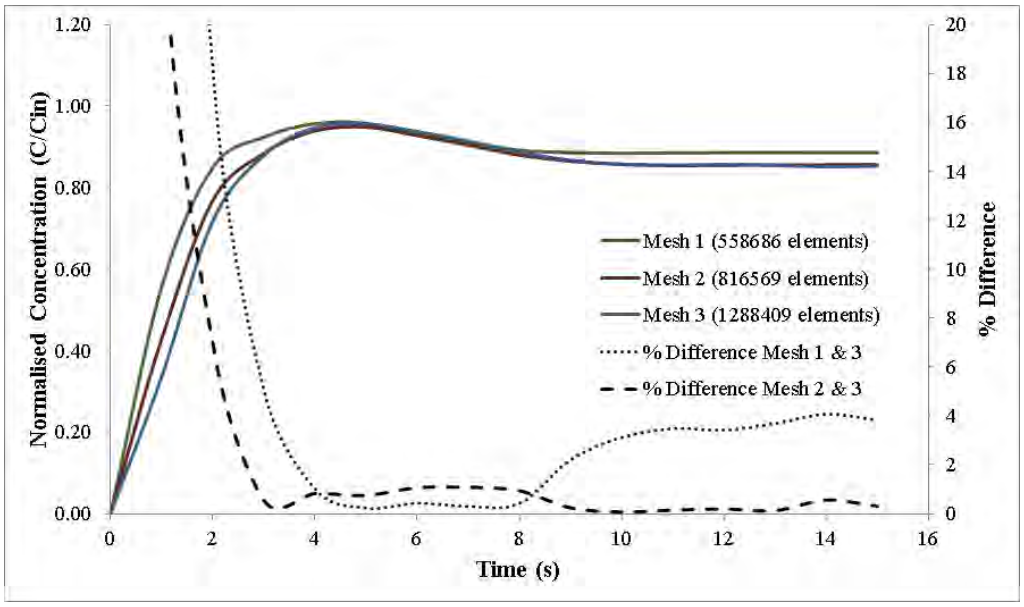

Figure 4.12: Normalised concentration (C/C_{in}) at point on aneurysm dome wall for different mesh sizes

Figure 4.12 plots the normalised concentration at a point of reduced concentration within the aneurysm dome for three mesh sizes. Similar to the grid independence study for WSS, the results for each solution are compared to the finest mesh of 1,288,409 elements. Results show considerable differences between results during the initial stages of the simulations as the concentration increases at the aneurysm dome wall. However, once the concentration has stabilised and the long-term distribution of ATP concentration at the wall is established, in this case after 10 seconds, is can be seen that the difference between the mesh of 816,569 elements and the finest mesh of 1,288,409 elements drops to below 2%, suggesting a grid independent solution.

It can therefore be concluded that a mesh of ~800,000 or larger is appropriate for use in this study of the computational analysis of mass transport within an aneurysm, as the solution has been shown to be grid independent for both WSS and species concentration. Furthermore, it has been established that the mass transport analyses

should be run for a time period of sufficient length to allow the concentration to stabilise at the aneurysm wall, reaching an estimation of the long-term distribution of blood-borne species within the aneurysm dome.

4.8 Discussion

In this chapter, the steps taken to prepare the geometric models described in Chapter 3 for computational analysis were outlined. This involved first establishing a method that could be used to extract results from the 3D cerebral aneurysm models and present the results for analysis. The governing equations solved by Comsol are described, which consist of the continuity, Navier-Stokes and conservation of species equations. A description of any assumptions made in the study follows, along with the application of boundary conditions to describe the flow environment. Finally, a description of the mesh generation and the grid independence study carried out complete the chapter.

Several assumptions are made in this study, including the treatment of the arterial wall as rigid and the assumption that blood is Newtonian and steady in nature. The decision to neglect the compliance of the arterial and aneurysm wall is justified by the location of aneurysms within the cerebral vasculature, which are believed to be stiffer in nature than the more elastic arteries found closer to the heart (Jou *et al.* 2003), and the negligible differences in results between studies of rigid and elastic models (Tateshima *et al.* 2003).

Blood is assumed to be Newtonian in nature in this study, which was shown to be appropriate in a comparison of results from the mass transport of ATP within a lateral and bifurcation aneurysm for both a Newtonian and non-Newtonian fluid. Minimal differences were seen between results for the different rheological models, suggesting that although shear rates of $< 100s^{-1}$ are found within the aneurysm sac and parent artery, the effect of non-Newtonian flow is negligible. It is possible that this can be attributed to the low residence time found within some aneurysms, as the red blood cells do not have time to aggregate and form rouleaux before being convected back into the main arterial flow stream. The Carreau-Yasuda equation estimates the viscosity of blood instantaneously based on shear rate, but this may not be physiologically realistic for aneurysms with low residence times and high washout of blood-borne species. Therefore, the computational effects of non-Newtonian flow may

over-estimate the physiological effects which may be closer to Newtonian flow, thus justifying the assumption made for this study.

Validation of the assumption of steady flow was carried out as part of the ASME 2012 Summer Bioengineering Conference CFD Challenge, in which it was determined that the difference between the steady and pulsatile results were negligible in the study of flow within a patient-specific cerebral aneurysm. Furthermore, numerous previous studies have highlighted the lack of significant differences between steady and pulsatile simulations of mass transport. Although steady flow simulations may not completely capture all instantaneous flow effects that occur within pulsatile flow, steady simulations have been shown to give reasonable approximations when compared to time-averaged pulsatile results. It is also noteworthy that in this study, it is not the instantaneous distribution of the blood-borne species within the aneurysm dome that is of interest. Instead, it is the long-term concentration distribution that is analysed for its relationship with growth and rupture, and so the assumption of steady flow is reasonable in this study.

As outlined in Section 4.5, the choice of boundary conditions is a key aspect of computational modelling. Furthermore, the boundary condition selected to describe the wall when modelling the mass transport of species within an artery or aneurysm is extremely important. Although multi-layer models are considered to be the most realistic and appropriate method of describing the wall, their complex nature increases computational expense. In order to reduce the computational expense and simplify the already complex 3D patient-specific aneurysm geometries, the wall was described via a simple boundary condition. This study aims to analyse the relationship between the geometric features of the aneurysm and the distribution of species at the wall, thus the concentration profiles within the different arterial layers in outside the scope of this study. Therefore, the wall-free model is appropriate for this study.

The final section of this chapter outlined the grid independence study which was carried out in order to build confidence in the computational solution. However, as described by Prakash and Ethier (2000), grid independence studies are not the only method of determining the suitability of a computational simulation. It is suggested that the comparison of computational solutions with experimental data can also increase confidence in results from a CFD analysis. Therefore, the next step in this study was to undertake an experimental validation of the computational approach.

CHAPTER 5

EXPERIMENTAL VALIDATION

Chapter 5 Experimental Validation

5.1 Introduction

The overall objective of this study is to explore the relationship between geometric parameters, mass transport of blood-borne species and cerebral aneurysm growth and rupture potential. Chapter 3 outlined the steps involved in the preparation of the geometric models for computational analysis of mass transport within aneurysms. However, in order to test the efficacy of the computational approach employed, an experimental validation was carried out. The aim of this experimental validation was to experimentally mimic the computational approach used in this study to investigate the mass transport of blood-borne species in patient-specific cerebral aneurysms, so as to gain confidence in the computational approach and results. This validation involved creating a physical flow environment identical to that modelled computationally, allowing the suitability of the numerical models to be assessed.

A dye density technique developed by Lutostansky *et al.* (2003) was employed for the experimental validation. An identical computational simulation was performed, thus allowing for direct comparison between the computational and experimental results. In this chapter, the development of two 3D printed lateral patient-specific aneurysm models is presented, and the process involved in the dye density technique is explained. The flow system set-up is described, and a comparison of the computational and experimental results is presented. This comparison allowed for the validation of the computational model of mass transport of blood-borne species in a patient-specific cerebral aneurysm.

5.2 Experimental Model Development

The process of the experimental model development involved several steps, beginning with the consideration of the most appropriate development technique. As outlined in Section 2.4.1, previous studies have used numerous methods to develop aneurysm models for experimental analysis, including glass, silicone and latex models, the lost-material method and rapid prototyping. The lost-wax method was initially considered to create patient-specific silicone aneurysm models. However, this technique tends to

have limitations that include the presence of air bubbles, surface irregularities and inconsistent wall thickness values. Furthermore, the patient-specific nature of the models means that several individual moulds would first need to be developed, resulting in higher costs of production. Instead, 3D printing was selected as a suitable alternative for the development of the experimental aneurysm models.

3D printing, a similar process to rapid prototyping, uses CAD models and drawings to develop 3D physical models through an additive process. Successive layers of material are laid down, building the final model from a series of layered cross-sections (Rengier *et al.* 2010). One of the main advantages of 3D printing is its ability to create geometric shapes within short time periods. Furthermore, it has the capability to create complex patient-specific models, and so it was considered to be an ideal technique to create experimental models for this study.

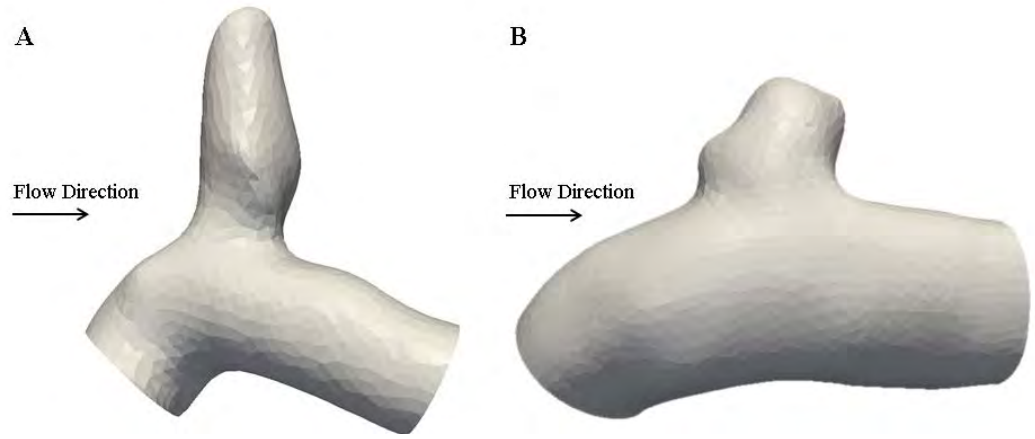

Figure 5.1: Patient-specific geometries used for experimental validation (A) Model 1 – anterior choroidal segment ICA (B) Model 2 – ophthalmic segment ICA

Two patient-specific lateral saccular aneurysm models were chosen for the experimental validation within this study (see Figure 5.1). The first, hereafter referred to as Model 1, is found at the anterior choroidal segment of the ICA, while the second aneurysm - referred to as Model 2 - is from the ophthalmic segment of the ICA. The geometric measurements of each aneurysm can be found in Table 5.1. Model 1 consists of a deep, narrow, small-necked aneurysm, while Model 2 contains a small, multi-lobed aneurysm with a wide-neck orifice.

Table 5.1: Geometric measurements for experimental models 1 and 2. All units in mm, except Tilt Angle (º).

Geometric Measurement	Model 1	Model 2
Height (H)	6.2	2.7
Neck Width (N)	3.1	2.9
Diameter (D)	3.6	3.0
Dist. To Max. Diameter (h)	1.5	0.9
Tilt Angle (θ_T)	13.8	46.8
Aspect Ratio (AR)	2.0	0.9
Parent Artery Inlet Diameter	3.2	2.9
Parent Artery Outlet Diameter	2.4	3.1

The aneurysm model geometries were prepared for 3D printing over a series of steps. Using the 3D graphics and animation software Blender, the overall geometry was first segmented to a section containing the aneurysm and a length of its inlet and outlet parent arteries. In order to ensure flow was fully developed within the artery, inlet extrusions were added to both models, representing the entrance length of 90 mm. A 10 mm extrusion was added to the outlets to avoid outlet effects. A second 6 mm diameter extrusion of 10 mm in length was added to both the inlet and outlet of both models to facilitate smooth connection of the tubing to the finalised block model. Six narrow extrusion ports of 0.6 mm diameter were added at different locations throughout the aneurysm so as to hold 23-gauge needles flush with the aneurysm wall, allowing for small amounts of the test fluid to be extracted over the course of the experiment. A Boolean difference modifier was used to subtract the aneurysm geometry from a 3D block volume, resulting in final hollow CAD block models that were used for 3D printing (see Figure 5.2).

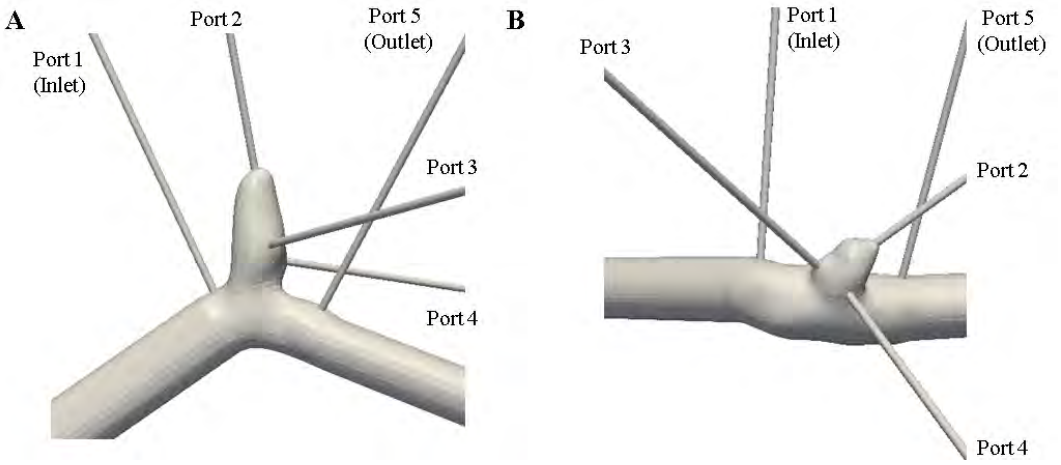

Figure 5.2: Extruded experimental models (A) Model 1 and (B) Model 2 with labelled extraction ports

The Objet Connex 500 3D printing system was used to develop the finalised experimental models. This model of 3D printing system uses two materials when developing geometric models – the first is the part material, with the second acting as a support material. The support material is included in the initial construction of the model, but is then removed either through heating or is dissolved, after the model has been formed. Using 16-micron, high-resolution layers, the experimental models were created from the transparent rigid material Veroclear-RGD810, allowing for visualisation of the flow through the models during the experimental simulations. The final printed models are shown in Figure 5.3 below.

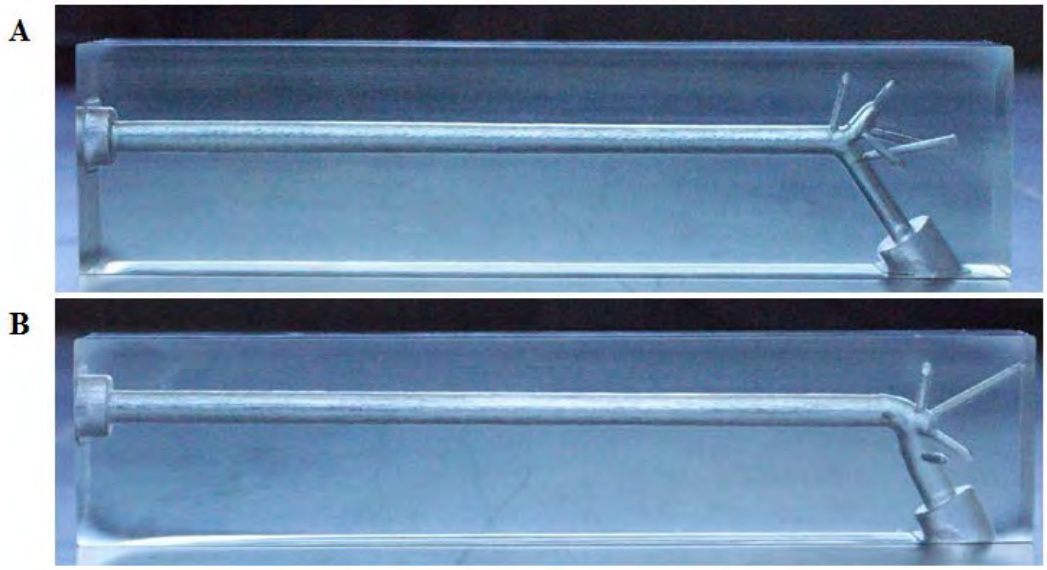

Figure 5.3: 3D printed rigid experimental aneurysm models with extruded inlet and outlet sections (A) Model 1 (B) Model 2

5.3 Dye Density Technique

A dye density technique was employed to quantify the change in concentration of species at the aneurysm wall over time. Developed by Lutostansky *et al.* (2003), the technique involves circulating a water/dye mixture through the silicone aneurysm model, while extracting small concentrations from extraction ports along the aneurysm dome wall throughout the duration of the experiment. The powdered food dye FD&C Blue #1 was used as the transported species as it has a Schmidt number of 3200 in water, which is in the range of blood-borne species such as ATP or oxygen free radicals (Carroll *et al.* 2010, Kaazempur-Mofrad and Ethier 2001). The variation of the concentration at the wall at different locations throughout the aneurysm dome provides a basis for comparison of the computational and experimental results.

In order to determine the concentration of the water/dye samples at each extraction point along the aneurysm wall, the absorbance or optical density of the samples was measured using the El_x800 Automated Microplate Reader from BioTek Instruments Inc. The El_x800 contains 5 wavelength lenses that can be used to measure the amount of light absorbed by a sample. Absorbance values range from 0, indicating no light being absorbed, to 3, which indicates all light has been absorbed by the sample (Ball 2001), and an increase in absorbance indicates higher concentration levels.

The absorbance of the sample depends on a number of factors including the wavelength of light and the depth of the sample. The El_x800 microplate reader has the capability to read samples at 5 light wavelengths – 405, 450, 570, 630 and 690 nm. A comparison of the ability of each wavelength to detect changes in absorbance over a range of water/dye concentrations from 0.01 g/L to 0.1 g/L is shown in Figure 5.4. The 630 nm lens was unable to read water/dye concentrations of greater than 0.03 g/L and thus is omitted from the results. It can be seen from the results of the comparison that the greatest change in absorbance values between concentrations is found using the 570 nm lens, and so it was deemed the most appropriate for the application of this study.

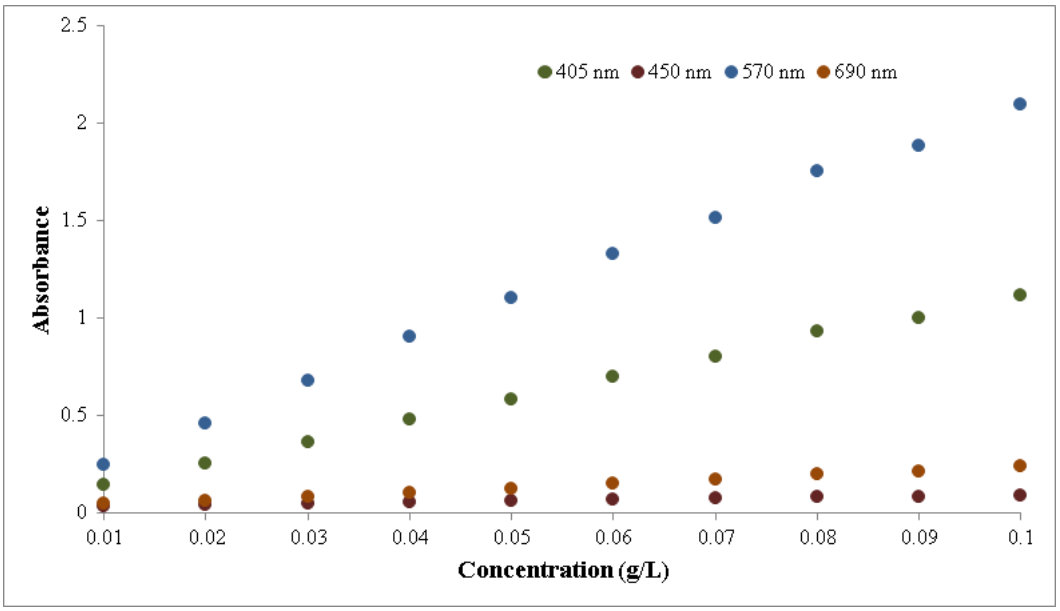

Figure 5.4: Change in absorbance values over range of concentration values for light wavelength values 405, 450, 570 and 690 nm

As previously mentioned, the depth or thickness of the sample used can affect the absorbance values, and so samples depths of 50 µL, 100 µL and 200 µL were evaluated. A comparison of the different depth values is illustrated in Figure 5.5, where it can be seen that a depth of 200 µL shows the greatest difference in

absorbance over the range of concentration values. As a result, all samples used in this experimental analysis were 200 µL in depth.

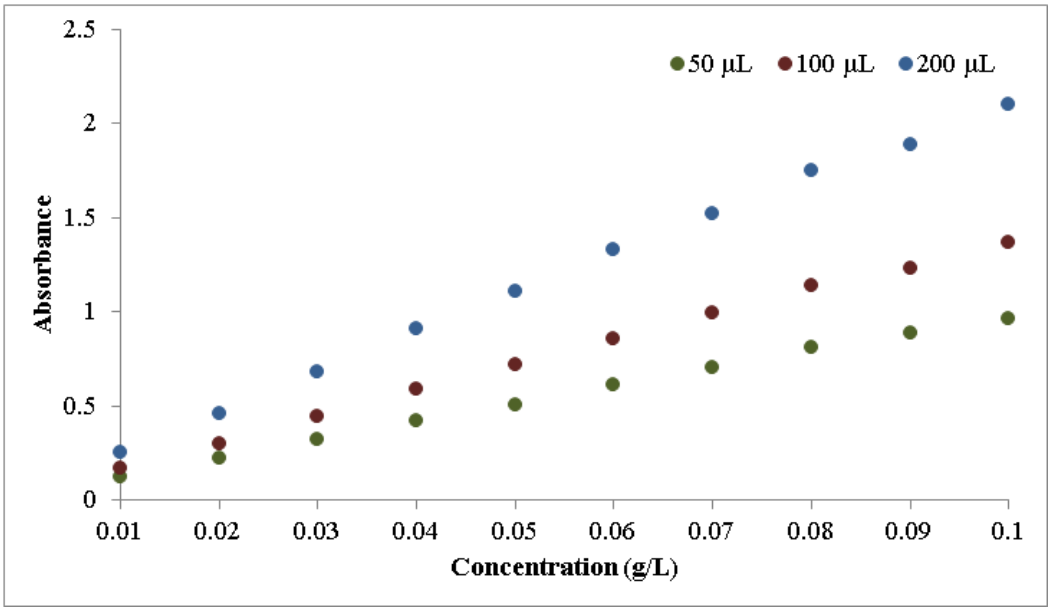

Figure 5.5: Change in absorbance over range of concentration values for sample sizes 50µL, 100µL and 200µL

5.4 Experimental Flow Parameters

The aneurysm models used in this experimental validation are found at the anterior choroidal segment and the ophthalmic segment of the ICA for Models 1 and 2 respectively. Therefore, a flow rate of 260 ml/min was chosen as the inlet flow rate, representing the average flow rate found within the ICA (Alnaes *et al.* 2007, Cebral *et al.* 2008, Fahrig *et al.* 1999, Ford *et al.* 2005, Moore *et al.* 2006). Taking the viscosity and density of blood as 3.4 mPa·s and 1050 kg/m³ respectively and inserting them into Equation 4.10, this flow rate gives a Reynolds number of 518 for Model 1and 549 for Model 2.

The test fluid used in this study comprised of a water/dye mixture, with a density of 1000 kg/m³ and a viscosity of 1 mPa·s (Carroll *et al.* 2010). In order to account for the difference in viscosity and density values, and so as to achieve dynamic similarity between the experimental and computational models, the experimental inlet flow parameters are scaled so that the Reynolds number of both the experimental and computational analyses is equal. The conversion from computational to experimental parameters was carried out as follows:

$$\frac{\rho u d}{\mu}_{(Computational)} = \frac{\rho u d}{\mu}_{(Experimental)} \quad (5.1)$$

Further steps taken to achieve dynamic similarity involved the calculation of the diffusivity of species in the test fluid. The food dye FD&C Blue #1 was selected as the transport species as it has a diffusivity of 3.125×10^{-10} m^2/s in water, resulting in a Schmidt number of 3200, which is similar to that of species such as ATP in blood (Carroll *et al.* 2010, Gutti *et al.* 2012). As a result, the corresponding Peclet number is calculated as 1,638,400. Using this Peclet number value and Equation 5.2, the diffusivity of the computational blood-borne species is calculated as follows:

$$\frac{ud}{D}_{(Computational)} = \frac{ud}{D}_{(Experimental)} \quad (5.2)$$

Table 5.2 lists the computational and experimental parameters used in the experimental validation study.

Table 5.2: Parameters used in experimental and computational flow analysis of mass transport within Model 1 and 2

Parameter	Model 1		Model 2	
	Experimental	**Computational**	**Experimental**	**Computational**
Density (kg/m³)	1000	1050	1000	1050
Viscosity (Pa·s)	0.001	0.0035	0.001	0.0035
Reynolds Number	518	518	574	574
Peclet Number	1638400	1638400	1837440	1837440
Schmidt Number	3200	3174	3200	3205
Diffusivity (m²/s)	3.125×10^{-10}	1.05×10^{-09}	3.125×10^{-10}	1.04×10^{-09}

Using scale analysis in conjunction with the Navier-Stokes equations (see Equation 4.4), Equation 5.3 accounts for the difference in time scales between the experimental and computational simulations, ensuring results were extracted at the same reference time point:

$$\frac{\rho u t}{L}_{(Computational)} = \frac{\rho u t}{L}_{(Experimental)} \quad (5.3)$$

5.5 Experimental Set-Up

A flow system was developed to allow for the experimental validation to be performed on the previously described 3D printed patient-specific cerebral aneurysm models. A schematic of the flow system and the various components is illustrated in Figure 5.6. The water/dye mixture, with an inlet concentration of 0.05 g/L, was supplied to a pressure head tank via a supply reservoir and a diaphragm pump. The pressure head was calculated using the following equation (Massey 2006):

$$h = \frac{P}{\rho g} \tag{5.4}$$

The pressure head tank contained a divide which allowed the water/dye mixture to be held at a constant height above the test section. This ensured an inlet pressure of 100 mmHg, which is within the typical physiological range of arterial pressure within the cerebral vasculature (Moore *et al.* 2006).

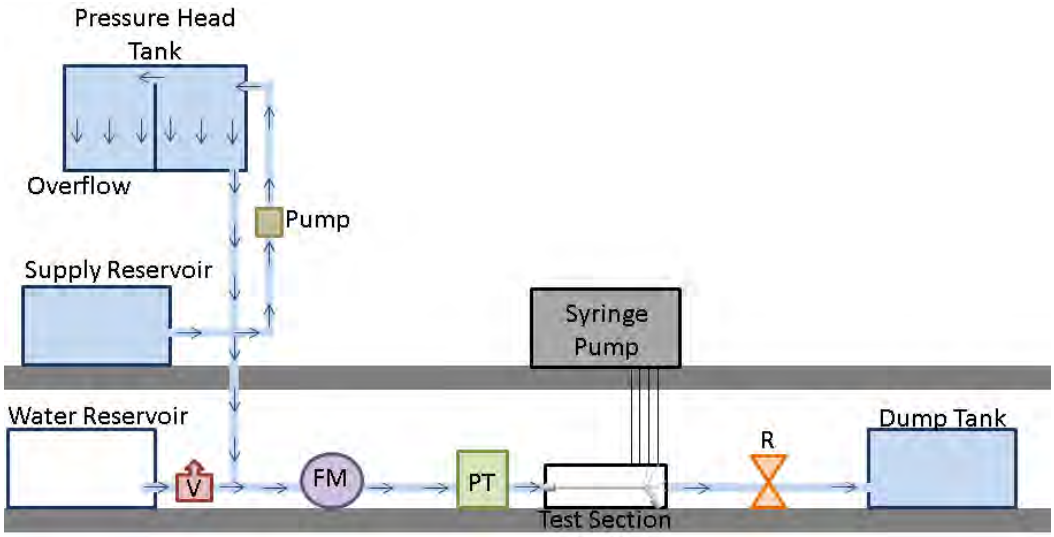

Figure 5.6: Experimental flow set-up (V = valve, FM = flow meter, PT = pressure transducer, R = resistance)

The water/dye mixture was moved through the flow system using rigid silicone tubing with an inner diameter of 4 mm, representing the average internal carotid artery diameter of 4.02 mm (Alastruey *et al.* 2007, Devault *et al.* 2008, Fahrig *et al.* 1999, Krabbe-Hartkamp *et al.* 1998, Moore *et al.* 2006, Roessler *et al.* 2006). Upon exiting the pressure head tank, the flow entered a Sensirion SLQ-QT500 liquid flow sensor. The flow meter operates on a principle of calorimetric sensing: a temperature sensor measures the fluid before a negligible amount of heat is added, upon which the fluid

temperature is measured a second time. The temperature differentials are then correlated to actual flow. One of the main advantages of using thermal sensors is the low pressure drop of approximately 0.75 mmHg across the flow meter. Using the flow meter, the inlet flow rate was monitored throughout the experiment.

Following the flow meter, the flow entered a Sensortechnics pressure transducer, which measured the inlet pressure applied via the pressure head tank, ensuring it was within the physiological range. The water/dye mixture then entered the 3D printed aneurysm model, which contained five ports to allow for the extraction of small amounts of fluid during the course of the experiment. Each port was 0.6 mm in diameter and held a 23-gauge needle attached to silicone tubing of 0.8 mm in diameter. The tubing was attached to 10 ml syringes fixed to a Harvard Apparatus syringe pump, which was used to extract the water/dye mixture at a low extraction rate, so as to avoid disturbance to the flow.

Upon exiting the aneurysm model, flow entered a ball and needle valve that was used to set the resistance, ensuring an accurate inlet flow rate. Finally, the flow entered a dump tank, where it was disposed of. Flow was not recirculated through the system. A reservoir containing water was used to flush and clean the system between each experimental run, ensuring no contamination of results by residual dye particles within the aneurysm model. The main components of the flow system are illustrated in Figure 5.7.

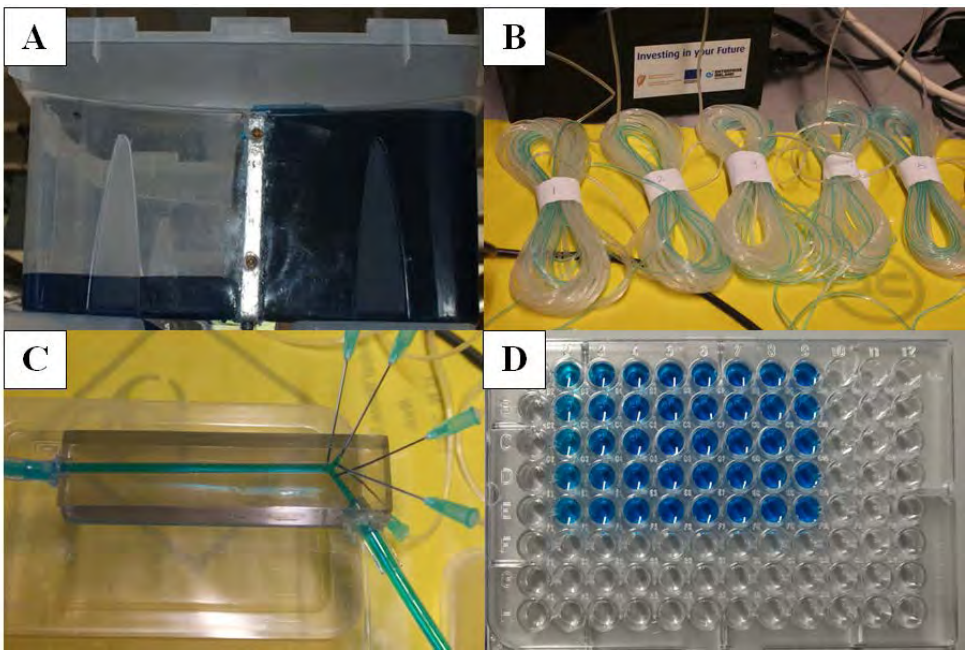

Figure 5.7: Main components of flow system (A) Pressure head tank (B) Tubing for flow extraction (C) 3D printed aneurysm model filled with water/dye test fluid and (D) Water/dye samples for each extraction port (top to bottom) at each minute (left to right)

5.6 Results

The following section presents the results for the experimental validation study. First, a comparison of experimental simulations using an extraction rate of 0.6 ml/min and 0.8 ml/min is presented. Following this, results for the experimental validation of the computational simulation of mass transport of ATP within Model 2 is presented.

5.6.1 Extraction Rate

The dye density technique employed in this study is invasive, as the dye sample extraction procedure could potentially cause flow disturbance (Lutostansky *et al.* 2003). An extraction rate of 0.8 ml/min was initially selected for this study based on the parameters used in a similar study carried out within the CABER group on an idealised abdominal aortic aneurysm (Carroll *et al.* 2010). An experimental analysis was also carried out using a lower extraction rate of 0.6 ml/min to ensure no significant differences occur, which would indicate whether the higher extraction rates cause disturbance to the flow within the aneurysm model.

Figure 5.8 highlights the normalised dye concentration values at the aneurysm wall at the five extraction port locations in Model 2 at two extraction rates. It can be seen from the results that there are differences between the concentration values at each extraction port within the initial stages of the experiment, as the water/ dye mixture slowly fills the aneurysm and the concentration builds up at the wall. As the concentration stabilises at the aneurysm wall after the aneurysm fills with the water/dye mixture, the difference between the results is less than 10% between extraction rates. Therefore, it was concluded that the variation of the extraction rate did not impact significantly on the final concentration measurements which are of interest in this study, and so an extraction rate of 0.8 ml/min was used in all following experimental analysis.

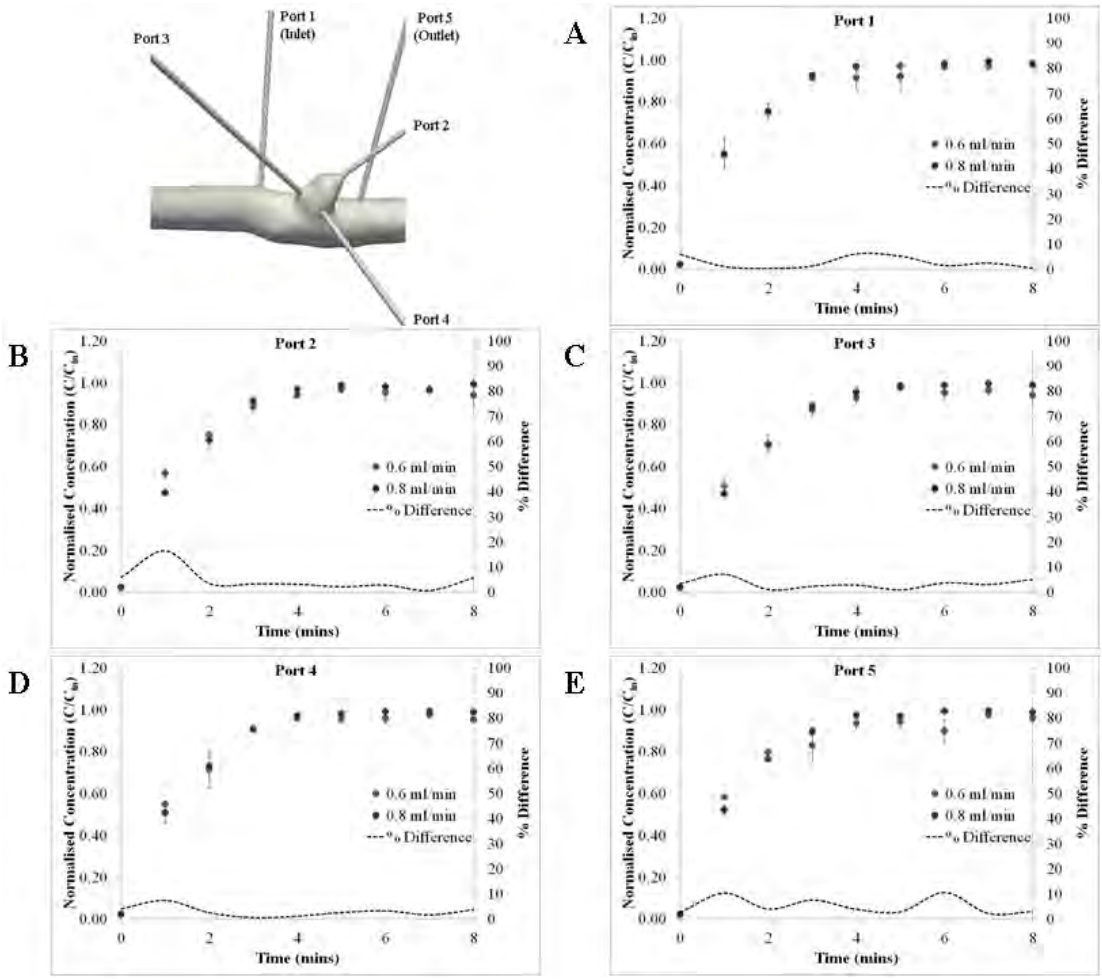

Figure 5.8: Comparison of concentration values at Model 2 aneurysm wall (top left) over 8 minutes for extraction rates of 0.6 ml/min and 0.8 ml/min for (A) Port 1 (B) Port 2 (C) Port 3 (D) Port 4 and (E) Port 5. All values normalised to inlet concentration (C/C_{in}).

5.6.2 All Experimental Results

Using the experimental methods, set-up and parameters outlined in the previous sections in this chapter, experimental versions of the computational simulation of the mass transport of ATP within Model 1 and Model 2 were carried out. The results presented in this section examine the distribution of species within two patient-specific lateral aneurysm models. Results are illustrated in Figure 5.9 and Figure 5.10, with each graph illustrating a comparison of the dye concentration at specific sites within the aneurysm. Results are shown at 1 minute intervals over the 8 minute experimental period.

Results for both experimental models illustrate a slow build-up in concentration over approximately 4 minutes as the water/dye mixture disperses throughout the aneurysm sac. After this initial build-up period, the concentration at the wall reaches a uniform

distribution of the same value as the inlet concentration ($C = C_{in}$). This is evident in both models at all extraction ports, although the rate of concentration build up varies. The concentration at ports 1 and 5, the inlet and outlet respectively, for Model 1 and 2 increases at a slightly faster rate than ports 2, 3 and 4, which are found within the aneurysm sac. Port 3 shows a marginally slower increase in concentration at the aneurysm wall for Model 1 and Model 2 over time.

On comparison with the computational results, a substantial difference is evident for the initial build-up of concentration at the aneurysm wall. In the computational models, the dye disperses throughout the aneurysm rapidly, with the concentration increasing from zero to the inlet concentration at a much faster rate than the experimental model. However, although the experiments yielded lower values than the computational results, the concentration values for the final minutes of the computational and experimental models are similar, with differences within ±2% found between the final values for both models at all sample locations.

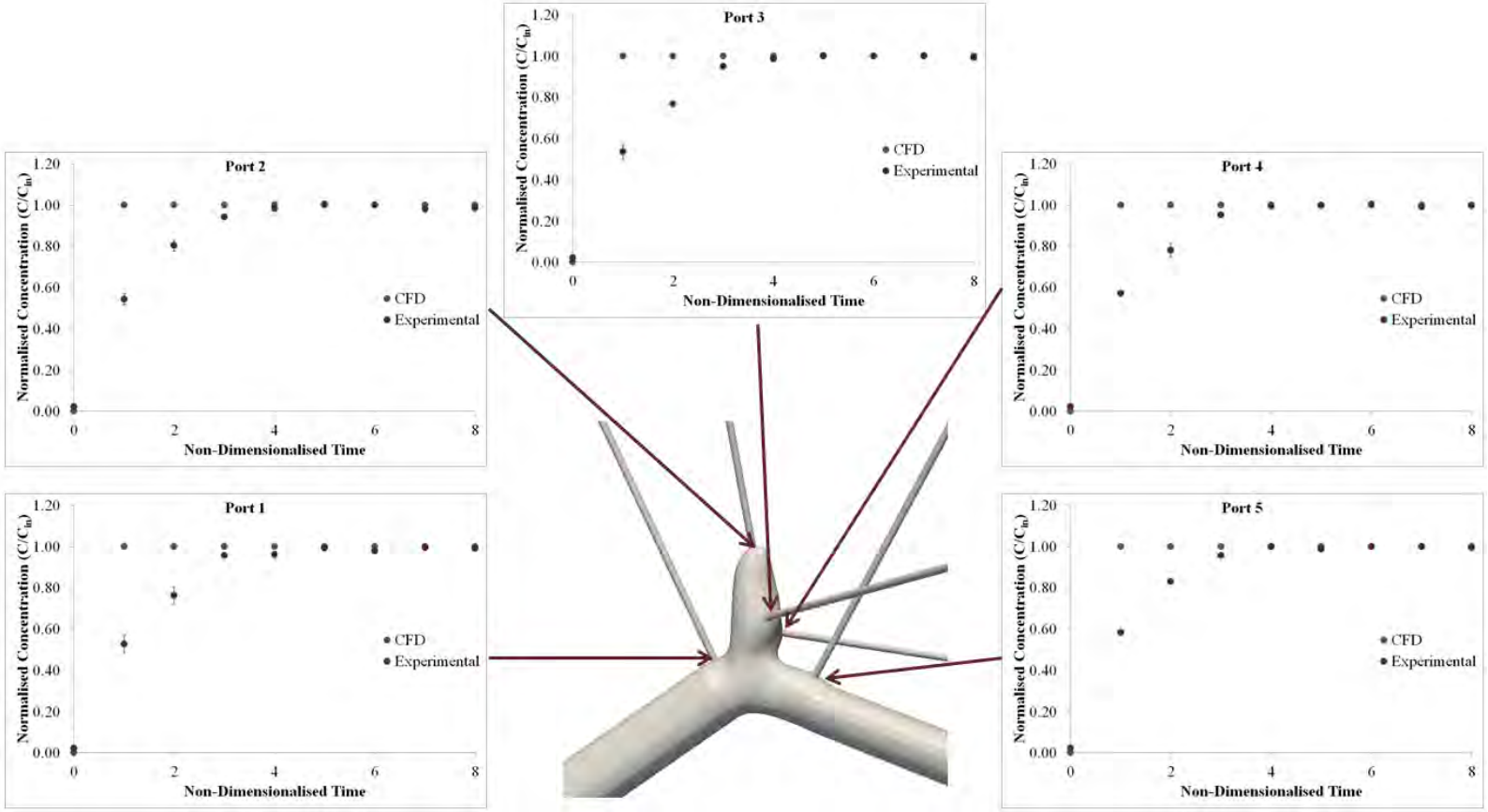

Figure 5.9 Illustration of results for Model 1, including CFD (green) and experimental (red) for Ports 1-5

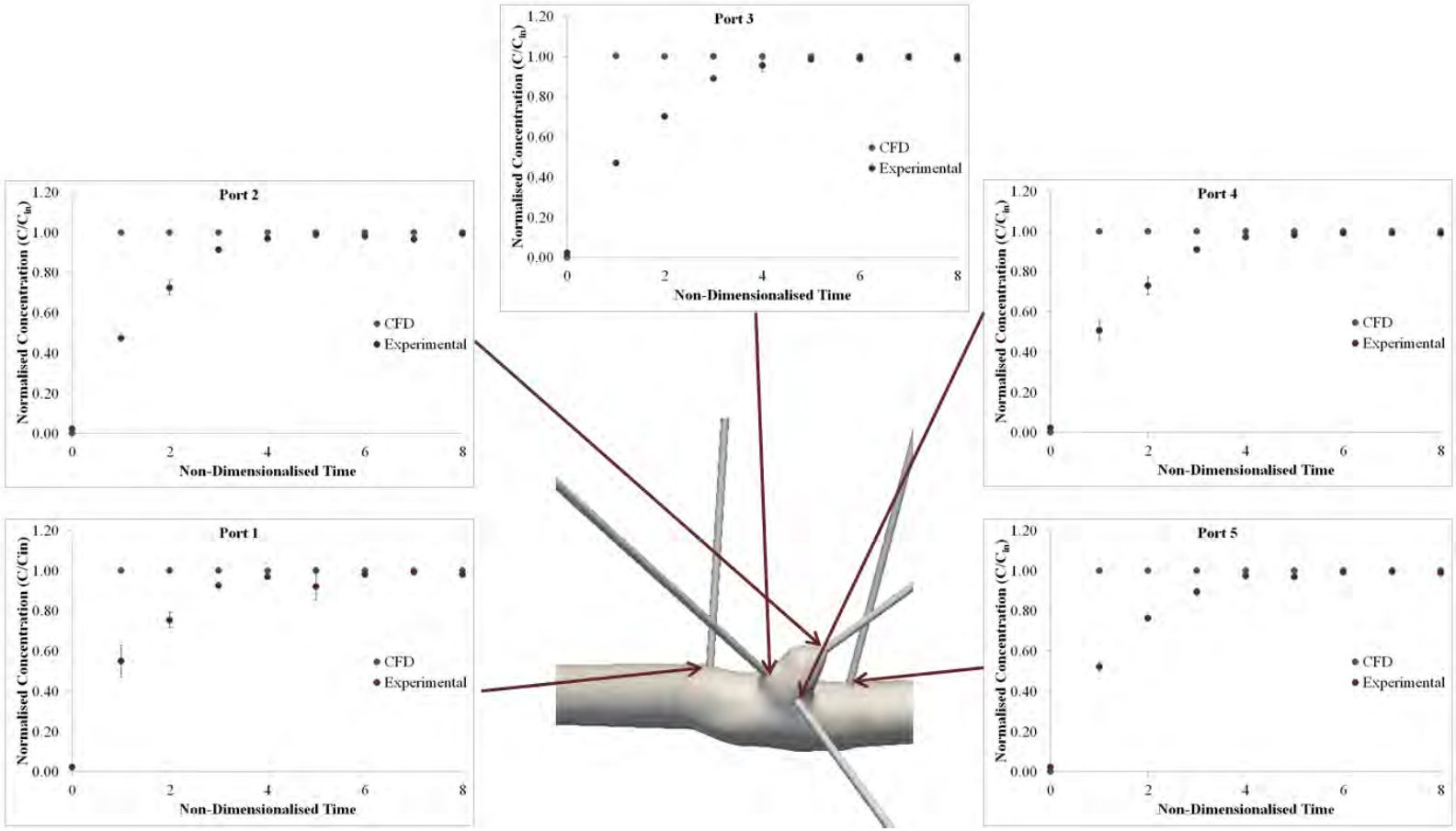

Figure 5.10: Illustration of results for Model 2, including CFD (green) and experimental (red) for Ports 1-5

5.7 Discussion

The overall aim of this study is to investigate the relationship between geometric parameters, mass transport of blood-borne species and cerebral aneurysm growth and rupture, through the use of computational methods. The significance of an experimental validation study such as described in this chapter is to gain confidence in computational results. In this experimental validation study, the transport of blood-borne species within two patient-specific lateral cerebral aneurysms was investigated. The study first involved preparing the two geometric aneurysm models for 3D printing. The experimental set-up was constructed as outlined in Section 5.5, and different aspects of the dye density technique such as the extraction rate, inlet concentration and sample size were investigated. In order to achieve similitude between the computational and experimental models, scaling of the dimensionless Reynolds number and Peclet number was carried out to account for the differences in density and viscosity values between the experimental test fluid of a water/dye mixture and the computational parameters describing blood. The experimental and computational results from both Model 1 and Model 2 were then compared and contrasted.

The mass transport of blood-borne species within an aneurysm is a long-term process that takes place over many years. In this study, which aims to establish if a relationship exists between the geometric parameters that define the aneurysm shape, the mass transport of vital blood-borne species and the potential of the aneurysm to grow or rupture, it is the long-term distribution of species throughout the aneurysm sac that is of interest. Therefore, before analysis of results from this experimental validation study takes place, it should be noted that although this experimental method allows for examination of the slow accumulation of species at the aneurysm wall over time, and exhibits the difference in species build-up based on location within the aneurysm, the period of interest for this study is found within the final stages of the experimental analysis, as the species distribution stabilises through the aneurysm sac. This stabilised concentration distribution represents the aneurysm species distribution following long-term mass transport within the cerebral vasculature.

Keeping this in mind, for the period of interest in this study - the final concentration value which represents the long-term concentration distribution at the aneurysm wall - there is excellent agreement between the computational and experimental results

regarding the final concentration values throughout the aneurysm model. For each sample location in both Model 1 and Model 2, the experimental results at the final minute show negligible differences, with experimental values falling within ±2% of the computational results. It is interesting to note that for both of the lateral models investigated in this study, the final results show a uniform distribution of $C = C_{in}$ at all extraction ports, suggesting that as a result of the flow haemodynamics within the aneurysm sac, good washout of species occurs and so the aneurysm wall does not experience an under-expression or lack of blood-borne species. However, differences can be found in the build-up of concentration for the different extraction port locations. Port 1 and 5 in both models represent the inlet and outlet arteries respectively and reach the inlet concentration within a shorter time period than the ports found within the aneurysm sac, as they are exposed to a constant supply of the test fluid. Within the aneurysm dome however, Port 2, which represents the tip of each model, takes longer than Ports 3 and 4 to reach the stabilised concentration value. This is attributed to the time taken for the water/dye mixture to circulate through the entire aneurysm and towards the tip of the dome.

The differences between the experimental and computational results during the initial stages of the simulation, as the concentration builds up slowly at the aneurysm wall, may be attributed to the experimental set-up and the inclusion of water in the system before the introduction of the test fluid. In the computational simulations, the transport of species is governed by the velocity field from the laminar flow study. As a result, the flow is not impeded, and convection dominates. However, in the experimental set-up, water is present in the system before the water/dye mixture is introduced in order to avoid any air bubbles entering the system, and so the dye has to diffuse slowly through the water already present in the aneurysm, rather than entering an "empty" aneurysm and being convected directly to the wall. Therefore, the build-up of concentration at the aneurysm wall within the experimental system takes longer than the computational version. Nevertheless, a similar trend is seen in both the experimental and computational simulations, with an initial build-up phase evident before the concentration stabilises as the aneurysm fills, with each extraction port eventually reaching the inlet concentration value. This is in keeping with previously published studies, in which a gradual build-up of species occurs at the wall, before the concentration stabilises (Carroll *et al.* 2010, Lutostansky *et al.* 2003).

It should be noted that the experimental system described in this chapter does not completely describe physiological mass transport, as the uptake of species at the arterial and aneurysm wall is neglected. However, the experimental model is believed to sufficiently describe the movement of species within an aneurysm, and so can serve as a comparison to computational results, increasing confidence in the computational approach used in the investigation of mass transport of blood-borne species in patient-specific cerebral aneurysms.

CHAPTER 6

TOWARDS THE USE OF RADIOLOGICALLY MEASURABLE PARAMETERS IN CEREBRAL ANEURYSM RUPTURE PREDICTION

Chapter 6 Towards the Use of Radiologically Measurable Parameters in Cerebral Aneurysm Rupture Prediction

Jennifer A. Costelloe[1], Ignacio Larrabide[2], Daniel A. Rüfenacht[3] and Michael T. Walsh[1]

1: Centre for Applied Biomedical Engineering Research (CABER), Department of Mechanical and Aeronautical and Biomedical Engineering, Materials and Surface Science Institute (MSSI), University of Limerick, Limerick, Ireland.

2: PLADEMA-CONICET and Universidad Nacional del Centro, Tandil, Argentina.

3: Department of Neuroradiology, Swiss Neuro Institute Hirslanden, Clinic Hirslanden, Zurich, Switzerland.

British Journal of Neurosurgery (submitted)

Abstract

BACKGROUND The management of unruptured cerebral aneurysms is controversial, as the current intervention techniques carry substantial risks. Identifying parameters that contribute to rupture is imperative, as it may lead to improved management of unruptured aneurysms. The use of clinically measurable parameters in rupture risk assessment would allow for immediate decisions to be made by clinicians based on direct measurements from scans.

OBJECTIVE The aim of the study was to investigate the relationship between radiologically measurable parameters and cerebral aneurysm rupture risk.

METHODS The relationship between radiologically measurable parameters (height, neck width, diameter, distance to maximum diameter, tilt angle, aspect ratio, location, shape, size group and neck size group) and aneurysm rupture was investigated in a cohort of 168 aneurysms. Parameters were analysed using Mann Whitney U and chi-square tests for univariate analysis, and logistic regression analysis was performed. Receiver operating characteristic analysis and area under the curve values were calculated for the individual parameters and for the final model.

RESULTS Significant differences ($p<0.05$) were found between height, diameter, distance to maximum diameter, tilt angle, aspect ratio, location, shape and size grouping for the univariate statistical analysis. Following multivariate logistic regression analysis, a rupture prediction equation was developed using the final, independently significant parameters tilt angle ($p = 0.018$), aspect ratio ($p = 0.013$), location ($p = 0.006$) and shape ($p = 0.01$).

CONCLUSIONS Results from the statistical analysis of aneurysm rupture suggests that the odds of an aneurysm rupturing increase with increasing tilt angle, increasing aspect ratio, if it is of the posterior circulation and if it is bifurcating in shape.

KEYWORDS: Cerebral aneurysm, Rupture, Risk Factors, Geometry, Morphology.

6.1 Introduction

The rupture of a cerebral aneurysm can have devastating effects, with high rates of morbidity and mortality associated with the event. Approximately 12% of patients who suffer a subarachnoid haemorrhage (SAH) due to the rupture of an aneurysm die immediately, a further 40% die within one month and up to one third of those that survive are left with neurological defects.[1,2] Improved imaging techniques have allowed for better detection of unruptured cerebral aneurysms.[3] However, the management of unruptured aneurysms, which are estimated to affect 5-8% of the population,[4] is disputed and current intervention methods carry substantial risks for the patient. The decision to treat patients is typically based on the likelihood of aneurysm rupture. Therefore, identifying factors that can adequately indicate aneurysm rupture potential is paramount to distinguishing patients at need of surgical or endovascular intervention from those who can undergo observation.

Currently, aneurysm risk stratification is determined based on the size of the aneurysm, with large aneurysms believed to be at greater risk of rupture.[5-7] However, more recent studies have established that size alone is not a reliable predictor, with small aneurysms < 10mm found to rupture,[8-12] while large aneurysms remain unruptured. Thus, in order to determine the necessity of intervention for unruptured lesions, there exists a need for more precise indicators of rupture potential.

Recent advances in 3D imaging techniques has allowed for more accurate information regarding the geometric measurements, shape and morphology of the aneurysm and the surrounding vasculature to be immediately determined by clinicians. Several previous studies have examined the relationship between different geometric and morphological features and aneurysm rupture. One parameter that has consistently shown strong correlation with rupture is the aspect ratio (AR), the ratio of the aneurysm height to its neck width. Ujiie *et al.* (2001) found significant differences between the aspect ratios of ruptured and unruptured aneurysms, with approximately 80% of ruptured aneurysms having an AR >1.6 and almost 90% of unruptured lesions with an AR <1.6.[12] Lall et al. (2009) published results of a review of anatomical and morphological features of aneurysms reported in literature and found that although differences in AR values for ruptured and unruptured aneurysms were statistically significant in several studies, there is some disagreement with regards to the threshold

value for rupture potential.[7] Results indicate that aneurysms with an AR >3 are at significant risk of rupture, while those with an AR <1.4 a less likely to rupture.

Several other parameters have shown strong correlation with rupture risk, such as aneurysm location, neck size, size ratio (aneurysm height/average vessel diameter), aneurysm angle, undulation index, ellipticity index, non-sphericity index, curvature of the aneurysm wall and shape.[8, 13-16] However, it is not possible to directly measure many of these parameters using typical imaging techniques. If clinically measurable geometric and morphological parameters were found to correlate with aneurysm rupture, immediate decisions regarding aneurysm intervention could be made by clinicians based on direct measurements from 3D scans.

The aim of the current study is to investigate the influence of clinically relevant and measurable parameters on aneurysm rupture, and to determine if some or all of these geometric and morphological features can be used to predict the rupture potential of an aneurysm.

6.2 Materials and Methods

Study Population

The study population used in this geometric and morphological study comprised of a database of 168 cerebral aneurysms from 153 patients, found at 131 locations throughout the cerebral vasculature. The aneurysm geometries are a subset of the @neurIST: Integrated Biomedical Informatics for the Management of Cerebral Aneurysms project,[2] consisting of 3D patient-specific vascular models constructed from three-dimensional rotational angiography (3DRA) images.

Measured Parameters

Ten clinically measurable parameters in total were investigated. For ease of analysis, these were split into two groups – continuous and categorical parameters. The first step in the analysis was to classify the database based on the four categorical parameters, which consisted of location within the cerebral vasculature, shape, size group and neck size group. The aneurysms in the current study were found at 13

locations throughout the cerebral vasculature and grouped according to their location in the anterior or posterior circulation. The individual aneurysm shape was classified based on the shape of the aneurysm in relation to its parent artery geometry, with the categories lateral and bifurcating/terminal.[17] The aneurysm size groups, which refer to the largest diameter within the dome, were categorised according to small (≤5mm), medium (5<x<15mm), large (15≤x<25mm) and giant (≥25mm) aneurysms.[18] Neck size groups were classified as narrow necked if the neck width was ≤4mm, with neck widths >4mm categorised as wide-necked.[15] Results from the classification are listed in Table 6.1.

Table 6.1: Aneurysm classification results

Parameter	No. of Aneurysms	%
Location		
Anterior	107	64
Posterior	61	36
Shape		
Lateral	56	33
Bifurcating/Terminal	112	67
Size		
Small	77	46
Medium	86	51
Large	4	2
Giant	1	1
Neck Size		
Narrow	74	44
Wide	95	56

Six continuous parameters, namely the height (H), neck width (N), diameter (D), distance to maximum diameter (h), tilt angle (θ_T) and aspect ratio (AR) were measured using commercially available computer aided design software (Creo 1.0, PTC, Massachusetts). In this study, height was measured as the longest distance between the centre of the neck and the dome. Neck width was taken to be the widest distance across the neck orifice. The diameter was defined as the widest section of the dome in parallel with the neck plane. The distance to the maximum diameter, also known as semi-axis height[19] or bulge location[20] was calculated as the perpendicular distance from the neck width to the diameter. For the aneurysm tilt angle, the angle between the centre point of the neck and the height of the aneurysm was measured. Aspect ratio was defined as the height divided by the neck width.[12] An illustration of the measured parameters is shown in Figure 6.1.

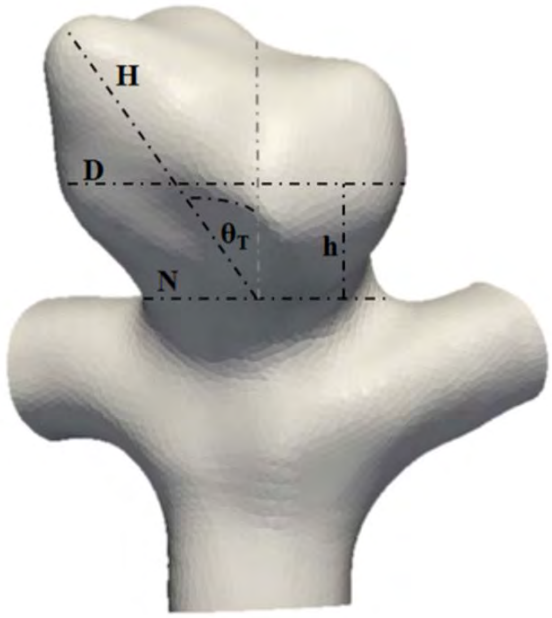

Figure 6.1: Definition of measured parameters (H = height, N = neck width, D = diameter, h = distance to maximum diameter, θ_T = tilt angle)

Statistical Analysis

In order to determine if a relationship could be established between the ten geometric and morphological parameters and aneurysm rupture potential, statistical analysis was carried out using IBM SPSS Statistics V 21 (SPSS Inc., Chicago, Ill.), with significance assumed for $p<0.05$. The study population was divided into unruptured (n = 98) and ruptured (n = 70). A test for departure from normal distribution was performed on each parameter for both groups. Differences between the two groups were made using the non-parametric Mann Whitney U and chi-square tests for continuous and categorical parameters respectively. Multivariate logistic regression analysis was carried out on all parameters in order to determine independently significant parameters. A receiver operating characteristic (ROC) curve for the individual parameters and for the model output was generated, and the area under the curve (AUC), sensitivity and specificity of the final model were calculated.

6.3 Results

Anatomical Classification

Results from the classification of the database revealed that 64% (n = 107) of aneurysms were found within the anterior circulation while 36% (n = 61) were found in the posterior circulation. A large number of aneurysms (14%, n = 24) were found at the ophthalmic segment of the internal carotid artery (ICA) for the unruptured lesions, and at the posterior communicating artery (15%, n = 25) for the ruptured lesions. Most aneurysms were bifurcating or terminal in shape, with just 33% lateral aneurysms found within the database. The difference between the number of lateral and bifurcating aneurysms is more prominent in the ruptured group, with 54 bifurcating versus 16 lateral aneurysms. Aneurysm size for the overall study population ranged from 1.5mm to 25mm, with an average size of 6.3mm. The smallest aneurysm was found at the sylvian bifurcation while the largest was found at the ophthalmic segment of the ICA. Both the smallest and largest aneurysms belonged to the unruptured group. Only 4 large aneurysms and 1 giant aneurysm were found within the entire cohort. The aneurysm neck widths ranged from 1.8mm to 10mm, with an average neck size of 4.5mm. Wide necks (>4mm) were more common than narrow necks in both the unruptured and ruptured groups. Aspect ratio (aneurysm height/aneurysm neck width) ranged from 0.35 to 3.26 for the entire database, with an average of 1.25. Within the unruptured group, the mean aspect ratio was found to be 1.13±0.5 while the ruptured group had a mean aspect ratio of 1.43±0.6.

Statistical Analysis

A departure from normal distribution was seen for all parameters. Results from the non-parametric Mann Whitney U test, shown in Table 6.2, highlighted significant differences between median values for the ruptured and unruptured groups for height, diameter, distance to maximum diameter, tilt angle and aspect ratio. For the chi-square analysis, also shown in Table 6.2, significant differences between the ruptured and unruptured groups were found for location, shape, and size, with no significance found for neck size.

Table 6.2: Results from univariate statistical analysis for all parameters (*significant at p <0.05, **significant at p<0.01, NS = not significant)

Parameter	Median		p value
	Unruptured (n = 98)	Ruptured (n = 70)	
Mann Whitney U			
Height (H)	4.39	5.78	0.002**
Neck Width (N)	4.13	4.34	NS
Diameter (D)	4.91	6.13	0.017*
Distance to Max. Diameter (h)	1.42	1.99	0.02*
Tilt Angle(θ_T)	24.57	33.85	0.009**
Aspect Ratio (AR)	1.09	1.34	0.001**
Chi-Square			
Location	-	-	0.001**
Shape	-	-	0.015*
Size	-	-	0.043*
Neck Size	-	-	NS

Using a bootstrapping method, a multivariate logistic regression analysis was performed. The final, parsimonious logistic regression model was statistically significant (χ^2 (8) = 39.970, p< 0.001), correctly classifying 71 % of cases. Four parameters were found to be independently statistically significant: tilt angle, aspect ratio, posterior location and bifurcating shape (see Table 6.3).

Table 6.3: Results from the multivariate logistic regression (SE = standard error, OR = odds ratio, CI = confidence interval, ROC-AUC = receiver operating characteristic-under the curve)

Parameter	B	SE	p Value	OR	95% CI	ROC-AUC
Tilt Angle (θ_T)	0.026	0.011	0.018	1.026	1.004-1.048	0.618
Aspect Ratio (AR)	1.781	0.717	0.013	5.939	1.458-24.189	0.647
Location	1.043	0.376	0.006	2.838	1.358-5.928	0.63
Shape	1.053	0.411	0.01	2.866	1.280-6.417	0.59

Using the final independently statistically significant parameters, a rupture probability equation was developed, with a probability >0.5 indicating rupture (see Equation 1).

$$\text{Probability of Rupture} = \frac{e^{0.026*\text{Tilt Angle}+1.781*\text{Aspect Ratio}+1.043*\text{Location}+1.053*\text{Shape}-4.117}}{1+e^{0.026*\text{Tilt Angle}+1.781*\text{Aspect Ratio}+1.043*\text{Location}+1.053*\text{Shape}-4.117}} \quad (6.1)$$

ROC analysis of the individual parameters and the final parsimonious model are shown in Figure 6.2, with the ROC-AUC for the significant parameters listed in Table 2. The highest AUC values were found for aspect ratio, tilt angle and location.

Sensitivity and specificity values for the final model were calculated as 71.4 and 72.4 respectively, with an AUC of 0.762, for a null predictor with an AUC of 0.5.

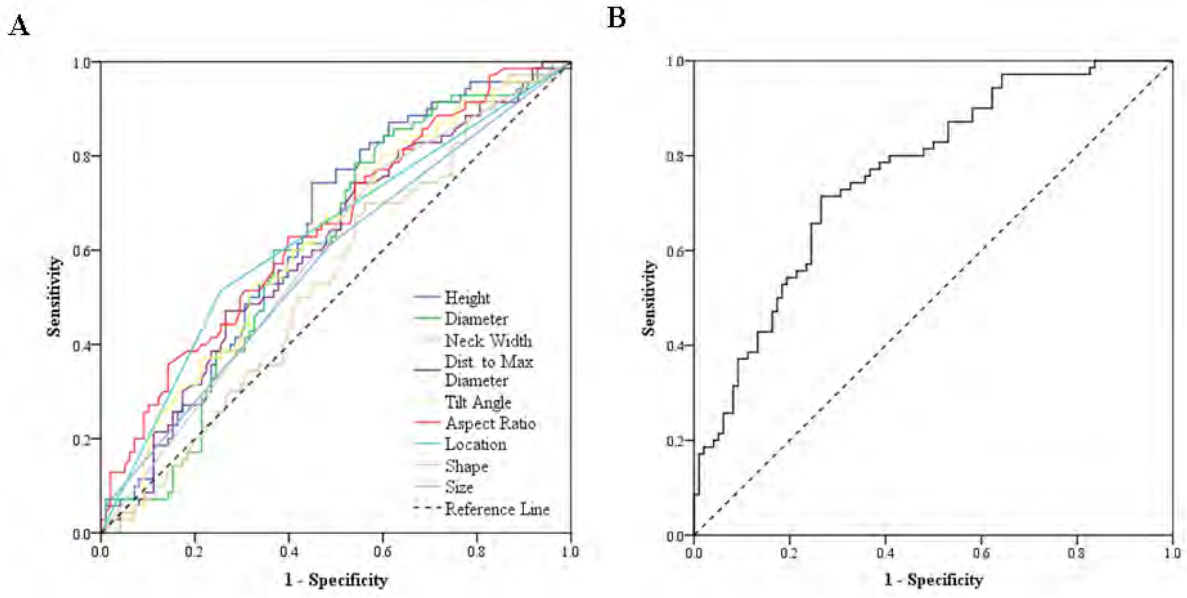

Figure 6.2: (A) ROC curve for all parameters (B) ROC curve for final regression model

6.4 Discussion

The management of patients with unruptured cerebral aneurysms is contentious due to the lack of a precise rupture prediction method. Identifying the main parameters that contribute to rupture may lead to improved management of unruptured cerebral aneurysms. The current study investigates the relationship between clinically measurable geometric and morphological parameters, and cerebral aneurysm rupture potential. The establishment of such a relationship would allow direct measurements taken by clinicians from 3D scans to be used as an indicator of aneurysm rupture potential, thus allowing improved decisions regarding surgical intervention. In this study, statistical analysis was performed on a cohort of 168 cerebral aneurysms in order to determine the relationship between ten clinically measurable parameters and aneurysm rupture. Following multivariate logistic regression, only tilt angle, aspect ratio, posterior location and bifurcating shape remained as independently statistically significant parameters. These parameters were used to develop a rupture probability equation that indicates that aneurysm rupture risk increases with increasing tilt angle, increasing aspect ratio, posterior location and bifurcating shape.

The definition of the measured parameters in this study, namely the height, neck width, diameter, distance from neck to diameter and tilt angle allows for more accurate measurements to be taken from 3D scans or geometries. One issue that has been raised with previous studies regarding aneurysm shape analyses refers to the use of 2D angiographic images which may not account for the asymmetric nature of aneurysms.[16] The three-dimensional nature of the geometries used in this study allows measurements to be obtained that may be difficult to measure using 2D images e.g. tilt angle.[21]

Results from the univariate statistical analysis indicate significant differences between the ruptured and unruptured groups for aneurysm height, distance to maximum diameter, tilt angle, aspect ratio, location and shape. However, univariate analysis fails to account for confounding variables that may falsely indicate a relationship with aneurysm rupture, and so a multivariate logistic regression analysis was performed to identify parameters that are independently statistically significant. In this study, the final, independently significant parameters used to develop the rupture probability model (Equation 1) were tilt angle, aspect ratio, location and shape.

It was determined in this study that increasing aspect ratio is significantly associated with higher odds of aneurysm rupture. The inclusion of aspect ratio in the final prediction model is unsurprising, as it has been consistently linked with aneurysm rupture throughout previous studies.[7,12,16,22] Although a definitive threshold value is yet to be established, aneurysms with larger aspect ratios have been found to be at risk of rupture, and should be considered for surgical intervention.

There is some disagreement in literature with regards to the most common location of aneurysm rupture, with studies disagreeing between the anterior and posterior circulation for greatest rupture potential.[8,10,15,23] Results from the current study population support the theory that posterior circulation aneurysms are more prone to rupture, with results suggesting that aneurysms of the posterior circulation are 2.8 times as likely to rupture as those of the anterior circulation. Furthermore, the majority of ruptured aneurysms in this study were found within the posterior circulation, at the posterior communicating artery and at the basilar tip.

In the current study, aneurysms that are bifurcating or terminal in shape were found to be 2.9 times more likely to rupture than lateral aneurysms. It is possible that this may be attributed to the differences in flow haemodynamics and wall shear stress levels

seen between bifurcating/terminal and lateral aneurysms.[17] Flow haemodynamics may also play a role in the relationship between aneurysm rupture and tilt angle. It has been suggested that an increase in aneurysm angle may be a result of daughter blebs on the aneurysm dome, or as a result of the growth of the aneurysm due to the inflow direction.[15] In the current study, aneurysm tilt angle was shown to be statistically significant in the logistic regression analysis, with results indicating that an increase in tilt angle increases the odds of aneurysm rupture.

Overall, results from the statistical analysis of aneurysm rupture suggest that the odds of an aneurysm rupturing increase with increasing tilt angle, with increasing aspect ratio, if it is of the posterior circulation and is bifurcating in shape.

Limitations

There are several limitations associated with this study. Firstly, the population size, while larger than some previous studies, is still relatively small. Therefore, a similar study on a much larger population is necessary to confirm the outcome. There were no aneurysms of the anterior communicating artery (ACoA) within the database, which may have affected the findings of the investigation into the relationship between aneurysm rupture and location within the vasculature. Several studies have shown that ACoA aneurysms have higher ratios of ruptured to unruptured aneurysms than other locations,[7,8,10] and so future study populations should include aneurysms of the ACoA so as to fully investigate the influence of location on aneurysm rupture potential. However, a recent study has suggested that small aneurysms of the ACoA behave similarly to posterior circulation aneurysms in terms of rupture odds, and so would be considered at higher risk of rupture.[24]

This study, like many rupture risk studies, was completed under the assumption that the rupture of an aneurysm does not affect the size and shape of the aneurysm, with many of the 3D images used to develop the geometries taken pre-rupture. If the aneurysm is altered due to the rupture event, analysis of measurements taken from a ruptured aneurysm may not accurately represent the size of the aneurysm pre-rupture. An investigation was carried out into changes in the aneurysm shape and size of four aneurysms before and after rupture, with all aneurysms increasing in size following rupture.[25] Furthermore, a similar study carried out by Schneiders *et al.* (2014) reported

that for a dataset of 9 aneurysms imaged before and after rupture, significant changes in volume and new lobulations were evident following rupture.[26] However, it is suggested that due to the time period between imaging before and after rupture, it is difficult to determine whether the changes in aneurysm size and shape occur before, during or after the rupture event.

6.5 Conclusions

In summary, this study classified and measured a database of 168 patient-specific cerebral aneurysm geometries based on radiologically measurable parameters. The relationship between these morphological and geometric parameters and cerebral aneurysm rupture was investigated using univariate and multivariate analysis. Following multivariate logistic regression analysis, a rupture probability equation was developed that indicates aneurysms in this study population have a higher probability of rupture if they have a large tilt angle, large aspect ratio, are found within the posterior circulation and are bifurcating in shape. Should these results be verified on a larger study population, improved, more immediate decisions regarding surgical intervention for unruptured aneurysms will be possible for clinicians based on direct measurements from 3D imaging techniques.

ACKNOWLEDGEMENTS The authors would like to thank Dr. Jean Saunders of the Statistical Consulting Unit/CSTAR at the University of Limerick for her advice regarding statistical analysis.

FUNDING This work was supported by the Irish Research Council "Embark Initiative" (Grant RS/2010/2942) and the Friends of A/ Adrienne Hussey Scholarship.

COMPETING INTERESTS None

CONTRIBUTORSHIP JAC and MTW were primarily responsible for study concept and design, data analysis and interpretation, writing the manuscript and are guarantors of the work. IL and DAR were involved in data collection, editing, critical revision and final approval of the manuscript.

DATA SHARING STATEMENT Geometric parameter measurements are freely available upon request.

REFERENCES

1. Schievink, WI. Intracranial Aneurysms. *N Engl J Med* 1997; 336(1): 28-40.
2. Villa-Uriol M, Berti G, Hose D R, *et al.* @neurIST complex information processing toolchain for the integrated management of cerebral aneurysms. *Interface Focus* 2011; 1(3): 308-319.
3. Mehan W A, Romero J M, Hirsch J A, *et al.* Unruptured intracranial aneurysms conservatively followed with serial CT angiography: could morphology and growth predict rupture? *J Neurointerv Surg* 2014; 6(10):761-766.
4. Xiang J, Yu J, Choi H, *et al.* Rupture Resemblance Score (RRS): toward risk stratification of unruptured intracranial aneurysms using hemodynamic-morphological discriminants. *J Neurointerv Surg* 2014.
5. Cebral JR, Mut F, Weir J, *et al.* Quantitative Characterization of the Hemodynamic Environment in Ruptured and Unruptured Brain Aneurysms. *AJNR Am J Neuroradiol* 2011; 32:145-151.
6. ISUIA Investigators. Unruptured Intracranial Aneurysms – Risk of Rupture and Risks of Surgical Intervention. *N Engl J Med* 1998; 339(24):1725-1733.
7. Lall R R, Eddleman C S, Bendok B R, Batjer H H. Unruptured Intracranial Aneurysms and the Assessment of Rupture Risk Based on Anatomical and Morphological Factors: Sifting Through the Sands of Data. *Neurosurg Focus* 2009; 26(5).
8. Beck J, Rohde S, Berkefeld J, *et al.* Size and Location of Ruptured and Unruptured Intracranial Aneurysms Measured by 3-Dimensional Rotational Angiography. *Surg Neurol* 2006; 65(1): 18-25.

9. Ohashi Y, Horikoshi T, Sugita M, *et al.* Size of cerebral aneurysms and related factors in patients with subarachnoid haemorrhage. *Surg Neurol* 2004; 61(3):239-245.
10. Orz Y, Kobayashi S, Osawa M, Tanaka Y. Aneurysm size: a prognostic factor for rupture. *Br J Neurosurg* 1997; 11(2):144-149.
11. Rinkel GJE, Djibuti M, Algra A, van Gijn J. Prevalence and Risk of Rupture of Intracranial Aneurysms: A Systematic Review. *Stroke* 1998; 29(1):251-256.
12. Ujiie H, Tamano Y, Sasaki K, Hori T. Is the Aspect Ratio a Reliable Index for Predicting the Rupture of a Saccular Aneurysm? *Neurosurgery* 2001; 48(3):495-503.
13. Baharoglu M I, Schirmer C M, Hoit D A, *et al.* Aneurysm Inflow-Angle as a Discriminant for Rupture in Sidewall Cerebral Aneurysms: morphometric and computational fluid dynamic analysis. *Stroke* 2010; 41:1423-1430.
14. Dhar S, Tremmel M, Mocco J, *et al.* Morphology parameters for intracranial aneurysm rupture risk assessment. *Neurosurgery* 2008; 63(2):185-197.
15. Hademenos G J, Massoud T F, Turjman F, Sayre J W. Anatomical and morphological factors correlating with rupture of intracranial aneurysms in patients referred for endovascular treatment. *Neuroradiology* 1998; 40:755-760.
16. Raghavan M L, Ma B, Harbaugh R E. Quantified Aneurysm Shape and Rupture Risk. *J Neurosurg* 2005; 102:355-362.
17. Liou T M, Liou S N. A Review on In-Vitro Studies of Hemodynamic Characteristics in Terminal and Lateral Aneurysm Models. *Proc Natl Sci Counc* 1999; 23(4):133-148.
18. Meyers P M, Schumacher H C, Higashida R T, *et al.* Reporting Standards for Endovascular Repair of Saccular Intracranial Cerebral Aneurysms. *Stroke* 2009; 40:366-379.
19. Parlea L, Fahrig R, Holdsworth DW and Lownie SP. An Analysis of the Geometry of Saccular Intracranial Aneurysms. *AJNR Am J Neuroradiol* 1999; 20: 1079 - 1089.
20. Ma B, Harbaugh R E and Raghavan M L. Three-dimensional geometrical characterization of cerebral aneurysms. *Ann Biomed Eng* 2004; 32(2)264-273.
21. Larrabide I, Villa-Uriol MC, Cárdenes R, *et al.* Three-dimensional morphological analysis of intracranial aneurysms: a fully automated method for aneurysm sac isolation and quantification. *Med Phys* 2011; 38(5):2439-2449.

22. Mut F, Löhner R, Chien A, *et al.* Computational Hemodynamics Framework for the Analysis of Cerebral Aneurysms. *Int J Numer Method Biomed Eng* 2011; 27:822-839.
23. Baumann F, Khan N, Yonekawa Y. Patient and aneurysm characteristics in multiple intracranial aneurysms in Changing aspects in Stroke Surgery: Aneurysms, Dissections, Moyamoya Angiopathy and EC-IC Bypass. Springer, Vienna: 19-28.
24. Bijlenga P, Ebeling C, Jaegersberg M, *et al.* Risk of Rupture of Small Anterior Communicating Artery Aneurysms is Similar to Posterior Circulation Aneurysms. *Stroke* 2013; 44(11): 3018-3026.
25. Chien A, Sayre J. Morphologic and Hemodynamic Risk Factors in Ruptured Aneurysms Imaged Before and After Rupture. *AJNR Am J Neuroradiol* 20142014; 35:2130-2135.
26. Schneiders J J, Marquering HA, van de n Berg R, *et al.* Rupture-Associated Changes of Cerebral Aneurysm Geometry: High-Resolution 3D Imaging Before and After Rupture. *AJNR Am J Neuroradiol* 2014; 35(7): 1358-1362.

CHAPTER 7

ON THE RELATIONSHIP BETWEEN MASS TRANSPORT OF BLOOD-BORNE SPECIES AND CERERBRAL ANEURYSM GROWTH AND RUPTURE

Chapter 7 On the Relationship between Mass Transport of Blood-Borne Species and Cerebral Aneurysm Growth and Rupture

7.1 Introduction

In the previous chapter, the relationship between key geometric parameters and cerebral aneurysm rupture was investigated, with results demonstrating that the risk of rupture increases for aneurysms of the posterior location, that are bifurcating in shape, with increasing tilt angle and with increasing aspect ratio. However, the hypothesis presented in this study is that the growth and rupture of an aneurysm may be linked to a combined relationship between geometric parameters and the species mass transport distribution seen within the aneurysm. Therefore, the next step is to undertake an investigation into the relationship between mass transport of blood-borne species and cerebral aneurysm growth and rupture.

With recent advances and improvements in medical imaging techniques, the use of patient-specific computational geometries has increased (Dillard *et al.* 2014). However, patient-specific models are computationally expensive, and require flow data that isn't typically taken during standard medical procedures. Therefore, in this study, the use of representative aneurysm models is proposed as an alternative to the complex patient-specific models. These models, which are developed based on patient-specific geometries (see Chapter 3), reduce the need for computationally intensive CFD simulations, and can be carried out using averaged flow data taken from literature. If representative models can be shown to accurately predict the mass transport within patient-specific geometries, and if a relationship can be defined between the geometry-defining parameters used in their development, mass transport and rupture, then the prediction of whether an aneurysm is at risk of rupture could be made based on mass transport simulations using representative geometries developed using radiologically measurable parameters, rather than complex patient-specific geometries. Therefore, the first study in this chapter investigates the efficacy of representative models in the prediction of mass transport of species seen within the aneurysm dome.

The following chapter is split into several sections. First, the concept of a concentration species threshold is introduced, and the hypothesis of the amount of the aneurysm dome exposed to low concentration being related to aneurysm rupture in discussed. Next, an investigation into the use of representative cerebral aneurysm geometries as an alternative to simplified idealised and complex patient-specific model is carried out. The mass transport within patient-specific lateral and bifurcation aneurysm geometries is computed, and the relationship between aneurysm growth and rupture potential and the mass transport distribution within the dome is statistically analysed. A separate study is also conducted to investigate the influence of different blood-borne species on mass transport results.

7.2 Species Threshold

In this study, species concentration threshold values are introduced that are used in the investigation into the relationship between the mass transport of species and aneurysm growth and rupture. The hypothesis motivating this study is that the transport of blood-borne species within a cerebral aneurysm may lead to an under- or over-expression of species at the aneurysm wall, resulting in negative wall remodelling, growth and eventual rupture of the aneurysm. There is limited existing literature regarding the mass transport of species within aneurysms, and so it is difficult to hypothesise as to the extent of species depletion or saturation that would cause negative wall remodelling, and at what level the aneurysm is at risk of growth and rupture.

Therefore, a species concentration threshold value is introduced which analyses the relationship between mass transport and rupture at different species concentration threshold values. Due to the lack of information regarding a threshold for species concentration at which negative wall remodelling can occur, several threshold values are included, allowing a sensitivity study to be carried out. The threshold values used in this study are based on the inlet species concentration values. Four threshold values are included, which are used to highlight the areas within the aneurysm where the concentration is found to be 1%, 5%, 10% and 20% less than the inlet concentration (C_{in}). Importantly, this allows for an investigation into correlation between the amount of the aneurysm surface found under the individual threshold value and rupture status to be performed on the patient-specific aneurysm models. Furthermore, using threshold values allows for direct comparison between the idealised, representative

and patient-specific models which will be carried out in the following section. An example of the species threshold value is illustrated in Figure 7.1, where the percentage of the aneurysm dome found below 1%, 5%, 10% and 20% of C_{in} is illustrated in red, while the amount of the dome surface found above this threshold is illustrated in blue.

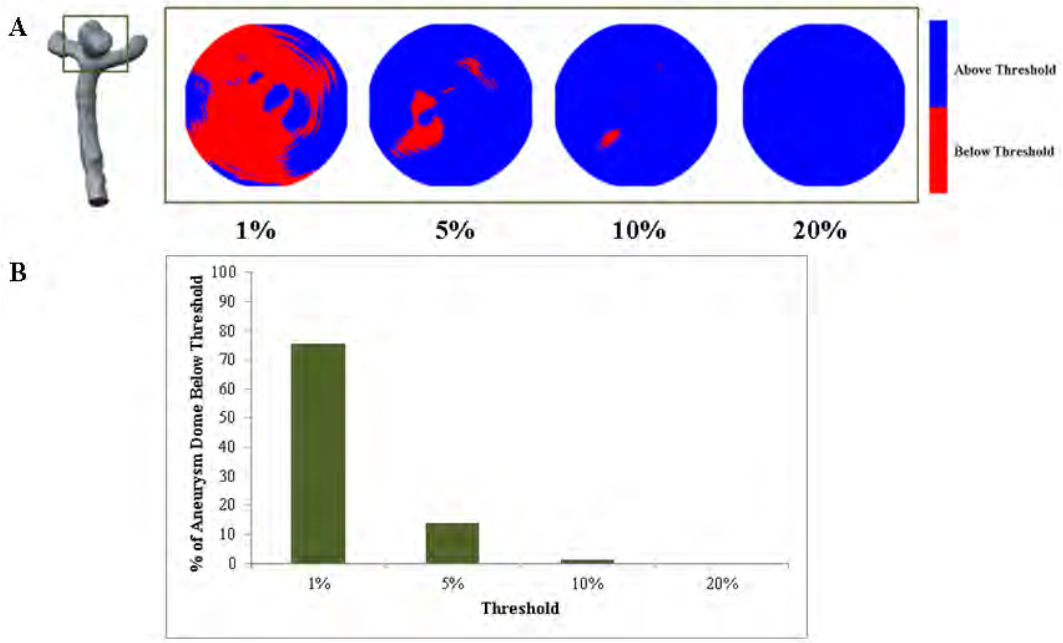

Figure 7.1: Illustration of (A) areas within the aneurysm dome with concentration below threshold values of 1%, 5%, 10% and 20% of C_{in} and (B) percentage of aneurysm dome found below different threshold values

7.3 On the Use of Representative Models as an Alternative to Idealised and Patient-Specific Models in Computational Modelling

One of the sub-objectives of this study is to determine if representative geometric models of cerebral aneurysms are a viable alternative to simple idealised and complex patient-specific geometries in the investigation of the relationship between mass transport of blood-borne species and cerebral aneurysm growth and rupture. The following section describes the steps taken in the investigation of this sub-objective, beginning with a description of the lateral and bifurcation aneurysm models selected and developed for the study. A description of the CFD analysis follows, before results are presented and discussed.

7.3.1 Model Selection

In order to determine the viability of representative models as an alternative to idealised or patient-specific geometries in the analysis of the mass transport of blood-borne species within cerebral aneurysms, representative models were developed using the methods described in Section 3.5.2. As previously mentioned, aneurysms most commonly occur along curved arteries and at arterial branch points and bifurcations, and so representative models of both lateral and bifurcation configurations were examined.

7.3.1.1 Lateral Aneurysm Model Selection

Three aneurysms of the ophthalmic segment of the ICA were selected to represent lateral aneurysms found within the CoW. The geometric measurements taken from these patient-specific models were used to develop representative models based on the methods described previously. The aneurysms selected represent a range of sizes, with a small, medium and large aneurysm chosen. Furthermore, both narrow and wide neck sizes are represented. The patient-specific models and their representative counterparts developed for this study, along with the idealised ophthalmic segment ICA model, are illustrated in Figure 7.2.

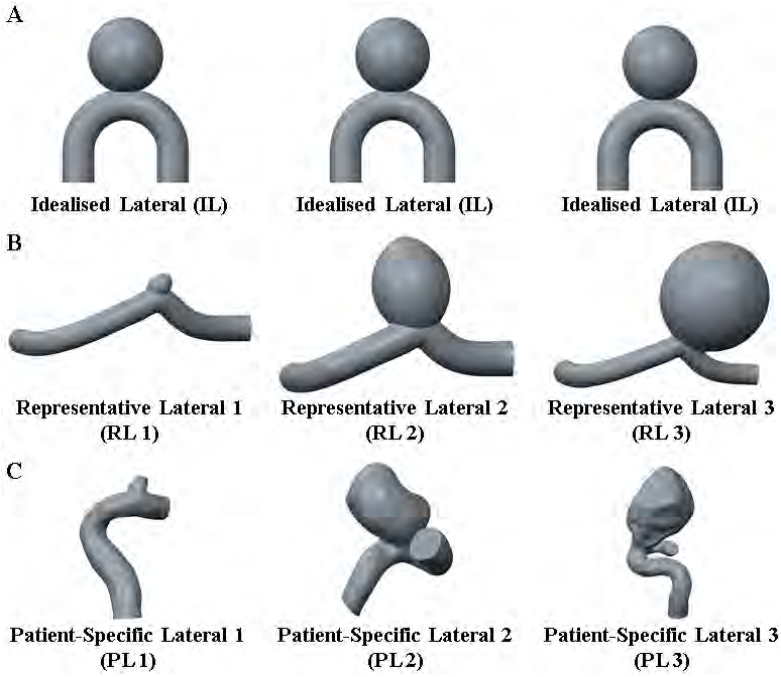

Figure 7.2: (A) Idealised lateral ophthalmic segment ICA geometric model, (B) representative lateral ophthalmic segment ICA geometric models and (C) corresponding patient-specific lateral ophthalmic ICA geometric models

The geometric models are named as follows: the idealised model is labelled as Idealised Lateral (IL), while the representative models are referred to as Representative Lateral 1 (RL 1), Representative Lateral 2 (RL 2) and Representative Lateral 3 (RL 3). Their patient-specific counterparts are referred to as Patient-Specific Lateral 1 (PL 1), Patient-Specific Lateral 2 (PL 2) and Patient-Specific Lateral 3 (PL 3). The geometric parameters taken from the patient-specific models and used to develop the representative models are listed in Table 7.1.

Table 7.1: Geometric parameter measurements used to develop representative lateral models. Measurements taken from three patient-specific aneurysms of the ophthalmic segment ICA. All measurements shown in mm, except Tilt Angle (º).

Parameter	PL 1	PL 2	PL 3
Height (H)	2.74	12.44	18.57
Neck Width (N)	2.98	6.71	5.70
Diameter (D)	3.00	11.38	17.07
Dist. To Max. Diameter (h)	0.88	4.54	5.70
Tilt Angle (θ_T)	46.82	20.53	41.28
Aspect Ratio (AR)	0.92	1.85	3.26

7.3.1.2 Bifurcation Aneurysm Model Selection

In a similar fashion to the lateral models described in the previous section, three bifurcation aneurysms of the sylvian bifurcation were selected in the investigation of the efficacy of representative models, so as to represent aneurysms that occur at different branching or bifurcation points within the CoW. The aneurysms selected represent a range of sizes, with two small and one medium aneurysm selected, including both narrow and wide necks. The idealised, representative and patient-specific sylvian bifurcation aneurysms developed for this study are illustrated in Figure 7.3.

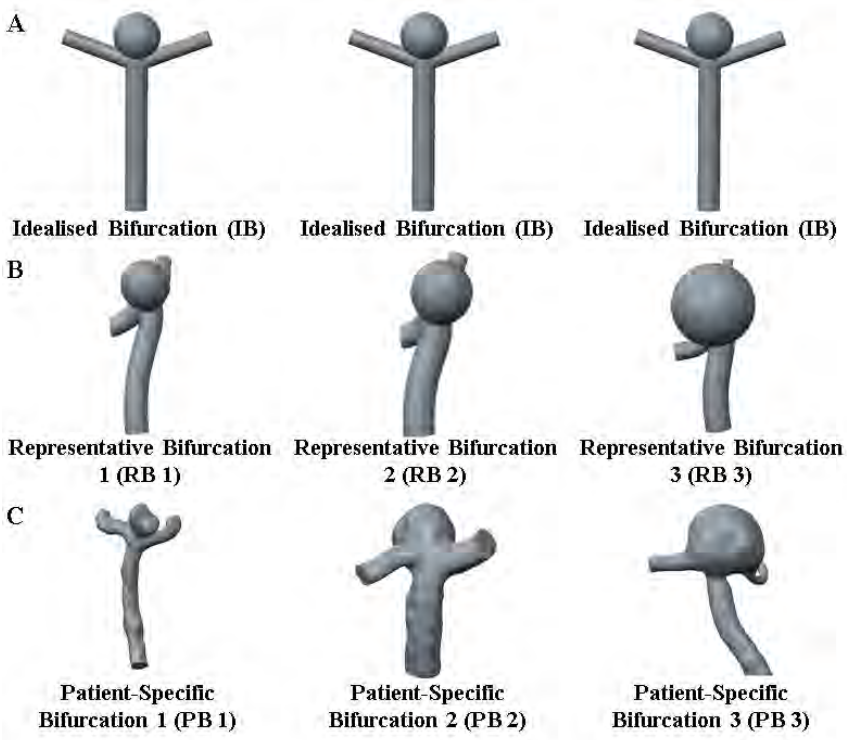

Figure 7.3: (A) Idealised sylvian bifurcation geometric model (B) representative sylvian bifurcation geometric models and (C) corresponding patient-specific sylvian bifurcation geometric models

As presented in Figure 7.3, the representative sylvian bifurcation model is referred to as Idealised Bifurcation (IB). The representative models are referred to as Representative Bifurcation 1 (RB 1), Representative Bifurcation 2 (RB 2) and Representative Bifurcation 3 (RB 3), with their patient-specific counterparts labelled as Patient-Specific Bifurcation 1 (PB 1), Patient-Specific Bifurcation 2 (PB 2) and Patient-Specific Bifurcation 3 (PB 3) respectively. The geometric parameters measured from PS 1-3 and used to develop RB 1-3 are listed in Table 7.2.

Table 7.2: Geometric parameter measurements used to develop representative bifurcation models. Measurements taken from three patient-specific aneurysms of the sylvian bifurcation. All measurements shown in mm, except Tilt Angle (º).

Parameter	PB 1	PB 2	PB 3
Height (H)	4.42	5.77	8.06
Neck Width (N)	3.23	4.75	8.96
Diameter (D)	4.31	6.30	10.57
Dist. To Max. Diameter (h)	2.52	2.34	2.06
Tilt Angle (θ_T)	36.07	18.72	23.64
Aspect Ratio (AR)	1.37	1.21	0.90

7.3.2 Results

The computational mass transport investigation into the use of representative geometries was carried out under the assumptions outlined in Section 4.4 and using Comsol Multiphysics 4.4. Steady flow analyses were carried out in which blood was treated as a Newtonian fluid with a density of 1050 kg/m^3 and a constant viscosity of 3.5 mPa·s. As outlined in Section 4.5, boundary conditions for the fluid flow analysis were applied as follows: at each artery inlet, a flow rate of 260 ml/min and 138 ml/min were applied for the lateral and bifurcation aneurysms respectively, representing the average flow rates that are found at the ophthalmic segment of the ICA and the sylvian bifurcation (Alastruey *et al.* 2007, Alnaes *et al.* 2007, Cebral *et al.* 2008, Cieslicki and Ciesla 2005, Fahrig *et al.* 1999, Ford *et al.* 2005, Moore *et al.* 2006). A zero pressure condition was applied at the outlets, and a no-slip condition was applied at the walls. For the mass transport analysis, an inlet concentration of 0.0001 mol/m^3 was used to represent the average concentration of ATP in blood, the species diffusivity was defined as 2.4x 10^{-10} m^2/s, and a flux was applied to the wall with a mass transfer coefficient of 1.68x10^{-6} m/s (Imai *et al.* 2010). Results from the investigation into the efficacy of representative aneurysm geometries as an alternative to idealised and patient-specific geometries in the CFD analysis of mass transport of blood-borne species are presented in the following section.

7.3.2.1 Lateral Aneurysms

Results from the laminar flow and mass transport simulations within the idealised, representative and patient-specific lateral aneurysms presented in Section 7.3.1 are illustrated. Results are presented using the methods outlined in Section 4.2, with unwrapped 2D disc plots highlighting normalised WSS and concentration values found within each aneurysm dome. The results are divided into the following sections for clarity: WSS, concentration and species concentration threshold.

Wall Shear Stress

In order to compare the flow haemodynamics found within the aneurysm dome between the different aneurysm geometry models, Figure 7.4 illustrates the 2D

unwrapped normalised WSS plots of the idealised, representative and patient-specific aneurysm geometries for all three lateral aneurysms investigated, which are labelled A-C. Results are normalised to the average parent artery WSS for each individual geometry. Lowest WSS levels are seen within the simple idealised aneurysm models, with the highest values seen within the smallest patient-specific aneurysm, PL1. For all geometries, an area of increased WSS is evident which corresponds with the location of the inflow jet entering the aneurysm dome at the distal neck.

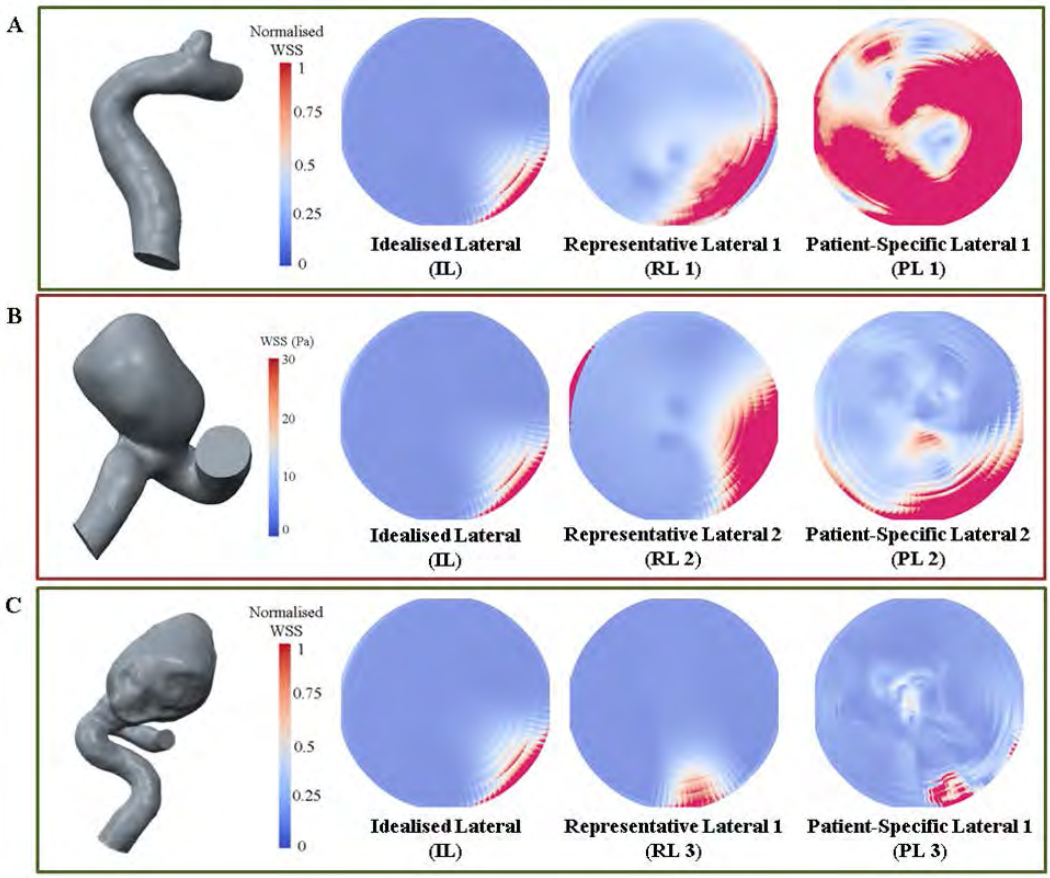

Figure 7.4: Illustration of 2D unwrapped WSS plots (normalised to average parent artery WSS) for lateral aneurysm geometries A-C, highlighting results from idealised, representative and patient-specific models

Substantial differences are evident between the unwrapped WSS plots for the different geometries, with the idealised and representative geometries tending to underestimate the WSS found within the dome of their patient-specific counterparts. This is especially evident in the case of PL1, where the patient-specific aneurysm dome sees markedly increased WSS values in comparison to the idealised and representative geometries. The differences between the idealised and representative versions of PL2 and PL3 are not of the same magnitude, although some areas of increased WSS are

seen within the patient-specific geometries that are not found in the corresponding idealised and representative geometries. These areas of increased WSS correspond to undulations and a neurysmal blebs that are not captured by the more simplified geometries.

The differences in WSS distribution between the idealised, representative and patient-specific geometries are further evidenced in the quantitative comparison of the average WSS found within each aneurysm dome, illustrated in Figure 7.5. For each of the lateral aneurysms investigated, the average WSS is considerably underestimated by the idealised and representative geometries. In the case of PL 1, the average WSS found within the dome of the patient-specific model is 8.7 Pa, while the idealised and representative average WSS are much lower, calculated as 0.2 and 3 Pa respectively. Similarly, the average WSS in the idealised and representative versions of PL 2 (0.2 and 0.6 Pa respectively) are lower than the patient-specific model at 1.8 Pa. A similar trend is seen in the third aneurysm, where the idealised geometry illustrates the lowest average WSS within the dome at 0.2 Pa, the representative geometry is higher at 0.3 Pa but the patient-specific model has the highest WSS at 1.4 Pa.

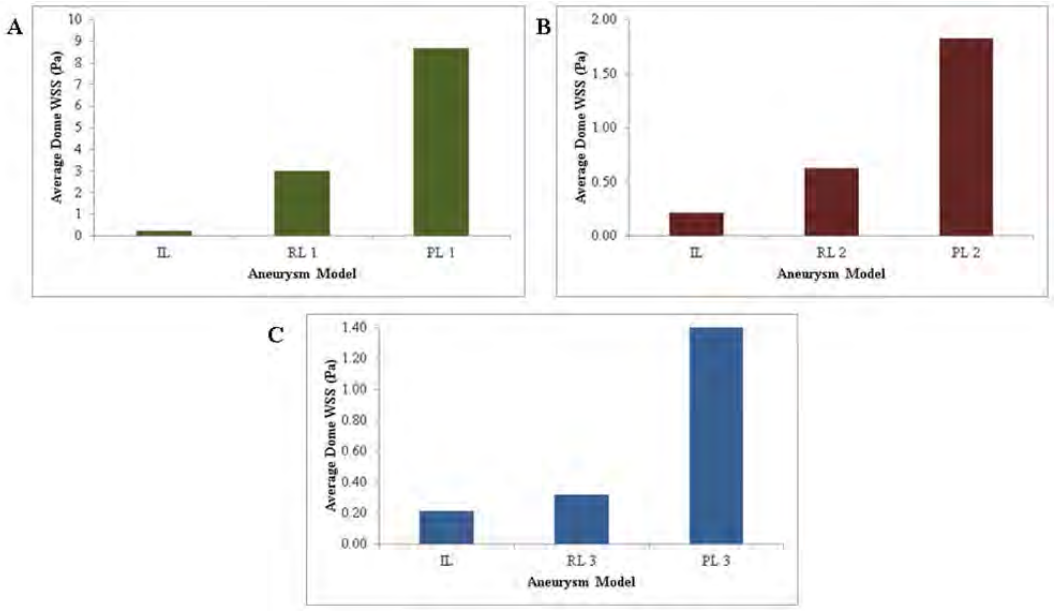

Figure 7.5: Average dome WSS found within idealised, representative and patient-specific aneurysm models of lateral aneurysm geometries A-C

It is evident that the representative geometries replicate the WSS levels found within the patient-specific geometries with greater accuracy when compared to the more

simple idealised geometries. However, a difference of 65-78% is seen between the average WSS found within the representative and patient-specific models for all three aneurysms investigated, suggesting the WSS seen within the dome of the patient-specific aneurysms is not accurately captured by the representative geometries.

Concentration

The 2D unwrapped concentration plots for each lateral aneurysm geometry, highlighting the normalised concentration (C/C_{in}) for the idealised, representative and patient-specific models of the three lateral aneurysms is illustrated in Figure 7.6.

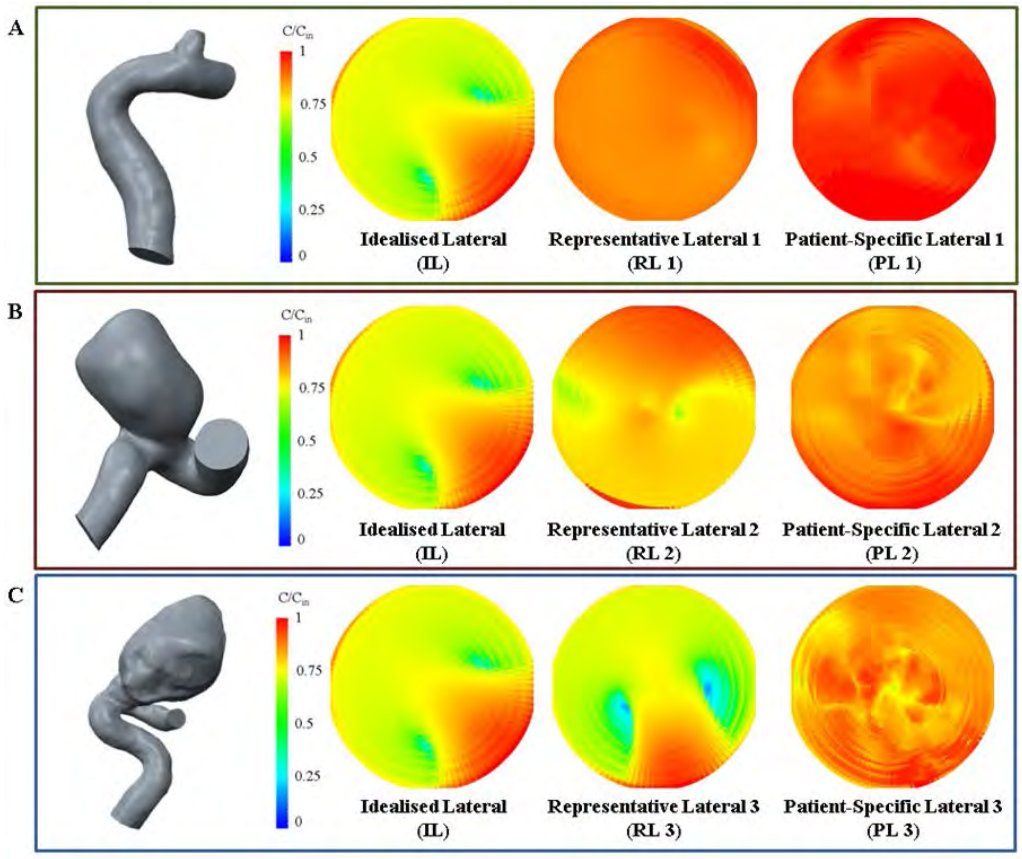

Figure 7.6: Illustration of 2D unwrapped concentration plots (normalised to inlet concentration) for lateral aneurysm geometries A-C, highlighting results from idealised, representative and patient-specific models

Similar to the WSS results presented in the previous section, the idealised and representative geometries tend to underestimate the patient-specific results, with lower concentration values found within the aneurysm dome for the idealised and representative versions of the patient-specific geometries. However, the representative

geometries capture a more realistic concentration distribution than the idealised geometries. Furthermore, although the representative geometries display lower concentration values than their patient-specific counterparts, similar patterns are found with the aneurysm dome e.g. RL1 and PL1 both display close to a uniform concentration distribution throughout the aneurysm dome, while the remaining geometries show more uneven patterns, with areas of low concentration found at areas corresponding to undulations throughout the dome. The patterns of concentration distribution for RL2 and RL3 do not directly mimic the patterns seen in PL2 and PL3, but demonstrate a better representation of the patient-specific results than the idealised geometries. It is also interesting to note that the areas of increased concentration seen within the unwrapped plots correspond with areas of increased WSS seen in Figure 7.4, which is particularly noticeable at the aneurysm neck, as the inflow jet enters the aneurysm dome, and at the areas of undulations within the aneurysm dome.

Species Concentration Threshold

Results highlighting the percentage of the aneurysm dome that is found to have a normalised concentration less than the specified species concentration threshold value for the idealised, representative and patient specific geometries for each lateral aneurysm investigated are illustrated in Figure 7.7, Figure 7.8 and Figure 7.9. Threshold values of 1%, 5%, 10% and 20% are used, as discussed in Section 7.2.

Looking to the first lateral aneurysm geometry shown in Figure 7.7, the idealised and representative versions do not accurately capture the amount of the aneurysm surface with concentration levels under a threshold of 1% of C_{in}, with the patient-specific geometry PL1 displaying a much lower percentage of the dome surface under the threshold value. For threshold values of 5%, 10% and 20% of $C_{in,}$ the patient-specific geometry has a higher concentration than the threshold values, which is mimicked by the representative model after a threshold of 20% is introduced. It is evident from the results for this first lateral aneurysm geometry that the representative model replicates the concentration distribution in the patient-specific model, although only when a threshold of 10% or higher in included.

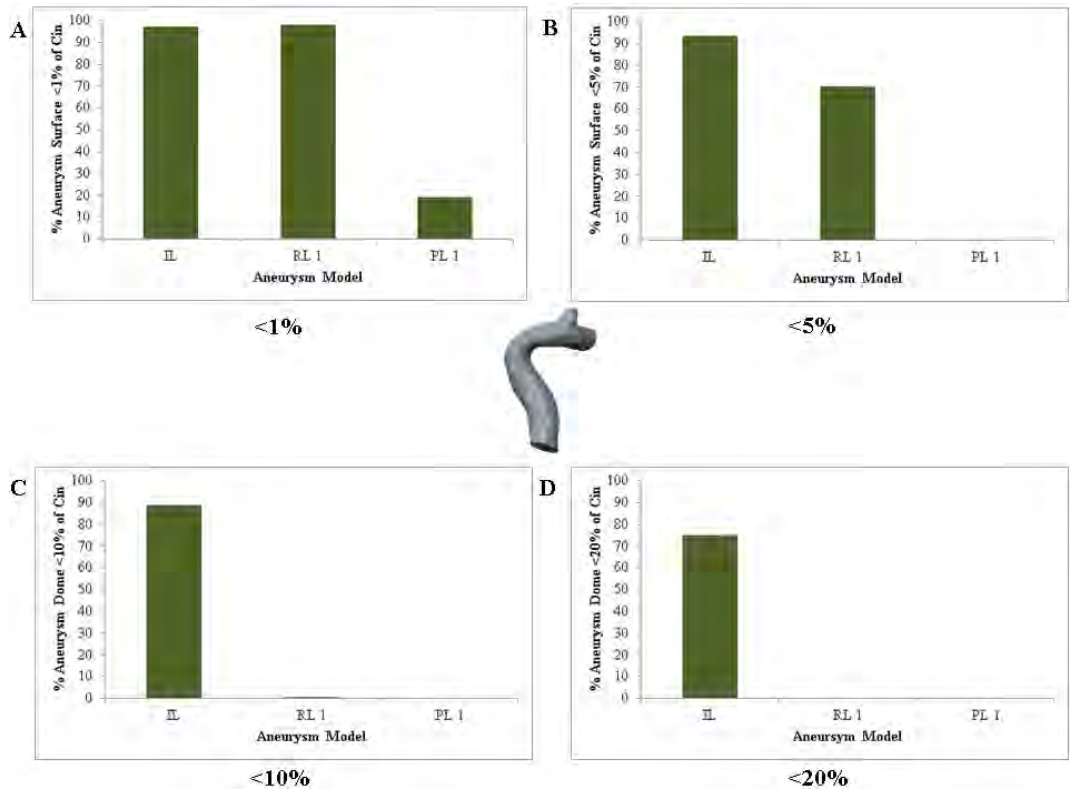

Figure 7.7: Comparison of percentage of aneurysm dome surface concentration found under threshold of (A) 1% (B) 5% (C) 10% and (D) 20% of inlet concentration for idealised, representative and patient-specific versions of aneurysm PL 1(centre)

Results for the representative geometries of the second lateral aneurysm are presented in Figure 7.8, and are more promising than the first aneurysm, with similar results seen for the representative and patient-specific geometries at threshold values of 1% and 5% of C_{in}. However, when a threshold of 10% is introduced, the percentage of the aneurysm dome found below 10% of C_{in} drops to approximately 35% for the patient-specific geometry while the amount of the representative geometry dome is over double that. Similarly, for a threshold of 20%, a much larger percentage of the representative geometry is found below the threshold value compared to the patient-specific version. It is worth noting that the representative geometry emulates the patient-specific results more accurately than the idealised geometry, in which the percentage of the dome found under the threshold concentration does not reduce significantly, despite the change in threshold value.

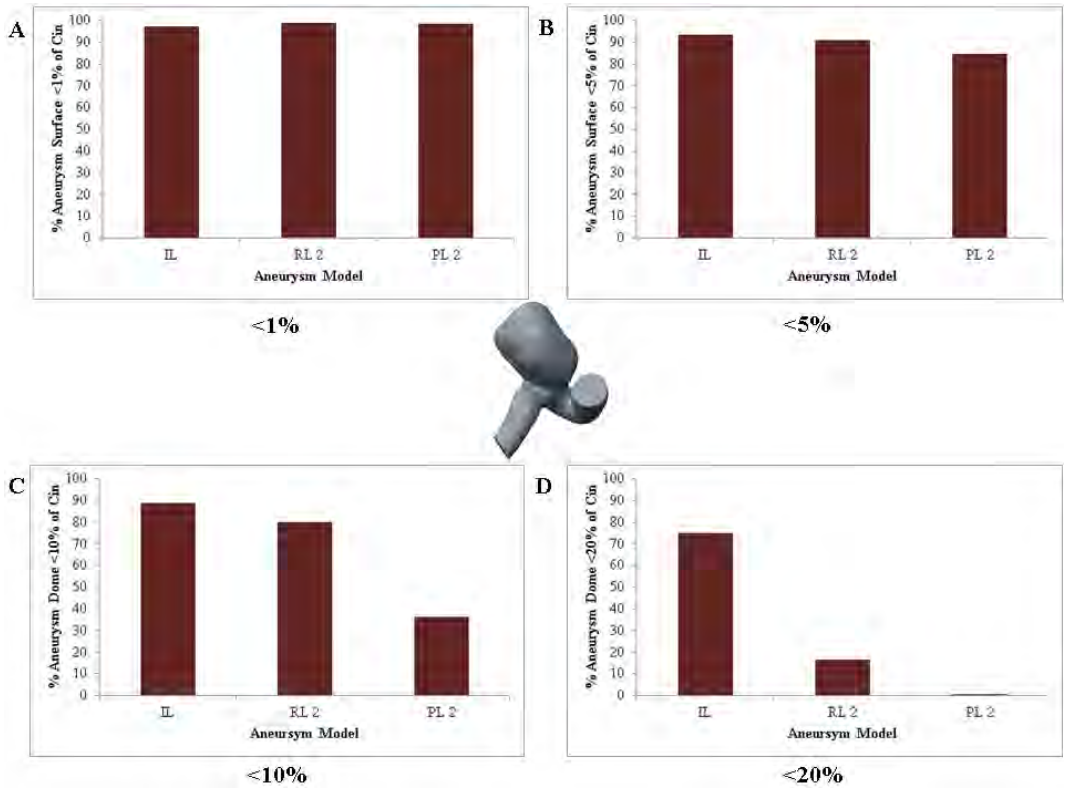

Figure 7.8: Comparison of percentage of aneurysm dome surface concentration found under threshold of (A) 1% (B) 5% (C) 10% and (D) 20% of inlet concentration for idealised, representative and patient-specific versions of aneurysm PL 2(centre)

The final lateral aneurysm investigated (see Figure 7.9) demonstrates that the representative geometry captures similar results to the patient-specific geometry at threshold levels of 1% and 5% of C_{in}. However, more substantial differences are seen between the representative and patient-specific geometries at threshold levels of 10% and 20%, where the amount of the surface found under the threshold reduces considerably for the patient-specific geometry, while the amount of the representative geometry dome surface does not reduce as much. On comparison of the idealised geometry with the representative and patient-specific results, it is evident that the representative geometry replicates the patient-specific concentration distribution with closer accuracy at species threshold values of 1% and 5% of C_{in}, but not at the higher threshold values of 10% and 20% of C_{in}.

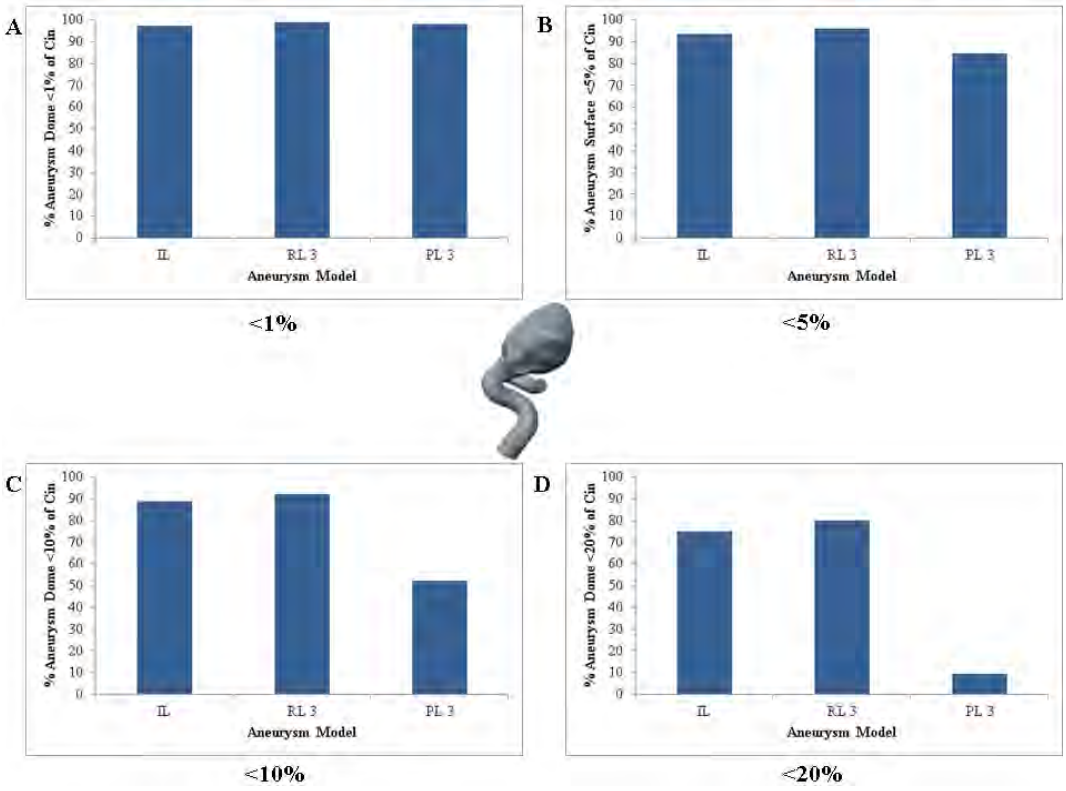

Figure 7.9: Comparison of percentage of aneurysm dome surface concentration found under threshold of (A) 1% (B) 5% (C) 10% and (D) 20% of inlet concentration for idealised, representative and patient-specific versions of aneurysm PL 3(centre)

7.3.2.2 Bifurcation Aneurysms

The following section presents results from the laminar flow and mass transport simulations within the idealised, representative and patient-specific bifurcation aneurysm geometries discussed in Section 7.3.1. Similar to the previous section, results are presented using the methods outlined in Section 4.2, with 2D unwrapped disc plots highlighting WSS and normalised concentration values found within each aneurysm dome. As with the lateral geometries, the results are divided into WSS, concentration and species threshold sections.

Wall Shear Stress

Figure 7.10 illustrates the 2D unwrapped WSS plots of the idealised, representative and patient-specific aneurysm geometries for the three bifurcation aneurysms investigated, which are labelled A-C. Within the unwrapped plots, areas shaded in grey (e.g. towards the periphery of the idealised model) represent locations within the

aneurysm dome where the outlets overlapped with the aneurysm and results were not calculated.

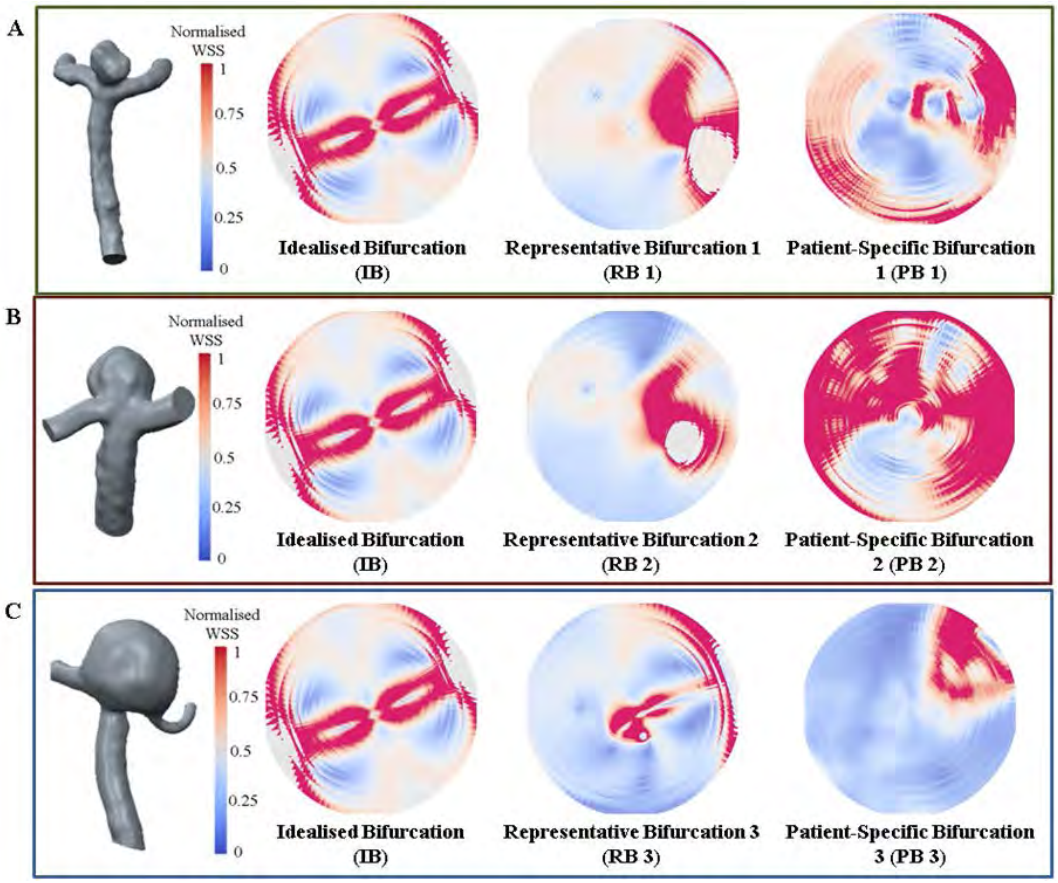

Figure 7.10: Illustration of 2D unwrapped WSS plots (normalised to average parent artery WSS) for bifurcation aneurysm geometries A-C, highlighting results from idealised, representative and patient-specific models

The 2D unwrapped WSS distribution plots of the representative geometries appear to replicate the patient-specific results reasonably well, as the WSS distribution within the representative geometries shows more similar results than the idealised models. Although the patterns of WSS distribution within the representative plots differ from their patient-specific versions, similar trends are seen within the unwrapped plots, with higher WSS levels found towards the neck and outlets. It is noteworthy that unlike the other bifurcation geometries, an increase in WSS is found with RB3 which isn't seen within PB3 and corresponds to the neck and the location of one of the outlets. Furthermore, within the patient-specific geometries, areas of increased WSS are also found as a result of undulations and aneurysmal blebs found throughout the dome, which are not captured by the idealised and representative geometries, and so are not replicated in their results.

Further investigation of the ability of the representative models to replicate the WSS results found within the patient-specific geometries is achieved through the comparison of the average WSS found within the dome of the idealised, representative and patient-specific geometries, which is presented in Figure 7.11. It is evident from the comparison that there are substantial differences between the average WSS found in the representative and patient-specific geometries, with the representative geometries failing to accurately replicate the WSS levels seen within the dome. The percentage difference between the average WSS for the representative and patient-specific geometries for the bifurcation aneurysms PB 1, PB 2 and PB 3 are calculated as 13%, 35% and 30% respectively. Furthermore, for the geometries PB2 and PB3, the idealised geometries replicate the results seen in the patient-specific geometries with greater accuracy than the representative versions.

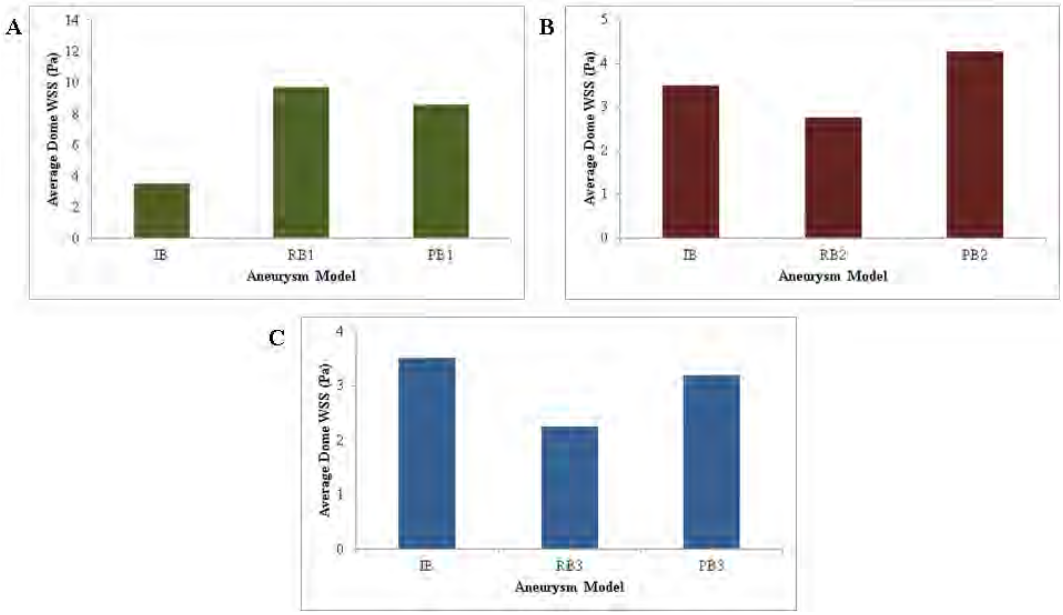

Figure 7.11: Average dome WSS found within idealised, representative and patient-specific aneurysm models of bifurcation aneurysm geometries A-C

Concentration

An illustration of the 2D unwrapped normalised concentration plots for each bifurcation aneurysm (labelled A-C) is presented in Figure 7.12. Again, grey areas within the unwrapped plots indicate areas where the outlet(s) overlapped with the dome and results were not calculated.

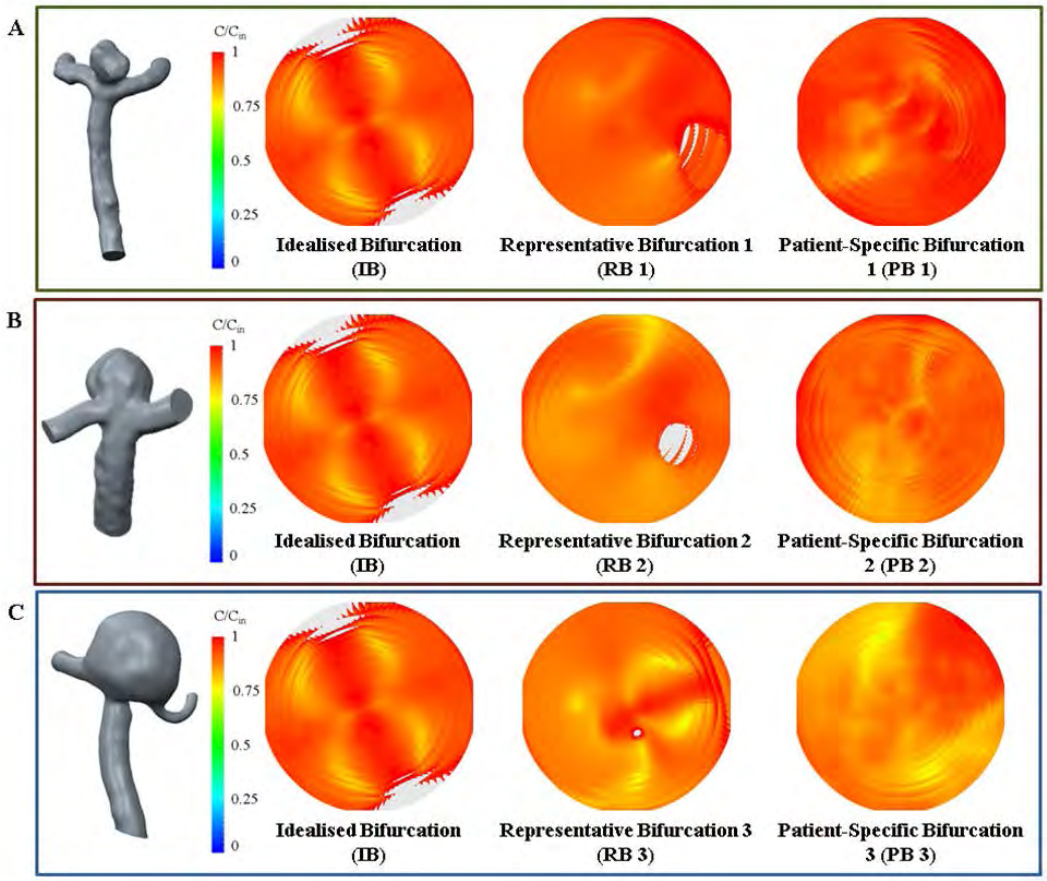

Figure 7.12: Illustration of 2D unwrapped concentration plots (normalised to inlet concentration) for bifurcation aneurysm geometries A-C, highlighting results from idealised, representative and patient-specific models

The unwrapped idealised and representative concentration plots demonstrate similar trends to their patient-specific counterparts, although the patterns within the dome are not replicated exactly. The representative geometries appear to capture the concentration distribution within the patient-specific geometries more realistically than the idealised, with the idealised plots demonstrating higher normalised concentration values throughout the aneurysm dome than the corresponding representative and patient-specific versions.

Species Concentration Threshold

Using threshold values of 1%, 5%, 10% and 20% of C_{in}, the percentage of the aneurysm dome surface that is exposed to concentration levels lower than the threshold values are quantified in Figure 7.13, Figure 7.14 and Figure 7.15 for the three bifurcation aneurysms investigated.

For the first aneurysm, illustrated in Figure 7.13, strong agreement is seen on comparison of the results for each geometry at the lower threshold values of 1% and 5% of C_{in}. However, as the threshold value increases to 10% of the inlet concentration, the difference between the results increases, with the representative geometry displaying better correlation to the patient-specific geometry than the simple idealised geometry. However, at a threshold level of 20% of C_{in}, all three geometries have concentrations throughout the dome that are greater than the threshold value, and so the results correspond between the idealised, representative and patient-specific geometries.

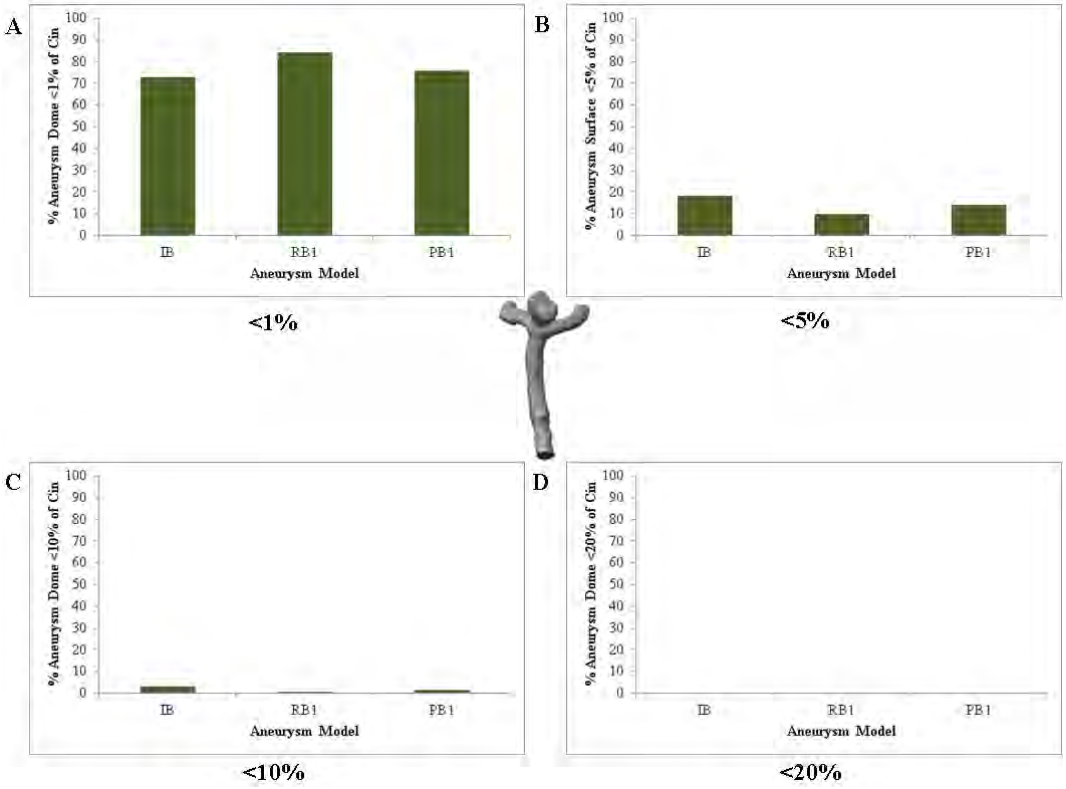

Figure 7.13: Comparison of percentage of aneurysm dome surface concentration found under threshold of (A) 1% (B) 5% (C) 10% and (D) 20% of inlet concentration for idealised, representative and patient-specific versions of aneurysm PB 1 (centre)

For the second aneurysm geometry, shown in Figure 7.14, the representative geometry replicates the patient-specific results with excellent accuracy at a threshold level of 1% of the inlet concentration. However, as the threshold level is increased to 5% and 10% of C_{in}, the ability of the representative geometry to replicate the results seen within the patient-specific geometry decreases. Similar to results for the first bifurcation aneurysm, the concentration within the aneurysm dome for the idealised, representative and patient-specific geometries at a concentration threshold level of

20% of C_{in} is greater than the threshold level, and so the results are the same for all three geometries.

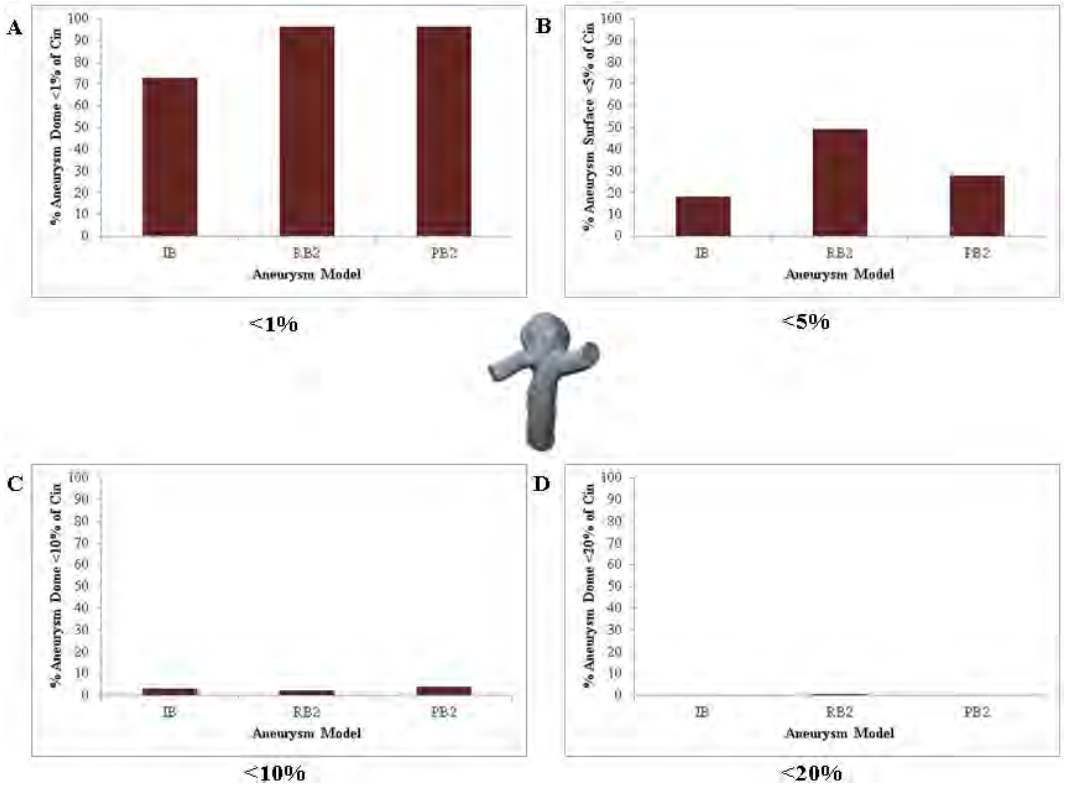

Figure 7.14: Comparison of percentage of aneurysm dome surface concentration found under threshold of (A) 1% (B) 5% (C) 10% and (D) 20% of inlet concentration for idealised, representative and patient-specific versions of aneurysm PB 2 (centre)

For the final bifurcation aneurysm investigated, which is illustrated in Figure 7.15, the representative geometry is again seen to replicate the percentage of the aneurysm surface found to have a concentration under the threshold value within the patient-specific geometry reasonably well, and at a better estimation than the idealised version for all threshold levels. However, the same level of accuracy is not seen as within the previous two aneurysms investigated. Interestingly, unlike the previous bifurcation aneurysms, at a threshold of 20% of C_{in} only the idealised aneurysm dome has a concentration above the threshold value, with the representative and patient-specific geometries demonstrating a low percentage of the aneurysm dome with concentration values lower than the threshold value.

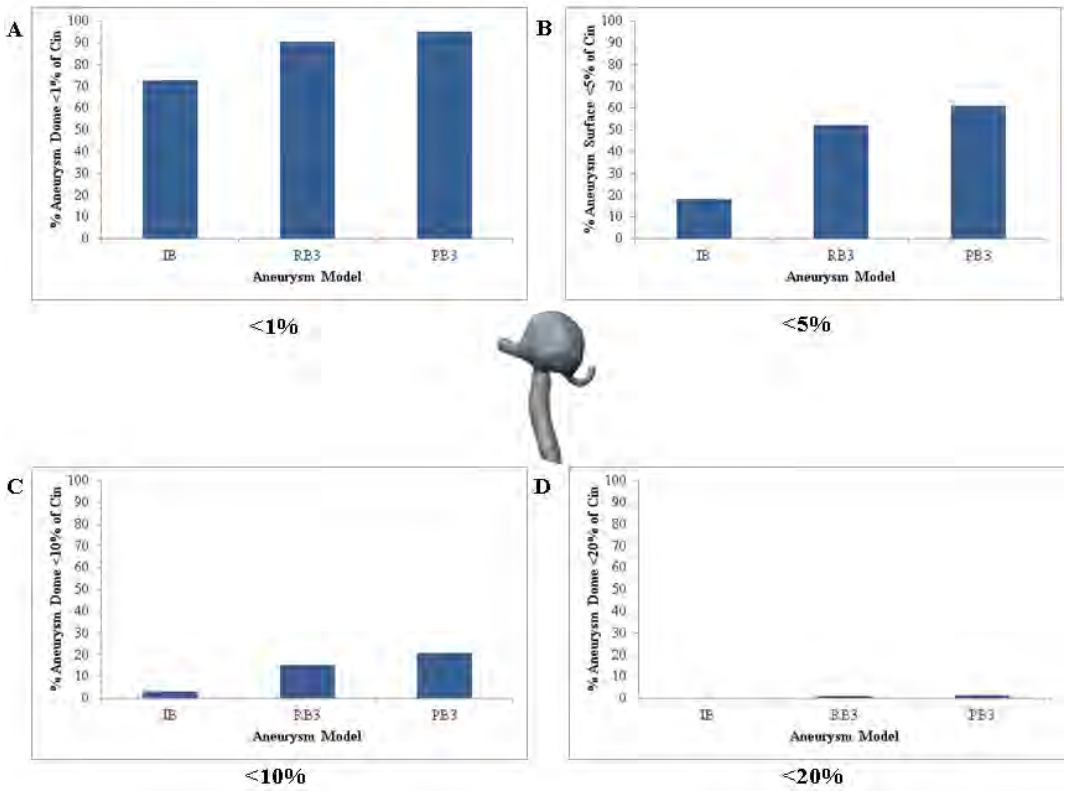

Figure 7.15: Comparison of percentage of aneurysm dome surface concentration found under threshold of (A) 1% (B) 5% (C) 10% and (D) 20% of inlet concentration for idealised, representative and patient-specific versions of aneurysm PB 3 (centre)

7.3.2.3 Computational Time

Due to the complex nature of the geometries in this study and the resulting meshes generated, the central processing unit (CPU) time needed to solve for the mass transport within patient-specific geometries is lengthy. Therefore, one of the main aims of the representative geometries is to reduce the CPU time needed for computational analysis of mass transport. On comparison of the computational time needed to solve for mass transport within both the representative and patient-specific geometries, it was found that the representative geometries took up to 66% less time than the patient-specific geometries to solve within Comsol Multiphysics. Therefore, representative geometries are advantageous over patient-specific geometries in terms of CPU solving time.

7.3.3 Discussion

The main objective of this study is to determine if a link exists between geometric features and the mass transport of blood-borne species, and to investigate their combined relationship with cerebral aneurysm growth and rupture potential. One sub-objective is to determine if representative models, which are developed based on key geometry-defining features from patient-specific geometries, can accurately predict the mass transport within patient-specific geometries. This analysis is based on the health of the aneurysm wall tissue, investigating if the representative models can adequately predict the amount of the aneurysm dome that is exposed to concentrations below the different threshold levels. If representative models can adequately replicate patient-specific mass transport results, then the need for computationally intensive patient-specific CFD simulations would be negated, and further steps could be taken towards the development of a prognostic tool that could aid surgeons in pre-operative cerebral aneurysm rupture prediction.

In order to investigate this sub-objective, two idealised and six representative cerebral aneurysm geometries were developed from two locations within the CoW – the ophthalmic segment of the ICA, in order to represent typical lateral aneurysms, and the sylvian bifurcation, serving to represent typical bifurcation aneurysms. The idealised geometries were developed based on average values taken from literature, while the representative geometries were constructed based on key geometric measurements from patient-specific aneurysms that describe the aneurysm dome (height, neck width, diameter, distance to maximum diameter and tilt angle), and using location-specific average parent and daughter artery measurements. One limitation of the representative model development is seen in the representative bifurcation models, in which the outlets overlap with the aneurysm dome. This is due to the averaging of the parent and daughter artery centrelines (see Section 3.5.2) with more extreme bifurcation geometries skewing the results, resulting in the unusual shaped representative bifurcation parent artery geometry. Therefore, during the post-processing of the WSS and concentration results, the aneurysm dome had patches where results were not calculated at the overlap between the outlet(s) and the dome.

It is clear from the comparison of the 2D unwrapped WSS plots of the idealised, representative and patient-specific geometries that the representative geometries cannot accurately replicate the WSS distribution seen within the patient-specific

aneurysm for both the lateral and bifurcation aneurysms examined. Although similar trends are seen between the different plots, the representative geometries consistently underestimate the WSS levels. This is further evidenced by the comparison of the average WSS values within each aneurysm dome. This is also the case for the unwrapped normalised concentration plots, where similar trends are seen in both the representative and patient-specific geometries for all lateral and bifurcation aneurysms investigated, but the representative geometries once again underestimate the concentration values seen throughout the aneurysm dome.

Upon comparison of the representative and patient-specific models under different concentration threshold values, it is evident that excluding PL1, the representative geometries of both the lateral and bifurcation aneurysms can predict the percentage of the aneurysm dome with concentration levels under the threshold of 1% of C_{in} with excellent accuracy, with results from the representative geometries falling within 10% of the patient-specific results. This accuracy is maintained at a threshold value of 5% of C_{in} for the representative versions of PL2 and PL3, but a larger percentage difference is found for the bifurcation aneurysms PB1, PB2 and PB3. However, reasonable accuracy is still seen for the representative versions of the bifurcation aneurysms at this concentration threshold value. Increasing the threshold to 10% sees excellent agreement between representative and patient-specific results for PL1, but moderate agreement only between the remaining geometries. Finally, at a threshold of 20%, mixed agreement is seen between representative and patient-specific results, with the representative bifurcation aneurysms replicating the patient-specific geometries more closely than the lateral aneurysms.

In summary, in the analysis of the efficacy of representative models developed based on patient-specific geometries in the prediction of mass transport within patient-specific models, it is clear that the representative models cannot accurately replicate the WSS and concentration distributions seen within the patient-specific geometries. However, it is also evident from this investigation that the representative models developed in this study provide improved information regarding the mass transport of blood-borne species within cerebral aneurysms when compared to simplified idealised models, but representative models cannot fully replicate mass transport within patient-specific models. Importantly, upon application of a concentration threshold value, below which the aneurysm may be at risk of negative wall remodelling, growth and eventual rupture, greater accuracy is seen in the representative models ability to

predict the mass transport of blood-borne species. For five of the six aneurysm geometries investigated, a threshold value of 1% yields excellent agreement between representative and patient-specific results. Mixed agreement between results is evident at higher threshold values, with lateral models replicating the patient-specific results with better accuracy at lower threshold values of 1% and 5%, while the bifurcation models tended to be more precise at higher threshold values of 10% and 20%.

Currently, it is difficult to speculate on the effect of reduced concentration within the aneurysm dome on aneurysm growth and rupture potential, and so the next step in this study will be to investigate if a relationship can be established between mass transport and rupture, in a cohort of patient-specific geometries. This will potentially establish a threshold of species concentration at which the aneurysm is in danger of negative wall remodelling and possible growth and rupture, and so would further elucidate the use of representative models as an alternative to complex patient-specific models in the computational analysis of mass transport of blood-borne species.

7.4 Mass Transport of Blood-Borne Species within Patient-Specific Cerebral Aneurysms

The following section describes the investigation into the relationship between the mass transport of blood-borne species and cerebral aneurysm growth and rupture potential. First, the influence of the use of different blood-borne species is analysed, before the twelve patient-specific geometries used in the computational analysis are described. Results of the mass transport simulations are presented and the statistical analysis of the relationship with rupture is described. Finally, the results and the implications for the prediction of aneurysm rupture are discussed.

7.4.1 Influence of Use of Different Blood-Borne Species

The influence of the inclusion of different blood-borne species on mass transport within the aneurysm dome was investigated. Until now, all simulations within this study have been carried out using the blood-borne species ATP and its associated inlet concentration, diffusivity and mass transport coefficient values. However, it is the aim of this study that the results would not be restricted to transport of ATP alone, and that

results could be extrapolated to other blood-borne species of low diffusivity. Therefore, in the following section, results from a comparison of the mass transport seen within both a patient-specific ophthalmic segment ICA and sylvian bifurcation aneurysm for the blood-borne species ATP and LDL are presented and discussed. Mass transport simulations were carried out under the assumptions, flow conditions and mass transport parameters as outlined in Chapter 4.

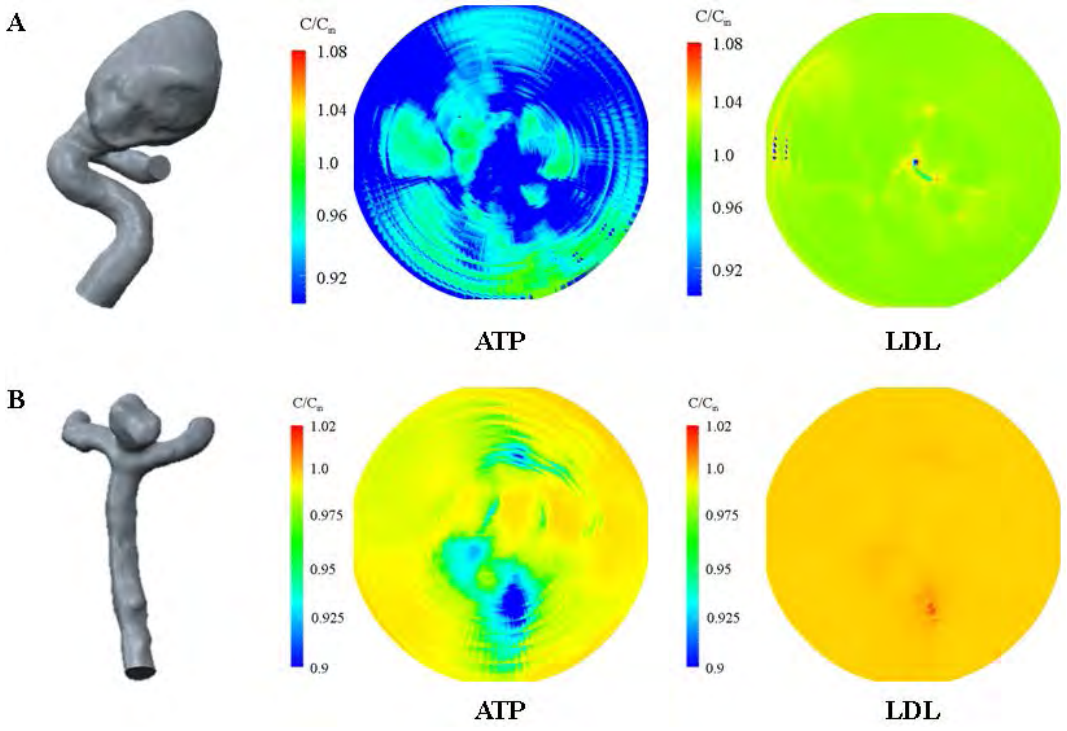

Figure 7.16: Unwrapped normalised concentration plots (C/C_{in}) comparing mass transport of ATP (centre) and LDLs (right) for (A) patient-specific ophthalmic segment ICA lateral aneurysm and (B) patient-specific sylvian bifurcation aneurysm

The unwrapped 2D concentration plots, normalised to the individual species inlet concentration, are illustrated in Figure 7.16. As can be seen from the results, the values seen in the normalised concentration plots differ extensively for ATP and LDL for both aneurysm geometries, with concentration values within the LDL plots found to be equal to or higher than the inlet concentration. This can be attributed to the differences in the transport models of ATP and LDL that were discussed in Chapter 4.5.2. ATP typically undergoes a reaction at the wall as it is hydrolysed to ADP, while LDL transport, which is regulated by the endothelium, involves permeation of the arterial wall, and is aided by the filtration velocity found at the arterial wall. As a result of the filtration velocity, concentration polarization of LDL can occur, leading to localised increased concentrations of LDL at the arterial wall that doesn't occur in the transport

of ATP. However, despite the differences in concentration values, the patterns of concentration distribution are similar for both plots, with areas of decreased concentration seen in the ATP plots corresponding with increased concentration within the LDL plots.

The overall hypothesis presented in this study is that an under-expression or lack of blood-borne species could lead to negative wall remodelling, growth and rupture of an aneurysm. However, research has shown that in the case of LDL, it is possible that an over-expression or saturation of LDL may be favourable in disease pathogenesis (Wada and Karino 2002). Thus, results from mass transport analyses involving ATP can be extrapolated to LDL, with areas of low ATP concentration corresponding to areas of increased LDL concentration. Therefore, it can be concluded that results from mass transport simulations of ATP within cerebral aneurysms are not restricted to ATP alone, and can be applied to other species of low diffusivity. Furthermore, if a relationship can be established between aneurysm rupture potential and a threshold of C_{in}, results from simulations of mass transport of ATP would apply to other species of similar low diffusivity values, although the threshold may need to be inverted to represent an over-expression of species rather than an under-expression. Following this comparative study, all further mass transport simulations will be carried out using ATP as the blood-borne species, with results applicable to other similar species.

7.4.2 Mass Transport Simulations

Twelve patient-specific aneurysm geometries in total were selected from the overall database (see Section 3.2) for the CFD investigation into the relationship between mass transport and aneurysm rupture potential. Mass transport simulations were carried out using the assumptions, flow conditions and mass transport parameters as discussed in Chapter 4. As described previously, it was the aim of the study to investigate both lateral and bifurcation aneurysms within the CoW, as aneurysms are typically found along curved arteries and at arterial branching points. Therefore, six lateral and six bifurcation geometries, which are illustrated in Figure 7.17, were investigated in the computational analysis. The preparation of the patient-specific geometries for CFD analysis is described in Section 3.5.3.

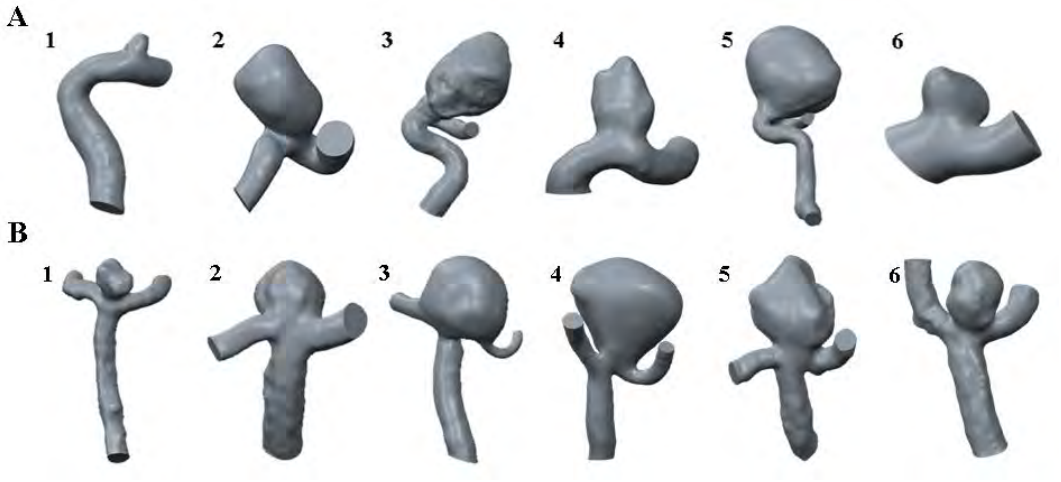

Figure 7.17: Patient-specific (A) ophthalmic segment ICA lateral and (B) sylvian bifurcation geometries used in computational analysis of mass transport of species within cerebral aneurysms

The twelve patient-specific aneurysms represent a range of aneurysm sizes and shapes, with small, medium and large aneurysms of both narrow and wide neck configurations present in the selection. Furthermore, the rupture status of the aneurysms varies, with seven unruptured and five ruptured aneurysms found between the two groups. The key geometry-defining measurements of each aneurysm dome are listed in Table 7.3.

Table 7.3: Geometric parameter measurements for patient-specific lateral and bifurcation aneurysm geometries 1-6. All measurements shown in mm, except Tilt Angle (º).

Parameter	Aneurysm Geometry					
	1	2	3	4	5	6
Ophthalmic Segment ICA						
Height	2.74	12.44	18.57	7.05	22.90	4.20
Neck Width	2.98	6.71	5.70	4.60	8.08	4.37
Diameter	3.00	11.38	17.07	5.82	25.01	5.60
Dist. To Max. Diameter	0.88	4.54	5.70	2.76	14.03	1.53
Tilt Angle	46.82	20.53	41.28	17.82	16.74	38.44
Aspect Ratio	0.92	1.85	3.26	1.53	2.84	0.96
Sylvian Bifurcation						
Height	4.42	5.77	8.06	8.71	8.94	4.76
Neck Width	3.23	4.75	8.96	3.47	4.67	3.60
Diameter	4.31	6.30	10.57	9.51	8.05	4.75
Dist. To Max. Diameter	2.52	2.34	2.06	4.24	3.74	2.08
Tilt Angle	36.07	18.72	23.64	25.55	26.19	0.94
Aspect Ratio	1.37	1.21	0.90	2.51	1.92	1.32

7.4.2.1 Results

In the following section, results for the patient-specific mass transport simulations are presented. Analysis of the flow patterns, haemodynamics and mass transport

distributions seen within each aneurysm geometry was carried out, and included flow characterisation outlined by Cebral *et al.* (2010), as described in Chapter 2, with flow categorised as simple or complex, and inflow jet described as diffuse or concentrated. Results include velocity streamlines and 2D unwrapped plots of the WSS and concentration distributions within the aneurysm dome.

Ophthalmic Segment ICA Results

The velocity streamlines seen within each patient-specific lateral aneurysm geometry are presented in Figure 7.18. It is evident from the results for the lateral aneurysm geometries that the flow within the dome differs depending on the shape of the aneurysm, and the curvature of the parent artery geometry.

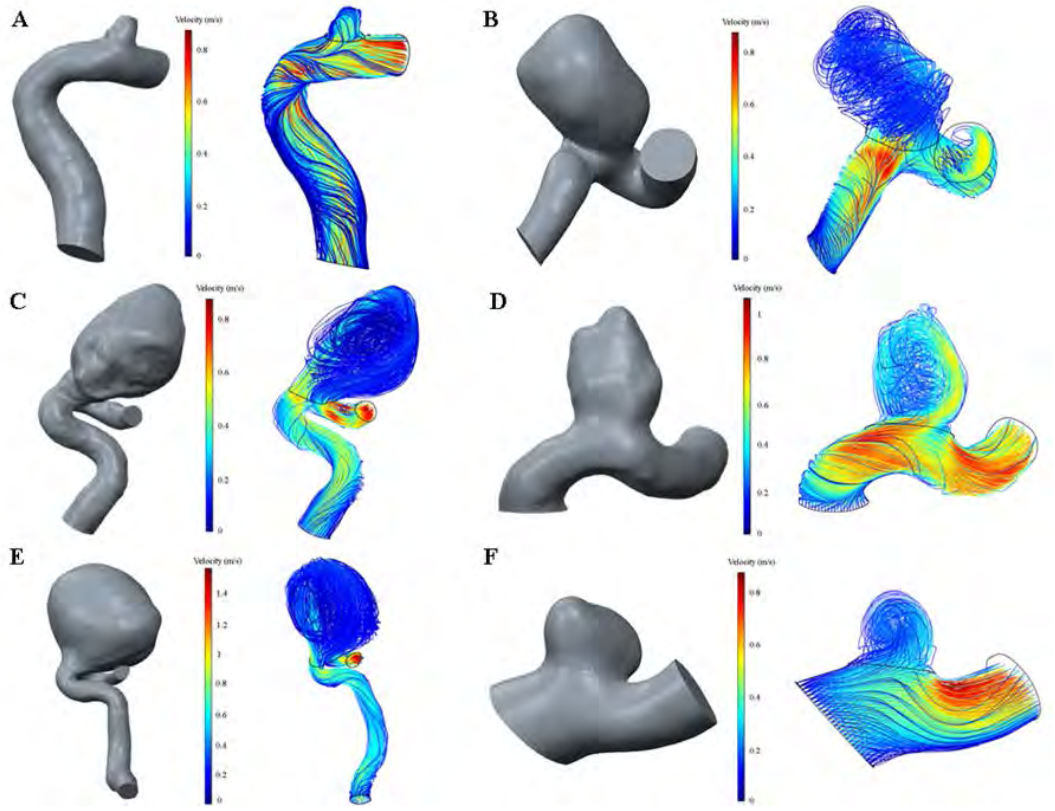

Figure 7.18: Velocity streamlines for patient-specific ophthalmic segment ICA aneurysm geometries 1-6 (labelled A-F)

Looking at aneurysm 1, which is labelled A in Figure 7.18, a concentrated inflow jet is seen to enter the aneurysm at the distal neck, impinging on the aneurysm wall before forming a large recirculation zone that fills the aneurysm dome. Complex flow is found within this geometry, with two smaller flow vortices forming within the small

bleb-like structures within the dome. Although the velocity is low within these two small recirculation zones, the majority of the dome sees high velocity flow recirculation, with the aneurysmal flow re-joining the main arterial flow towards the proximal neck, although no distinct exit path is evident. For aneurysm 2, labelled B, the inflow jet is more diffuse and enters at the proximal neck. One large, slow-moving, spiralling flow recirculation forms that fills the entire aneurysm dome, with flow exiting the aneurysm towards the distal neck. A similar result is seen in aneurysm 3, labelled C, which demonstrates a concentrated inflow at the proximal neck that penetrates deeply into the aneurysm sac, before impinging on the wall towards the tip of the dome. Simple flow is found within the geometry, with flow entering a large, slow-moving vortex that fills the entire aneurysm dome, before flow re-enters the main arterial flow via a distinct exit path at the distal neck. Aneurysm 4 sees a diffuse inflow jet penetrate into the aneurysm at the distal neck, flowing along the distal wall before forming a large, relatively fast-moving flow vortex that fills the dome, with flow exiting the aneurysm at the proximal neck. A smaller, slow-moving recirculation region forms within the small aneurysmal bleb towards the tip of the dome. Results for aneurysm 5 are similar to that seen for aneurysm 3, with a diffuse, high-velocity inflow jet found at the proximal neck that penetrates into the large aneurysm dome, impinging on the tip and forming a large, slow-moving recirculation zone that fills the entire dome. Simple flow is evident within the dome, with flow exiting the aneurysm at a distinctive exit found at the distal neck. The final lateral geometry, aneurysm 6, also displays simple flow patterns, with a diffuse inflow jet entering the aneurysm at the distal neck before filling the dome with a large flow vortex. Flow then re-enters the main arterial flow, although a distinct exit location is not evident within the dome.

WSS plots for the six lateral aneurysm geometries are presented in Figure 7.19, and it is evident that the WSS levels vary throughout the geometries. Although differences are seen between the patterns within each aneurysm dome, the location of highest wall shear stress for all six geometries is found to correspond with the location of the inflow jet as it enters the aneurysm at the neck. Aside from the increased WSS found at the neck, the WSS within the aneurysm dome is generally found to be low, although slight increases are found to correspond to the high-velocity inflow jets as they begin to form flow recirculation regions. Areas of low velocity display low WSS levels, particularly within the aneurysmal blebs where small flow vortices are found.

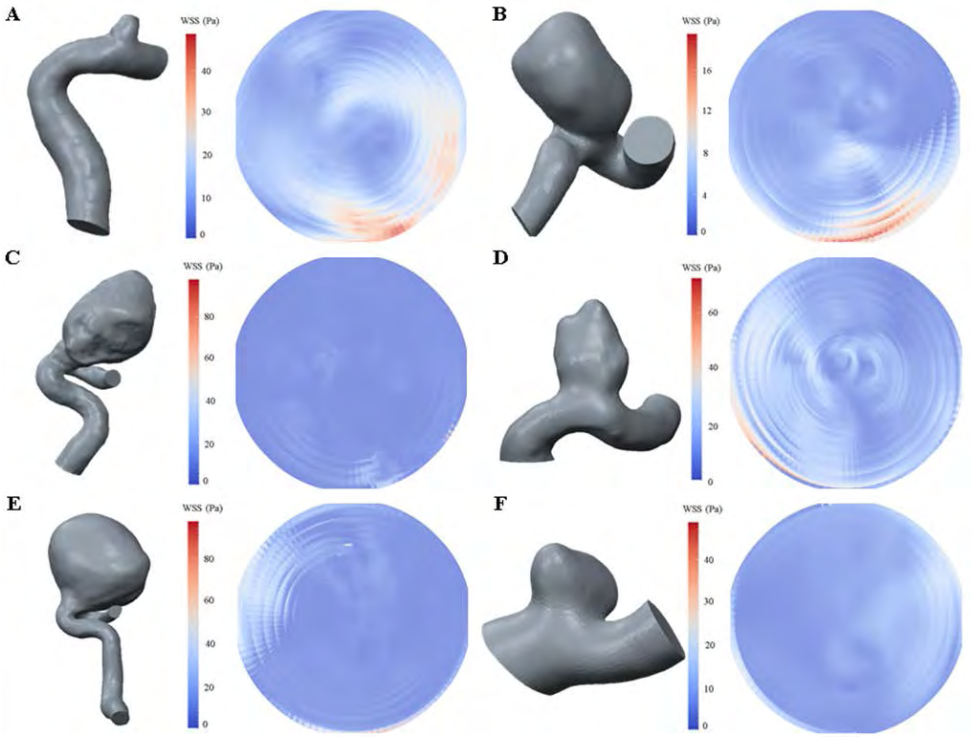

Figure 7.19: 2D unwrapped WSS plots for patient-specific ophthalmic segment ICA aneurysm geometries 1-6 (labelled A-F)

Results from the investigation into the mass transport of ATP within the six lateral aneurysm geometries are illustrated in Figure 7.20, in which the unwrapped normalised species concentration plots are presented. Upon comparison of the concentration distribution plots with the WSS plots, it is evident that areas of increased WSS correspond to higher concentration within the aneurysm dome. This is evidenced by the high concentration levels that are found within each aneurysm dome at the location of the inflow jet, where the WSS is found to be increased. This is especially evident in aneurysm 5, where the majority of the aneurysm dome sees reduced concentration levels, except at the neck, where an increase in WSS is found as the flow enters and exits the aneurysm dome.

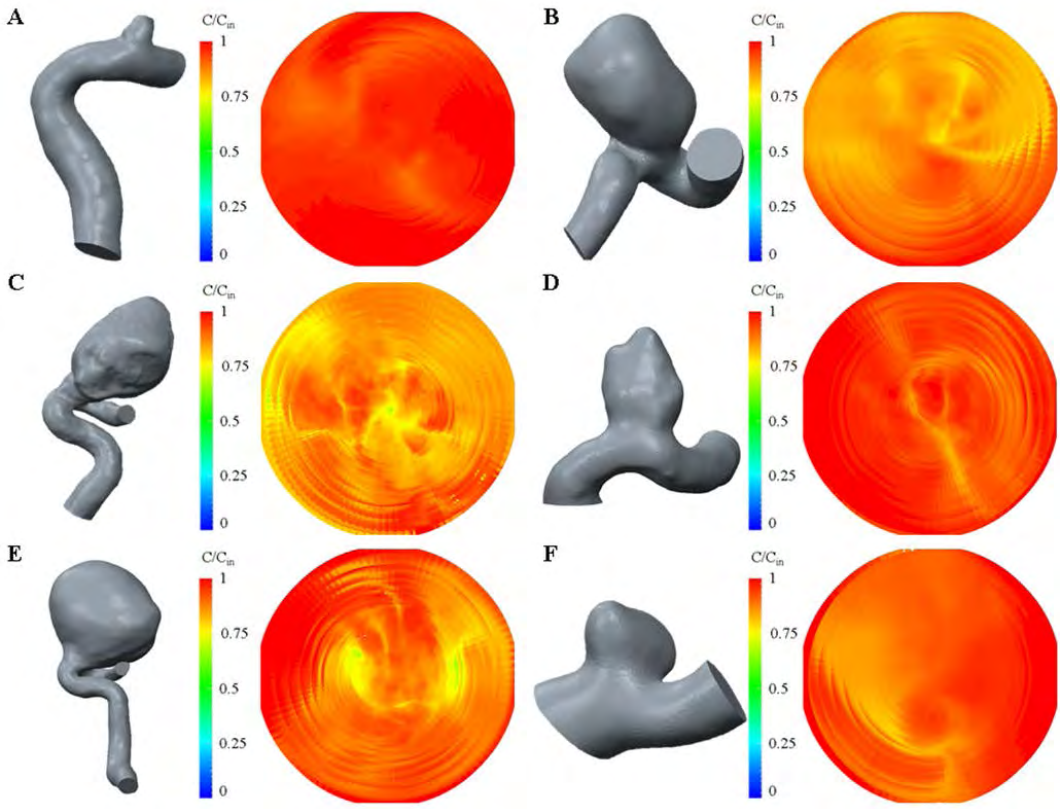

Figure 7.20: 2D unwrapped plots of concentration (normalised to inlet concentration) for patient-specific ophthalmic segment ICA aneurysm geometries 1-6 (labelled A-F)

As well as the areas of high concentration corresponding with increased WSS levels, areas of reduced concentration within each aneurysm tend to be found at areas of low WSS. An example of this can be seen in aneurysm 1, where the concentration is uniformly distributed, except for two areas with slightly reduced concentration that correspond to the two small recirculation zones described previously. Further evidence is seen in aneurysms 3 and 5, where the low WSS levels found throughout the dome due to the slow-moving flow vortices correspond to reduced concentration levels throughout the majority of the dome. However, it should be noted that within aneurysms 3 and 5 only, two small areas of substantially reduced concentration are found that do not have corresponding significantly low WSS. These low concentration points are found at either side of the recirculation zone, at areas of low velocity.

Of the lateral aneurysms investigated in this study, the results generally indicate that geometries that were found to have flow vortices of higher velocities tended to be more uniformly distributed, with higher concentrations. This is evident in aneurysms 1, 4 and 6, all of which display recirculation zones of higher velocity that exhibit good washout of species, with the species distributed evenly throughout the majority of the

dome. Conversely, aneurysms 2, 3 and 5 have much slower moving recirculation zones and display lower concentration levels, suggesting poor washout of species.

The percentage of the aneurysm dome found to have concentration levels lower than threshold values of 1%, 5%, 10% and 20% of the inlet concentration were calculated, and results are illustrated in Figure 7.21 for each aneurysm geometry. Although results differ between the aneurysms, a common trend is seen throughout the graphs, with the amount of the aneurysm dome found below the threshold concentration reducing as the threshold level increases.

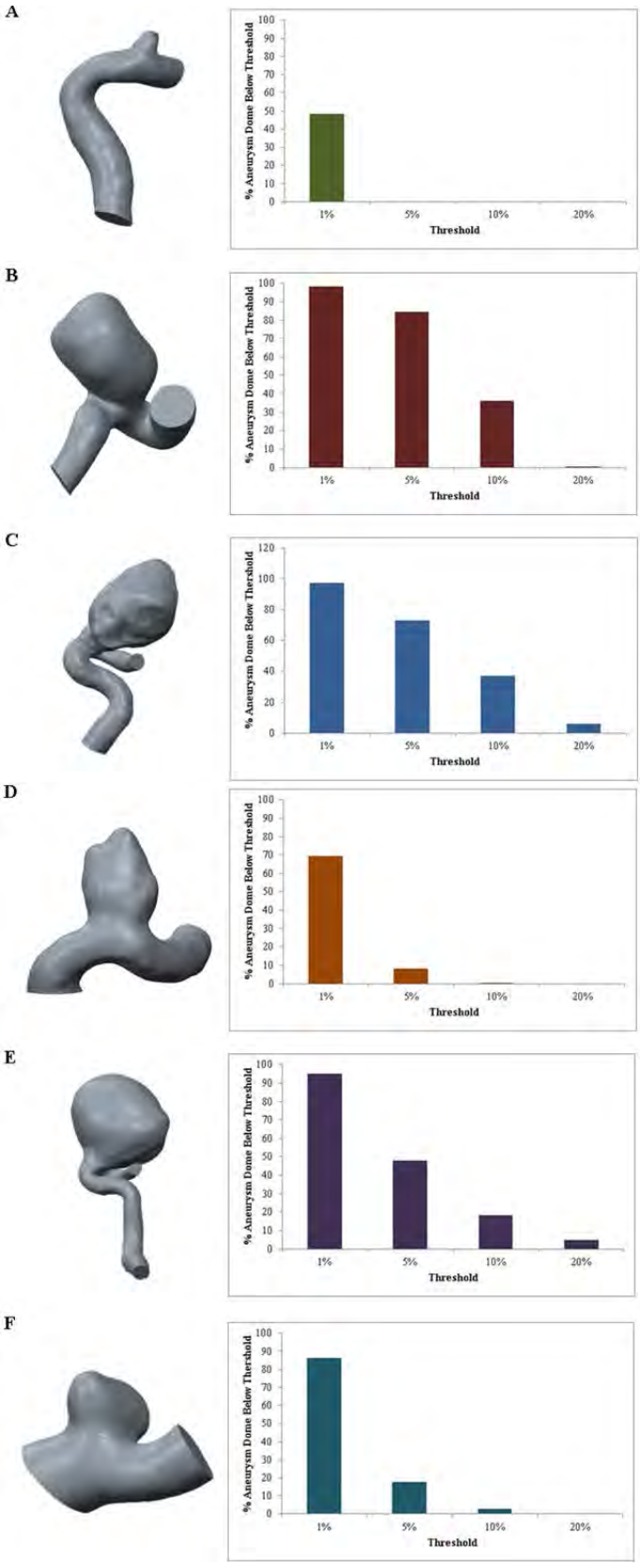

Figure 7.21: Percentage of aneurysm dome with concentration values found under threshold of 1%, 5%, 10% and 20% of C_{in} for patient-specific ophthalmic segment ICA aneurysm geometries 1-6 (A-F)

Figure 7.22 compares the percentage of the aneurysm dome found under the threshold values for each of the six lateral aneurysms at each threshold level. It can be seen from the results that at a threshold level of 1% of C_{in}, all aneurysms have a substantial amount (>45%) of their dome exposed to concentration values lower than the threshold level. Once a threshold of 5% is introduced, the amount of the dome found below the threshold for aneurysms 1, 4 and 6 reduces substantially, while aneurysms 2, 3 and 5 remain high. As the threshold level increases to 10% and 20% of C_{in}, aneurysms 1, 2, 5 and 6 drop to zero or near zero. Although the amount of the dome found below the threshold reduces in aneurysms 3, 4 and 5, it never drops to zero for the higher thresholds of 10% and 20% of C_{in}, with parts of the aneurysm dome still exposed to low concentration levels.

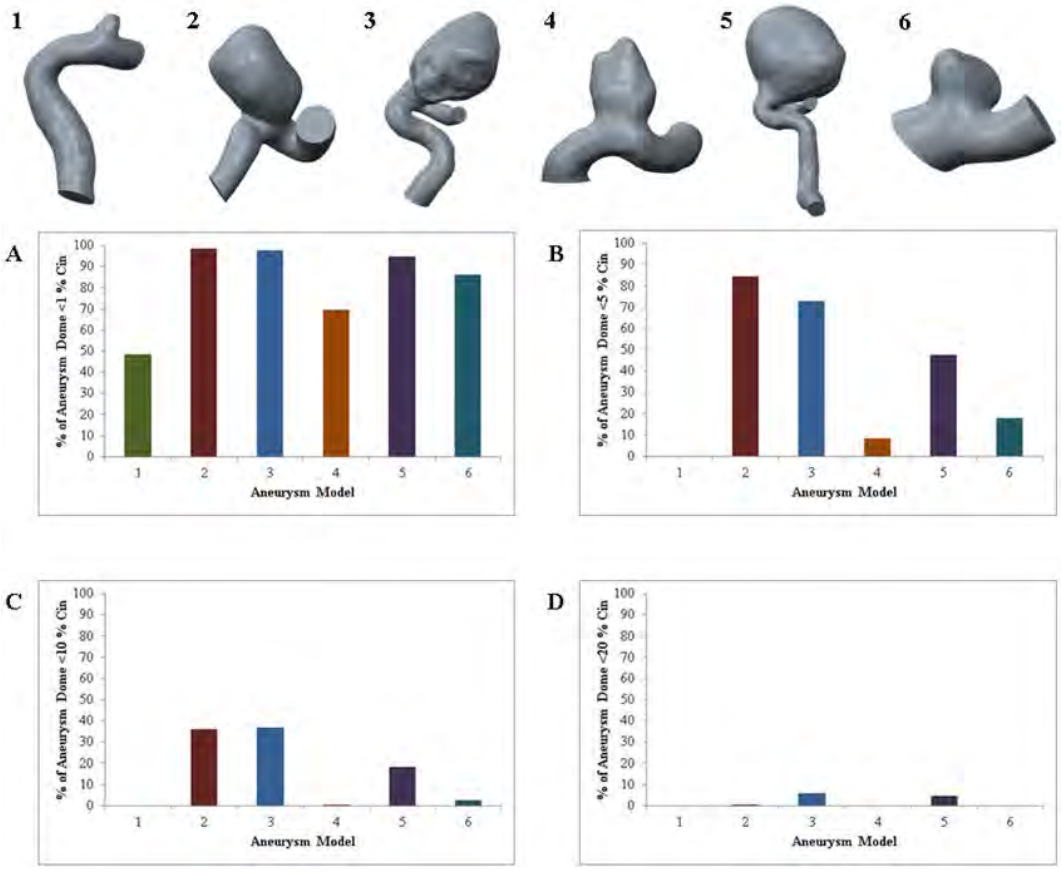

Figure 7.22: Percentage of aneurysm dome with concentration values found under threshold values of (A) 1% (B) 5% (C) 10% and (D) 20% of C_{in} for patient-specific ophthalmic segment ICA aneurysm geometries 1-6

Sylvian Bifurcation Results

Velocity streamlines for the six patient-specific sylvian bifurcation aneurysms are illustrated in Figure 7.23. Similar patterns are seen within aneurysms 1, 2, 5 and 6, with diffuse inflow jets penetrating into the aneurysm dome and impinging the aneurysm wall directly above the inflow jet before forming a large recirculating flow vortex that fills the aneurysm dome. Flow then exits the aneurysm dome and enters the daughter outlets. Similar flow patterns are seen within aneurysms 3 and 4, although the inflow jet is more concentrated. Furthermore, for aneurysms 3 and 4, the majority of the recirculated flow leaves via the smaller daughter artery. Simple flow is found in five of the six aneurysms, with more complex flow found in aneurysm 5, where a small, slow-moving recirculation zone is found within the bleb towards the tip of the dome.

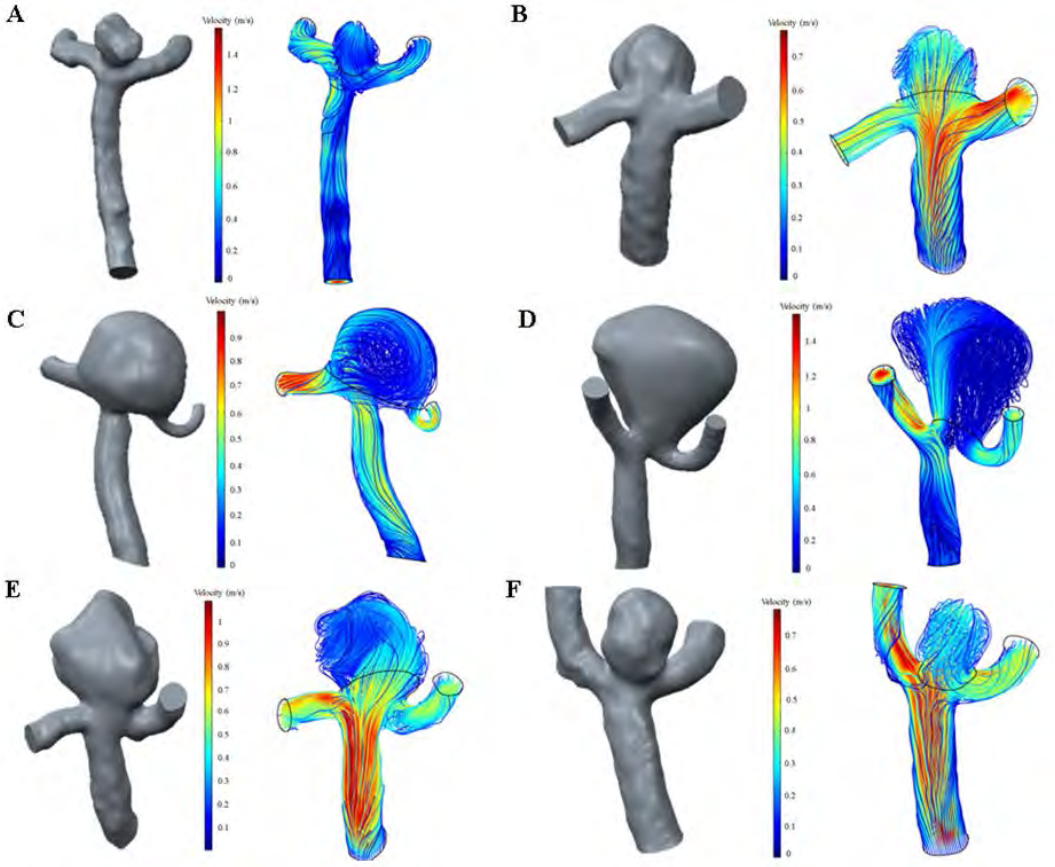

Figure 7.23: Velocity streamlines for patient-specific sylvian bifurcation aneurysm geometries 1-6 (labelled A-F)

The 2D unwrapped WSS plots, shown in Figure 7.24, illustrate the WSS distribution found within each aneurysm dome. Similar to that seen for the lateral aneurysms, areas of increased WSS are found at the aneurysm neck at the location when the inflow jet

penetrates into the aneurysm dome. Areas of increased WSS are also found as the flow exits the aneurysm and enters the daughter arteries in all six geometries. Although WSS levels vary for the six geometries, the WSS within the aneurysms is generally low (<20 Pa), with areas of low WSS corresponding to the slow-moving flow vortices found within the dome. Furthermore, WSS is seen to be increased at areas of higher velocity, such as along the path of the inflow jet, and near the point of flow impingement on the aneurysm dome.

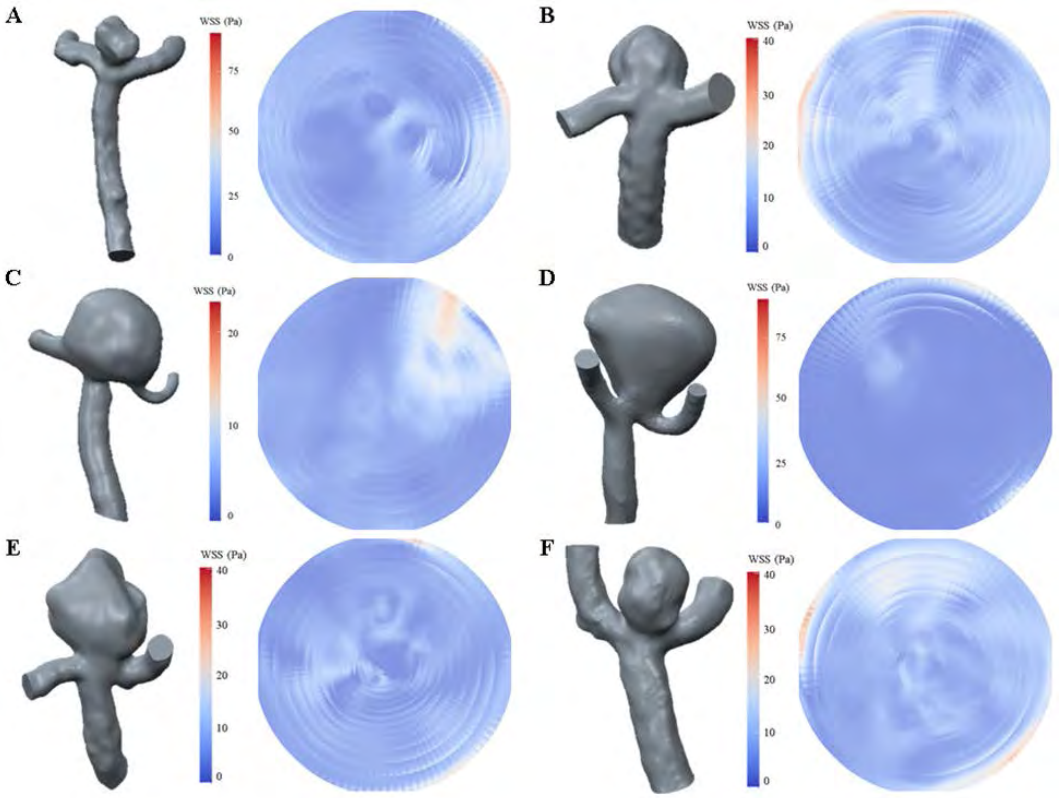

Figure 7.24: 2D unwrapped WSS plots for patient-specific sylvian bifurcation aneurysm geometries 1-6 (labelled A-F)

Figure 7.25 illustrates the 2D unwrapped concentration distribution plots, with the concentration normalised to the species inlet concentration. The results plots demonstrate that areas of increased concentration correspond to areas of increased WSS, which is especially evident at the neck of the aneurysm where the inflow jet enters the dome, and at the outlet to the daughter arteries, as flow exits the aneurysm. Similarly, areas of decreased concentration, for instance as seen within aneurysm 6, correspond to areas of low WSS within the aneurysm dome. Areas of low concentration are also found to correspond with aneurysmal blebs, and undulations throughout the aneurysm dome, such as those seen in aneurysm 5.

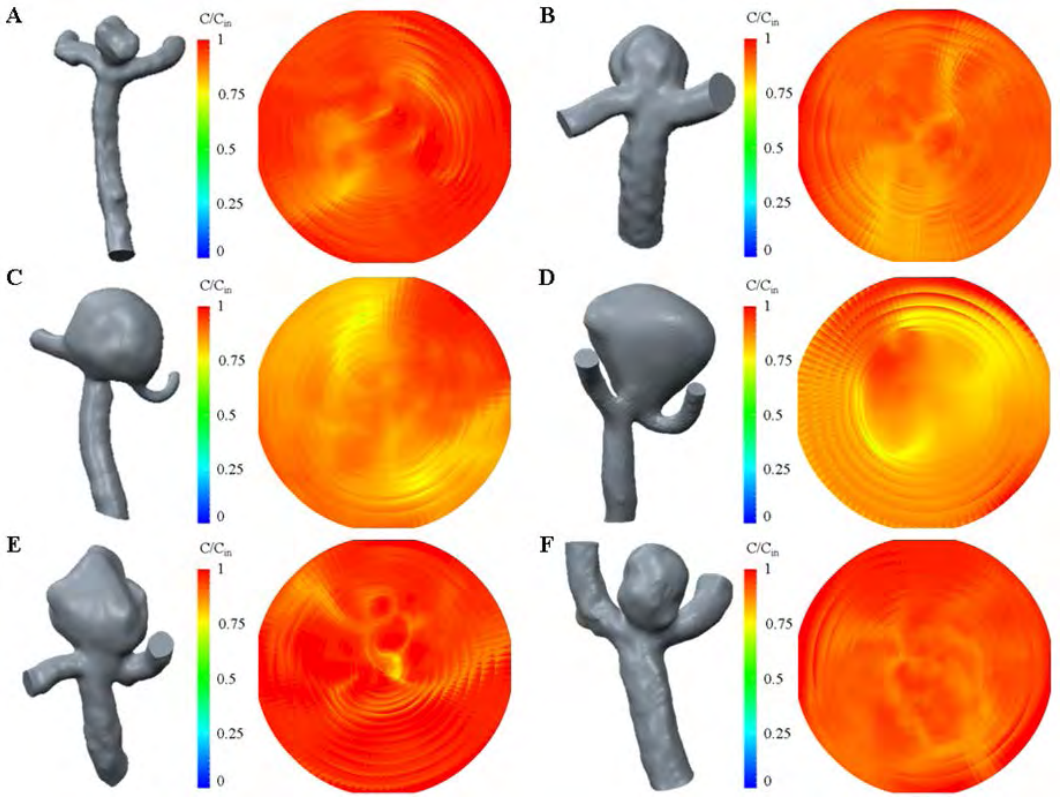

Figure 7.25: 2D unwrapped plots of concentration (normalised to inlet concentration) for patient-specific sylvian bifurcation aneurysm geometries 1-6 (labelled A-F)

As described previously for the lateral geometries, the bifurcation aneurysms with recirculation vortices of higher velocity demonstrate more uniform and higher concentration values than those with slow-moving flow vortices. An example of this can be seen on comparison of aneurysms 4 and 6. For aneurysm 6, a large fast-moving flow vortex fills the entire aneurysm dome, ensuring flow reaches all parts of the aneurysm dome. In contrast, aneurysm 4 develops a much slower moving recirculation zone, with parts of the dome not being exposed to enough flow for the aneurysm wall to reach the inlet concentration.

A comparison of the percentage of each aneurysm dome found below the concentration species threshold levels of 1%, 5%, 10% and 20% of C_{in} is illustrated in Figure 7.26. Although results differ between the aneurysm geometries, similar results are seen to the lateral results presented previously, with the amount of the aneurysm dome found below the threshold value tending to decrease as the threshold level increases.

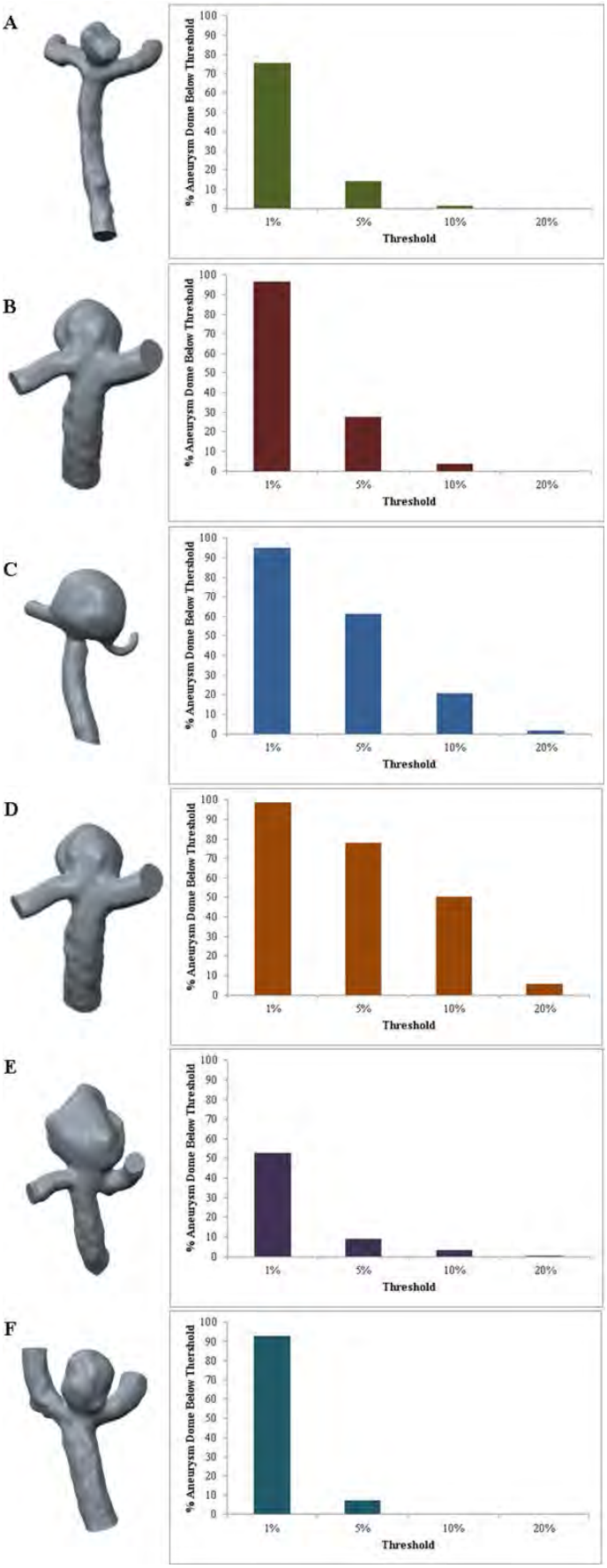

Figure 7.26: Percentage of aneurysm dome with concentration values found under threshold values of 1%, 5%, 10% and 20% of C_{in} for patient-specific sylvian bifurcation aneurysm geometries 1-6 (labelled A-F)

The amount of the aneurysm dome found to have concentration values lower than the species threshold is further compared at each threshold level in Figure 7.27. Results for the threshold level of 1% are similar for aneurysms 2, 3, 4 and 6, with the majority of the dome demonstrating concentration values lower than the threshold. Aneurysms 1 and 5 show lower results, but still demonstrated at least 50% of the aneurysm dome below the concentration threshold.

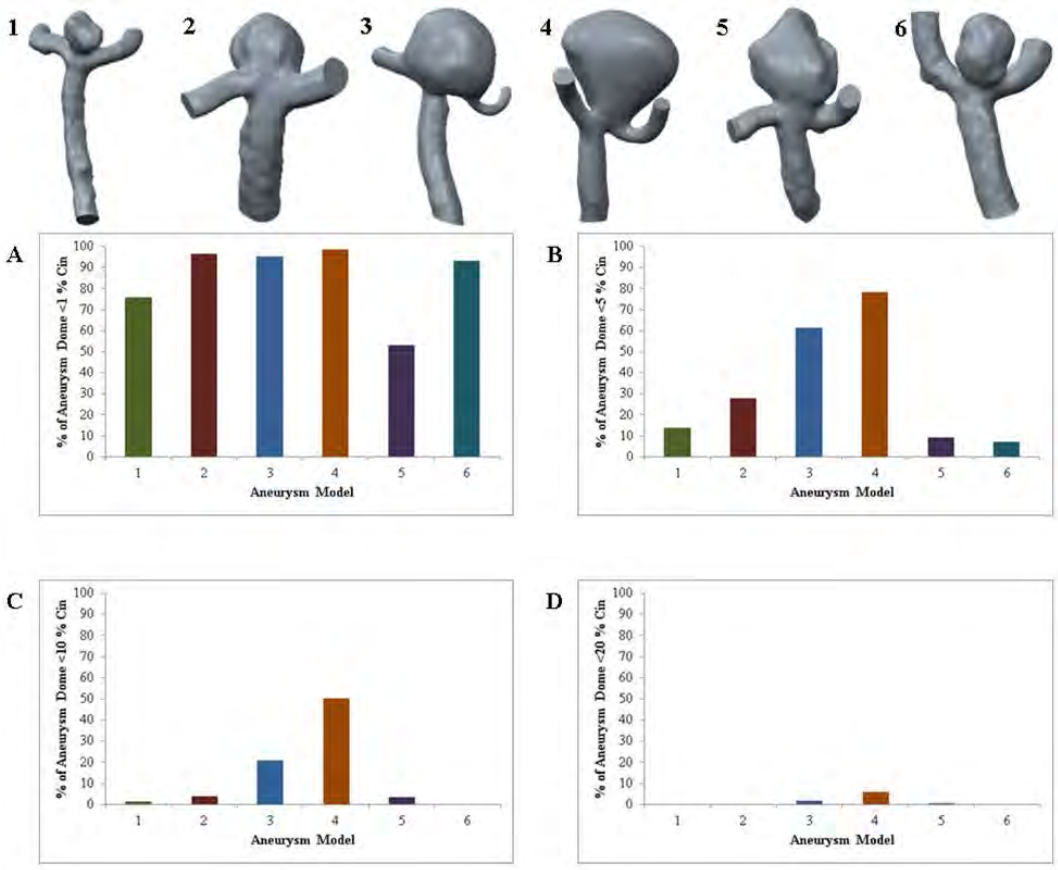

Figure 7.27: Percentage of aneurysm dome with concentration values found under threshold values of (A) 1 % (B) 5 % (C) 1 0% a nd (D) 2 0% o f C_{in} for p atient-specific s ylvian bifurcation a neurysm geometries 1-6

The a mount o f t he do me f ound und er t he t hreshold r educes s ubstantially a s t he threshold value increases. At a threshold level of 10% of C_{in}, aneurysms 1, 2, 5 a nd 6 all s how t hat the m ajority or a ll of t he dom e ha s c oncentration l evels a bove t he threshold, w ith onl y aneurysm 3 a nd 4 s howing more than 10% of their dome to be exposed to concentration values lower than the threshold. Finally, as the threshold is increased to 20% of C_{in}, only aneurysms 3, 4 a nd 5 ha ve areas within the aneurysm dome displaying a concentration lower than the threshold, with aneurysms 1, 2 a nd 6 having concentration values above 20% of C_{in} throughout the dome.

7.4.3 Statistical Analysis

In order to determine if a relationship exists between the different species threshold values and the rupture status of an aneurysm, statistical analysis was carried out on the results of the CFD simulations using IBM SPSS Statistics v20 (SPSS Inc., Chicago, Ill.). The rupture status of the six ophthalmic segment ICA aneurysms and six sylvian bifurcation aneurysms was already known, and the twelve aneurysms were analysed together, divided into unruptured (n = 7) and ruptured (n = 5) groups (see Table 7.4). Using results from the mass transport simulations, a statistical predictive model was developed with the intention of determining the rupture probability of an aneurysm based on the percentage of the dome that is exposed to concentration levels lower than the specified species threshold value.

Table 7.4: Percentage of aneurysm dome with concentration values found below species threshold of 1%, 5% , 10% and 20% of C_{in} for unruptured and ruptured patient-specific lateral and bifurcation aneurysms

		% of Aneurysm Dome Below Threshold			
Rupture Status	**Aneurysm**	**<1% of C_{in}**	**<5% of C_{in}**	**<10% of C_{in}**	**<20% of C_{in}**
Unruptured	Lateral 1	48.32	0.00	0.00	0.00
	Lateral 2	98.43	84.60	36.17	0.01
	Lateral 5	94.87	47.88	18.27	4.84
	Lateral 6	86.08	17.70	2.77	0.00
	Bifurcation 2	96.64	27.72	3.78	0.00
	Bifurcation 3	95.14	61.27	20.93	1.61
	Bifurcation 6	93.02	7.20	0.00	0.00
Ruptured	Lateral 3	97.61	73.03	36.95	5.96
	Lateral 4	69.49	8.17	0.46	0.00
	Bifurcation 1	75.68	13.93	1.27	0.00
	Bifurcation 4	98.57	78.19	50.35	5.78
	Bifurcation 5	52.94	9.09	3.37	0.16

First, a test for departure from normal distribution was performed on each threshold level for both the unruptured and ruptured groups. Results from the Shapiro-Wilk test for normality, which is recommended when the sample size is between 3 and 50 for non-integers, indicated a departure from normal distribution at all threshold levels. Therefore, the non-parametric Mann-Whitney U test was used to determine differences between the ruptured and unruptured groups, based on the different threshold levels. Logistic regression analysis was then carried out on all threshold levels in order to determine if any of the species concentration thresholds could predict

the probability that an aneurysm was at risk of rupture. Results from the Mann Whitney U and logistic regression analysis are listed in Table 7.5, with significance assumed for $p<0.05$.

Table 7.5: Results from non-parametric Mann Whitney U and logistic regression analysis (β = regression coefficient, SE = standard error, OR = odds ratio, CI = confidence interval)

Threshold	p value	β	SE	OR	95% CI
Mann-Whitney U					
% of Dome <1% of C_{in}	0.876	-	-	-	-
% of Dome <5% of C_{in}	1	-	-	-	-
% of Dome <10% of C_{in}	0.639	-	-	-	-
% of Dome <20% of C_{in}	0.432	-	-	-	-
Logistic Regression					
% of Dome <1% of C_{in}	0.971	-0.029	0.035	0.971	0.907-1.040
% of Dome <5% of C_{in}	0.942	0.001	0.019	1.001	0.964-1.040
% of Dome <10% of C_{in}	0.503	0.023	0.035	1.024	0.956-1.096
% of Dome <20% of C_{in}	0.31	0.266	0.262	1.305	0.781-2.181

It is clear from the results outlined in Table 7.5 that no significant relationship is found between the rupture status of the twelve patient-specific aneurysm geometries investigated in this study, and the percentage of the aneurysm dome found below species threshold levels of 1%, 5%, 10% and 20% of C_{in} as a result of mass transport within the aneurysm dome. Despite the lack of significance, results from the logistic regression analysis were used to develop a rupture probability equation at each threshold level, with a probability >0.5 indicating rupture:

$$\text{Probability of Rupture}_{1\%\text{ Threshold}} = \frac{e^{-0.029*\%\text{ of Aneurysm Dome }<1\%\text{ of Cin} + 2.086}}{1 + e^{-0.029*\%\text{ of Aneurysm Dome }<1\%\text{ of Cin} + 2.086}} \tag{7.1}$$

$$\text{Probability of Rupture}_{5\%\text{Threshold}} = \frac{e^{0.001*\%\text{ of Aneurysm Dome }<5\%\text{ of Cin} - 0.388}}{1 + e^{0.001*\%\text{ of Aneurysm Dome }<5\%\text{ of Cin} - 0.388}} \tag{7.2}$$

$$\text{Probability of Rupture}_{10\%\text{Threshold}} = \frac{e^{0.023*\%\text{ of Aneurysm Dome }<10\%\text{ of Cin} - 0.685}}{1 + e^{0.023*\%\text{ of Aneurysm Dome }<10\%\text{ of Cin} - 0.685}} \tag{7.3}$$

$$\text{Probability of Rupture}_{20\%\text{Threshold}} = \frac{e^{0.266*\%\text{ of Aneurysm Dome }<20\%\text{ of Cin} - 0.755}}{1 + e^{0.266*\%\text{ of Aneurysm Dome }<20\%\text{ of Cin} - 0.755}} \tag{7.4}$$

Using these four rupture prediction equations, the probability of the rupture of an aneurysm occurring based on the percentage of the dome found under the species threshold value can be calculated. The probability of rupture of the twelve patient-specific aneurysm geometries analysed in the mass transport simulations were calculated at each threshold level, with results listed in Table 7.6.

Table 7.6: Results of rupture prediction based on percentage of aneurysm dome with concentration values found below 1%, 5%, 10% and 20% of C_{in}

Rupture Equation	No. Correctly Predicted (/12)	% Correctly Predicted
% of Dome <1% of C_{in}	8	67%
% of Dome <5% of C_{in}	7	58%
% of Dome <10% of C_{in}	8	67%
% of Dome <20% of C_{in}	8	67%

It can be seen from the results that for concentration values of 1%, 10% and 20% of C_{in}, the rupture status of two thirds of the cohort of 12 aneurysms were predicted correctly, with 58% of the aneurysms predicted correctly at a threshold value of 5% of C_{in}, suggesting that a threshold of 5% may not be as accurate. It should be noted that these results are not statistically significant. However, results may give an indication of the efficacy of the species threshold method in the prediction of aneurysm rupture.

Earlier in this study, a relationship was established between aneurysm rupture and several geometric features, namely posterior location, lateral shape, increased tilt angle and increased aspect ratio (see Chapter 6). Furthermore, a tentative link has been made between the mass transport of blood-borne species and rupture, with aneurysms found to have concentrations lower than the species threshold more likely to rupture. Separate rupture probability equations have been developed that indicate whether an aneurysm is at risk of rupture based on (1) geometric features and (2) species threshold levels. However, the next step towards establishing a relationship between geometric features, mass transport and aneurysm rupture involves combining the probability equations to develop one overall rupture probability equation that could potentially distinguish whether an aneurysm is at risk of rupture, and thus should be put forward for surgery.

Statistical analysis of the overall patient-specific database of 168 cerebral aneurysm geometries led to the development of a rupture probability equation based on key geometric parameters, as described in Chapter 6. In order to develop a method of

predicting aneurysm rupture based on both geometric features and concentration species threshold values, further logistic regression analysis was carried out on the twelve patient-specific ophthalmic segment ICA and sylvian bifurcation aneurysms using the statistically significant parameters from the study of geometric features, and using each of the species threshold levels in turn. Results from the logistic regression analysis led to the development of four final rupture probability equations. However, it should again be noted that the rupture probability equations developed are not statistically significant, possibly as a result of the low sample size. The efficacy of these rupture probability equations in the prediction of aneurysm rupture, based on a combination of geometric features and mass transport species threshold values, will be carried out in the following chapter.

$$\text{Probability of Rupture}_{\text{Geometry+1\%Threshold}} = \frac{e^{-0.094*\text{Tilt Angle} +8.937*\text{Aspect Ratio}+8.814*\text{Shape}-0.411*\text{Threshold}+15.622}}{1+ e^{-0.094*\text{Tilt Angle} +8.937*\text{Aspect Ratio}+8.814*\text{Shape}-0.411*\text{Threshold}+15.622}} \quad (7.5)$$

$$\text{Probability of Rupture}_{\text{Geometry+5\%Threshold}} = \frac{e^{0.101*\text{Tilt Angle} +3.828*\text{Aspect Ratio}+3.078*\text{Shape}-0.068*\text{Threshold}-9.027}}{1+ e^{0.101*\text{Tilt Angle} +3.828*\text{Aspect Ratio}+3.078*\text{Shape}-0.068*\text{Threshold}-9.027}} \quad (7.6)$$

$$\text{Probability of Rupture}_{\text{Geometry+10\%Threshold}} = \frac{e^{0.098*\text{Tilt Angle} +2.817*\text{Aspect Ratio}+2.561*\text{Shape}-0.054*\text{Threshold}-8.357}}{1+ e^{0.098*\text{Tilt Angle} +2.817*\text{Aspect Ratio}+2.561*\text{Shape}-0.054*\text{Threshold}-8.357}} \quad (7.7)$$

$$\text{Probability of Rupture}_{\text{Geometry+20\%Threshold}} = \frac{e^{0.120*\text{Tilt Angle} +4.770*\text{Aspect Ratio}+2.922*\text{Shape}-0.9*\text{Threshold}-11.779}}{1+ e^{0.120*\text{Tilt Angle} +4.770*\text{Aspect Ratio}+2.922*\text{Shape}-0.9*\text{Threshold}-11.779}} \quad (7.8)$$

7.5 Discussion

The first half of this chapter describes the investigation into the use of representative aneurysm models, developed based on key patient-specific geometric measurements, as an alternative to simple idealised and complex patient-specific geometries. Results from the investigation have already been discussed in Section 7.3.3, with the representative models giving improved information regarding flow haemodynamics

and mass transport within the aneurysm dome compared to idealised models. In the second half of this chapter, a study of the mass transport seen in patient-specific aneurysms is carried out, with analysis of the influence of different blood-borne species on mass transport seen within the dome also carried out.

Twelve patient-specific geometries were included in this study, with six lateral ophthalmic segment ICA and six sylvian bifurcation aneurysms analysed. The twelve aneurysms selected came from a range of size, neck size and shape categories, allowing for the influence of the different geometric features on the flow and mass transport patterns to be examined. Furthermore, the locations used (ophthalmic segment ICA and sylvian bifurcation) were selected as they represent typical lateral and bifurcation aneurysm geometries, with no smaller branching arteries present, and so results can be applied to other lateral and bifurcation aneurysms throughout the CoW.

Results from the mass transport analysis highlight a distinct relationship between WSS and mass transport, with areas of increased WSS found within the aneurysm dome corresponding to higher levels of concentration, often close to the value of the inlet concentration. This is especially evident at the neck of the aneurysm, at the point where an inflow jet branches from the main arterial flow and enters the aneurysm, causing an increase in WSS at the neck and along the aneurysmal wall as it penetrates into the dome. The inverse is also seen, with areas demonstrating low WSS found to also display low concentration values, suggesting an under-expression of species at the wall of the aneurysm. This is especially evident within aneurysmal blebs and undulations, where low velocity flow recirculation regions form, leading to low WSS and low concentration distribution. However, areas of substantially reduced concentration are also seen within some the dome of some geometries that do not have corresponding significantly low WSS, suggesting that there are other factors that contribute to species depletion at the wall of the aneurysm.

The distribution of species within the aneurysm appears to be closely linked to the distribution of flow throughout the dome. High concentration values are seen within the aneurysms where the inflow jet disperses throughout the entire dome, leading to good washout and all parts of the aneurysm dome receiving a supply of species. Conversely, in aneurysms where the inflow jet remains concentrated throughout the dome, areas of decreased concentration are evident due to the slow moving flow

vortex not supplying the entire aneurysm dome with an adequate supply of species. This is further evidenced by locations throughout the aneurysm dome where the inflow jets do not penetrate into aneurysmal blebs or undulations, leading to localised reduced concentration. Results from this study suggest that smoother aneurysms demonstrate more uniform concentration distributions that are close to the inlet concentration, as the inflowing blood reaches all parts of the aneurysm dome, leading to a constant species supply.

In order to ensure that the results from the mass transport simulations could be extrapolated to other blood-borne species of low diffusivity such as LDLs, nitric oxide and albumin, the transport of LDLs within one ophthalmic segment ICA and one sylvian bifurcation aneurysm was simulated and results were compared to the concentration distribution of ATP within the aneurysm dome. The trends and patterns of concentration distribution were identical despite the difference in species. However, the values of concentration varied significantly, with ATP demonstrating areas of decreased concentration that corresponded to increased concentration within the LDL models. The differences seen in the unwrapped plots can be attributed to the different transport mechanisms seen for different blood-borne species; species such as ATP and oxygen undergo a reaction at or in the arterial wall, while LDLs and albumin permeate through the wall. Furthermore, due to the water filtration velocity found at the arterial wall, concentration polarization of LDLs can occur, leading to localised increased concentration associated with disease pathogenesis. It was established from this comparative study that results from the mass transport analysis of ATP can be extrapolated to other blood-borne species, but the transport method for the individual species should be considered, with an increase or reduction of species governed by the transport mechanism involved.

A hypothesis was developed that suggests that the rupture of an aneurysm may be related to the amount of the dome that is exposed to an under-expression (or saturation, in the case of LDLs) of vital blood-borne species. However, due to the lack of information regarding the threshold point at which a lack of species at the aneurysm wall could trigger negative wall remodelling leading to growth and eventual rupture, species threshold levels of 1%, 5%, 10% and 20% of the inlet concentration were used in the statistical analysis of the relationship between mass transport and rupture.

Statistical analysis did not find a significant relationship between the rupture status of the twelve patient-specific geometries investigated, and the amount of the aneurysm dome found below the different threshold levels. However, the lack of significant results does not necessarily indicate that a relationship does not exist, but instead suggests that it does not exist for this particular cohort of aneurysms, possibly due to the small sample size used. Despite this lack of significance, rupture probability equations were generated for the prediction of aneurysm rupture based on the mass transport species threshold values alone, and also based on a combined hypothesis of geometric parameters and species threshold values.

In order to determine the ability of the rupture probability equations to accurately predict aneurysms at risk of rupture, the equations need to be tested on an independent cohort of patient-specific cerebral aneurysms. This will be dealt with in the following chapter.

CHAPTER 8

BLIND STUDY OF THE RELATIONSHIP BETWEEN GEOMETRIC PARAMETERS, SPECIES CONCENTRATION AND CERERBAL ANEUYRSM RUPTURE

Chapter 8 Blind Study on the Relationship between Geometric Parameters, Species Concentration and Cerebral Aneurysm Rupture

8.1 Introduction

As stated previously, the overall aim of this study is to investigate if a relationship exists between geometric parameters, mass transport of blood-borne species and cerebral aneurysm growth and rupture potential. If such a relationship were to exist, it would allow improved decision-making regarding the treatment of unruptured aneurysms, as the key geometric features that define the shape of the aneurysm dome would indicate whether the mass transport of species within the dome would lead to aneurysm stabilisation or aneurysm rupture.

In the previous chapter, results from the analysis of mass transport of ATP within twelve patient-specific cerebral aneurysm geometries were presented, and the relationship between the amount of the aneurysm dome exposed to concentration values lower than threshold levels of 1%, 5%, 10% and 20% of the inlet concentration was investigated. Although no significance was found in the relationship between any of the concentration thresholds and aneurysm rupture, the results were used to develop rupture probability equations, which allows the probability of an aneurysm growing or rupturing to be calculated, based on concentration threshold levels. Furthermore, combined rupture probability equations were developed that incorporate results from the investigation into the relationship between geometric parameters and aneurysm growth and rupture potential, which was discussed in Chapter 6.

In order to investigate the hypothesis of aneurysm growth and rupture being related to a combination of geometric features and the mass transport of blood-borne species, the rupture probability equations were applied to a cohort of ten patient-specific aneurysm models in a blind study where the rupture status of the aneurysms was unknown prior to the study. In this chapter, the ten patient-specific aneurysm models used in the blind study are introduced, and results from the measurement of their geometric features and from the mass transport simulations carried out on their geometries are discussed. Finally, predictions are made as to the rupture status of the blind geometries based on the geometric, mass transport and combined rupture probability equations, and the results are compared to the actual rupture status of the geometries.

8.2 Blind Study Aneurysm Geometries

Ten patient-specific cerebral aneurysm geometries from 6 locations within the CoW (ACoA, BA, ICA, MCA, PCoA and VA) were made available by a research group in the University of Iowa, allowing for the hypothesis of aneurysm rupture being related to geometric parameters and mass transport to be tested. The aneurysm geometries were created from scans taken at time zero, at the beginning of the study. The ten aneurysms (see Figure 8.1) were observed without treatment over a period of time, and placed into one of two groups: stable, indicating that the aneurysm was unruptured and went on to remain stable, and unstable, where the aneurysm was unruptured and went to on be unstable, showing evidence of growth or rupture during the follow up period. However the stability of the ten aneurysms was kept blinded throughout the study, so as to avoid influencing of results.

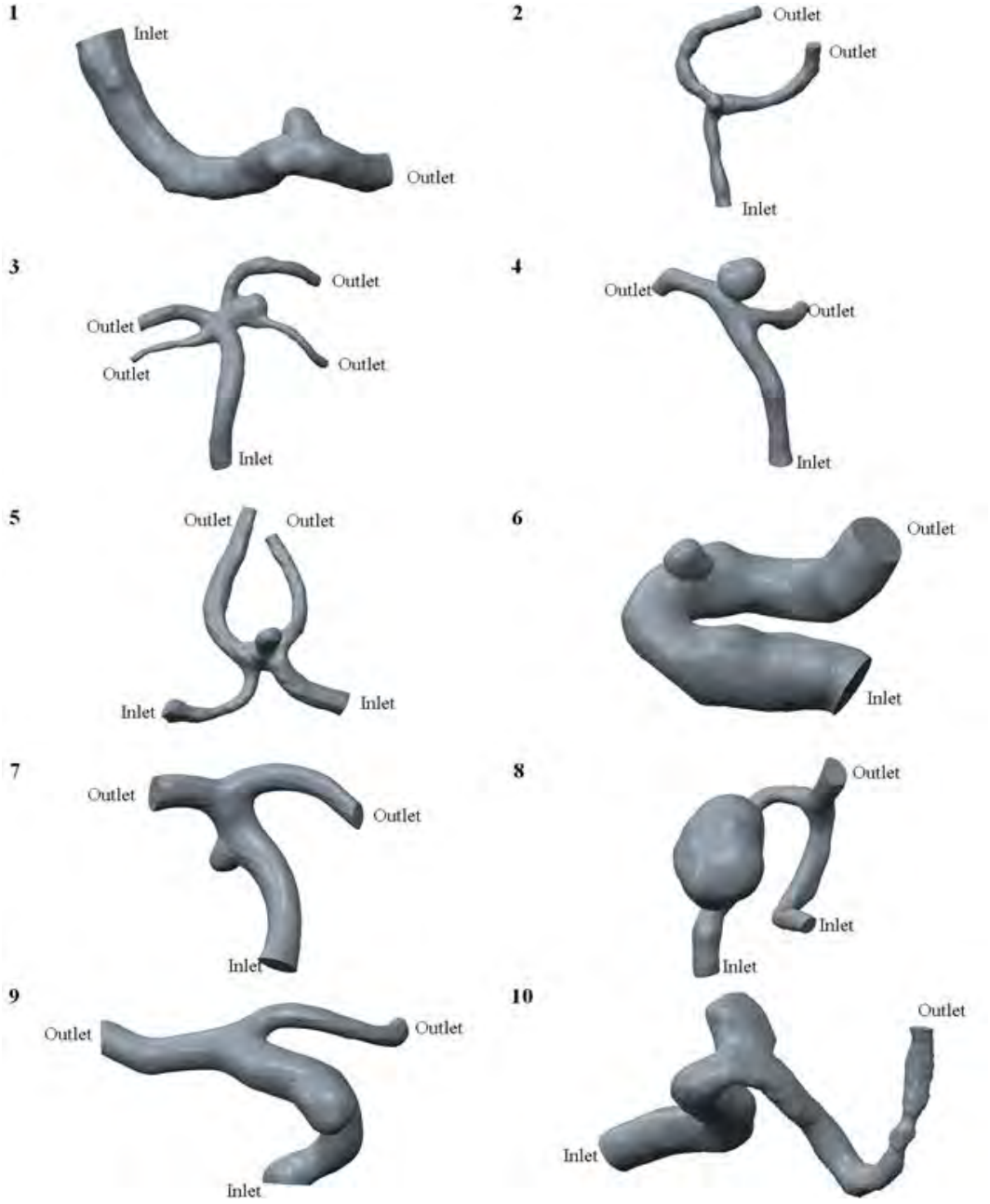

Figure 8.1: Illustration of patient-specific cerebral aneurysm geometries 1-10 used in blind study

The aneurysms were classified based on their location, shape, size and neck size, as outlined in Section 3.3, with results illustrated in Table 8.1. The aneurysm dome was segmented in a similar fashion to that described by Ma *et al.* (2004), with a cutting plane used to separate the aneurysm from the parent artery geometry using visual observation.

Table 8.1: Results from classification of 10 patient-specific blind study geometries

Aneurysm	Location	Shape	Size	Neck Size
1	RICA	Lateral	Small	Narrow
2	ACoA	Bifurcation	Small	Narrow
3	Basilar	Bifurcation	Small	Narrow
4	LMCA	Bifurcation	Small	Narrow
5	ACoA	Bifurcation	Small	Narrow
6	LICA	Lateral	Small	Narrow
7	RICA	Lateral	Small	Narrow
8	Vertebral	Lateral	Medium	Wide
9	PCoA	Lateral	Small	Wide
10	LICA	Lateral	Small	Narrow

Following the segmentation of the aneurysm dome, the height (H), neck width (N), diameter (D), distance to maximum diameter (h), tilt angle (θ_T) and aspect ratio (AR) were measured and calculated using the methods described in Section 3.4. Results from the measurement of the key geometric parameters for each geometry are listed in Table 8.2.

Table 8.2: Results from measurement of key parameters of 10 patient-specific blind study geometries. All values presented in mm, except Tilt Angle (º).

Aneurysm	Height (H)	Neck Width (N)	Diameter (D)	Distance to Max. Diameter (h)	Tilt Angle (θ_T)	Aspect Ratio (AR)
1	2.52	3.70	3.43	0.33	19.81	0.68
2	2.14	2.58	2.37	0.32	13.92	0.83
3	1.54	3.89	3.52	0.11	28.29	0.40
4	3.81	2.86	3.67	1.33	18.88	1.33
5	3.72	2.98	2.68	0.34	24.06	1.25
6	2.10	3.13	3.03	0.25	22.27	0.67
7	2.17	3.41	3.24	0.21	12.77	0.64
8	8.18	13.41	13.53	1.40	56.42	0.61
9	3.61	4.67	4.47	0.48	36.44	0.77
10	3.77	3.82	4.01	1.01	13.31	0.99

Following the methods outlined in Section 3.5.3, each of the patient-specific geometries were segmented and prepared for CFD analysis. The mass transport of ATP within each of the ten patient-specific blind study geometries was carried out using Comsol and the assumptions, flow conditions and mass transport parameters outlined in Chapter 4. Average flow rates were calculated for each of the aneurysm locations and implemented at the artery inlet (see Table 8.3).

Table 8.3: Average flow rates for different locations of blind study geometries

Location	Average Flow Rate (ml/min)
ACA	86
Basilar	197
ICA	260
MCA	138
Vertebral	85

8.3 Results

8.3.1 CFD Results

Velocity streamlines within the ten blind study aneurysm geometries are presented in Figure 8.2. Results indicate that for the majority of the aneurysms, flow enters at the distal neck and moves along the distal wall of the aneurysm, before forming a flow vortex that fills the aneurysm dome. An example of this can be seen in aneurysms 1 and 6. The velocity of the flow recirculation zone varies depending on the inflow jet and the shape of the aneurysm, with aneurysm 8 displaying a slow-moving recirculation zone while aneurysm 1 demonstrates a recirculation zone of higher velocity.

Results for aneurysm 2 and 4 differ from the rest of the aneurysms in that the majority of the flow bypasses the aneurysm dome, instead entering the daughter arteries. Due to the angle of the aneurysm with respect to the parent artery, only a small amount of flow enters the aneurysm, where it recirculates throughout the dome at low velocity, before re-joining the main arterial flow.

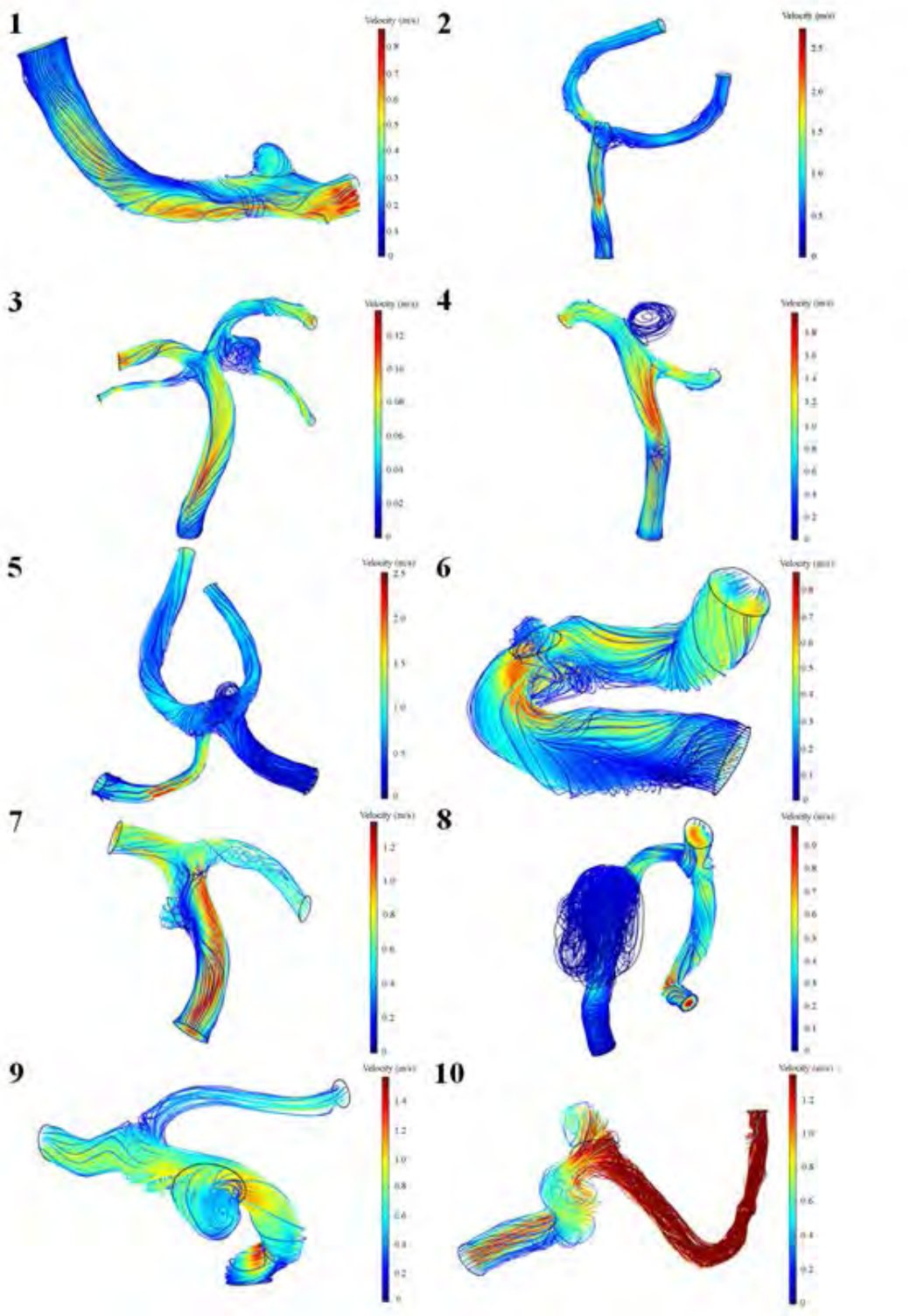

Figure 8.2: Velocity streamlines found within blind study geometries 1-10

Figure 8.3 illustrates the 2D unwrapped WSS plots for the ten blind study aneurysm geometries. As seen in previous results, an increase in WSS is seen in all the aneurysms that correspond with the location where the inflow jet enters the aneurysm dome. In general for all the aneurysm geometries, areas of increased WSS are found

along the inflow jet as it penetrates into the aneurysm dome, and at the aneurysm neck where the flow exits at high velocity in some geometries e.g. aneurysm 3. Areas of low WSS within the aneurysm are typically found to correspond to areas of low velocity flow recirculation within the dome. An example of this is seen in aneurysm 8, where an increase in WSS is evident at the distal neck, as the flow enters the aneurysm dome. However, the flow then forms a large, slow-moving recirculation zone that fills the entire dome, and so the unwrapped WSS plot displays uniformly low WSS throughout the dome.

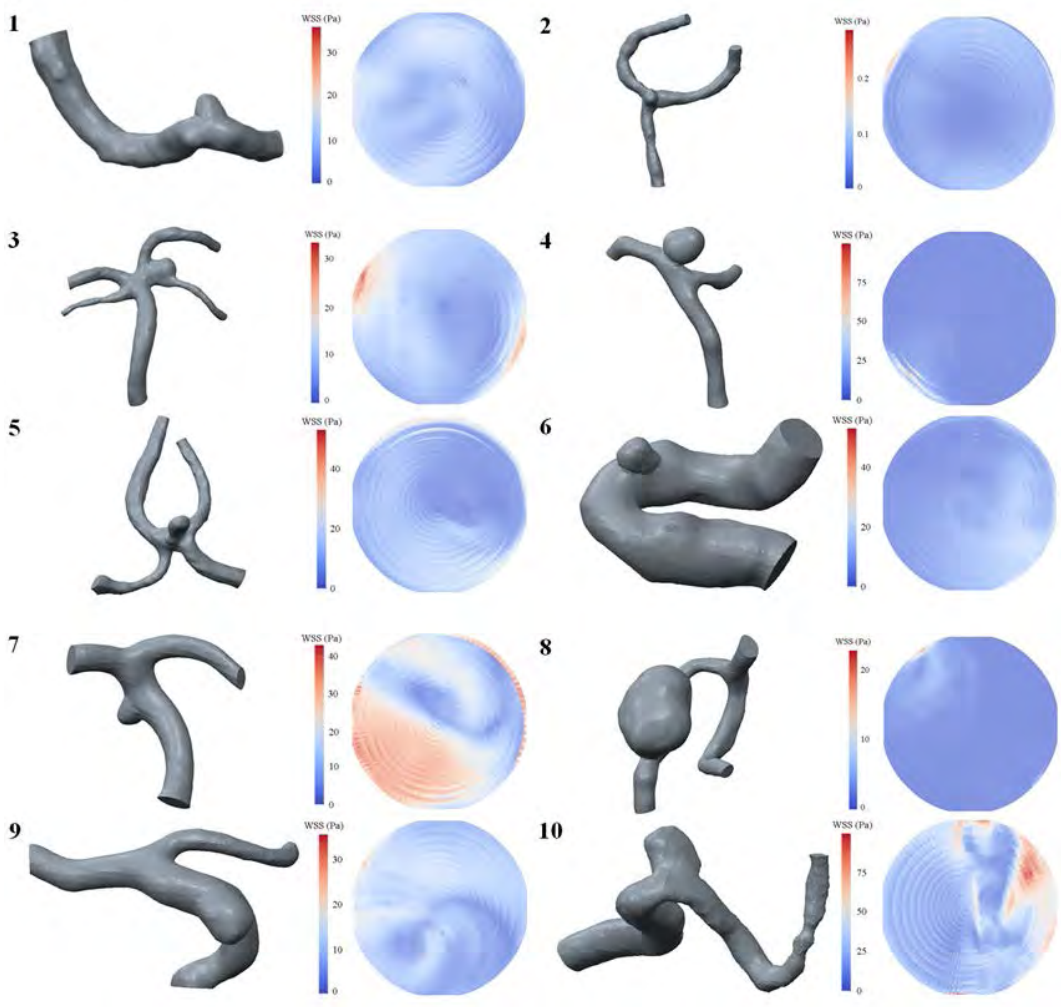

Figure 8.3: 2D unwrapped WSS plots for patient-specific blind study aneurysm geometries 1-10

The corresponding unwrapped concentration plots are illustrated in Figure 8.4, where an area of high concentration is found on the aneurysm neck in each geometry where the inflow jet enters the dome and increases in WSS are evident. Similar patterns are seen within the unwrapped WSS and concentration plots, where areas of increased WSS correspond to higher concentration, such as along the aneurysm wall where high

velocity jets penetrate into the aneurysm before entering the recirculating flow within the dome.

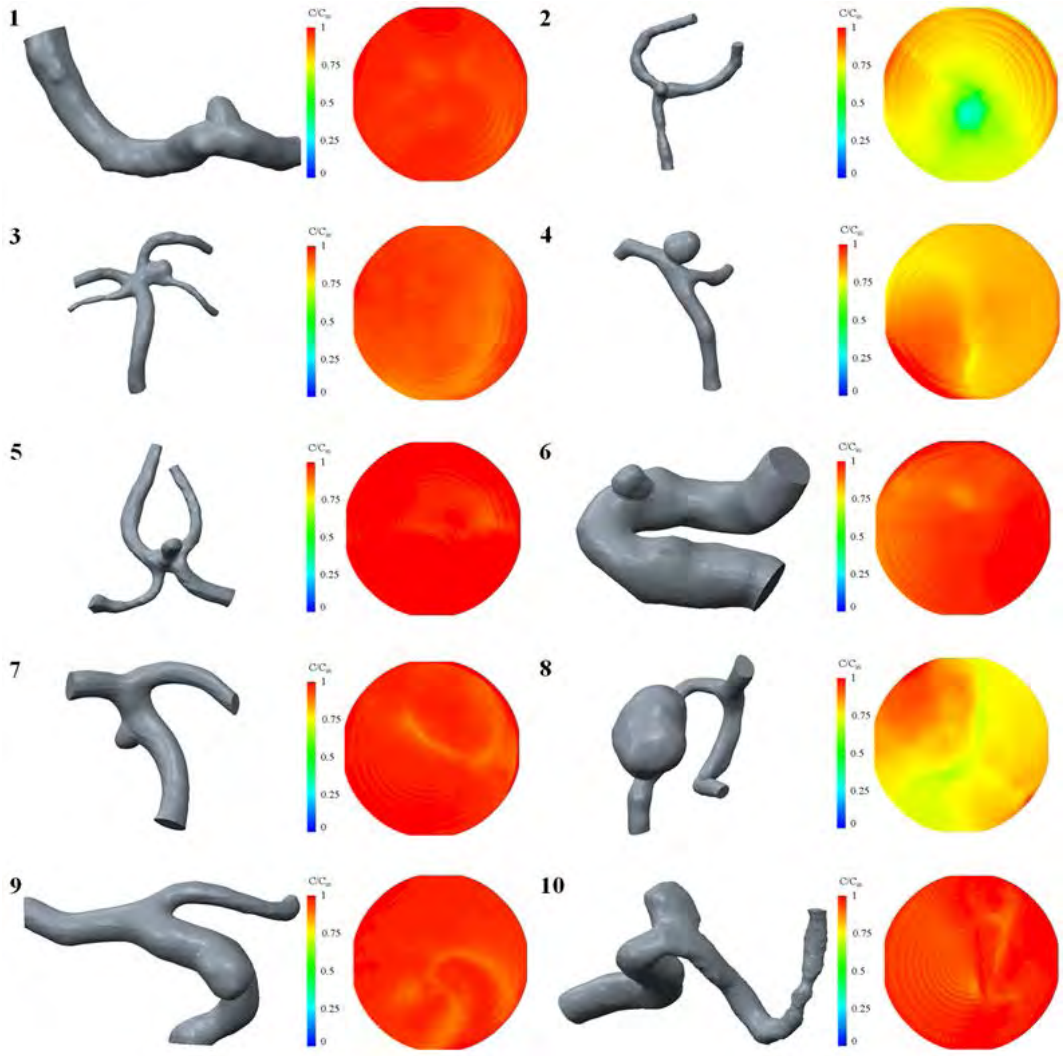

Figure 8.4: 2D unwrapped concentration plots (normalised to inlet concentration) for patient-specific blind study aneurysm geometries 1-10

Similarly, areas of low WSS are seen to correspond to lower concentration values. This is especially evident in aneurysms 2 and 8, where particularly low velocity flow fills the aneurysm and recirculates throughout the dome, displaying extremely low WSS levels that correspond to reduced concentration levels. In contrast, aneurysms 1 and 5 display almost uniform concentration distributions of values close to the inlet concentration, suggesting good washout of species.

Results from mass transport of ATP within the ten blind study aneurysm geometries are shown in Table 8.4. The results illustrate the amount of the aneurysm dome that is

found to have concentration values below the species concentration threshold of 1%, 5%, 10% and 20% of the inlet concentration.

Table 8.4: Results from the mass transport simulations of ten blind study aneurysm geometries, listing the percentage of each aneurysm dome found to have concentration values below the threshold levels of 1%, 5%, 10% and 20% of the inlet concentration

		% of Aneurysm Dome Below Threshold			
Aneurysm	**Location**	**<1% of C_{in}**	**<5% of C_{in}**	**<10% of C_{in}**	**<20% of C_{in}**
1	RICA	47.02	0.00	0.00	0.00
2	ACoA	100.00	98.37	94.71	81.56
3	Basilar	90.64	5.67	0.00	0.00
4	LMCA	97.45	85.07	62.79	2.27
5	ACoA	9.71	0.00	0.00	0.00
6	LICA	53.97	5.05	0.00	0.00
7	RICA	53.26	1.72	0.00	0.00
8	Vertebral	99.27	90.00	78.01	44.82
9	PCoA	48.25	0.02	0.00	0.00
10	LICA	33.13	0.76	0.00	0.00

It can be seen from Table 8.4 and from the comparison of the percentage of the aneurysm dome found below each threshold level (see Figure 8.5), that the amount of the aneurysm dome found to have concentration values below each threshold varies between the aneurysms. Similar trends are seen for each aneurysm, with the amount of the dome found below the threshold value decreasing as the threshold is increased.

At a threshold of 1% of C_{in}, all ten of the geometries show a percentage of their dome to have a concentration lower than the threshold, with the majority of the aneurysms having over half their dome falling below the threshold. However, once a threshold of 5% of C_{in} is introduced, the results change dramatically, with aneurysms 2, 4 and 8 displaying the majority of their domes to have concentration values lower than the threshold, while the remaining aneurysms drop to below 10%. Similar results are seen at a threshold of 10% of C_{in}, where all aneurysms drop to zero except for aneurysms 2, 4 and 8. Finally, at a threshold of 20% of C_{in}, aneurysm 4 shows a decrease in the amount of the dome exposed to a concentration below the threshold, but at least 40% of aneurysms 2 and 8 fall below the threshold concentration.

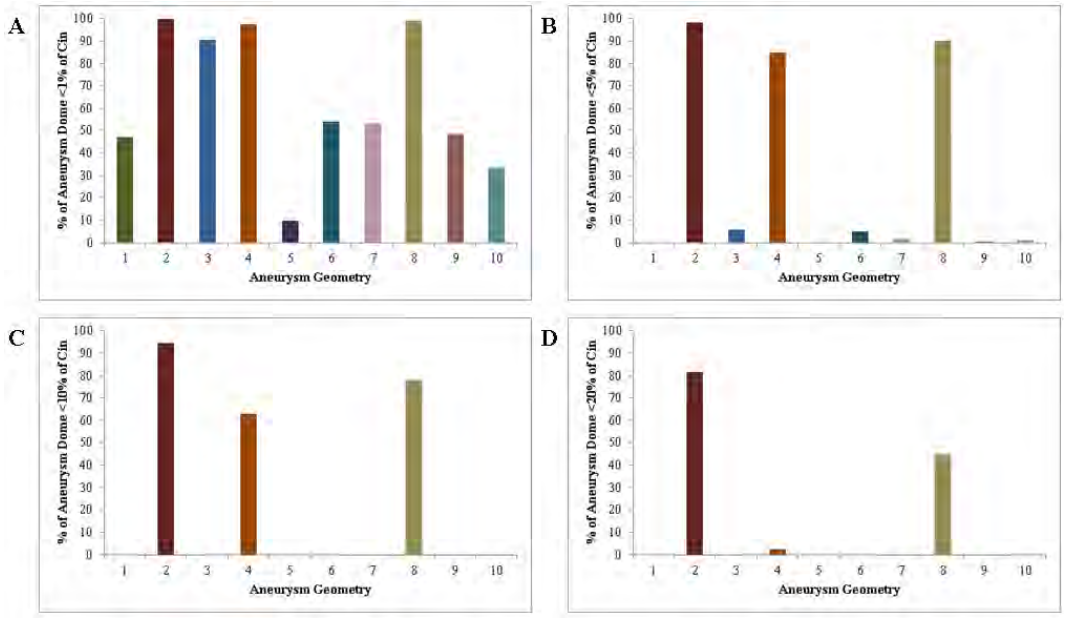

Figure 8.5: Percentage of aneurysm dome with concentration found under the threshold values of (A) 1% (B) 5% (C) 10% and (D) 20% of C_{in} for blind study aneurysm geometries 1-10

8.3.2 Rupture Prediction

Following measurement of the key geometric parameters and mass transport analysis, the rupture risk of each of the ten blind study aneurysms was calculated using the rupture probability equations developed based on geometric parameters, mass transport and a combination of both. The stability of the aneurysms was made available at this point, and can be found in Table 8.5. A label of unstable indicates that the aneurysm showed signs of growth or rupture, which stable aneurysms did not show signs of growth or rupture.

Table 8.5: Growth/ rupture status of blind study aneurysm geometries

Aneurysm	Rupture Status
1	Unstable
2	Stable
3	Stable
4	Unstable
5	Unstable
6	Unstable
7	Stable
8	Stable
9	Unstable
10	Unstable

Results from the rupture probability equations developed in Chapters 6 and 7 were compared to the actual growth and rupture status of the blind study aneurysms. The comparison of the actual status of the aneurysms to the predicted status was carried out using the individual rupture probability equations for geometric parameters and species threshold levels of 1%, 5%, 10% and 20% of C_{in} are shown in Table 8.6, with correctly predicted aneurysms highlighted in green. The total number of aneurysms with the correctly predicted stability status was also calculated.

Table 8.6: Comparison of predicted and actual growth or rupture status of aneurysms from rupture prediction equations developed using geometric parameters and species thresholds of 1%, 5%, 10% and 20% of C_{in}

Aneurysm	Actual Status	Predicted Status				
		Geometric Parameters	1% Threshold	5% Threshold	10% Threshold	20% Threshold
1	Unstable	Stable	Unstable	Stable	Stable	Stable
2	Stable	Stable	Stable	Stable	Unstable	Unstable
3	Stable	Stable	Stable	Stable	Stable	Stable
4	Unstable	Stable	Stable	Stable	Unstable	Stable
5	Unstable	Stable	Unstable	Stable	Stable	Stable
6	Unstable	Stable	Unstable	Stable	Stable	Stable
7	Stable	Stable	Unstable	Stable	Stable	Stable
8	Stable	Stable	Stable	Stable	Unstable	Unstable
9	Unstable	Stable	Unstable	Stable	Stable	Stable
10	Unstable	Stable	Unstable	Stable	Stable	Stable
Correct Predictions (/10)		**4**	**8**	**4**	**3**	**2**

Further comparisons were made between the actual stability of the aneurysms and the status that was predicted by the rupture probability equations developed using a combination of geometric parameters and species threshold levels of 1%, 5%, 10% and 20% of C_{in}. Results are shown in Table 8.7, where the correctly predicted aneurysms are again highlighted in green. The total number of aneurysms with the stability correctly predicted was also calculated.

Table 8.7: Comparison of predicted and actual stability status of aneurysms from rupture prediction equations developed combination of geometric parameters and species thresholds of 1%, 5%, 10% and 20% of C_{in} (GP = Geometric Parameters)

Aneurysm	Actual Status	Predicted Status			
		GP + 1% Threshold	GP + 5% Threshold	GP + 10% Threshold	GP + 20% Threshold
1	Unstable	Unstable	Unstable	Stable	Stable
2	Stable	Stable	Stable	Stable	Stable
3	Stable	Stable	Unstable	Stable	Stable
4	Unstable	Stable	Unstable	Stable	Stable
5	Unstable	Unstable	Unstable	Unstable	Stable
6	Unstable	Stable	Unstable	Stable	Stable
7	Stable	Stable	Unstable	Stable	Stable
8	Stable	Stable	Unstable	Stable	Stable
9	Unstable	Stable	Unstable	Stable	Stable
10	Unstable	Unstable	Unstable	Stable	Stable
Correct Predictions (/10)		**7**	**7**	**5**	**4**

Table 8.8 summarises the results of the rupture prediction equations, with the total number and percentage of the aneurysms that had a correctly predicted growth or rupture status for each of the predictive models developed in this study.

Table 8.8: Results from rupture prediction of blind study geometries compared to actual stability status (GP = Geometric Parameters)

Predictive Model	No. Correctly Predicted (/10)	% Correctly Predicted
<1% of C_{in} Threshold	8	80
GP +<1% of C_{in} Threshold	7	70
GP + <5% of C_{in} Threshold	7	70
GP + <10% of C_{in} Threshold	5	50
Geometric Parameters Only	4	40
<5% of C_{in} Threshold	4	40
GP + <20% of C_{in} Threshold	4	40
<10% of C_{in} Threshold	3	30
<20% of C_{in} Threshold	2	20

Looking at the results, it is clear that the most accurate predictive equation, predicting the stability of 80% of the aneurysms, was not any of the combined predictive models as originally hypothesised, instead involving the percentage of the aneurysm dome found below a threshold of 1% of C_{in} only. However, the combined predictive model of geometric features and the percentage of the aneurysm dome found below 1% of C_{in} was found to be reasonably accurate, predicting the stability status of 70% of the aneurysms. Similarly, the combined predictive model of geometric features and the

percentage of the aneurysm dome found below 5% of C_{in} was also found to predict the stability of 80% of the aneurysms. It is evident that the least accurate model was the predictive equation developed based on the percentage of the aneurysm dome with concentrations lower than 20% of C_{in}, correctly predicting only two of the ten aneurysms in the sample set.

8.4 Discussion

In this chapter, the hypothesis that the rupture of cerebral aneurysms is related to a combined relationship of geometric parameters and mass transport of blood-borne species was tested. Following the development of rupture prediction models based on geometric parameters, mass transport, and a combination of the two, an attempt was made to predict the rupture or stability status of an independent cohort of ten patient-specific cerebral aneurysms in which the status was kept blinded until after the predictions had been made.

Results of the mass transport simulations of ATP within the blind study geometries demonstrated similar results to those seen in the patient-specific aneurysms described in Chapter 7, with the concentration distribution influenced strongly by the geometry of the aneurysm and the resulting flow haemodynamics. Areas of high WSS were found at the neck as the flow enters the aneurysm, and throughout parts of the aneurysm where the inflow jet penetrates the dome at increased velocity. These areas of elevated WSS corresponded to higher concentration values, typically equal or close to the inlet concentration. Aneurysms with large, high velocity recirculation regions that filled the entire aneurysm dome saw more uniform, higher concentration distributions as good washout of the species occurred as a result of the high velocity flow recirculation. In contrast, aneurysms demonstrating areas of low WSS as a result of low velocity flow within the dome also displayed corresponding areas of low concentration, indicating an under-expression of species at the aneurysm wall. Similar to the results seen previously, the smoother, more spherical aneurysms saw a more uniform concentration distribution, with the unusual-shaped, undulating aneurysms demonstrating a localised depletion of species.

Using results from the geometric measurement and mass transport analysis of the blind study geometries, the rupture probability equations developed in Chapter 6 and

Chapter 7 were used to predict the rupture status of the ten blind study geometries. Results were then compared to the actual rupture status, where it was determined that the rupture probability equation developed based only on the percentage of the aneurysm dome with concentration values less than a threshold of 1% of C_{in} predicted the stability of the aneurysms with greatest accuracy, followed by the combined probability equation relating to geometric parameters and 1% species threshold, and the combined probability equation relating to geometric parameters and 5% species threshold. However, it must be noted that due to the small sample size used to develop the rupture probability equations, results are not significant and so can only give an indication as to the relationship between geometric parameters, mass transport and rupture.

Results from the blind study indicate that the hypothesis that aneurysm rupture is related to geometric parameters and the mass transport of blood-borne species is upheld, although it is not found to be statistically significant. Using the combined model, which correctly predicted the status of 70% of the blind study models, it can be concluded that aneurysms are at greater risk of rupture if they are bifurcating in shape, with increasing tilt angle, with increasing aspect ratio, and with an increasing amount of their dome found to have concentration values lower than 1% of C_{in}.

CHAPTER 9

DISCUSSION, CONCLUSIONS AND RECOMMENDATIONS FOR FUTURE WORK

Chapter 9 Discussion, Conclusions and Recommendations for Future Work

9.1 Discussion

High rates of morbidity and mortality are associated with the rupture of a cerebral aneurysm, as approximately 12% of patients who suffer a subarachnoid haemorrhage as a result of a ruptured aneurysm die immediately. A further 40% die within one month, and one third of survivors suffer neurological defects as a result of rupture (Schievink 1997). Improved imaging techniques has allowed for better detection of unruptured aneurysms (Dillard *et al.* 2014). However, the management of unruptured aneurysms is controversial, as interventional techniques such as clipping and coiling pose serious risks for the patient. To date, aneurysm risk stratification is based on the size of the aneurysm, with larger aneurysms believed to be at risk of rupture. However, studies have proven that size alone cannot adequately predict rupture, with large aneurysms remaining stable, while smaller aneurysms have been found to rupture (Beck *et al.* 2006, Lall *et al.* 2009). Therefore, the development of a reliable rupture prediction method is of utmost importance, allowing the rupture potential of an aneurysm to be determined. Although a distinct rupture prediction method is yet to be established, previous studies have demonstrated that rupture is related to geometric parameters and flow haemodynamics including wall shear stress (Cebral *et al.* 2011c, Meng *et al.* 2013, Raghavan *et al.* 2005, J. Xiang *et al.* 2011).

A hypothesis is presented in this study that suggests that the geometric features that define the shape of the aneurysm (i.e. height, neck width, diameter etc.) may influence the mass transport of vital blood-borne species within the aneurysm dome, leading to either an under-expression or saturation of species at the aneurysm wall, which may in turn lead to localised negative wall remodelling, growth and eventual rupture. It is proposed that a combination of geometric parameters and an under-expression of species may be used to predict the rupture of cerebral aneurysms. Accordingly, the main objective of this study was to use computational methods to establish if a relationship exists between cerebral aneurysm rupture and both geometric parameters and species concentrations. Further sub-objectives involved using experimental methods to validate the computational analyses, investigating if representative models could be used as an alternative to complex patient-specific geometries, and

investigating the influence of different species on the mass transport seen in aneurysms.

A study was carried out into the relationship between geometric and morphological parameters and cerebral aneurysm rupture, which is presented in Chapter 6. Although numerous studies have been conducted throughout literature into the influence of geometric and morphological parameters on cerebral aneurysm rupture, many of the parameters investigated cannot be directly measured using 3D scans. It would be of great clinical value if a relationship could be established between radiologically measurable parameters and aneurysm rupture, allowing for immediate decisions to be made regarding treatment of unruptured aneurysms. In the study of the relationship between 10 radiologically measureable parameters (location, shape, size, neck size, height, neck width, diameter, distance to maximum diameter, tilt angle and aspect ratio) and cerebral aneurysm rupture, statistical analysis was performed on 168 aneurysms from 13 locations throughout the CoW. Results from the study led to the development of a rupture probability equation, which is used to determine the probability of an aneurysm rupturing or remaining stable. Due to previous studies suggesting a critical size of aneurysm rupture, it was expected that the size of the aneurysm would influence the risk of rupture. However, this was not the case, with aneurysm diameter failing to demonstrate any multivariate relationship with rupture. The geometric study, which indicated that the odds of an aneurysm rupturing are increased with posterior location, bifurcating shape, increasing tilt angle and increasing aspect ratio, showed similar results to previous studies (Dhar *et al.* 2008, Lall *et al.* 2009, Ujiie *et al.* 1999, Ujiie *et al.* 2001) and so it was not surprising that these parameters were found to relate to rupture.

The computational study of mass transport within patient-specific aneurysms, which is presented in Chapter 7, suggested that the mass transport within aneurysms is strongly influenced by flow haemodynamics, which are in turn influenced by the shape of the aneurysm and its surrounding parent artery geometry. The distribution of concentration within the aneurysm dome was dictated by the flow of blood throughout the dome, indicating that the mass transport was convection dominated for all geometries. In general, bifurcation aneurysms tended to have higher concentrations and more uniform concentration distributions. This is as a result of the configuration of the parent artery. In most bifurcation cases, the main arterial flow is convected directly into the aneurysm dome, impinges near the top of the dome and forms

recirculating regions before exiting the aneurysm and continuing into the daughter arteries. This is not the case for many of the lateral aneurysms, as the majority of the flow bypasses the dome, with smaller inflow jets typically entering the dome at the distal side, penetrating into the aneurysm before forming a large recirculation region. As a result, higher concentrations in the lateral aneurysm tend to be seen towards the distal side of the aneurysm, corresponding to the inflow jet, while the higher concentration areas within the bifurcation geometries are more dispersed throughout the dome.

A relationship between WSS and concentration distribution is evident from the results, with areas of high WSS corresponding with high concentration values for all aneurysms investigated. This is particularly evident at the neck of the aneurysm, where the inflow jet enters the dome. Furthermore, increases in WSS are found throughout the dome along the inflow jet as it penetrates into the aneurysm, and near the impingement point on the aneurysm wall. Similarly, low WSS is found to relate to decreased concentration, with areas of low WSS that result from slow-moving flow vortices displaying reduced concentration levels. Therefore, results from this study support the low WSS rupture theory described by Meng *et al.* (2013).

In the aneurysms that demonstrated simple flow patterns with a single large recirculation region filling the aneurysm dome, the concentration tended to be almost uniform, reaching close to the inlet concentration as the aneurysm experiences good washout of species. Conversely, aneurysms with complex flow including small, slow-moving vortices tended to have localised concentration depletion. These concentration patterns appear to be influenced by the morphology of the aneurysm, as spherical, smooth aneurysms tended to have more uniform concentrations that equalled or came close to the inlet concentration, while the more unusual shaped aneurysms that contained aneurysmal blebs or undulations demonstrated localised concentration depletion as a result of the lack of species supplied from the main arterial flow.

It has been suggested in previous studies that rupture is a localised process that occurs due to wall weaknesses, where the wall stress exceeds the wall strength (Cebral and Raschi 2013) and so it is hypothesised in the current study that aneurysms with areas throughout the dome that demonstrate low concentration levels could be at risk of rupture, due to an under-expression of blood-borne species, leading to negative wall remodelling, growth and eventual rupture. Due to a lack of information regarding the

amount of species depletion that could be considered pathogenic, species threshold levels of 1%, 5%, 10% and 20% of the inlet concentration are proposed. Together with results from geometric parameter study, rupture probability equations were developed that indicated the risk of an aneurysm rupturing based on geometric parameters, mass transport species thresholds and a combination of both.

The viability of the rupture probability equations was tested on an independent cohort of 10 aneurysm geometries in a blind study. Results indicated that the most accurate prediction of the stability status of the aneurysms was for the rupture probability equation developed using the 1% threshold, followed by the combined prediction model based on the geometric parameters and the 1% threshold and the combined prediction model based on the geometric parameters and the 5% threshold. Although the results are not statistically significant, it is suggested from this study that aneurysms a high percentage of the aneurysm dome found under a threshold of 1% of the species inlet concentration are at risk of negative wall remodelling, growth and rupture, and should be recommended for treatment.

Although one would expect that an aneurysm with areas of the dome at concentration values of less than 10% or 20% of C_{in} would be at higher risk of rupture due to a greater under-expression of species, results indicate that for all anerysms investigated, the amount of the dome exposed to concentration levels less than 1% of C_{in} is greater than for the higher threshold values of 5%, 10% and 20% of C_{in}. It could therefore be postulated that with a greater percentage of the dome exposed to low concentration values, the rate of negative remodelling may be higher and thus the risk of rupture would increase.

One limitation of the combined prediction models that should be noted is that for the original rupture probability equation developed based on geometric parameters alone, aneurysms of the posterior circulation were found to be more likely to rupture. However, the twelve patient-specific aneurysm geometries used in the development of the combined prediction models are all found in the anterior circulation, and so posterior location no longer becomes a parameter associated with rupture. Therefore, if the sample size of twelve geometries was increased to include anerysms of the posterior circulation, the final prediction models could be altered to include these findings.

As medical imaging techniques have improved, the use of patient-specific geometries for computational modelling of flow within cerebral aneurysms has increased. However, patient-specific models are computationally intensive and require patient-specific flow data that isn't typically extracted during standard medical procedures. Idealised models are more simplified in nature and provide generalised information regarding flow patterns and haemodynamics, but cannot provide accurate information due to their simplified geometries and flow conditions. Therefore, the use of representative models was proposed in this study as a compromise between idealised and patient-specific models. The representative models were developed using key patient-specific measurements taken from patient-specific models, with the intention of investigating if representative geometries can accurately predict the mass transport within patient-specific geometries. The representative geometries gave improved information on WSS and concentration distributions when compared to the idealised geometries, but were unable to accurately capture the patterns seen within the aneurysm domes. This is due to the representative geometries neglecting to capture the undulations and aneurysmal blebs found within the patient-specific models. However, promising results are seen on comparison of the percentage of the aneurysm dome found below the different species threshold values. Excellent agreement is seen between the representative and patient-specific geometries at a threshold of 1%, which has been demonstrated to act as an indicator of aneurysm rupture potential. Therefore, although representative versions of patient-specific geometries cannot capture the haemodynamics or concentration distributions seen within the patient-specific geometries, they can accurately represent the amount of the dome found to have concentration values below a species threshold of 1% of C_{in}, thus allowing a prediction of rupture potential to be made.

The experimental validation of the computational methods used in this study, which is presented in Chapter 5, allowed for a comparison to be made between the build-up and long term concentration distribution seen in experimental and computational models of patient-specific lateral aneurysms. Excellent agreement is seen between the long-term distribution of species at the aneurysm wall, with the experimental results falling within ±2% of the computational results for both lateral models investigated. However, differences are evident in the initial stages of the experiment, as the concentration builds up at the aneurysm wall. In the experimental results, the concentration slowly builds up at the aneurysm wall over a period of 3-5 minutes,

before reaching its long-term distribution value. This slow build up is not echoed by the computational results, and can be attributed to the water that is present in the system before the experimental analysis is conducted. As a result, the dye has to diffuse through the water to the aneurysm wall, rather than being convected straight into the aneurysm dome. However, the differences seen in the initial stages are negligible for the current study, as it is the long-term concentration distribution and its relationship with rupture that is of interest.

9.2 Conclusions

- Representative geometries cannot adequately represent the WSS and concentration distribution seen within patient-specific aneurysms. However, representative geometries can accurately predict the amount of the aneurysm dome exposed to concentrations less than 1% of C_{in}.
- Assumptions of a rigid wall, Newtonian fluid and steady-state flow condition are appropriate for this study, reducing the complexity of modelling blood flow and mass transport of species within 3D patient-specific cerebral aneurysms.
- Results of an investigation into the relationship between geometric parameters and cerebral aneurysm growth and rupture indicate that the odds of an aneurysm rupturing increase if it is of the posterior circulation, if it is bifurcating in shape, with increasing tilt angle and with increasing aspect ratio.
- Rupture probability equations were tested on a cohort of 10 blinded cerebral aneurysm geometries, with results suggesting that rupture prediction based on the amount of the aneurysm dome exposed to species concentrations less than 1% of the inlet concentration is the most accurate, followed by a combined predictive model based on geometric parameters and the amount of the dome exposed to concentrations less than 1% of the inlet concentration and a combined predictive model based on geometric parameters and the amount of the dome exposed to concentrations less than 5% of the inlet concentration.
- Results from this study are not just applicable to ATP, but can be applied to other species of low diffusivity. However, the mechanism of transport across the wall should be considered, as it can influence whether a depletion or saturation of species occurs.

9.3 Recommendations for Future Work

The overall objective of this study was to investigate the relationship between geometric parameters, the mass transport of blood-borne species, and cerebral aneurysm growth and rupture potential. Although the conclusions presented in this study contribute advancements to research into cerebral aneurysm growth and rupture risk, the methods used and the findings of the study are not exhaustive. Therefore, in this section some recommendations for future work are presented that would further the research conducted in this study, adding to existing knowledge regarding geometric parameters, mass transport and cerebral aneurysm growth and rupture potential.

- **Increase Sample Size**

One of the main limitations of this study is the size of the aneurysm cohort that is used to develop the rupture prediction models based on geometric features and on the amount of the aneurysm dome that is exposed to low species concentration levels. In this study, the sample size was restricted to a database of 168 patient-specific aneurysms, as a subset of the @neurIST database was used to develop a rupture prediction equation based on the key geometric parameters that can be linked with growth and rupture. Furthermore, due to the time involved in computationally modelling the mass transport within patient-specific cerebral aneurysm geometries, the mass transport of species within just 12 geometries from the database of 168 patient-specific aneurysms were investigated, along with the 10 blind study geometries. Comsol uses all available processor cores and large amounts of physical RAM memory. The computer used in this study contained just four processors and 14 GB of RAM, and so a typical mass transport simulation carried out on a mesh size of ~850,000 cells took at least a week to solve. Therefore, the amount of mass transport simulations run for the study was restricted by the time taken for each simulation to solve.

The power of a statistical test in the determination of differences between groups (e.g. unruptured/ruptured aneurysms) is heavily influenced by the sample size, among other factors. As the sample size increases, the power of the statistical test increases dramatically. Therefore, a low sample size can affect the significance of the results. It

is suggested by Stevens (2012) that the power of the test is not an issue with larger sample sizes i.e. >100 subjects per group. However, in the study of the relationship between geometric parameters and aneurysm growth and rupture, the unruptured group contains just 98 aneurysms, while the ruptured group consists of 70 aneurysms. Therefore, the power of the test is compromised. Furthermore, the aneurysms used in the investigation of the relationship between mass transport and aneurysm growth and rupture contained sample sizes of 7 and 5 aneurysms for the unruptured and ruptured groups respectively, reducing the power of the statistical analysis significantly.

Therefore, if the sample size could be increased, the reliability and significance of the statistical tests would be increased, improving confidence in the results and further elucidating the relationship between geometric parameters, mass transport and cerebral aneurysms.

- **CFD Challenge**

Following from the original ASME 2012 Summer Bioengineering Conference CFD Challenge and from the CFD Rupture Challenge 2013, an International Aneurysm CFD Challenge 2015 has recently been announced that aims to establish (1) what variability can be seen within aneurysm geometries as a result of image segmentation (2) what differences are seen between CFD results if the surface and boundary conditions are not provided and (3) is CFD adding value with respect to rupture risk prediction?

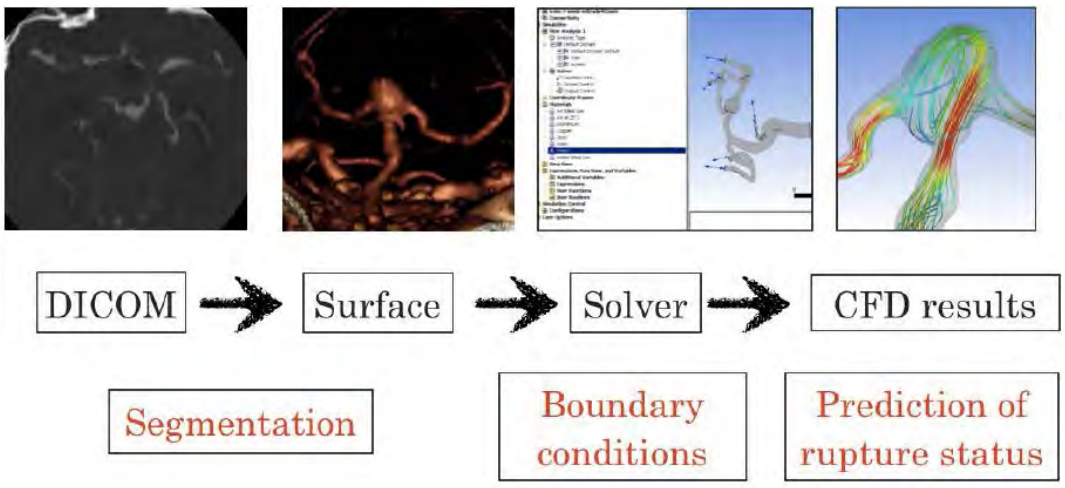

Figure 9.1: Steps involved in CFD Challenge 2015

The steps involved in the CFD challenge are illustrated in Figure 9.1. The first phase of the challenge involves the participants being supplied with DICOM data of 5 MCA aneurysms and using whatever rationale or hypothesis the group deems to be appropriate, the rupture status of the 5 aneurysms is to be predicted. Following Phase 1, additional CFD simulations may be required in an attempt to differentiate between effects of segmentation and boundary conditions. It is planned that results from Phase 1 will be presented at a workshop at the Summer Biomechanics, Bioengineering and Biotransport Conference in Utah, USA in June 2015 and at the Intracranial Stent Meeting which takes place in Australia in November 2015.

The CABER group intend to submit results to this challenge using three different computational softwares (Ansys Fluent 12.1.4, StarCCM+ 6.04.016 and Comsol Multiphysics 4.4), with the hypothesis used for rupture prediction based on results from this study. Therefore, the rupture status of the aneurysms will be predicted based on a combination of geometric features and the under-expression of species concentration seen within the aneurysm dome. It is hoped that through the testing of the hypothesis that aneurysm growth and rupture can be predicted based on a combination of geometric parameters and mass transport on another independent blinded sample, further confidence in the results and conclusions taken from this study can be achieved.

REFERENCES

REFERENCES

Ai, L. and Vafai, K. (2006) 'A coupling model for macromolecule transport in a stenosed arterial wall', *International Journal of Heat and Mass Transfer,* 49(9-10), 1568-1591.

Alastruey, J., Parker, K. H., Peiró, J., Byrd, S. M. and Sherwin, S. J. (2007) 'Modelling the circle of Willis to assess the effects of anatomical variations and occlusions on cerebral flows', *Journal of Biomechanics,* 40(8), 1794-1805.

Alnaes, M. S., Isaksen, J., Mardal, K. A., Romner, B., Morgan, M. K. and Ingebrigtsen, T. (2007) 'Computation of Hemodynamics in the Circle of Willis', *Stroke,* 38, 2500-2505.

Amili, O. and Fatouraee, N. (2005) *Lipoprotein Transport in the Blood Stream to the Arterial Wall in a Carotid Artery Bifurcation,* Shanghai, China: 2264-2267.

Appanaboyina, S., Mut, F., Löhner, R., Putman, C. M. and Cebral, J. R. (2008) 'Computational fluid dynamics of stented intracranial aneurysms using adaptive embedded unstructured grids', *International Journal for Numerical Methods in Fluids,* 57(5), 475-493.

Babiker, M. H., Gonzalez, L. F., Albuquerque, F., Collins, D., Elvikis, A. and Frakes, D. (2010) 'Quantitative Effects of Coil Packing Density on Cerebral Aneurysm Fluid Dynamics: An In Vitro Steady Flow Study', *Annals of Biomedical Engineering,* 38(7), 2293-2301.

Bacigaluppi, S., Piccinelli, M., Antiga, L., Veneziani, A., Passerini, T., Rampini, P., Zavanone, M., Severi, P., Tredici, G., Zona, G., Krings, T., Boccardi, E., Penco, S. and Fontanella, M. (2014) 'Factors affecting formation and rupture of intracranial saccular aneurysms', *Neurosurgical Review,* 37(1), 1-14.

Baharoglu, M. I., Schirmer, C. M., Hoit, D. A., Gao, B. L. and Malek, A. M. (2010) 'Aneurysm Inflow-Angle as a Discriminant for Rupture in Sidewall Cerebral Aneurysms: morphometric and computational fluid dynamic analysis', *Stroke,* 41, 1423-1430.

Balakrishnan, B., Dooley, J. F., Kopia, G. and Edelman, E. R. (2007) 'Intravascular drug release kinetics dictate arterial drug deposition, retention, and distribution', *Journal of Controlled Release,* 123(2), 100-108.

Ball, D. W. (2001) *The Basics of Spectroscopy,* WA, USA: SPIE - The International Society for Optical Engineering.

Baumann, F., Khan, N. and Yonekawa, Y. (2008) 'Patient and aneurysm characteristics in multiple intracranial aneurysms' in Yonekawa, Y., Tsukahara, T., Valavanis, A. and Khan, N., eds., *Changing Aspects in Stroke Surgery: Aneurysms, Dissections, Moyamoya Angiopathy and EC-IC Bypass*, Springer Vienna, 19-28.

Bazilevs, Y., Hsu, M. C., Zhang, Y., Wang, W., Liang, X., Kvamsdal, T., Brekken, R. and Isaksen, J. G. (2010) 'A fully-coupled fluid-structure interaction simulation of cerebral aneurysms', *Computational Mechanics,* 46(1), 3-16.

Beck, J., Rohde, S., Berkefeld, J., Seifert, V. and Raabe, A. (2006) 'Size and Location of Ruptured and Unruptured Intracranial Aneurysms Measured By 3-Dimensional Rotational Angiography', *Surgical Neurology,* 65(1), 18-25.

Beck, J., Rohde, S., el Beltagy, M., Zimmermann, M., Berkefeld, J., Seifert, V. and Raabe, A. (2003) 'Difference in configuration of ruptured and unruptured intracranial aneurysms determined by biplanar digital subtraction angiography', *Acta Neurochirurgica,* 145(10), 861-865.

Bederson, J. B., Awad, I. A., Wiebers, D. O., Piepgras, D., Haley, E. C., Brott, T., Hademenos, G., Chyatte, D., Rosenwasser, R. and Caroselli, C. (2000) 'Recommendations for the Management of Patients With Unruptured Intracranial Aneurysms: A Statement for Healthcare Professionals From the Stroke Council of the American Heart Association', *Circulation,* 102(18), 2300-2308.

Boussel, L., Rayz, V., McCulloch, C., Martin, A., Acevedo-Bolton, G., Lawton, M., Higashida, R., Smith, W. S., Young, W. L. and Saloner, D. (2008) 'Aneurysm Growth Occurs at Region of Low Wall Shear Stress: Patient-Specific Correlation of Hemodynamics and Growth in a Longitudinal Study', *Stroke,* 39(11), 2997-3002.

Boyd, J., Buick, J. M. and Green, S. (2007) 'Analysis of the Casson and Carreau-Yasuda non-Newtonian blood models in steady and oscillatory flows using the lattice Boltzmann method', *Physics of Fluids,* 19(9), 093103.

Brisman, J. L., Song, J. K. and Newell, D. W. (2006) 'Cerebral Aneurysms', *The New England Journal of Medicine,* 355(9), 928-939.

Campi, A., Ramzi, N., Molyneux, A. J., Summers, P. E., Kerr, R. S. C., Sneade, M., Yarnold, J. A., Rischmiller, J. and Byrne, J. V. (2007) 'Retreatment of Ruptured Cerebral Aneurysms in Patients Randomized by Coiling or Clipping

in the International Subarachnoid Aneurysm Trial (ISAT)', *Stroke,* 38, 1538-1544.

Carroll, G. T., Devereux, P. D., Ku, D. N., McGloughlin, T. M. and Walsh, M. T. (2010) 'Experimental validation of convection-diffusion discretisation scheme employed for computational modelling of biological mass transport', *BioMedical Engineering OnLine,* 9(34).

Castro, M. A., Putman, C. M. and Cebral, J. R. (2006) 'Computational Fluid Dynamics Modeling of Intracranial Aneurysms: Effects of Parent Artery Segmentation on Intra-Aneurysmal Hemodynamics', *American Journal of Neuroradiology,* 27, 1703-1709.

Cebral, J. R., Castro, M. A., Appanaboyina, S., Putman, C. M., Millan, D. and Frangi, A. F. (2005a) 'Efficient Pipeline for Image-Based Specific Analysis of Cerebral Aneurysm Hemodynamics: Technique and Sensitivity', *IEEE Transactions of Medical Imaging,* 24(4), 457-467.

Cebral, J. R., Castro, M. A., Burgess, J. E., Pergolizzi, R. S., Sheridan, M. J. and Putman, C. M. (2005b) 'Characterization of Cerebral Aneurysms for Assessing Risk of Rupture by Using Patient-Specific Computational Hemodynamics Models', *American Journal of Neuroradiology,* 26, 2550-2559.

Cebral, J. R., Castro, M. A., Millan, D., Frangi, A. F. and Putman, C. (2005) *Pilot clinical study of aneurysm rupture using image-based computational fluid dynamics models,* 245-256.

Cebral, J. R., Castro, M. A., Putman, C. M. and Alperin, N. (2008) 'Flow-area relationship in internal carotid and vertebral arteries', *Physiological Measurement,* 29(5), 585-594.

Cebral, J. R., Castro, M. A., Soto, O., Lohner, R. and Alperin, N. (2003) 'Blood-flow models of the circle of Willis from magnetic resonance data', *Journal of Engineering Mathematics,* 47(3-4), 369 - 386.

Cebral, J. R., Mut, F., Löhner, R. and Putman, C. M. (2010) 'Computational Analysis of Blood Flow Characteristics in Intracranial Aneurysms', *Mecánica Computacional,* XXIX(59), 5913-5927.

Cebral, J. R., Mut, F., Raschi, M., Scrivano, E., Ceratto, R., Lylyk, P. and Putman, C. M. (2011a) 'Aneurysm Rupture Following Treatment with Flow-Diverting Stents: Computational Hemodynamics Analysis of Treatment', *American Journal of Neuroradiology,* 32, 27-33.

Cebral, J. R., Mut, F., Weir, J. and Putman, C. (2011b) 'Quantitative Characterization of the Hemodynamic Environment in Ruptured and Unruptured Brain Aneurysms', *American Journal of Neuroradiology,* 32, 145-151.

Cebral, J. R., Mut, F., Weir, J. and Putman, C. M. (2011c) 'Association of Hemodynamic Characteristics and Cerebral Aneurysm Rupture', *American Journal of Neuroradiology,* 32, 264-270.

Cebral, J. R. and Raschi, M. (2013) 'Suggested Connections Between Risk Factors of Intracranial Aneurysms: A Review', *Annals of Biomedical Engineering,* 41(7), 1366-1383.

Chen, J., Gutmark, E., Mylavarapu, G., Backeljauw, P. F. and Gutmark-Little, I. (2014) 'Numerical investigation of mass transport through patient-specific deformed aortae', *Journal of Biomechanics,* 47(2), 544-552.

Chen, J. and Lu, X.-Y. (2004) 'Numerical investigation of the non-Newtonian blood flow in a bifurcation model with a non-planar branch', *Journal of Biomechanics,* 37(12), 1899-1911.

Chien, A., Sayre, J. and Viñuela, F. (2013) 'Quantitative comparison of the dynamic flow waveform changes in 12 ruptured and 29 unruptured ICA–ophthalmic artery aneurysms', *Neuroradiology,* 55(3), 313-320.

Choi, H. W., Ferrara, K. W. and Barakat, A. I. (2007) 'Modulation of ATP/ADP Concentration at the Endothelial Surface by Shear Stress: Effect of Flow Recirculation', *Annals of Biomedical Engineering,* 35(4), 505-516.

Choi, I. S. and David, C. (2003) 'Giant Intracranial Aneurysms: Development, Clinical Presentation and Treatment', *European Journal of Radiology,* 46(3), 178-194.

Chung, S. and Vafai, K. (2012) 'Effect of the fluid–structure interactions on low-density lipoprotein transport within a multi-layered arterial wall', *Journal of Biomechanics,* 45(2), 371-381.

Chung, S. and Vafai, K. (2014) 'Mechanobiology of Low-Density Lipoprotein Transport within an Arterial Wall - Impact of Hypothermia and Coupling Effects', *Journal of Biomechanics,* 47(1), 137-147.

Cieslicki, K. and Ciesla, D. (2005) 'Investigations of flow and pressure distributions in physical model of the circle of Willis', *Journal of Biomechanics,* 38(11), 2302-2310.

Comerford, A. and David, T. (2008) 'Computer Model of Nucleotide Transport in a Realistic Porcine Aortic Trifurcation', *Annals of Biomedical Engineering,* 36(7), 1175-1187.

Comerford, A., David, T. and Plank, M. (2006) 'Effects of Arterial Bifurcation Geometry on Nucleotide Concentration at the Endothelium', *Annals of Biomedical Engineering,* 34(4), 605-617.

COMSOL (2012) 'The Chemical Species Transport Branch' in *COMSOL Multiphysics User's Guide*, Sweden: COMSOL, 652-667.

Costalat, V., Sanchez, M., Ambard, D., Thines, L., Lonjon, N., Nicoud, F., Brunel, H., Lejeune, J. P., Dufour, H., Bouillot, P., Lhaldky, J. P., Kouri, K., Segnarbieux, F., Maurage, C. A., Lobotesis, K., Villa-Uriol, M. C., Zhang, C., Frangi, A. F., Mercier, G., Bonafé, A., Sarry, L. and Jourdan, F. (2011) 'Biomechanical wall properties of human intracranial aneurysms resected following surgical clipping (IRRAs Project)', *Journal of Biomechanics,* 44(15), 2685-2691.

Datta, A. and Rakesh, V. (2010) *An Introduction to Modeling of Transport Processes,* New York: Cambridge University Press.

David, T. (2003) 'Wall Shear Stress Modulation of ATP/ADP Concentration at the Endothelium', *Annals of Biomedical Engineering,* 31(10), 1231-1237.

Devault, K., Gremaud, P. A., Novak, V., Olufsen, M. S., Vernieres, G. and Zhao, P. (2008) 'Blood Flow in the Circle of Willis: Modeling and Calibration', *Multiscale Modeling & Simulation,* 7(2), 888 - 909.

Dhar, S., Tremmel, M., Mocco, J., Kim, M., Yamamoto, J., Siddiqui, A. H., Hopkins, L. N. and Meng, H. (2008) 'Morphology parameters for intracranial aneurysm rupture risk assessment', *Neurosurgery,* 63(2), 185-197.

Dillard, S. I., Mousel, J. A., Shrestha, L., Raghavan, M. L. and Vigmostad, S. C. (2014) 'From medical images to flow computations without user-generated meshes', *International Journal for Numerical Methods in Biomedical Engineering,* 30(10), 1057-1083.

Ernemann, U. U., Grönewäller, E., Duffner, F. B., Guervit, O., Claassen, J. and Skalej, M. D. (2003) 'Influence of Geometric and Hemodynamic Parameters on Aneurysm Visualization during Three-Dimensional Rotational Angiography: An in Vitro Study', *American Journal of Neuroradiology,* 24(4), 597-603.

Ethier, C. R. (2002) 'Computational Modeling of Mass Transfer and Links to Atherosclerosis', *Annals of Biomedical Engineering,* 30(4), 461-471.

Fahrig, R., Nikolov, H., Fox, A. J. and Holdsworth, D. W. (1999) 'A three-dimensional cerebrovascular flow phantom', *The International Journal of Medical Physics Research and Practice,* 26(8), 1589-1599.

Fahy, P., Delassus, P., McCarthy, P., Sultan, S., Hynes, N. and Morris, L. (2013) 'An In Vitro Assessment of the Cerebral Hemodynamics Through Three Patient Specific Circle of Willis Geometries', *Journal of Biomechanical Engineering,* 136(1), 011007-011007.

Fisher, C. and Rossmann, J. S. (2009) 'Effect of Non-Newtonian Behavior on Hemodynamics of Cerebral Aneurysms', *Journal of Biomechanical Engineering,* 131(9).

Ford, M. D., Alperin, N., Lee, S. H., Holdsworth, D. W. and Steinman, D. A. (2005) 'Characterization of Volumetric flow rate waveforms in the normal internal carotid and vertebral arteries', *Physiological Measurement,* 26, 477-488.

Ford, M. D., Nikolov, H., Milner, J. S., Lownie, S. P., Demont, E. M., Kalata, W., Loth, F., Holdsworth, D. W. and Steinman, D. A. (2008) 'PIV-measured versus CFD-predicted flow dynamics in an atomically realistic cerebral aneurysm models', *Journal of Biomechanical Engineering,* 130(2).

Foutrakis, G. N., Yonas, H. and Sclabassi, R. J. (1999) 'Saccular Aneurysm Formation in Curved and Bifurcating Arteries', *American Journal of Neuroradiology,* 20, 1309-1317.

Friedman, M. H. (2008) *Principles and Models of Biological Transport,* New York: Springer Science + Business Media, LLC.

Geers, A. J., Larrabide, I., Morales, H. G. and Frangi, A. F. (2014) 'Approximating hemodynamics of cerebral aneurysms with steady flow simulations', *Journal of Biomechanics,* 47(1), 178-185.

Geers, A. J., Larrabide, I., Radaelli, A. G., Bogunovic, H., Kim, M., Gratama van Andel, H. A. F., Majoie, C. B., VanBavel, E. and Frangi, A. F. (2011) 'Patient-Specific Computational Hemodynamics of Intracranial Aneurysms from 3D Rotational Angiography and CT Angiography: An In Vivo Reproducibility Study', *American Journal of Neuroradiology,* 32(3), 581-586.

Geyer, J. D. and Gomez, C. R. (2009) *Stroke: A Practical Approach,* Philadelphia: Lippincott Williams and Williams.

Gijsen, F. J. H., van de Vosse, F. N. and Janssen, J. D. (1999) 'The influence of the non-Newtonian properties of blood on the flow in large arteries: steady flow in a carotid bifurcation model', *Journal of Biomechanics,* 32(6), 601-608.

Gordon, J. L. (1986) 'Extracellular ATP: effects, sources and fate.', *Biochemical Journal,* 233, 309-319.

Goubergrits, L., Schaller, J., Kertzscher, U., van den Bruck, N., Poethkow, K., Petz, C., Hege, H.-C. and Spuler, A. (2012) 'Statistical wall shear stress maps of ruptured and unruptured middle cerebral artery aneurysms', *Journal of the Royal Society Interface,* 9(69), 677-688.

Gussenhoven, E. J., Essed, C. E., Lancee, C. T., Mastik, F., Frietman, P., Egmond, F. C. v., Reiber, J., Bosch, H., Urk, H. v., Roelandt, J. and Bom, N. (1989) 'Arterial Wall Characteristics Determined by Intravascular Ultrasound Imaging: An in vitro study', *Journal of the American College of Cardiology,* 14(4), 947-952.

Gutti, B., Susu, A. and Fasanmade, O. (2012) 'Mass Transport in Arteries and the Localization of Atherosclerosis in Human', *International Journal of Engineering and Applied Sciences,* 2(3), 53-62.

Hademenos, G. J., Massoud, T. F., Turjman, F. and Sayre, J. W. (1998) 'Anatomical and morphological factors correlating with rupture of intracranial aneurysms in patients referred for endovascular treatment', *Neuroradiology,* 40(11), 755-760.

Haljasmaa, I. V., Robertson, A. M. and Galdi, G. P. (2001) 'On the Effect of Apex Geometry on Wall Shear Stress and Pressure in Two-Dimensional Models of Arterial Bifurcations', *Mathematical Models and Methods in Applied Sciences,* 11(3), 499-520.

Hartkamp, M. J., Grond, J. v. d., Everdingen, K. J. v., Hillen, B. and Mali, W. P. T. M. (1999) 'Circle of Willis Collateral Flow Investigated by Magnetic Resonance Angiography', *Stroke,* 30, 2671-2678.

Hashimoto, T., Meng, H. and Young, W. L. (2006) 'Intracranial aneurysms: links among inflammation, hemodynamics and vascular remodeling', *Neurological Research,* 28(4), 372-380.

Hoi, Y., Meng, H., Woodward, S. H., Bendok, B. R., Hanei, R. A., Guterman, L. R. and Hopkins, L. N. (2004) 'Effects of arterial geometry on aneurysm growth: three-dimensional computational fluid dynamics study', *Journal of Neurosurgery,* 101(4), 676-681.

Holzapfel, G. A. and Gasser, T. C. (2000) 'A New Constitutive Framework for Arterial Wall Mechanics and a Comparative Study of Material Models', *Journal of Elasticity,* 61(1-3), 1-48.

Imai, Y., Sato, K., Ishikawa, T., Comerford, A., David, T. and Yamaguchi, T. (2010) 'ATP Transport in Saccular Cerebral Aneurysms at Arterial Bends', *Annals of Biomedical Engineering,* 38(3), 927-934.

Imai, Y., Sato, K., Ishikawa, T. and Yamaguchi, T. (2008) 'Inflow into Saccular Cerebral Aneurysms at Arterial Bends', *Annals of Biomedical Engineering,* 36(9), 1489-1495.

Inci, S. and Spetzler, R. F. (2000) 'Intracranial Aneurysms and Arterial Hypertension: A Review and Hypothesis', *Surgical Neurology,* 53(6), 530-542.

ISAT Collaborative Group (2002) 'International Subarachnoid Aneurysm Trial (ISAT) of neurosurgical clipping versus endovascular coiling in 2143 patients with ruptured intracranial aneurysms: a randomised trial', *The Lancet,* 360(9342), 1267-1274.

Ishikawa, T., Guimaraes, L. F. R., Oshima, S. and Yamane, R. (1998) 'Effect of non-Newtonian property of blood on flow through a stenosed tube', *Fluid Dynamics Research,* 22(5), 251-264.

ISUIA Investigators (1998) 'Unruptured Intracranial Aneurysms — Risk of Rupture and Risks of Surgical Intervention', *New England Journal of Medicine,* 339(24), 1725-1733.

Jeong, W. and Rhee, K. (2012) 'Hemodynamics of Cerebral Aneurysms: Computational Analyses of Aneurysm Progress and Treatment', *Computational and Mathematical Methods in Medicine,* 2012, 11.

John, K. and Barakat, A. I. (2001) 'Modulation of ATP/ADP Concentration at the Endothelial Surface by Shear Stress: Effect of Flow-Induced ATP Release', *Annals of Biomedical Engineering,* 29(9), 740 - 751.

Johnston, B. M., Johnston, P. R., Corney, S. and Kilpatrick, D. (2004) 'Non-Newtonian blood flow in human right coronary arteries: steady state simulations', *Journal of Biomechanics,* 37(5), 709-720.

Johnston, S. C., Wilson, C. B., Halback, V. V., Higashida, R. T., Dowd, C. F., McDermott, M. W., Applebury, C. B., Farley, T. L. and Gress, D. R. (2000) 'Endovascular and Surgical Treatment of Unruptured Cerebral Aneurysms - Comparison of Risks', *Annals of Neurology,* 48(1), 11-19.

Johnston, S. C., Zhao, S., Dudley, R. A., Berman, M. F. and Gress, D. R. (2001) 'Treatment of Unruptured Cerebral Aneurysms in California', *Stroke,* 32(3), 597-605.

Jou, L.-D., Quick, C. M., Young, W. L., Lawton, M. T., Higashida, R., Martin, A. and Saloner, D. (2003) 'Computational Approach to Quantifying Hemodynamic Forces in Giant Cerebral Aneurysms', *American Journal of Neuroradiology,* 24(9), 1804-1810.

Kaazempur-Mofrad, M. R. and Ethier, C. R. (2001) 'Mass Transport in an Anatomically Realistic Human Right Coronary Artery', *Annals of Biomedical Engineering,* 29(2), 121-127.

Kaazempur-Mofrad, M. R., Wada, S., Myers, J. G. and Ethier, C. R. (2005) 'Mass Transport and Fluid Flow in Stenotic Arteries: Axisymmetric and Asymmetric Models', *International Journal of Heat and Mass Transfer,* 48(21-22), 4510-4517.

Kallmes, D. F., Ding, Y. H., Dai, D., Kadirvel, R., Lewis, D. A. and Cloft, H. J. (2007) 'A New Endoluminal, Flow-Disrupting Device for Treatment of Saccular Aneurysms', *Stroke,* 38(8), 2346-2352.

Karner, G. and Perktold, K. (2000) 'Effect of endothelial injury and increased blood pressure on albumin accumulation in the arterial wall: a numerical study', *Journal of Biomechanics,* 33(6), 709-715.

Khakpour, M. and Vafai, K. (2008a) 'A Comprehensive Analytical Solution of Macromolecular Transport within an Artery', *International Journal of Heat and Mass Transfer,* 51(11-12), 2905-2913.

Khakpour, M. and Vafai, K. (2008b) 'Critical assessment of arterial transport models', *International Journal of Heat and Mass Transfer,* 51(3-4), 807-822.

Kim, C. S., Kiris, C., Kwak, D. and David, T. (2005) 'Numerical Simulation of Local Blood Flow in the Carotid and Cerebral Arteries Under Altered Gravity', *Journal of Biomechanical Engineering,* 128(2), 194-202.

Kim, M., Taulbee, D. B., Tremmel, M. and Meng, H. (2008) 'Comparison of Two Stents in Modifying Cerebral Aneurysm Hemodynamics', *Annals of Biomedical Engineering,* 36(5), 726-741.

Knox, K., Kerber, C. W., Singel, S. A., Bailey, M. J. and Imbesi, S. G. (2005) 'Rapid prototyping to create vascular replicas from CT scan data: Making tools to

teach, rehearse, an d choose t reatment s trategies', *Catheterization and Cardiovascular Interventions,* 65(1), 47-53.

Knox, K ., K erber, C . W., S ingel, S . A ., B ailey, M . J . a nd I mbesi, S . G . (2005) 'Stereolithographic V ascular R eplicas f rom CT S cans: C hoosing T reatment Strategies, T eaching, and R esearch from Live P atient S can D ata', *American Journal of Neuroradiology,* 26(6), 1428-1431.

Kolachalama, V. B., Tzafriri, A. R., Arifin, D. Y. and Edelman, E. R. (2009) 'Luminal flow p atterns d ictate arterial d rug d eposition in s tent-based de livery', *Journal of Controlled Release,* 133(1), 24-30.

Krabbe-Hartkamp, M. J., Grond, J. v. d., L eeuw, F. E. d., G root, J. C. d., A lgra, A., Hillen, B., Breteler, M. M. B. and Mali, W. P. T. M. (1998) 'Circle of Willis: Morphologic V ariation on T hree-dimensional T ime-of-Flight M R Angiograms', *Radiology,* 207(1), 103-111.

Lall, R . R ., E ddleman, C. S ., B endok, B . R . and B atjer, H. H . (2009) 'Unruptured Intracranial A neurysms a nd t he A ssessment of R upture R isk B ased on Anatomical a nd M orphological F actors: S ifting Through t he S ands of D ata', *Neurosurgical Focus,* 26(5).

Larrabide, I., Villa-Uriol, M. C., Cárdenes, R., Pozo, J. M., Macho, J., Roman, L. S., Blasco, J., Vivas, E., Marzo, A., Hose, D. R. and Frangi, A. F. (2011) 'Three-dimensional mo rphological a nalysis o f in tracranial a neurysms: A f ully automated m ethod for aneurysm s ac i solation and qua ntification', *Medical Physics,* 38(5), 2439-2449.

Lasheras, J . C . (2007) 'The B iomechanics of A rterial A neurysms', *Annual Review of Fluid Mechanics,* 39(1), 293-319.

Levick, J . R . (2010) *An Introduction to Cardiovascular Physiology,* 5th E dition e d., London: Hodder Arnold.

Liou, T.-M., Li, Y.-C. and Juan, W.-C. (2007) 'Numerical and experimental studies on pulsatile f low i n an eurysms ar ising l aterally from a cu rved p arent v essel at various angles', *Journal of Biomechanics,* 40(6), 1268-1275.

Liou, T. M., Chang, W. C. and Liao, C. C. (1997) 'Experimental Study of Steady and Pulsatile F lows i n Cerebral A neurysm M odel of V arious S izes a t B ranching Site', *Journal of Biomechanical Engineering,* 119(3), 325-332.

Liou, T. M. and Liao, C. C. (1997) 'Flowfields in lateral aneurysm models arising from parent ve ssels w ith di fferent c urvatures us ing PTV', *Experiments in Fluids,* 23(4), 288-298.

Liou, T. M. and Liou, S. N. (1999) 'A Review on In-Vitro Studies of Hemodynamic Characteristics in Terminal and Lateral Aneurysm Models', *Proceedings of the National Science Council,* 23(4), 133-148.

Liu, J., Xiang, J., Zhang, Y., Wang, Y., Li, H., Meng, H. and Yang, X. (2014) 'Morphologic and hemodynamic analysis of paraclinoid aneurysms: ruptured versus unruptured', *Journal of NeuroInterventional Surgery,* 6, 658-663.

Liu, X., Fan, Y. and Deng, X. (2011) 'Effect of the endothelial glycocalyx layer on arterial LDL transport under normal and high pressure', *Journal of Theoretical Biology,* 283(1), 71-81.

Liu, X., Fan, Y., Deng, X. and Zhan, F. (2011) 'Effect of non-Newtonian and pulsatile blood flow on mass transport in the human aorta', *Journal of Biomechanics,* 44(6), 1123-1131.

Lu, J., Zhou, X. and Raghavan, M. (2008) 'Inverse method of stress analysis for cerebral aneurysms', *Biomechanics and Modeling in Mechanobiology,* 7(6), 477-486.

Lutostansky, E. M., Karner, G., Rappitsch, G., Ku, D. N. and Perktold, K. (2003) 'Analysis of Hemodynamic Fluid Phase Mass Transport in a Separated Flow Region', *Journal of Biomechanical Engineering,* 125(2), 189-196.

Ma, B., Harbaugh, R. E. and Raghavan, M. L. (2004) 'Three-dimensional geometrical characterization of cerebral aneurysms', *Annals of Biomedical Engineering,* 32(2), 264-273.

Manguoglu, M., Takizawa, K., Sameh, A. and Tezduyar, T. (2010) 'Solution of linear systems in arterial fluid mechanics computations with boundary layer mesh refinement', *Computational Mechanics,* 46(1), 83-89.

Mantha, A., Karmonik, C., Benndorf, G., Strother, C. and Metcalfe, R. (2006) 'Hemodynamics in a Cerebral Artery before and after the Formation of an Aneurysm', *American Journal of Neuroradiology,* 27, 1113-1118.

Massey, B. (2006) *Mechanics of Fluids,* London and New York: Taylor and Francis.

Mehra, M., Spilberg, G., Gounis, M. and Wakhloo, A. (2011) 'Intracranial Aneurysms: Clinical Assessment and Treatment Options' in McGloughlin, T., ed. *Biomechanics and Mechanobiology of Aneurysms*, Springer Berlin Heidelberg, 331-372.

Meng, H., Metaxa, E., Gao, L., Liaw, N., Natarajan, S. K., Swartz, D. D., Siddiqui, A. H., K olega, J . a nd M occo, J . (2011) 'Progressive a neurysm de velopment following hemodynamic insult', *Journal of Neurosurgery,* 114(4), 1095-1103.

Meng, H., Tutino, V. M., Xiang, J. and Siddiqui, A. (2013) 'High WSS or Low WSS? Complex Interactions of Hemodynamics with Intracranial Aneurysm Initiation, Growth, a nd R upture: T oward a U nifying Hypothesis', *American Journal of Neuroradiology,* 35, 1254-1262.

Meng, H ., W ang, Z ., H oi, Y ., G ao, L ., M extexa, E ., S wartz, D . D . a nd K olega, J . (2007) 'Complex H emodynamics at t he A pex of a n A rterial Bifurcation Induces Vascular R emodeling R esembling C erebral A neurysm Initiation', *Stroke,* 38, 1924-1931.

Meyers, P . M ., S chumacher, H . C ., H igashida, R . T ., D erdeyn, C . P ., N esbit, G . M ., Sacks, D., W echsler, L. R., B ederson, J . B ., Lavine, S . D . and R asmussen, P . (2009) 'Reporting S tandards for E ndovascular R epair of S accular Intracranial Cerebral A neurysms', *Journal of Vascular and Interventional Radiology,* 20(7), S435-S450.

Miura, Y ., Ishida, F ., Umeda, Y ., Tanemura, H ., S uzuki, H ., M atsushima, S ., Shimosaka, S . a nd T aki, W . (2013) 'L ow W all S hear S tress Is Independently Associated W ith t he R upture S tatus of M iddle Cerebral A rtery A neurysms', *Stroke,* 44(2), 519-521.

Moon, J. Y., Suh, D. C., Lee, Y. S., Kim, Y. W. and Lee, J. S. (2014) 'Considerations of Blood Properties, Outlet Boundary Conditions and Energy Loss Approaches in Computational Fluid Dynamics Modeling', *Neurointervention,* 9(1), 1-8.

Moore, S., David, T., Chase, J. G., Arnold, J. and Fink, J. (2006) '3D models of blood flow in the cerebral vasculature', *Journal of Biomechanics,* 39(8), 1454-1463.

Morales, H . G ., Larrabide, I., G eers, A . J ., A guilar, M . L. a nd F rangi, A . F . (2013) 'Newtonian and n on-Newtonian bl ood f low i n c oiled cerebral aneurysms', *Journal of Biomechanics,* 46(13), 2158-2164.

Müller, J . D ., Jitsumura, M . a nd M uller-Kronast, N . H . F . (2012) 'Sensitivity o f flow simulations i n a cer ebral an eurysm', *Journal of Biomechanics,* 45(15), 2539-2548.

Mut, F ., Löhner, R ., C hien, A ., Tateshima, S ., Vinuela, F ., P utman, C . and C ebral, J . R . (2011) ' Computational H emodynamics F ramework f or t he A nalysis of Cerebral A neurysms', *International Journal for Numerical Methods in Biomedical Engineering,* 27(6), 822-839.

Nematollahi, A ., S hirani, E ., M irzaee, I. a nd Sadeghi, M . R . (2012) ' Numerical simulation of LDL p articles m ass t ransport i n human c arotid artery under steady state conditions', *Scientia Iranica,* 19(3), 519-524.

O'Connell, B. M. (2009) *On the Mass Transport Behaviour of Drugs in the Treatment of Coronary Artery Disease Using Drug Eluting Stents*, unpubl ished t hesis (PhD), University of Limerick.

Ohashi, Y ., H orikoshi, T., S ugita, M ., Y agishita, T . a nd N ukui, H . (2004) ' Size of cerebral a neurysms a nd r elated f actors i n pa tients w ith s ubarachnoid hemorrhage', *Surgical Neurology,* 61(3), 239-245.

Orz, Y ., K obayashi, S ., O sawa, M . a nd T anaka, Y . (1997) ' Aneurysm s ize: a prognostic factor for rupture', *British Journal of Neurosurgery,* 11(2), 144-149.

Parlea, L., Fahrig, R., Holdsworth, D. W. and Lownie, S. P. (1999) 'An Analysis of the Geometry o f S accular Intracranial A neurysms', *American Journal of Neuroradiology,* 20, 1079-1089.

Paszkowiak, J. J. and Dardik, A. (2003) 'Arterial Wall Shear Stress: Observations from the Bench to the Bedside', *Vascular and Endovascular Surgery,* 37(1), 47-57.

Prakash, S . a nd E thier, C . R . (2000) 'Requirements f or M esh R esolution i n 3D Computational H emodynamics', *Journal of Biomechanical Engineering,* 123(2), 134-144.

Prosi, M ., Z unino, P ., Perktold, K . a nd Q uarteroni, A . (2005) ' Mathematical a nd numerical m odels f or t ransfer of l ow-density l ipoproteins t hrough t he arterial walls: a n ew m ethodology for the model set up with applications to the study of disturbed lumenal flow', *Journal of Biomechanics,* 38(4), 903-917.

Qian, Y ., T akao, H ., Umezu, M . a nd M urayama, Y . (2011) 'Risk A nalysis of Unruptured A neurysms Using C omputational F luid D ynamics T echnology: Preliminary Results', *American Journal of Neuroradiology,* 32(10), 1948-1955.

Raghavan, M. L., Ma, B. and Harbaugh, R. E. (2005) 'Quantified Aneurysm Shape and Rupture Risk', *Journal of Neurosurgery,* 102(2), 355-362.

Rappitsch, G . a nd P erktold, K . (1996) 'Computer s imulation of c onvective di ffusion processes in large arteries', *Journal of Biomechanics,* 29(2), 207-215.

Rengier, F ., M ehndiratta, A ., von T engg-Kobligk, H ., Zechmann, C . M ., Unterhinninghofen, R ., Kauczor, H . U . a nd G iesel, F . L. (2010) '3D p rinting

based on imaging data: review of medical applications', *International Journal of Computer Assisted Radiology and Surgery,* 5(4), 335-341.

Rinkel, G. J. E., Djibuti, M., Algra, A. and van Gijn, J. (1998) 'Prevalence and Risk of Rupture of Intracranial Aneurysms: A Systematic Review', *Stroke,* 29(1), 251-256.

Ritman, E. L. and Lerman, A. (2007) 'The Dynamic Vasa Vasorum', *Cardiovascular Research,* 75(4), 649-658.

Roessler, F. C., Reith, W. and Siegel, G. (2006) 'Simulation of Cerebral Hemodynamics for Preoperative Risk Assessment', *Brain Research,* 1118(1), 183 - 191.

Roy, D., Raymond, J., Bouthillier, A., Bojanowski, M. W., Moumdjian, R. and L'Espérance, G. (1997) 'Endovascular treatment of ophthalmic segment aneurysms with Guglielmi detachable coils', *American Journal of Neuroradiology,* 18(7), 1207-1215.

Sato, K., Imai, Y., Ishikawa, T., Matsuki, N. and Yamaguchi, T. (2008) 'The importance of parent artery geometry in intra-aneurysmal hemodynamics', *Medical Engineering and Physics,* 30(6), 774-782.

Schievink, W. I. (1997) 'Intracranial Aneurysms', *The New England Journal of Medicine,* 336(1), 28-40.

Sen, Y., Qian, Y., Avolio, A. and Morgan, M. (2014) 'Image segmentation methods for intracranial aneurysm haemodynamic research', *Journal of Biomechanics,* 47(5), 1014-1019.

Sforza, D. M., Putman, C. M. and Cebral, J. R. (2009) 'Hemodynamics of Cerebral Aneurysms', *Annual Review of Fluid Mechanics,* 41(a), 91-107.

Shen, J., Gimbrone, M. A., Luscinskas, F. W. and Jr., C. F. D. (1993) 'Regulation of adenine nucleotide concentration at endothelium-fluid interface by viscous shear flow', *Biophysical Journal,* 64(4), 1323-1330.

Shibeshi, S. S. and Collins, W. E. (2005) 'The Rheology of Blood Flow in a Branched Arterial System', *Applied Rheology,* 15(6), 398 - 405.

Shojima, M., Oshima, M., Takagi, K., Torii, R., Hayakawa, M., Katada, K., Morita, A. and Kirino, T. (2004) 'Magnitude and Role of Wall Shear Stress on Cerebral Aneurysm: Computational Fluid Dynamic Study of 20 Middle Cerebral Artery Aneurysms', *Stroke,* 35, 2500-2505.

Soulis, J., Giannoglou, G., Papaioannou, V., Parcharidis, G. and Louridas, G. (2008) 'Low-density lipoprotein concentration in the normal left coronary artery tree', *BioMedical Engineering OnLine*, 7(1), 26.

Spiegel, M., Regel, T., Zhang, Y. J., Struffert, T., Hornegger, J., Grossman, R. G., Doerfler, A. and Karmonik, C. (2011) 'Tetrahedral vs. polyhedral mesh size evaluation on flow velocity and wall shear stress for cerebral hemodynamic simulation', *Computer Methods in Biomechanics and Biomedical Engineering*, 14(1), 9-22.

Stangeby, D. K. and Ethier, C. R. (2002) 'Computational Analysis of Coupled Blood-Wall Arterial LDL Transport', *Journal of Biomechanical Engineering*, 124(1), 1-8.

Stehbens, W. E. (1959) 'Turbulence of Blood Flow', *Experimental Physiology*, 44(1), 110-117.

Steinman, D. A., Hoi, Y., Fahy, P., Morris, L., Walsh, M. T., Aristokleous, N., Anayiotos, A. S., Papaharilaou, Y., Arzani, A., Shadden, S. C., Berg, P., Janiga, G., Bols, J., Segers, P., Bressloff, N. W., Cibis, M., Gijsen, F. H., Cito, S., Pallarés, J., Browne, L. D., Costelloe, J. A., Lynch, A. G., Degroote, J., Vierendeels, J., Fu, W., Qiao, A., Hodis, S., Kallmes, D. F., Kalsi, H., Long, Q., Kheyfets, V. O., Finol, E. A., Kono, K., Malek, A. M., Lauric, A., Menon, P. G., Pekkan, K., Esmaily Moghadam, M., Marsden, A. L., Oshima, M., Katagiri, K., Peiffer, V., Mohamied, Y., Sherwin, S. J., Schaller, J., Goubergrits, L., Usera, G., Mendina, M., Valen-Sendstad, K., Habets, D. F., Xiang, J., Meng, H., Yu, Y., Karniadakis, G. E., Shaffer, N. and Loth, F. (2013) 'Variability of Computational Fluid Dynamics Solutions for Pressure and Flow in a Giant Aneurysm: The ASME 2012 Summer Bioengineering Conference CFD Challenge', *Journal of Biomechanical Engineering*, 135(2), 021016-021016.

Steinman, D. A., Milner, J. S., Norley, C. J., Lownie, S. P. and Holdsworth, D. W. (2003) 'Image-Based Computational Simulation of Flow Dynamics in a Giant Intracranial Aneurysm', *American Journal of Neuroradiology*, 24(4), 559-566.

Stevens, J. P. (2012) *Applied Multivariate Statistics for the Social Sciences*, 5th ed., New York, USA: Routledge.

Sun, N., Wood, N. B., Hughes, A. D., Thom, S. A. M. and Xu, X. Y. (2006) 'Fluid-Wall Modelling of Mass Transfer in an Axisymmetric Stenosis: Effects of Shear-Dependent Transport Properties', *Annals of Biomedical Engineering*, 34(7), 1119-1128.

Sun, N., Wood, N. B., Hughes, A. D., Thom, S. A. M. and Zu, X. Y. (2007) 'Effects of transmural pressure and wall shear stress on LDL accumulation in the arterial wall: a numerical study using a multilayered model', *American Journal of Physiology Heart and Circulatory Physiology*, 292(6), H3148 - H3157.

Tada, S. and Tarbell, J. M. (2004) 'Internal elastic lamina affects the distribution of macromolecules in the arterial wall: a computational study', *American Journal of Physiology Heart and Circulatory Physiology*, 287, H905-H913.

Takao, H., Murayama, Y., Otsuka, S., Qian, Y., Mohamed, A., Masuda, S., Yamamoto, M. and Abe, T. (2012) 'Hemodynamic Differences Between Unruptured and Ruptured Intracranial Aneurysms During Observation', *Stroke*, 43(5), 1436-1439.

Takeuchi, S. and Karino, T. (2010) 'Flow patterns and distributions of fluid velocity and wall shear stress in the human internal carotid and middle cerebral arteries', *World Neurosurgery*, 73(3), 174-185.

Takizawa, K., Moorman, C., Wright, S., Christopher, J. and Tezduyar, T. (2010) 'Wall shear stress calculations in space–time finite element computation of arterial fluid–structure interactions', *Computational Mechanics*, 46(1), 31-41.

Tarbell, J. M. (2003) 'Mass Transport in Arteries and the Localization of Atherosclerosis', *Annual Review of Biomedical Engineering*, 5, 79-118.

Tarbell, J. M. and Qiu, Y. (2000) 'Arterial Wall Mass Transport: The Possible Role of Blood Phase Resistance in the Localization of Arterial Disease', *Biomedical Engineering Handbook: Second Edition*.

Tateshima, S., Murayama, Y., Pablo, J., Villablanca, P., Morino, T., Nomura, K., Tanishita, K. and Vinuela, F. (2003) 'In Vitro Measurement of Fluid-Induced Wall Shear Stress in Unruptured Cerebral Aneurysms Harboring Blebs', *Stroke*, 34, 187-192.

Taylor, C. A. and Figueroa, C. A. (2009) 'Patient-Specific Modeling of Cardiovascular Mechanics', *Annual Review of Biomedical Engineering*, 11(1), 109-134.

Torii, R., Oshima, M., Kobayashi, T., Takagi, K. and Tezduyar, T. E. (2007) 'Influence of wall elasticity in patient-specific hemodynamic simulations', *Computers & Fluids*, 36(1), 160-168.

Ujiie, H., Tachibana, H., Hiramatsu, O., Hazel, A. L., Matsumoto, T., Ogasawara, Y., Nakajima, H., Hori, T., Takakura, K. and Kajiya, F. (1999) 'Effects of Size and Shape (Aspect Ratio) on the Hemodynamics of Saccular Aneurysms: A

Possible Index for Surgical Treatment of Intracranial Aneurysms', *Neurosurgery,* 45(1), 119-129.

Ujiie, H., Tamano, Y., Sasaki, K. and Hori, T. (2001) 'Is the Aspect Ratio a Reliable Index for Predicting the Rupture of a Saccular Aneurysm?', *Neurosurgery,* 48(3), 495-503.

Valencia, A., Morales, H., Rivera, R., Bravo, E. and Galvez, M. (2008) 'Blood Flow Dynamics in Patient-Specific Cerebral Aneurysm Models: The Relationship Between Wall Shear Stress and Aneurysm Area Index', *Medical Engineering and Physics,* 30(3), 329 - 340.

Valencia, A. and Solis, F. (2006) 'Blood flow dynamics and arterial wall interaction in a saccular aneurysm model of the basilar artery', *Computers and Structures,* 84(21), 1326-1337.

Valencia, A., Zarate, A., Galvez, M. and Badilla, L. (2006) 'Non-Newtonian blood flow dynamics in a right internal carotid artery with a saccular aneurysm', *International Journal for Numerical Methods in Fluids,* 50(6), 751-764.

Valencia, A. A., Guzmán, A. M., Finol, E. A. and Amon, C. H. (2006) 'Blood Flow Dynamics in Saccular Aneurysm Models of the Basilar Artery', *Journal of Biomechanical Engineering,* 128(4), 516-526.

Vega, C., Kwoon, J. V. and Lavine, S. D. (2002) 'Intracranial Aneurysms: Current Evidence and Clinical Practice', *American Family Physician,* 66(4), 601-609.

Villa-Uriol, M. C., Berti, G., Hose, D. R., Marzo, A., Chiarini, A., Penrose, J., Pozo, J., Schmidt, J. G., Singh, P., Lycett, R., Larrabide, I. and Frangi, A. F. (2011) '@neurIST complex information processing toolchain for the integrated management of cerebral aneurysms', *Interface Focus,* 1(3), 308-319.

Vincent, P. E. and Weinberg, P. D. (2013) 'Flow-dependent concentration polarization and the endothelial glycocalyx layer: multi-scale aspects of arterial mass transport and their implications for atherosclerosis', *Biomechanics and Modeling in Mechanobiology*, 1-14.

Volkau, I., Weili, Z., Baimouratov, R., Aziz, A. and Nowinski, W. L. (2005) 'Geometric modeling of the human normal cerebral arterial system', *Medical Imaging, IEEE Transactions on,* 24(4), 529-539.

Wada, S. and Karino, T. (2000) 'Computational Study on LDL Transfer from Flowing Blood to Arterial Walls' in Yamaguchi, T., ed. *Clinical Application of Computational Mechanics to the Cardiovascular System*, Springer Japan, 157-173.

Wada, S. and Karino, T. (2002) 'Theoretical Prediction of Low-Density Lipoproteins Concentration at the Luminal Surface of an Artery with a Multiple Bend', *Annals of Biomedical Engineering,* 30(6), 778-791.

Wada, S., Koujiya, M. and Karino, T. (2002) 'Theoretical study of the effect of local flow disturbances on the concentration of low-density lipoproteins at the luminal surface of end-to-end anastomosed vessels', *Medical and Biological Engineering and Computing,* 40(5), 576-587.

Wetzel, S. G., Ohta, M., Handa, A., Auer, J.-M., Lylyk, P., Lovblad, K.-O., Babic, D. and Rufenacht, D. A. (2005) 'From Patient to Model: Stereolithographic Modeling of the Cerebral Vasculature Based on Rotational Angiography', *American Journal of Neuroradiology,* 26(6), 1425-1427.

Wiebers, D. O., Piepgras, D. G., Meyer, F. B., Kallmes, D. F., Meissner, I., Atkinson, J. L. D., Link, M. J. and Brown, R. D. (2004) 'Pathogenesis, Natural History, and Treatment of Unruptured Intracranial Aneurysms', *Mayo Clinic Proceedings,* 79(12), 1572-1583.

Wood, N. B. (1999) 'Aspects of Fluid Dynamics Applied to the Larger Arteries', *Journal of Theoretical Biology,* 199(2), 137-161.

Xiang, J., Natarajan, S. H., Tremmel, M., Ma, D., Mocco, J., Hopkins, L. N., Siddiqui, A. H., Levy, E. I. and Meng, H. (2011) 'Hemodynamic-Morphologic Discriminants for Intracranial Aneurysm Rupture', *Stroke,* 42, 144-152.

Xiang, J., Tremmel, M., Kolega, J., Levy, E. I., Natarajan, S. K. and Meng, H. (2011) 'Newtonian viscosity model could overestimate wall shear stress in intracranial aneurysm domes and underestimate rupture risk', *Journal of NeuroInterventional Surgery*.

Yang, N. and Vafai, K. (2006) 'Modeling of Low-Density Lipoprotein (LDL) Transport in the Artery - Effects of Hypertension', *International Journal of Heat and Mass Transfer,* 49(5-6), 850-867.

Yu, S. C. M. and Zhao, J. B. (1999) 'A steady flow analysis on the stented and non-stented sidewall aneurysm models', *Medical Engineering & Physics,* 21(3), 133-141.

Yu, S. C. M. and Zhao, J. B. (2000) 'A particle image velocimetry study on the pulsatile flow characteristics in straight tubes with an a symmetric bulge', *Proceedings of the Institution of Mechanical Engineers, Part C: Journal of Mechanical Engineering Science,* 214(5), 655-671.

Zakaria, H., Robertson, A. M. and Kerber, C. W. (2008) 'A Parametric Model for Studies of Flow in Arterial Bifurcations', *Annals of Biomedical Engineering,* 36(9), 1515-1530.

APPENDIX

JOURNAL PUBLICATIONS

Journal of Biomechanical Engineering

2013 Volume 135 Issue 2

Variability of Computational Fluid Dynamics Solutions for Pressure and Flow in a Giant Aneurysm: The ASME 2012 Summer Bioengineering Conference CFD Challenge

http://dx.doi.org/ 10.1115/1.4023382